

Nanomaterials for Biomedical Applications: Synthesis, Characterization, and Applications

Guest Editors: M. Bououdina, S. Rashdan, J. L. Bobet, and Y. Ichiyanagi





Nanomaterials for Biomedical Applications: Synthesis, Characterization, and Applications

Journal of Nanomaterials

**Nanomaterials for Biomedical Applications:
Synthesis, Characterization, and Applications**

Guest Editors: M. Bououdina, S. Rashdan, J. L. Bobet,
and Y. Ichiyanagi



Copyright © 2013 Hindawi Publishing Corporation. All rights reserved.

This is a special issue published in "Journal of Nanomaterials." All articles are open access articles distributed under the Creative Commons Attribution License, which permits unrestricted use, distribution, and reproduction in any medium, provided the original work is properly cited.

Editorial Board

- Katerina E. Aifantis, Greece
Nageh K. Allam, USA
Margarida Amaral, Portugal
Xuedong Bai, China
Lavinia Balan, France
Enrico Bergamaschi, Italy
Theodorian Borca-Tasciuc, USA
C. Jeffrey Brinker, USA
Christian Brosseau, France
Xuebo Cao, China
Shafiq Chowdhury, USA
Kwang-Leong Choy, UK
Cui ChunXiang, China
Miguel A. Correa-Duarte, Spain
Shadi A. Dayeh, USA
Claude Estournès, France
Alan Fuchs, USA
Lian Gao, China
Russell E. Gorga, USA
Hongchen Chen Gu, China
Mustafa O. Guler, Turkey
John Zhanhu Guo, USA
Smrati Gupta, Germany
Michael Harris, USA
Zhongkui Hong, China
Michael Z. Hu, USA
David Hui, USA
Y.-K. Jeong, Republic of Korea
Sheng-Rui Jian, Taiwan
Wanqin Jin, China
Rakesh K. Joshi, UK
Zhenhui Kang, China
Fathallah Karimzadeh, Iran
Alireza Khataee, Iran
- Do Kyung Kim, Korea
Alan K. T. Lau, Hong Kong
Burtrand Lee, USA
Jun Li, Singapore
Benxia Li, China
Xing-Jie Liang, China
Shijun Liao, China
Gong Ru Lin, Taiwan
J. -Y. Liu, USA
Tianxi Liu, China
Jue Lu, USA
Songwei Lu, USA
Daniel Lu, China
Ed Ma, USA
Gaurav Mago, USA
Santanu K. Maiti, India
Sanjay R. Mathur, Germany
Vikas Mittal, UAE
Weihai Ni, Germany
Sherine Obare, USA
Atsuto Okamoto, Japan
Abdelwahab Omri, Canada
Edward Andrew Payzant, USA
Kui-Qing Peng, China
Anukorn Phuruangrat, Thailand
Suprakas Sinha Ray, South Africa
Ugur Serincan, Turkey
Huaiyu Shao, Japan
Donglu Shi, USA
Vladimir Sivakov, Germany
Marinella Striccoli, Italy
Bohua Sun, South Africa
Saikat Talapatra, USA
Nairong Tao, China
- Titipun Thongtem, Thailand
Somchai Thongtem, Thailand
Alexander Tolmachev, Ukraine
Valeri P. Tolstoy, Russia
Tsun-Yen Tsai, Taiwan
Takuya Tsuzuki, Australia
Raquel Verdejo, Spain
Mat U. Wahit, Malaysia
Zhenbo Wang, China
Ruiping Wang, Canada
Shiren Wang, USA
Cheng Wang, China
Yong Wang, USA
Jinquan Wei, China
Ching-Ping Wong, Hong Kong
Xingcai Wu, China
Guodong Xia, Hong Kong
Zhi Li Xiao, USA
Ping Xiao, UK
Yangchuan Xing, USA
Shuangxi Xing, China
N. Xu, China
Doron Yadlovker, Israel
Yingkui Yang, China
Khaled Youssef, USA
Kui Yu, Canada
William W. Yu, USA
Haibo Zeng, China
Tianyou Zhai, Japan
Renyun Zhang, Sweden
Bin Zhang, China
Yanbao Zhao, China
Lianxi Zheng, Singapore
Chunyi Zhi, Hong Kong

Contents

Nanomaterials for Biomedical Applications: Synthesis, Characterization, and Applications,

M. Bououdina, S. Rashdan, J. L. Bobet, and Y. Ichiyanagi

Volume 2013, Article ID 962384, 4 pages

Antifungal Applications of Ag-Decorated Hydroxyapatite Nanoparticles, C. A. Zamperini, R. S. André,

V. M. Longo, E. G. Mima, C. E. Vergani, A. L. Machado, J. A. Varela, and E. Longo

Volume 2013, Article ID 174398, 9 pages

Adsorption of Albumin on Silica Surfaces Modified by Silver and Copper Nanoparticles,

Prity Kumari and Peter Majewski

Volume 2013, Article ID 839016, 7 pages

Nanoscaffolds for Guided Cardiac Repair: The New Therapeutic Challenge of Regenerative Medicine,

Letizia Ventrelli, Leonardo Ricotti, Arianna Menciassi, Barbara Mazzolai, and Virgilio Mattoli

Volume 2013, Article ID 108485, 16 pages

Fabrication, Characterization, and Antimicrobial Activity, Evaluation of Low Silver Concentrations in Silver-Doped Hydroxyapatite Nanoparticles, A. Costescu, C. S. Ciobanu, S. L. Iconaru, R. V. Ghita,

C. M. Chifriuc, L. G. Marutescu, and D. Predoi

Volume 2013, Article ID 194854, 9 pages

Facile and Sensitive Epifluorescent Silica Nanoparticles for the Rapid Screening of EHEC,

Pravate Tuitemwong, Nut Songvorawit, and Kooranee Tuitemwong

Volume 2013, Article ID 706354, 8 pages

Retinoic Acid Decorated Albumin-Chitosan Nanoparticles for Targeted Delivery of Doxorubicin Hydrochloride in Hepatocellular Carcinoma, Jaleh Varshosaz, Farshid Hassanzadeh, Hojjat Sadeghi,

Zahra Ghelich Khan, and Mahboobeh Rostami

Volume 2013, Article ID 254127, 12 pages

Electrodeposition, Characterization, and Corrosion Stability of Nanostructured Anodic Oxides on New Ti-15Zr-5Nb Alloy Surface, Jose M. Calderon Moreno, Cora Vasilescu, Silviu Iulian Drob, Monica Popa,

Paula Drob, and Ecaterina Vasilescu

Volume 2013, Article ID 858935, 11 pages

Effect of SPIO Nanoparticle Concentrations on Temperature Changes for Hyperthermia via MRI,

Alsayed A. M. Elsherbini and Ahmed El-Shahawy

Volume 2013, Article ID 467878, 6 pages

Melatonin Nanoparticles Adsorbed to Polyethylene Glycol Microspheres as Activators of Human Colostrum Macrophages, Cristiane de Castro Pernet Hara, Adenilda Cristina Honorio-França,

Danny Laura Gomes Fagundes, Paulo Celso Leventi Guimarães, and Eduardo Luzía França

Volume 2013, Article ID 973179, 8 pages

Editorial

Nanomaterials for Biomedical Applications: Synthesis, Characterization, and Applications

M. Bououdina,¹ S. Rashdan,² J. L. Bobet,³ and Y. Ichiyanagi⁴

¹ Nanotechnology Centre, University of Bahrain, P.O. Box 21038, Bahrain

² Department of Chemistry, College of Science, University of Bahrain, P.O. Box 21038, Bahrain

³ Institut de Chimie de la Matière Condensée de Bordeaux, University Bordeaux I, CNRS-UPR 9048, France

⁴ Department of Physics, Yokohama National University, Yokohama 240-8501, Japan

Correspondence should be addressed to M. Bououdina; mboudina@gmail.com

Received 18 July 2013; Accepted 18 July 2013

Copyright © 2013 M. Bououdina et al. This is an open access article distributed under the Creative Commons Attribution License, which permits unrestricted use, distribution, and reproduction in any medium, provided the original work is properly cited.

Nanoscience and nanotechnology and their wide applications have become spread field worldwide because nanomaterials have novel and unique properties. The properties at the nanoscale are dependent on the size, the shape, and the components. There are a variety of nanoparticle systems currently under investigation to be applied in biomedical with the emphasis on cancer therapeutics. There are a variety of nanoparticle systems currently investigated and explored for biomedical applications with some particular emphasis for cancer therapeutics; hence some precious metals (mainly gold and silver systems, Au, and Ag) and some magnetic oxides (in particular magnetite Fe_3O_4) received much interest including quantum dots and some of what is called “natural nanoparticles.”

Also, various chemical routes have been reported for the synthesis and surface functionalisation by the attachment of specific biomolecules, optical properties, and biomedical applications of noble metal nanoparticles with various sizes, desirable shapes (nanospheres, nanodots, nanoshells, etc.), different structures, and hence tunable plasmonic properties.

This special issue is devoted to the latest techniques in nanomaterials synthesis, characterization, and biomedical applications and cancer treatment and includes broad topics such as recent development in nanomaterial synthetic methods, in particular magnetic nanoparticles, gold Nanoparticles, latest development in nanoparticle coating/core-shell, nanoparticle surface modification, role of nanomaterials

in cancer treatment, identifying the mechanism of cell penetration of the nanomaterials, and recent development in using nanomaterials in photo-killing of bacteria.

The special issue received 18 papers and after peer-reviewing process only 9 papers (50%) have been accepted. The paper presented by C. A. Zamperini et al. was devoted to the study of antifungal effect of hydroxyapatite $\text{Ca}_{10}(\text{PO}_4)_6(\text{OH})_2$ (HA) nanorods decorated with silver (Ag) nanospheres against *Candida albicans* planktonic cells. Fungistatic and fungicidal effects against tested microorganisms were observed, indicating the possibility of developing new antimicrobial agents with multiple applications in biomedical field. Moreover, a significant reduction in the number of CFU/mL was observed only at concentration of 1000 $\mu\text{g}/\text{mL}$. The biofilm matrix acts as a barrier thus protecting the deep layers of cells. SEM images reveal alterations in cell morphology (“shriveled” cells appearance), which are proportional to the concentration of HA@Ag NPs, even though some intact cells remain for higher NPs concentration. A reaction mechanism involving O_2 and H_2O adsorption was proposed to justify the antifungal activity by the interaction between the structure and the defects density variation in the interfacial (HA@Ag) and interfacial (HA) region with the fungal medium. The decomposition and desorption of the final products as well as the electron/hole recombination process have an important role in fungicidal effects.

The paper presented by Alsayed A. M. Elsherbini discusses the possibility of using magnetic NPs, for this case magnetite Fe_3O_4 suspended in glycerine solution, for hyperthermia via alternating magnetic field (AMF), in Ehrlich carcinoma cells implanted in female mice. It was found that both the specific energy dose (SED, $\text{J}\cdot\text{g}^{-1}$) and the heat deposition rate (HDR, $\text{J}\cdot\text{g}^{-1}\cdot\text{s}^{-1}$) are directly proportional to the amount (dose) of Fe_3O_4 NPs injected within tumors. The maximum temperature recorded inside the tumor subjected to AMF increases with increasing MNPs dose, varying in the range 40.11–48.6 °C for 200–1000 μg .

C. Hara et al. investigated the adsorption of the hormone melatonin to polyethylene glycol (PEG) microspheres and its functional activity of human colostrum phagocytes. Fluorescence microscopy and flow cytometry showed that PEG microspheres had ellipsoid shapes and were easily separated from the suspension, with a size in the range of 5.8 μm . After adsorption of melatonin, the size was reduced to approximately 5.35 μm , suggesting that melatonin may bind at the same site as the marker. It is found that this microsphere-based polymeric substance stimulates the functional activity of colostrum phagocytes as evidenced by the release of superoxide and intracellular calcium and thus can be used for controlled drug delivery. The superoxide anion release decreased but remained higher than that found during spontaneous release. This suggested that PEG microspheres can modify the release of melatonin while maintaining cellular activation. It is stated that the beneficial actions of melatonin are associated with its ability to remove free radicals and increase the enzymatic activity of antioxidants, as well as its immunostimulatory effects, and can stimulate cells of the immune system.

L. Ventrelli et al. presented a review paper titled “Nanoscaffolds for guided cardiac repair: the new therapeutic challenge of regenerative medicine.” The authors reported and discussed in detail the most recent achievements in the field of cell therapy for myocardial infarction treatment and heart regeneration, focusing on the commonly used cell sources, traditional approaches used to delivery cells at the damaged site. Moreover, a series of novel technologies based on recent advancements of bioengineering and tissue engineering have been illustrated, as well as highlighting patches, fragments, and biomaterials. Additionally, an original strategy for cardiac repair based on magnetic nanosheets has been discussed, highlighting the tremendous potential and promises that nanoscaffolds have within the therapeutic challenge related to heart regeneration. Finally, based on the previous findings, the authors concluded that magnetic nanofilm-based approach looks really the most promising. This therapeutic philosophy implies that the injection of cell-seeded nanosheets inside the body and its guidance up to the damaged heart site can deeply improve MI therapeutic outcomes. Furthermore, the possibility of loading the nanofilm with specific growth factors or drugs makes this new bioengineering approach even more appealing and promising.

A paper titled “Adsorption of albumin on silica surfaces modified by silver and copper nanoparticles” was presented

by P. Kumari and P. Majewski. Using magnetron sputtering method, Cu and Ag NPs were produced on the surface of silica slides (confirmed by that UV-V is spectra), where size, shape (spherical to random), and concentration depend on sputter time and plasma power. XPS reveals formation of metal oxides, Ag_2O , and CuO . Matrix-assisted laser desorption/ionization mass spectrometry analyses of the albumin adsorption on the surface with attached Ag-NPs indicate a significant delay compared to pure silica surface; albumin¹⁺ and albumin²⁺ peaks appear after 24 hrs. For the case of Cu-NPs, albumin¹⁺ and albumin²⁺ are visible after 3 hrs and 24 hrs, but it was noticed that the peaks are significantly weaker compared to those on pure silica and silica with Ag-NPs at albumin exposure for 24 hrs. This is because Cu-NPs (1 to 5 nm) are smaller than Ag-NPs (10 to 20 nm), thereby larger albumin molecules (about 8 to 10 nm) are able to attach to the silica surface to some extent by bridging smaller NPs. Finally, it was concluded that if protein attachment can be prevented during that time period, as shown for surfaces coated with Ag-NPs, the chance of infection is clearly reduced.

N. Songvorawit et al. presented a study devoted to development of antibodies conjugated fluorescent dye-doped silica nanoparticles (FDS-NPs) for the rapid detection of *Escherichia coli* O157:H7 with glass slide method. FDS-NPs were successfully synthesized by modified sol-gel reaction via water-in-oil microemulsion method, giving spherical shape with average sizes of 47 ± 6 nm. High hydrophilic Rubpy dye was chosen as an inorganic fluorescent dye. SEM-EDS results show the presence of Si (11.31% atomic), O (64.43% atomic), Ru (0.15% atomic), and C (24.11% atomic). The existence of Ru confirmed that Rubpy dye was doped inside the particles. FTIR spectra of FDS-NPs confirm that the amine group was successfully attached onto particles' surface, which facilitate the bioconjugation with the target antibodies. Thus, glutaraldehyde, which is well known as a cross-linking reagent between two amino groups of protein, was used for FDS-NPs-IgGs conjugation. Results of antibodies conjugation (IgGs) with FDS-NPs show that the average amount of immobilized IgGs on amino-modified FDS-NPs increases with increasing incubation time and temperature (4 and 37 °C). Hence, condition of 37 °C and 24 h was used as an appropriate condition for IgG coating for subsequent experiments. Zeta potential of uncoated FDS-NPs at all ionic strengths was well below -30 mV indicating that FDS-NPs were well dispersed and stable when ionic strength was 0.167. The zeta potentials of IgG coated FDS-NPs at all ion concentrations were about -40 mV and slightly decreased when ionic strength increased, which means that FDS-NPs are, moderately to well, dispersed in all conditions. Tests with bacteria reveal that IgG coated FDS-NPs tended to create aggregates in the detection of target bacteria; the detection of *E. coli* O157:H7 on glass slide was successful. FDS-NPs could attach onto target organism and give distinctively bright color. The authors conclude that the detection of bacteria with FDS-NPs is very promising though at low levels of the cells due to their ability of amplify light signal in the detection step. Capture efficiency at 0.2 mg/mL FDS-NPs

and 60 min incubation was 87.31%. IgG coated FDS-NPs had low cross-reaction to nontarget bacteria despite using polyclonal antibody with affinity purification.

The paper “*Fabrication, characterization, and antimicrobial activity, evaluation of low silver concentrations in silver-doped hydroxyapatite nanoparticles*” presented by A. Costescu et al. aims to evaluate $\text{Ca}_{10-x}\text{Ag}_x(\text{PO}_4)_6(\text{OH})_2$ nanoparticles (Ag:Hap-NPs) for their antibacterial and antifungal activities, for $x_{\text{Ag}} = 0.02, 0.05, 0.07, \text{ and } 0.10$. X-ray diffraction confirms the formation of pure single nanocrystalline HAp phase, which demonstrates that Ag^+ ions have been successfully substituted Ca^{2+} ions without affecting its crystal structure. TEM observations reveal uniform ellipsoidal morphology with sizes in the range 5–15 nm and the rings of selected area electron diffraction (SAED) pattern can be indexed with Hap reflections. Both FTIR and Raman spectra clearly reveal the presence of various vibrational modes corresponding to phosphate and hydroxyl groups. Chemical analysis confirms that Ca/P and (Ca + Ag)/P atomic ratios are close to the stoichiometric value of Hap, that is, 1.67. The antimicrobial activity of Ag:Hap ($0 \leq x_{\text{Ag}} \leq 0.1$) NPs was tested using strains belonging to the most commonly encountered pathogens: *E. coli* ATCC 25922, *E. coli* 714, *K. pneumoniae* 2968, *B. subtilis*, and *C. krusei* 963. The results indicate that low Ag concentrations are required to be effective against Gram-negative bacterial and fungal strains and that the intensity of the antimicrobial effect against these strains increases with Ag concentration. Only high Ag:HAP concentration of 5 mg/mL was effective against the Gram-positive bacterial strains. The authors concluded that the antimicrobial properties of Ag:HAP NPs support their potential use for various medical applications, for example, textile dressings, orthopedic and dental prostheses, or implants with improved resistance to microbial colonization.

J. Moreno presented a paper titled “*Electrodeposition, characterization, and corrosion stability of nanostructured anodic oxides on new Ti-15Zr-5Nb alloy surface*.” A new Ti-15Zr-5Nb alloy was elaborated by vacuum, cold-crucible, semilevitation melting method. A continuous nanostructured layer of protective TiO_2 oxide was deposited galvanostatic anodization in 0.3 and 1 M H_3PO_4 (orthophosphoric acid) solution, where three processing parameters were varied: the solution concentration, current density, and time. SEM observations of 0.3 M H_3PO_4 show a layer having two hierarchical features: hill-like protuberances with a typical width between 5 and 10 μm and nanotube-like porosity with diameters in the one to a few hundred nanometers. For 1 M H_3PO_4 showed the deposition of loose aggregates of submicron sized particles on top of a porous layer. Raman spectrum clearly shows the existence TiO_2 anatase-like structure, indicated by the existence of a strong band at 149 cm^{-1} . There was no evidence of the presence of the main characteristic vibrational band of PO_4^{3-} group. Furthermore, FT-IR spectrum shows two broad bands which were attributed to the ν_3 bending mode of the P–O–P bonds in phospho-titanate glass oxide, due to the incorporation of P^{5+} ions into the oxide coating. Cyclic potentiodynamic curves make evident a much improved behaviour of the anodized alloy than that of

the bare one, due to the formation of nanostructured layer that improves the protective properties of the native passive film by its thickening. Electrochemical impedance spectroscopy (EIS) spectra revealed a better capacitive behaviour and a more insulating protective film. This was attributed to the nanostructured film, which is formed by two layers: an inner, barrier layer that assures the alloy very good anticorrosive resistance, and an outer, porous layer that can provide the good conditions for the bone cell adhesion. Corrosion and ion release rates have lower values showing a better resistance to corrosion and implicitly a more reduced quantity of ions released in biofluid, namely, a lower toxicity of the anodized alloy. The open circuit potentials for the nanostructured alloy shifted to more positive values in time, indicating the increase of its protective layer thickness. The open circuit potential gradients have very low values that cannot generate galvanic corrosion. The obtained material satisfies the most important requirements of an implant material. Its biocompatibility and anticorrosive properties were enhanced by TiO_2 oxide which incorporated phosphorus as phospho-titanate ($\text{P}_2\text{O}_5^{2-}$) ions, thus increasing the alloy bioactivity. This composition can stimulate the formation of the bone and the porosity can offer a good scaffold for the bone cell attachment.

The paper titled “*Retinoic acid decorated albumin-chitosan nanoparticles for targeted delivery of doxorubicin hydrochloride in hepatocellular carcinoma*” was presented by J. Varshosaz et al. Retinoic acid-chitosan conjugate (RC) copolymer was confirmed by ^1H NMR and FT-IR. Twelve different formulations of RC-albumin NPs loaded with doxorubicin were prepared and their particle size, PdI zeta potential, loading efficiency (%), and release efficiency within 60 min ($\text{RE}_{60\%}$) were determined. Statistical analysis showed an increase in degree of substitution of retinoic acid in copolymer which led to a decrease in particle size. Zeta potential demonstrates that the NPs dispersion obtained by coacervation method in an aqueous system is a physically stable system. The amount of total RC and albumin was the most important factor affecting the entrapment efficiency while the role of albumin alone was negligible. In vitro drug release shows a fast release profile for doxorubicin was observed in all formulations. Also, increasing the total mass of RC and albumin significantly decreased the RE. Albumin content had low effect on release behaviour of doxorubicin from NPs. Optimization was done using design expert software and $\text{A}_{10}\text{B}_1\text{C}_{0.37}\text{R}_2$ was suggested as the optimum formulation which showed a good particle size of 286 nm, zeta potential of 30.5 mV, an acceptable entrapment efficiency of 43.6%, and relatively high release efficiency of 56.17%. TEM analysis shows NPs with spherical and some irregular shapes. Cell proliferation assay shows that IC_{50} is decreased in both targeted and nontargeted NPS compared to free doxorubicin; retinoic acid targeted NPs had the lowest IC_{50} and the highest growth inhibitory effect was observed in cells treated with RC-albumin NPs at 0.5 $\mu\text{g}/\text{mL}$. However, the cell survival percentage shows an increase in doxorubicin loaded RC-albumin NPs treated group at 1 $\mu\text{g}/\text{mL}$ concentration. Finally, Cellular uptake study reveals uptake of NPS in HepG2 cells.

Although the issue covered broad topics related to the biomedical applications of NPs, the presented papers discussed some exciting subjects within the scope of Journal of Nanomaterials, which will be beneficial for the readers and scientists.

Acknowledgments

The editors would like to express their deep appreciation to the authors for their excellent contributions and patience during the reviewing process. Additionally, all reviewers are acknowledged for their great efforts and precious time in assisting us reviewing the papers and their fruitful comments and recommendation for the authors, which improve the quality and depth of the papers.

*M. Bououdina
S. Rashdan
J. L. Bobet
Y. Ichiyanagi*

Research Article

Antifungal Applications of Ag-Decorated Hydroxyapatite Nanoparticles

C. A. Zamperini,^{1,2} R. S. André,³ V. M. Longo,¹ E. G. Mima,² C. E. Vergani,²
A. L. Machado,² J. A. Varela,¹ and E. Longo¹

¹ LIEC, UNESP-Univ Estadual Paulista, P.O. Box 355, 14801-907 Araraquara, SP, Brazil

² Department of Dental Materials and Prosthodontics, Araraquara Dental School, UNESP-Univ Estadual Paulista, 14801-903 Araraquara, SP, Brazil

³ LIEC, CMDMC, Department of Chemistry, Universidade Federal de São Carlos (UFSCar), 13565-905, São Carlos, SP, Brazil

Correspondence should be addressed to C. A. Zamperini; cazamperini@yahoo.com.br

Received 1 February 2013; Revised 23 May 2013; Accepted 26 May 2013

Academic Editor: Mohamed Bououdina

Copyright © 2013 C. A. Zamperini et al. This is an open access article distributed under the Creative Commons Attribution License, which permits unrestricted use, distribution, and reproduction in any medium, provided the original work is properly cited.

Pure hydroxyapatite (HA) and hydroxyapatite decorated with silver (HA@Ag) nanoparticles were synthesized and characterized. The antifungal effect of HA@Ag nanoparticles in a distilled water solution was evaluated against *Candida albicans*. The origin of the antifungal activity of the HA@Ag is also discussed. The results obtained showed that the HA nanorod morphology remained the same with Ag ions decorations on the HA structure which were deposited in the form of nanospheres. Interaction where occurred between the structure and its defect density variation in the interfacial HA@Ag and intrafacial HA region with the fungal medium resulted in antifungal activity. The reaction mechanisms involved oxygen and water adsorption which formed an active complex cluster. The decomposition and desorption of the final products as well as the electron/hole recombination process have an important role in fungicidal effects.

1. Introduction

HA, $\text{Ca}_{10}(\text{PO}_4)_6(\text{OH})_2$, is the major mineral component of human bone and other calcified tissues [1]. Thus, due to the similarity with bone composition and its ability to bond strongly with human hard tissue, the synthesis of HA (a bio-ceramic material) is of great interest for several clinical applications in the biomedical field [2, 3]. Synthetic HA is a versatile inorganic material that also exhibits desirable properties such as biocompatibility, bioactivity, and osteoconductivity. In medicine and dentistry, due to its bioactive properties, HA has been successfully used for bone reconstructions and as coatings for dental implants; also, the structure is similar to the human bone mineral component. However, various sources of infections exist in these biomedical interventions, including environment surfaces and surgical equipment as well as microorganisms present in body tissues. Hence, the risk of infectious complications is high and may lead to failures which entail the need for subsequent surgery

and medical costs in addition to the pain and suffering of patients. *Candida albicans* is among the most frequently isolated microorganisms from human infections, mainly in immunocompromised patients [4–6]. Although *C. albicans* is an eukaryotic commensal microorganism of human mucosal surfaces, when there is impairment of the host immunity, it can cause serious superficial and deep infections [4]. In general, the in vivo colonization of tissues and surfaces by microorganisms is related to biofilm formation. Biofilm-associated *C. albicans* cells are more resistant to antifungals commonly used compared to cells grown in planktonic form [5]. Therefore, the synthesis of HA with antifungal properties against planktonic and biofilm cells would be an important strategy to inhibit fungal colonization and, consequently, the incidence of surgical infections.

Researchers have reported that Ag-based compounds have broad-spectrum activity and a low propensity to induce microbial resistance. Silver nanoparticles (AgNPs) may attach to the cell membrane [3, 7] and cause structural

changes, and, consequently, cell death. Additionally, the formation of free radicals [8] and the release of ions by nanoparticles may contribute to the antimicrobial activity of AgNP [9, 10]. These results suggest that the incorporation of an antifungal agent such as AgNP on HA could be a step toward the formulation of new therapeutic agents.

Different synthesis methods have been reported in the literature to obtain HA crystals [11–13]. However, these procedures require long processing times as well as high temperatures which creates challenges in the development of a feasible method for the synthesis of HA nanocrystals. In this context, to obtain lower synthesis time and temperature requirements, the microwave-assisted hydrothermal (HTMW) [14, 15] method has been used in recent years and is one of the most promising methods to prepare nanomaterials with controlled size and shape [16]. Nevertheless, the challenge remains to prepare multicomponent or hybrid structures where two or more nanocrystal domains of different materials with individually tailored properties are integrated into one nanostructure.

Recently, the synthesis of Ag-doped nanocrystalline HA nanoparticles by a coprecipitation method has been reported and the antibacterial and antifungal activities were evaluated [17–19]. In these investigations, an antimicrobial effect was observed against Gram-negative and Gram-positive bacteria [17, 18] and *Candida krusei*, a fungal species [19]. In the present study, we report the synthesis of HA nanoparticles decorated with silver through a co-precipitation method with an HTMW treatment using calcium nitrate and ammonium phosphate as precursors. The silver was incorporated into the HA matrix after the synthesis. The HA@Ag powder was structurally characterized by high-resolution transmission electron microscopy (HR-TEM), X-ray diffraction (XRD), FT-Raman spectroscopy, and UV-visible spectroscopy (UV-vis). The potential fungistatic and fungicidal effects of the HA@Ag in solution against *C. albicans* were evaluated by determining the minimum inhibitory concentration (MIC) and minimum fungicidal concentration (MFC). In addition, the effects of the HA@Ag solution against the biofilm formation of *C. albicans* were also evaluated. To the authors' knowledge, such effects of HA@Ag on *C. albicans* have not been widely evaluated [20].

2. Experimental Section

2.1. Materials and Synthesis. For the synthesis of HA, two aqueous solutions were prepared: a calcium nitrate tetrahydrate solution (Mallinckrodt, 99.9%) and an ammonium phosphate solution (Mallinckrodt 99.4%). The ammonium phosphate solution was then dripped into the calcium solution with constant agitation. The system was kept under flowing N_2 throughout the mixing, and the pH solution was maintained at approximately 11 with the addition of ammonium hydroxide. The suspension containing the white solid precipitate was placed in a 100 mL Teflon autoclave which was sealed and loaded into the HTMW system using 2.45 GHz microwave radiation with 800 W of power. The system was heated to 140°C and maintained at this temperature for 1 minute at a heating rate of 140°C/min under

constant pressure (approximately 3.0 bar). After treatment, the autoclave was naturally cooled to room temperature. The resultant product was washed with deionized water several times until a neutral pH was obtained and then dried in an oven. HA@Ag was synthesized using the previously prepared HA powder dispersed in distilled water, and the pH was adjusted to 5 with HNO_3 . The solution was stirred at 60°C, and then 5 mL of $AgNO_3$ solution (1.4×10^{-2} M) was added. The precipitate was washed to pH 7 and then again dried in an oven. The working concentration was 1 mol HA : 1 mol Ag.

2.2. Characterization of the HA@Ag. Morphology and size characterizations were performed by transmission electron microscopy (TEM, Tecnai G2TF20, FEI). To confirm the presence of Ag, an energy dispersive X-ray (EDX) measurement was taken in the same apparatus. All measurements were taken at room temperature. HA@Ag samples were characterized by XRD using a Rigaku DMax 2500PC diffractometer at 40 kV and 150 mA with Cu $K\alpha$ radiation, a graphite monochromator, and a rotary anode. Raman spectra were recorded on a RFS/100/S Bruker Fourier transform Raman (FT-Raman) spectrometer with a 1064 nm excitation wavelength using a Nd:YAG laser in a spectral resolution of 4 cm^{-1} . UV-vis absorption was recorded using a Cary 5G spectrometer in total reflectance mode by the integration cell.

2.3. Antifungal Activity. *C. albicans* (ATCC 90028) was grown in Sabouraud dextrose agar (SDA, Acumedia Manufacturers Inc., Baltimore, MD, USA) containing $5\text{ }\mu\text{g/mL}$ gentamicin for 48 h at 37°C, followed by 21 h at 37°C in an RPMI-1640 culture medium. Cells of the resultant culture were harvested by centrifugation at 4000 g for 5 min, washed twice with a phosphate-buffered saline solution (PBS; pH 7.2), and resuspended in the RPMI-1640 culture medium. The estimation of minimum inhibitory concentration (MIC) and minimum fungicidal concentration (MFC), using a broth microdilution assay [21], was used to evaluate the antifungal activity of the HA@Ag solution. The determination of MIC and MFC was used because it is a standard methodology for antimicrobial tests. *C. albicans* was incubated on a 96-well microtiter plate for 48 hours at 35°C and exposed to a serial two-fold dilution in the RPMI-1640 culture medium of the HA@Ag solution (from 1000 $\mu\text{g/mL}$ to 3.90 $\mu\text{g/mL}$). The MIC value was the lowest concentration of the HA@Ag solution which resulted in no visible growth (by visual inspection). Thereafter, aliquots from each well were diluted (10^{-1} , 10^{-2} , 10^{-3} , and 10^{-4}) in PBS and inoculated on SDA (in duplicate) in order to establish the MFC. After 48 h at 37°C, the colony-forming units per milliliter (CFU/mL) were calculated, and a \log_{10} transformation was plotted. The MFC value was defined as the lowest concentration of the HA@Ag solution resulting in 99% reduction of fungal growth (UFC/mL). The assays were performed in triplicate on three separate occasions.

Additionally, the effects of the HA@Ag solution against biofilm formation of *C. albicans* also were evaluated. *C. albicans* suspensions were spectrophotometrically standardized in an RPMI-1640 culture medium at 1×10^7 CFU/mL. Initially, 200 μL aliquots were placed in each well of the 96-well

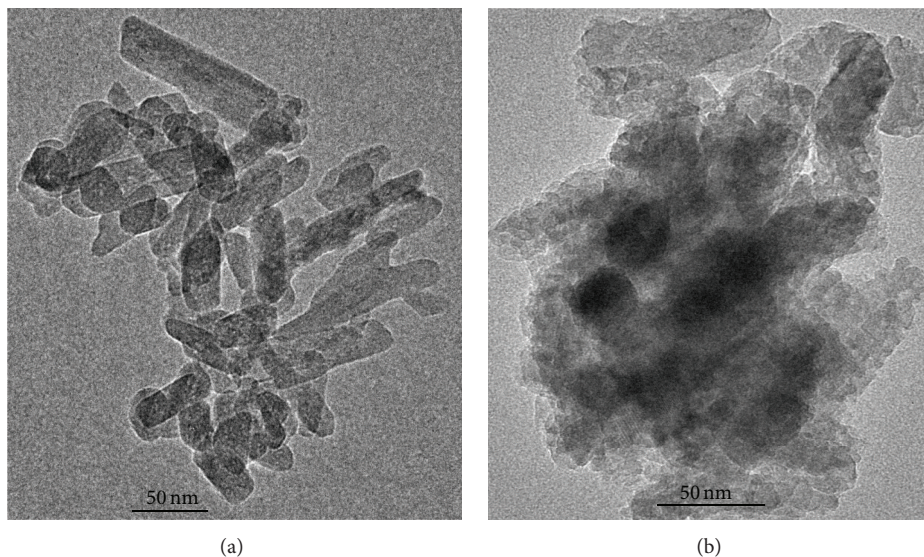


FIGURE 1: (a) TEM image of pure HA and (b) TEM image of HA@Ag.

microtiter plates and maintained for 90 min at 37°C (adhesion phase) in an orbital shaker [5]. Then, the loosely adhered cells were removed by washing twice with 200 μL of PBS. Each one of the wells was filled with 200 μL of fresh RPMI-1640 culture medium containing different concentrations of the HA@Ag solution (from 1000 $\mu\text{g}/\text{mL}$ to 3.90 $\mu\text{g}/\text{mL}$), and the plates were incubated at 37°C in an orbital shaker at 75 rpm for 48 h. After biofilm formation, the wells were carefully washed twice with 200 μL of PBS to remove nonadherent cells.

The number of viable *C. albicans* and the total biomass of the biofilms exposed to different concentrations of the HA@Ag solution were evaluated by counting the colonies which formed units (CFU/mL) and measuring the absorbance of the crystal violet staining, respectively. To enumerate the CFU/mL, biofilms were scraped out of the wells of the 96-well microtiter plate and suspended by vigorous vortex mixing (1 min) in PBS. Thereafter, 10^{-1} , 10^{-2} , 10^{-3} , and 10^{-4} dilutions were performed, and aliquots of 25 μL were inoculated on SDA plates (in duplicate). For the determination of the total biomass, the biofilms were fixed with methanol and stained with 1% violet crystal solution for 5 min. The stain bonded to biofilm was dissolved in acetic acid at 33% and the optical density was measured (570 nm) using a spectrophotometer (Thermo Plate—TP Reader). Data obtained from CFU/mL quantification and total biomass were statistically analyzed by ANOVA and Tukey's *post hoc* tests at 5% of significance.

The morphological characteristics of the biofilms formed in the presence of the HA@Ag solution also were evaluated using a field emission gun-scanning electron microscopy (FEG-SEM). For this procedure, *C. albicans* biofilms were cultured and exposed to different concentrations of HA@Ag solution on the bottom of a 24-well plate, as described previously. Following biofilm formation, these products were fixed with 2.5% glutaraldehyde in PBS for 24 hours, dehydrated in

increasing concentrations of ethanol (70%, 85%, and 90%) for 5 min each and observed in FEG-SEM (Jeol, JSM 7500 F).

3. Results and Discussion

Figure 1 shows TEM morphologies of pure HA and the HA@Ag synthesized under the same conditions, respectively. Figure 1 shows that there was very little difference between the two samples in particle size and morphologies. The pure HA (see Figure 1(a)) has a nanorod structure with a diameter varying from 12 to 27 nm. A closer look at a comparatively thin rod plate which provides sufficient transparency of electrons for high resolution is provided in Figure 2; a layered structure is apparent.

However, silver is observed in the nanospherical morphology with an interplanar distance of 0.276 nm which corresponds to the Ag (111) plane (the preferential growth plane) (see Figure 2(c)) according to the JCPDS 65-2871. The EDX spectrum of HA@Ag confirms calcium (Ca), phosphor (P), oxygen (O), and silver (Ag) in the samples (see Figure 2(a)). The presence of copper (Cu) and silicon (Si) was attributed to the sample grid support.

The characterization in a long-range order of the pure HA and HA@Ag samples was performed by XRD (see Figures 3(a) and 3(b), resp.). The HA single phase formation has a hexagonal structure with a P 63/m space group even with Ag. No planes related to the Ag phase were located. Secondary phases such as calcium carbonate, CaCO_3 , were not found in XRD results.

The HA@Ag structure in a short-range order was performed by FT-Raman analyses as a complementary structural study for XRD data. Raman spectra at room temperature in the frequency range of 400 to 1200 cm^{-1} for the HA@Ag powder processed in the HTMW system during 1 min are displayed in Figure 4. According to Penel et al. [22], all

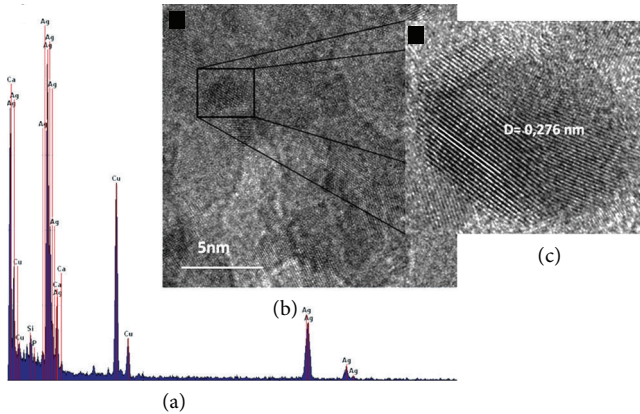


FIGURE 2: (a) An EDX measurement of HA@Ag nanoparticles; (b) HRTEM image of Ag nanospheres; and (c) a zoom of a nanoparticle with (111) interplanar distance.

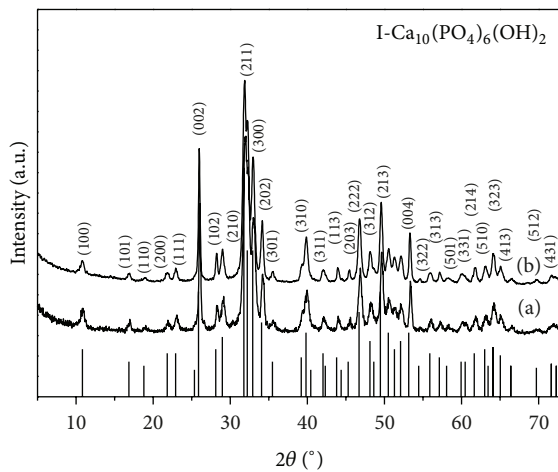


FIGURE 3: XRD patterns for (a) pure HA and (b) HA@Ag sample.

Raman modes are related to the HA phase. From Raman studies on carbonated apatite, two distinct wavenumbers of the ν_1 carbonate mode have been suggested according to OH^- or PO_4^{3-} site substitution at 1108 and 1070 cm^{-1} , respectively. Variable numbers of bands in the $\nu_1\text{PO}_4^{3-}$ domain were also detected by the authors [22]. Since none of these characteristics were found in the Raman spectrum (see Figure 4), we conclude that the HA@Ag obtained does not present the concurrent calcium carbonate phase as a second phase which agrees with XRD results that indicate the HA single phase formation.

A UV-vis analysis was conducted (see Figures 5(a) and 5(b)) to determine the electronic structure of HA@Ag. Moreover, the GAP energy was calculated by using the Wood and Tauc method from the UV-spectra for pure HA and HA@Ag. The values obtained were 4.7 eV for pure HA and 3.6 eV for HA@Ag. There is a significant difference between band gap values for both samples. The exponential optical absorption edge and the optical band gap energy are controlled by the degree of structural disorder in the lattice. The decrease in the

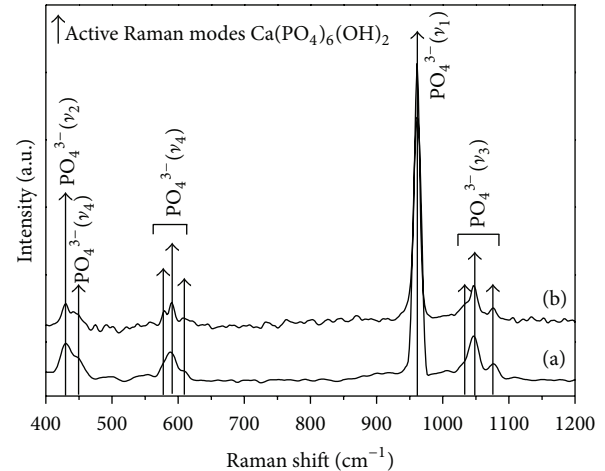


FIGURE 4: FT-Raman spectra for (a) pure HA and (b) HA@Ag.

band gap can be attributed to defects, local bond distortion, and intrinsic surface and/or interface states (HA and Ag) which yield localized electronic levels in the forbidden band gap.

We believe that this significant difference is attributed to Ag surface defects and (HA@Ag) interface defects [23] (see Figure 6).

MIC and MFC values were 62.5 $\mu\text{g}/\text{mL}$ and 250 $\mu\text{g}/\text{mL}$, respectively (Figure 7). These results demonstrate that the HA@Ag solution has fungistatic and fungicidal effects against the microorganism tested and thus indicate that it may be a potential candidate for developing new antimicrobial agents with multiple applications in the biomedical field. Although these MIC and MFC values against *C. albicans* are higher than those values obtained with commonly used antifungal agents [5] and different nanoparticles [24–26], other important aspects should be considered. First, when composites are used, the concentrations of individual nanoparticles can be decreased as well as the cytotoxicity to eukaryotic human cells [27]. Moreover, in this study, the amount of AgNO_3 used was $7 \cdot 10^{-5}$ mol with a Ag/HA ratio of 1. Hence, the combination of different nanoparticles could have a positive impact in avoiding the development of microbial resistance [27].

Bearing in mind the biofilm architecture and its role on resistance against antimicrobial agents, it was considered important to evaluate the possible effects of the HA@Ag solution against cells and extracellular polymeric matrix. The results demonstrated that, when the *C. albicans* biofilms were exposed to different concentrations of the HA@Ag solution, a significant reduction in the number of CFU/mL was observed only at a concentration of 1000 $\mu\text{g}/\text{mL}$ (see Figure 8). This result can be attributed to the higher resistance of *C. albicans* cells grown in biofilms [5, 24–26]. Although mechanisms of biofilm drug resistance are not fully understood, factors such as decreased growth rate, expression of resistance genes, and an extracellular polymeric matrix can contribute to increased tolerance of cells in biofilms [28]. The biofilm matrix acts as a barrier, protecting the deep layers of cells. Recently, Ciobanu et al. [19] evaluated the effect of nanosized particles

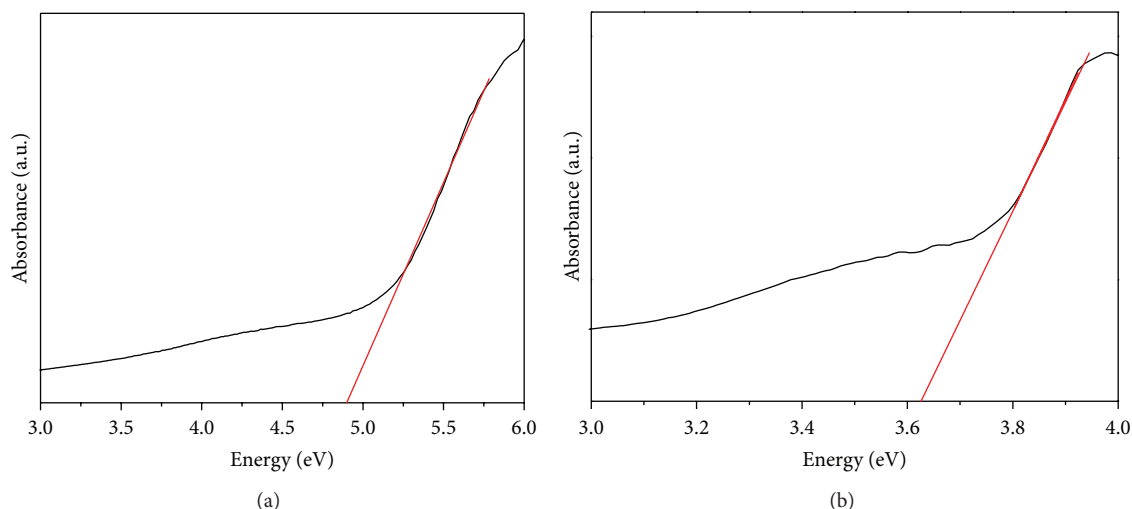


FIGURE 5: UV-vis absorbance spectra for (a) pure HA and (b) HA@Ag samples.

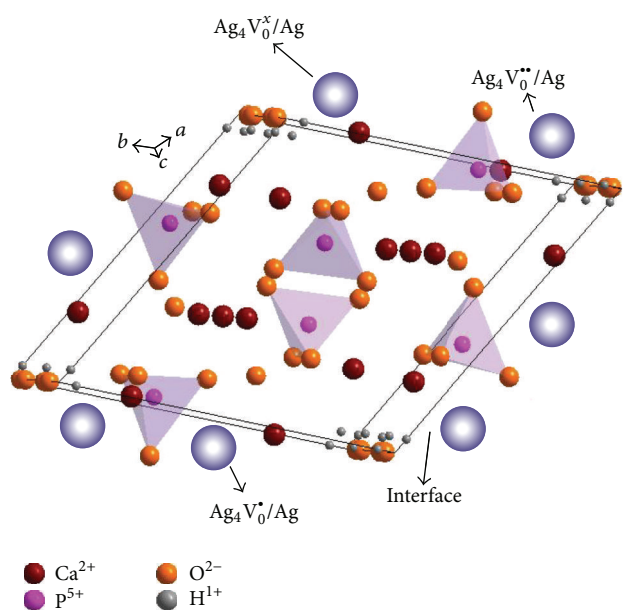


FIGURE 6: Illustration of the system with the formation of a complex cluster $[Ag_4]_d$.

of Ag-doped HA on the first step of bacterial adherence to the inert substratum and on a 24 h preformed biofilm. These authors also observed that the inhibitory effect against biofilm formation was dependent on the concentration of the nanoparticles evaluated. Other recent studies that evaluated the effect of silver nanoparticles against *C. albicans* biofilms also observed a high tolerance of this fungal specie grown in biofilms when compared to planktonic cells [24–26].

The results obtained after crystal violet staining showed significant decreases of the total biomass values when *C. albicans* biofilms were exposed to HA@Ag solution at concentrations of 1000 $\mu\text{g/mL}$, 500 $\mu\text{g/mL}$, and 250 $\mu\text{g/mL}$ (see Figure 9), showing clearly that the HA@Ag solution

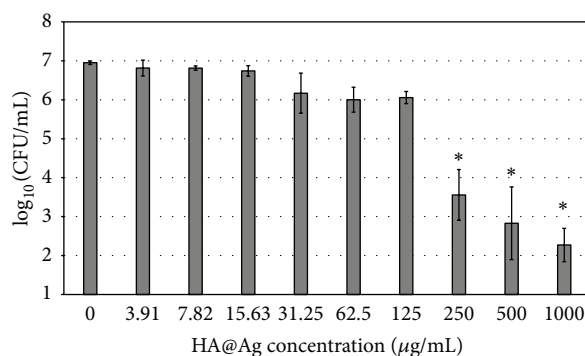


FIGURE 7: Mean values of \log_{10} (CFU/mL) of planktonic cultures of *C. albicans* exposed to HA@Ag solution. Errors bars: standard deviation. *: significant differences compared with control (0 $\mu\text{g/mL}$).

affected the extracellular matrix production. This result is important because biofilm formation is one of the major virulence factors of *C. albicans*, and its reduction makes the microorganisms more susceptible to antifungal agents and more vulnerable to host defense mechanisms. Although the biofilms matrix was reduced by the HA@Ag solution, this effect was not observed in the terms of CFU/mL. This finding suggests that the cells exhibit recovery ability after the plating, and thus, the HA@Ag solution can have a temporary and reversible effect against *C. albicans* biofilms. These results are in agreement with those observed in a recent study in which Ag nanoparticles were effective in reducing biofilm biomass when applied to biofilms of *C. albicans* and *C. glabrata*. However, the effect of Ag nanoparticles in the number of viable biofilm cells of *C. albicans* was less evident [26].

Moreover, the results obtained also demonstrated that the total biomass values of *C. albicans* biofilms exposed to concentrations of 7.82 and 3.91 $\mu\text{g/mL}$ of the HA@Ag solution were significantly higher as compared with the control (0 $\mu\text{g/mL}$). It has been reported that subinhibitory concentrations of antimicrobial agents could up regulate

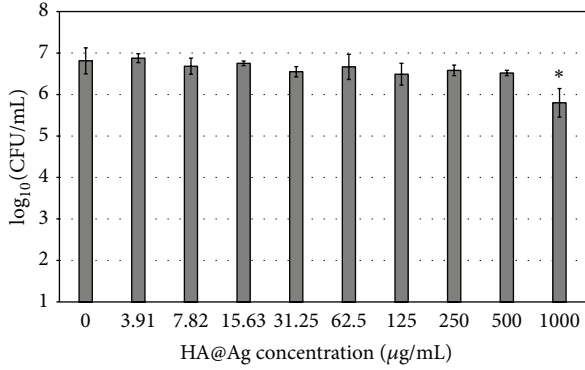


FIGURE 8: Mean values of \log_{10} (CFU/mL) of *C. albicans* biofilm exposed to HA@Ag solution. Errors bars: standard deviation. *: significant difference compared with control (0 $\mu\text{g/mL}$).

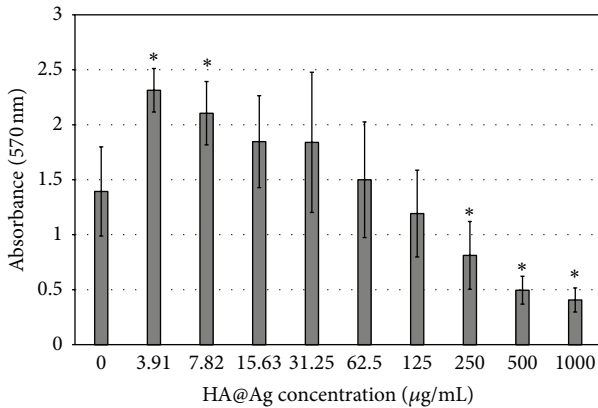


FIGURE 9: Total biomass of *C. albicans* biofilms exposed to HA@Ag solution. Errors bars: standard deviation. *: significant differences compared with control (0 $\mu\text{g/mL}$).

genes related to virulence factors, such as enzyme production [29] and biofilm formation [30].

FEI-SEM images confirm the quantitative outcomes obtained with biofilms (see Figure 10) since alterations in cell morphology (“shriveled” cells appearance) were observed proportional to the concentration of HA@Ag nanoparticles. However, as can be seen in Figure 10, some intact cells remain even in the presence of high concentrations of nanoparticles. Micrographs with none (control) or low HA@Ag content showed more cell aggregates and higher quantity of hyphal cells. *C. albicans* is able to change its morphology between yeast and filamentous (hyphae and pseudohyphae) forms in a process called polymorphism. Hyphal cells are responsible for infection in the host and are able to invade tissues. These findings show that the HA@Ag solution exhibited an antifungal property against *C. albicans* biofilms.

The performance of HA and silver is primarily dictated not only by physicochemical and mechanical properties, but also by biological activity [31]. HA is known as a biocompatible ceramic, and Ag has long been studied as

an antimicrobial agent which has been successfully used in biomedical prosthesis and surgical instruments [31–35]. The antimicrobial activity of Ag can be explained in many ways. It has been reported that Ag ions can damage the bacterial outer membrane which causes cell death [34–36]. A similar mechanism seems to occur for *C. albicans*. Kim et al. [37] reported a potent antifungal effect of Ag nanoparticles against *C. albicans* with MIC values similar to amphotericin B. In this study [37], several methodologies such as flow cytometry analysis, glucose and trehalose release, plasma membrane fluorescence anisotropy, and transmission electron microscopy (TEM) were used to elucidate the mechanism of antifungal action. Membrane depolarization, the arrest of the fungal cell cycle by flow cytometry, the release of intracellular glucose and trehalose, a decrease in plasma membrane fluorescence with increasing concentrations of Ag nanoparticles, pits in the cell wall, and pores in the plasma membrane on the TEM images were observed. These findings demonstrate that Ag nanoparticles destruct the fungal membrane integrity and inhibit the normal budding process.

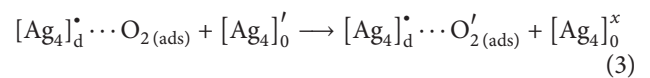
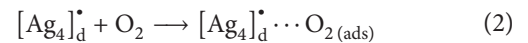
Disorders in surfaces and interfaces occur in HA@Ag synthesized by the HTMW method and create disordered sites [38]. This fact induces restructuring at the intermediate range which results in structural and electronic alterations to both the surface and interface. Disordered sites yield a local lattice distortion that is propagated along the overall material which pushes the surrounding clusters away from their ideal positions. Thus, complex clusters (disordered clusters) must move for these properties to occur which changes the electronic distribution along the network of these polar clusters [39]. This electronic structure may dictate the biological activity and plays a major role in determining the reactivity and stability of the cluster.

The mechanism of cluster complex $[\text{Ag}_4]^*$ activity with oxygen essentially depends on the complex cluster with the formation of a superoxide and/or a hydroxyl radical. $[\text{Ag}_4]_d^*$ and $[\text{Ag}_4]_d'$ can create hydroxyl radicals (OH^*) and superoxide anions (O_2H^*) by electron/hole reactions which can facilitate protein inactivation and eventual cell apoptosis where $d = \text{disorder}$ and $O = \text{order}$.

Moreover, an effective charge separation requires an electric field between the sample bulk and surface. Consequently, the effect of surface properties on electron/hole reaction performance should be considered in terms of the following:



The reactivity of molecular oxygen with a complex cluster $[\text{Ag}_4]_d^*$ on the surface of silver oxide results in a chemisorbed species and subsequent oxygen incorporation into the lattice:



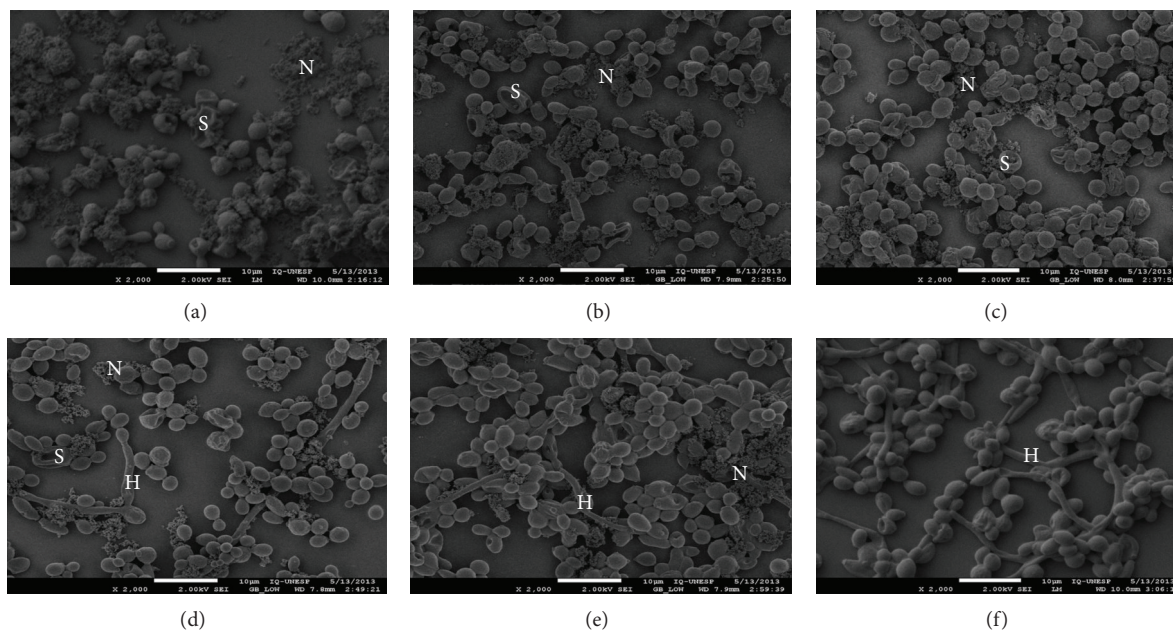
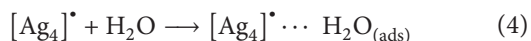


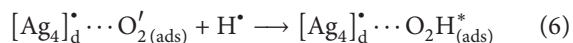
FIGURE 10: FEG-SEM of *C. albicans* biofilms with different concentrations of the HA@Ag solution: (a) 1000, (b) 500, (c) 250, (d) 125, (e) 62.5, and (f, control) 0 $\mu\text{g/mL}$. N: HA@Ag nanoparticles, S: “shriveled” cells appearance, H: Hyphae.

The clusters formed by the complex silver oxide also interact with water and split into hydroxyl radicals and hydrogen ions according to the following reactions:



Products of the partial oxidation reaction between water and a complex cluster $[\text{Ag}_4]^\bullet_d$ are hydroxyl radicals, OH^* , and hydrogen ions. These radicals exhibit high oxidation power which produces a microorganism mineralization in water (anodic oxidation) (5).

Primary reaction (cathodic) is the formation of a superoxide species $[\text{Ag}_4]^\bullet_d \cdots \text{O}_2^{\prime}$ (2) and (3). These species then react with H^\bullet (5) and produce the formation of hydrogen peroxide radicals (HO_2^*) according to the following reactions:



The radicals OH^* and O_2H^* may react with the fungal cells which ultimately results in their oxidation.

The nature of the superoxide or hydroxyl radicals can be described using a complex cluster model where the electron transfer from the surface to the adsorbed molecular oxygen occurs [40–42].

These reaction mechanisms involve oxygen and water adsorptions that form an active complex cluster. Its decomposition, desorption of the final products, and the electron hole recombination process may have an important role in fungicidal effects.

Therefore, HA@Ag was successfully obtained by maintaining the structure of HA nanorods overlapped by nanosphere Ag as confirmed by TEM images. The HA@Ag

obtained shows efficient antifungal action. The results of antifungal tests can be explained by the interaction between the structure and the defect density variation in the interfacial (HA@Ag) and intrafacial (HA) region with the fungal medium which results in antifungal activity.

4. Conclusions

HA@Ag was successfully obtained by maintaining the HA nanorods structure overlapped by nanosphere Ag through a co-precipitation method with HTMW. The HA@Ag solution showed fungistatic and fungicidal effects against *C. albicans* planktonic cells with MIC and MFC values of 62.5 $\mu\text{g/mL}$ and 250 $\mu\text{g/mL}$, respectively. Additionally, the HA@Ag solution at concentrations of 1000 $\mu\text{g/mL}$, 500 $\mu\text{g/mL}$, and 250 $\mu\text{g/mL}$ also exhibited antibiofilm activity, affecting mainly the extracellular matrix production. The morphological characteristics of cells were altered, and the density of hyphal cells was less noticeable in presence of the HA@Ag solution at higher concentrations. A mechanism was proposed to justify the antifungal activity by the interaction between the structure and the defect density variation in the interfacial (HA@Ag) and intrafacial (HA) region with the fungal medium.

Acknowledgment

This research was supported by grants 2011/06786-0, and 2011/24004-0, São Paulo Research Foundation (FAPESP).

References

- [1] K. P. Tank, P. Sharma, D. K. Kanchan, and M. J. Joshi, “FTIR, powder XRD, TEM and dielectric studies of pure and zinc

- doped nano-hydroxyapatite,” *Crystal Research and Technology*, vol. 46, no. 12, pp. 1309–1316, 2011.
- [2] N. Rameshbabu, T. S. S. Kumar, T. G. Prabhakar, V. S. Sastry, K. V. G. K. Murty, and K. Prasad Rao, “Antibacterial nanosized silver substituted hydroxyapatite: synthesis and characterization,” *Journal of Biomedical Materials Research A*, vol. 80, no. 3, pp. 581–591, 2007.
 - [3] M. Miranda, A. Fernández, S. Lopez-Esteban, F. Malpartida, J. S. Moya, and R. Torrecillas, “Ceramic/metal biocidal nanocomposites for bone-related applications,” *Journal of Materials Science*, vol. 23, no. 7, pp. 1655–1662, 2012.
 - [4] R. Manfredi, S. Sabbatani, and L. Calza, “Recurring *Candida albicans* esophagitis in a HIV-infected patient undergoing long-term antiretroviral therapy, and with absent-negligible immunodeficiency,” *Brazilian Journal of Infectious Diseases*, vol. 11, no. 6, pp. 605–609, 2007.
 - [5] J. Chandra, P. K. Mukherjee, S. D. Leidich et al., “Antifungal resistance of candidal biofilms formed on denture acrylic in vitro,” *Journal of Dental Research*, vol. 80, no. 3, pp. 903–908, 2001.
 - [6] P. Badiee and A. Alborzi, “Invasive fungal infections in renal transplant recipients,” *Experimental and Clinical Transplantation*, vol. 9, no. 6, pp. 355–362, 2011.
 - [7] I. Sondi and B. Salopek-Sondi, “Silver nanoparticles as antimicrobial agent: a case study on *E. coli* as a model for Gram-negative bacteria,” *Journal of Colloid and Interface Science*, vol. 275, no. 1, pp. 177–182, 2004.
 - [8] J. S. Kim, E. Kuk, K. N. Yu et al., “Antimicrobial effects of silver nanoparticles,” *Nanomedicine*, vol. 3, no. 1, pp. 95–101, 2007.
 - [9] J. R. Morones, J. L. Elechiguerra, A. Camacho et al., “The bactericidal effect of silver nanoparticles,” *Nanotechnology*, vol. 16, no. 10, pp. 2346–2353, 2005.
 - [10] M. A. Afzal, S. Kalmodia, P. Kesarwani, B. Basu, and K. Balani, “Bactericidal effect of silver-reinforced carbon nanotube and hydroxyapatite composites,” *Journal of Biomaterials Applications*, vol. 27, no. 8, pp. 967–978, 2012.
 - [11] Z. Lu, Y. Liu, B. Liu, and M. Liu, “Friction and wear behavior of hydroxyapatite based composite ceramics reinforced with fibers,” *Materials and Design*, vol. 39, pp. 444–449, 2012.
 - [12] D. Gopi, J. Indira, L. Kavitha, M. Sekar, and U. K. Mudali, “Synthesis of hydroxyapatite nanoparticles by a novel ultrasonic assisted with mixed hollow sphere template method,” *Spectrochimica Acta A*, vol. 93, pp. 131–134, 2012.
 - [13] F. Ren, Y. Ding, X. Ge, X. Lu, K. Wang, and Y. Leng, “Growth of one-dimensional single-crystalline hydroxyapatite nanorods,” *Journal of Crystal Growth*, vol. 349, no. 1, pp. 75–82, 2012.
 - [14] H. E. Wang, L. J. Xi, R. G. Ma et al., “Microwave-assisted hydrothermal synthesis of porous SnO₂ nanotubes and their lithium ion storage properties,” *Journal of Solid State Chemistry*, vol. 190, pp. 104–110, 2012.
 - [15] V. D. Maksimov, P. E. Meskin, and B. R. Churagulov, “Microwave-assisted hydrothermal synthesis of fine BaZrO₃ and BaHfO₃ powders,” *Inorganic Materials*, vol. 43, no. 9, pp. 988–993, 2007.
 - [16] V. D. Araújo, W. Avansi, H. B. de Carvalho et al., “CeO₂ nanoparticles synthesized by a microwave-assisted hydrothermal method: evolution from nanospheres to nanorods,” *CrytEngComm*, vol. 14, no. 3, pp. 1150–1154, 2012.
 - [17] C. S. Ciobanu, F. Massuyeau, L. V. Constantin, and D. Predoi, “Structural and physical properties of antibacterial Ag-doped nano-hydroxyapatite synthesized at 100°C,” *Nanoscale Research Letters*, vol. 6, no. 1, article 613, pp. 1–8, 2011.
 - [18] C. S. Ciobanu, S. L. Iconaru, P. le Coustumer, L. V. Constantin, and D. Predoi, “Antibacterial activity of silver-doped hydroxyapatite nanoparticles against gram-positive and gram-negative bacteria,” *Nanoscale Research Letters*, vol. 7, no. 1, article 324, 2012.
 - [19] C. S. Ciobanu, S. L. Iconaru, M. C. Chifiriuc, A. Costescu, P. le Coustumer, and D. Predoi, “Synthesis and antimicrobial activity of silver-doped hydroxyapatite nanoparticles,” *BioMed Research International*, vol. 2013, Article ID 916218, 10 pages, 2013.
 - [20] V. Stanić, D. Janačković, S. Dimitrijević et al., “Synthesis of antimicrobial monophase silver-doped hydroxyapatite nanopowders for bone tissue engineering,” *Applied Surface Science*, vol. 257, no. 9, pp. 4510–4518, 2011.
 - [21] CLSI, *Reference Method for Broth Dilution Antifungal Susceptibility Testing of Yeasts; Approved Standard*, CLSI Document M27-A3, Clinical and Laboratory Standards Institute, Wayne, Pa, USA, 3rd edition, 2008.
 - [22] G. Penel, G. Leroy, C. Rey, and E. Bres, “MicroRaman spectral study of the PO₄ and CO₃ vibrational modes in synthetic and biological apatites,” *Calcified Tissue International*, vol. 63, no. 6, pp. 475–481, 1998.
 - [23] C. W. Raubach, Y. V. B. de Santana, M. M. Ferrer et al., “Structural and optical approach of CdS@ZnS core-shell system,” *Chemical Physics Letters*, vol. 536, pp. 96–99, 2012.
 - [24] A. F. Wady, A. L. Machado, V. Zucolotto, C. A. Zamperini, E. Berni, and C. E. Vergani, “Evaluation of *Candida albicans* adhesion and biofilm formation on a denture base acrylic resin containing silver nanoparticles,” *Journal of Applied Microbiology*, vol. 112, no. 6, pp. 1163–1172, 2012.
 - [25] D. R. Monteiro, S. Silva, M. Negri et al., “Silver nanoparticles: influence of stabilizing agent and diameter on antifungal activity against *Candida albicans* and *Candida glabrata* biofilms,” *Letters in Applied Microbiology*, vol. 54, no. 5, pp. 383–391, 2012.
 - [26] D. R. Monteiro, L. F. Gorup, S. Silva et al., “Silver colloidal nanoparticles: antifungal effect against adhered cells and biofilms of *Candida albicans* and *Candida glabrata*,” *Biofouling*, vol. 27, no. 7, pp. 711–719, 2011.
 - [27] M. A. Vargas-Reus, K. Memarzadeh, J. Huang, G. G. Ren, and R. P. Allaker, “Antimicrobial activity of nanoparticulate metal oxides against peri-implantitis pathogens,” *International Journal of Antimicrobial Agents*, vol. 40, no. 2, pp. 135–139, 2012.
 - [28] G. Ramage, E. Mowat, B. Jones, C. Williams, and J. Lopez-Ribot, “Our current understanding of fungal biofilms,” *Critical Reviews in Microbiology*, vol. 35, no. 4, pp. 340–355, 2009.
 - [29] T. Wu, K. Wright, S. F. Hurst, and C. J. Morrison, “Enhanced extracellular production of aspartyl proteinase, a virulence factor, by *Candida albicans* isolates following growth in subinhibitory concentrations of fluconazole,” *Antimicrobial Agents and Chemotherapy*, vol. 44, no. 5, pp. 1200–1208, 2000.
 - [30] L. Dong, Z. Tong, D. Linghu et al., “Effects of sub-minimum inhibitory concentrations of antimicrobial agents on *Streptococcus mutans* biofilm formation,” *International Journal of Antimicrobial Agents*, vol. 39, no. 5, pp. 390–395, 2012.
 - [31] M. Roy, G. A. Fielding, H. Beyenal, A. Bandyopadhyay, and S. Bose, “Mechanical, in vitro antimicrobial, and biological properties of plasma-sprayed silver-doped hydroxyapatite coating,” *ACS Applied Materials and Interfaces*, vol. 4, no. 3, pp. 1341–1349, 2012.
 - [32] A. Ewald, D. Hösel, S. Patel, L. M. Grover, J. E. Barralet, and U. Gbureck, “Silver-doped calcium phosphate cements with antimicrobial activity,” *Acta Biomaterialia*, vol. 7, no. 11, pp. 4064–4070, 2011.

- [33] N. Matsumoto, K. Sato, K. Yoshida, K. Hashimoto, and Y. Toda, "Preparation and characterization of β -tricalcium phosphate co-doped with monovalent and divalent antibacterial metal ions," *Acta Biomaterialia*, vol. 5, no. 8, pp. 3157–3164, 2009.
- [34] W.-H. Song, S. R. Hyun, and S.-H. Hong, "Antibacterial properties of Ag (or Pt)-containing calcium phosphate coatings formed by micro-arc oxidation," *Journal of Biomedical Materials Research A*, vol. 88, no. 1, pp. 246–254, 2009.
- [35] K. Das, S. Bose, A. Bandyopadhyay, B. Karandikar, and B. L. Gibbins, "Surface coatings for improvement of bone cell materials and antimicrobial activities of Ti implants," *Journal of Biomedical Materials Research B*, vol. 87, no. 2, pp. 455–460, 2008.
- [36] X. Bai, K. More, C. M. Rouleau, and A. Rabiei, "Functionally graded hydroxyapatite coatings doped with antibacterial components," *Acta Biomaterialia*, vol. 6, no. 6, pp. 2264–2273, 2010.
- [37] K.-J. Kim, W. S. Sung, B. K. Suh et al., "Antifungal activity and mode of action of silver nano-particles on *Candida albicans*," *BioMetals*, vol. 22, no. 2, pp. 235–242, 2009.
- [38] P. G. Mendes, M. L. Moreira, S. M. Tebcherani et al., "SnO₂ nanocrystals synthesized by microwave-assisted hydrothermal method: towards a relationship between structural and optical properties," *Journal of Nanoparticle Research*, vol. 14, no. 3, article 750, 2012.
- [39] T. Badapanda, S. K. Rout, L. S. Cavalcante et al., "Optical and dielectric relaxor behaviour of Ba(Zr_{0.25}Ti_{0.75})O₃ ceramic explained by means of distorted clusters," *Journal of Physics D*, vol. 42, no. 17, Article ID 175414, pp. 1–9, 2009.
- [40] T. Bak, J. Nowotny, N. J. Sucher, and E. Wachsman, "Effect of crystal imperfections on reactivity and photoreactivity of TiO₂ (Rutile) with oxygen, water, and bacteria," *Journal of Physical Chemistry C*, vol. 115, no. 32, pp. 15711–15738, 2011.
- [41] A. Bielanski and W. C. D. Hare, "Investigation of some antimicrobial procedures on the in vitro development of early murine embryos aimed toward developing methods for the disinfection of mammalian embryos prior to transfer," *Journal of In Vitro Fertilization and Embryo Transfer*, vol. 8, no. 1, pp. 24–32, 1991.
- [42] J. P. Kehrer, "The Haber-Weiss reaction and mechanisms of toxicity," *Toxicology*, vol. 149, no. 1, pp. 43–50, 2000.

Research Article

Adsorption of Albumin on Silica Surfaces Modified by Silver and Copper Nanoparticles

Prity Kumari and Peter Majewski

School of Advanced Manufacturing and Mechanical Engineering, Mawson Institute, University of South Australia, Mawson Lakes, Adelaide, SA 5095, Australia

Correspondence should be addressed to Peter Majewski; peter.majewski@unisa.edu.au

Received 30 January 2013; Revised 27 May 2013; Accepted 27 May 2013

Academic Editor: Mohamed Bououdina

Copyright © 2013 P. Kumari and P. Majewski. This is an open access article distributed under the Creative Commons Attribution License, which permits unrestricted use, distribution, and reproduction in any medium, provided the original work is properly cited.

Silver and copper nanoparticles, respectively, were produced on glass slides via magnetron sputtering. The experiments show that with magnetron sputtering the size and concentration of the nanoparticles can be easily controlled via sputter time and plasma power. Silver nanoparticles grow much faster than copper nanoparticles, which also require higher plasma power for their synthesis. Exposed to albumin solution, the glass slides with silver nanoparticles clearly show a delay in albumin attachment compared to pure glass slides. Glass slides with copper nanoparticles show a slight attachment of albumin even after 3 h of exposure. However, the albumin concentration on the surface of the glass slides was much smaller compared to pure glass slides and did not increase within 24 h.

1. Introduction

Infection as a result of bacteria attachment and biofilm formation on biomedical devices and implants is a major problem for the health system world wide [1]. One potential approach for reducing the use of antibiotics is the introduction of antimicrobial surface coatings. Various antimicrobial materials have been investigated to develop antibiofouling surface coatings that have the ability to prevent the attaching of proteins, bacteria, or marine organisms [2–9]. However, many of the developed anti-biofouling coatings have failed in medical applications due to bacteria mutation and their ability to develop antibacterial resistance or because the employed anti-biofouling components are highly toxic and, therefore, not employable in medicine [10–12].

In recent times, the use of nanoparticles as antimicrobial agent is studied intensively. The most widely studied nanomaterial for this purpose is silver nanoparticles (AgNPs) and the antimicrobial [13–17], antiviral [18, 19], and even antifungal [20, 21] are studied in detail. AgNPs have efficient antimicrobial properties due to their extremely large surface area, which indicates that small AgNPs have better antimicrobial properties than larger particles [22]. AgNPs get attached to

the cell membrane and can also penetrate the membrane and travel into the bacteria. Studies indicate that AgNPs interact with sulphur-containing proteins in the bacteria membrane which results in the loss of essential bacteria functions like respiration and permeability [22–25]. Other studies suggest that AgNPs initiate the formation of radicals that interact with the bacterial membrane causing cell death [16]. Copper nanoparticles (CuNPs) have also attracted interest for applications as anti-biofouling agent, due to their catalytic and electrocatalytic properties [26, 27]. Although the antimicrobial effect of AgNPs has been studied widely, the attachment of proteins on surfaces coated with nanoparticles has been investigated to a much lesser extent [28], although it is known that proteins on surfaces can significantly accelerate bacterial attachment and biofilm formation [29]. Therefore, the prevention of protein attachment on surfaces and the investigation of the ability of nanoparticles to prevent this are well justified.

In this study, the attachment of albumin protein on surfaces coated with AgNPs and CuNPs versus time using matrix-assisted laser desorption/ionization mass spectrometry (MALDI-MS) is studied. A large number of different chemical (e.g., [16, 30]) and physical (e.g., [31]) methods have

been developed to prepare metal nanoparticles. In this study, nanoparticles on glass slides were synthesized via magnetron sputtering and their growth as a function of sputter time is also studied.

2. Experimental

2.1. Magnetron Sputtering. Glass slides with a dimension of $24 \times 75 \text{ mm}^2$ were used as substrates. Before sputtering, the substrates were cleaned with ethanol. For the deposition of copper and silver nanoparticles, copper and silver targets with a purity of 99.99% were used. After placing the substrates together with the grids for transmission electron microscopy (TEM, Philips CM 200 transmission electron microscope) into the sputter chamber, the chamber was evacuated down to 3×10^{-3} mbar and subsequently the Argon plasma was ignited. Copper nanoparticles were produced at room temperature using a plasma power of 50 W and sputter times of 10 and 20 s, respectively. Silver nanoparticles were produced at room temperature using a plasma power of 18 W and deposition times of 2, 5, and 10 seconds, respectively.

2.2. Albumin Attachment. Mouse serum albumin (MSA) was used for the experiments (Aldrich, nitrogen content 14.8%, fraction V (9048-46-8), EC no. 232-936-2, A-3139, lot 083K7607, desiccate). An amount of $10.03 \mu\text{g}$ of MSA powder was dissolved in 5 mL of milli-q water in a vial and stored at $+8^\circ\text{C}$ for further use. Before the analyses, a drop of the albumin solution was applied onto the samples by a syringe. The samples were placed into a Petri dish and covered with a wet cloth to avoid drying of the albumin solution during the adsorption process, as drying of the droplet would result in deposited, but not bonded, albumin on the surface, which would artificially alter the MALDI-MS results.

2.3. Matrix-Assisted Laser Desorption/Ionization Mass Spectrometry (MALDI-MS). For MALDI-MS analysis was performed using a Bruker Autoflex III MALDI MS/MS (Bruker, Germany).

2.4. Uv-Vis Spectroscopy. UV-Vis absorption spectra of the glass slides with deposited nanoparticles were obtained using Cary 5 UV-Vis spectrometer (Varian Australia Pty Ltd.).

3. Results and Discussion

3.1. UV-Vis Spectrometry. The UV-Vis spectra of the glass slide sputtered with silver for 5 s and copper for 10 s, respectively, are shown in Figure 1. The spectrum of the glass slide sputtered with silver clearly shows an absorption band at 420 nm which verifies the presence of AgNPs on the surface of the glass slide [32]. The glass slides sputtered with copper exhibits an absorption at about 600 nm which gives evidence for the presence of CuNPs on the glass slide [33].

3.2. X-Ray Photon Spectroscopy (XPS). XPS analysis of the surfaces of the glass slides shows clear peaks for silver and copper, respectively. The sample sputtered with silver shows

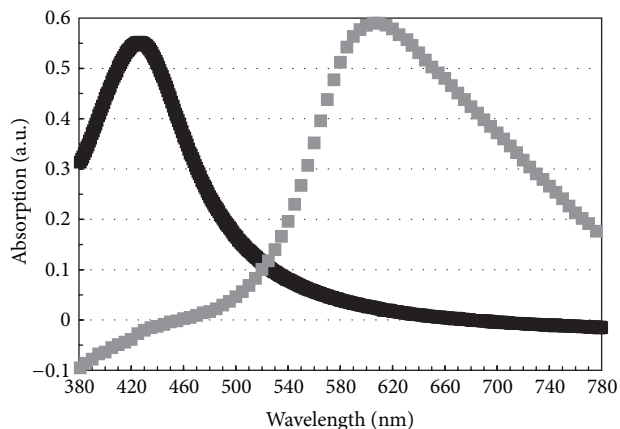


FIGURE 1: UV-Vis absorption spectra for glass slides with silver nanoparticles (black) and copper nanoparticles (grey).

a silver Ag 3d 3/2 and Ag 3d 5/2 peaks (Figure 2). The high resolution XPS scan reveals that the Ag 3d 3/2 peak can be split into a peak at a binding energy of 373.56 eV and a peak at a binding energy of 374.64 eV which gives evidence of the presence of ionic silver of Ag_2O and metallic silver, respectively [34, 35]. The Ag 3d 5/2 peak can also be split into two peaks at binding energies of 367.56 eV and 368.64 eV, respectively, also revealing the presence of Ag_2O and metallic silver [35, 36]. The presence of Ag_2O is presumably due to partial surface oxidation of the AgNPs after deposition.

The high resolution XPS scan for copper shows two Cu 2p 3/2 peaks at binding energies of 932.45 eV and 934.52 eV which can be attributed to metallic copper and ionic copper of CuO, respectively [37, 38] (Figure 3). The Cu 2p 1/2 peak can also be split into two peaks at binding energies of 952.26 eV and 953.77 eV which also gives evidence for the presence of metallic copper and CuO, respectively, on the surface of the sample [39, 40]. The presence of CuO on the surface is presumably also due to partial oxidation of the CuNPs after deposition of the nanoparticles.

3.3. Transmission Electron Microscopy. The TEM images of the samples clearly show the presence of nanoparticles on the surface of the silica slides (Figures 4 to 8). It is obvious that with increasing sputter time the size of the nanoparticles increases. The AgNPs increase in size from between 1 and 10 nm to between 5 and 50 nm within 10 seconds at a plasma power of 18 W. In addition, the shapes of the nanoparticles change from spherical (Figures 4 and 5) to irregular (Figure 6). In contrast, the CuNPs appear to grow much slower than the silver nanoparticles (Figures 7 and 8) and their size is still below about 5 nm even after sputter times of 20 seconds at much higher plasma power of 50 W. At plasma powers below 50 W, CuNPs could not be detected on the glass slides. The reason for this phenomenon is presumably the high melting temperature and ionization energy of copper compared to silver which influence the kinetics of grain growth during magnetron sputter deposition [41]. It also appears that with increasing sputter time, the

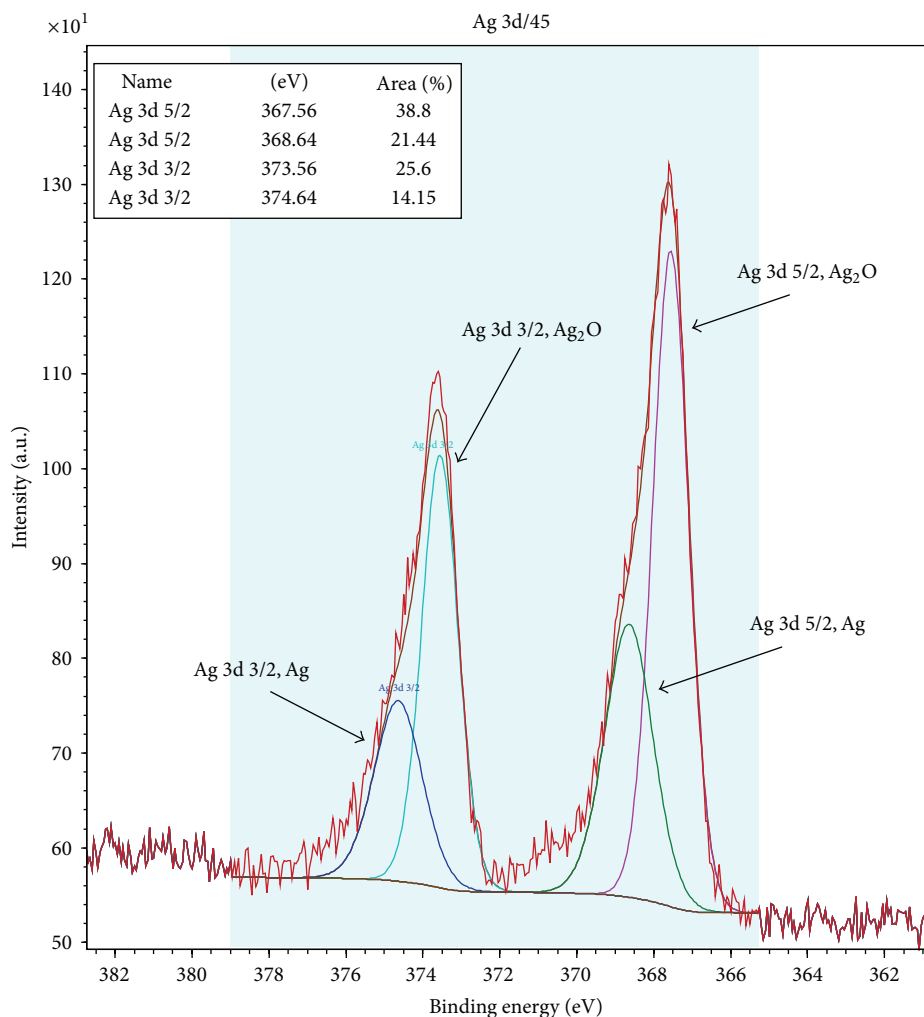


FIGURE 2: High resolution XPS spectrum of glass slide with silver nanoparticles.

size of the CuNPs does not increase, whereas the number of nanoparticles increases.

3.4. Matrix-Assisted Laser Desorption/Ionization Mass Spectrometry (MALDI-MS). The MALDI MS analyses of the albumin adsorption experiments are shown in Figures 9, 10, and 11. After only three hours of exposure to the MSA solution, the MALDI-MS analysis of the pure silica sample clearly shows pronounced peaks at about $35000 m/z$ and $62000 m/z$. All these peaks can be attributed to albumin^{about1+} and albumin^{about2+} peaks [42], although the peak at $62000 m/z$ is at slightly lower m/z value than that reported in the literature [42]. This phenomenon may be due to the attachment of none complete albumin molecules. Minor peaks can be identified at about $14000 m/z$, $22500 m/z$, and $28500 m/z$, which are not identified, but may be attributed to albuminⁿ⁺ peaks with $2 < n < 4$ [43].

The samples sputtered with silver for 5 s do not show any related peaks after 3 h of exposure to the MSA solution. However, after 24 h of exposure the albumin¹⁺ and albumin²⁺ peaks are clearly visible besides peaks at

$28500 m/z$, $22500 m/z$, and $14000 m/z$. This observation indicates that the adsorption of albumin on the surface with attached AgNPs is significantly delayed compared to the pure silica surface. However, after prolonged exposure, albumin is clearly adsorbed by the surface with AgNPs.

The samples containing CuNPs sputtered for 20 s show a very different result. Although albumin¹⁺ and albumin²⁺ peaks are visible after 3 h and 24 h, respectively, the peaks are significantly weaker compared to those on pure silica and silica with AgNPs at albumin exposure for 24 h and the peaks at $35000 m/z$ and $62000 m/z$ do not increase between 3 and 24 h of exposure to albumin. The reason for this phenomenon is believed to be caused by the fact that CuNPs are significantly smaller than AgNPs, so that the larger albumin molecule (about 8 to 10 nm [44]) is able to attach to the silica surface to some extent by bridging the smaller nanoparticle. Nevertheless, as the adsorption of albumin does not increase within 24 h of exposure, it is believed that CuNPs have the ability to prevent further adsorption of albumin. However, the underlying physical and chemical phenomena that delays albumin attachment is yet to be clarified and will be presented later.

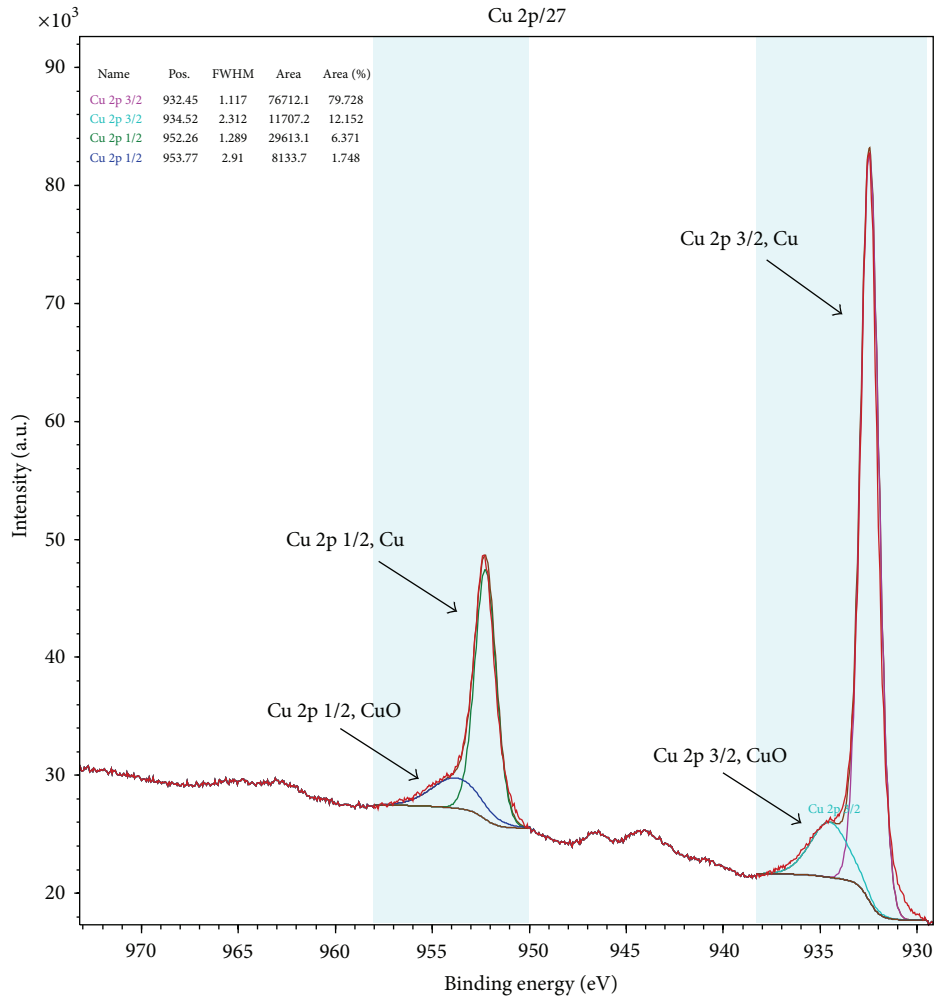


FIGURE 3: High resolution XPS spectrum of glass slide with copper nanoparticles.

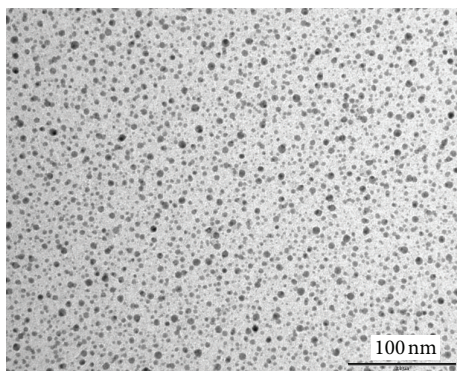


FIGURE 4: Ag nanoparticles sputtered on silica for 2 seconds.

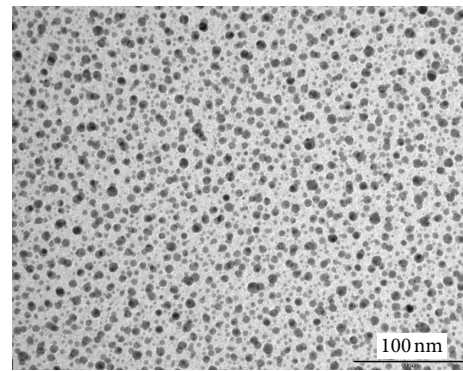


FIGURE 5: Ag nanoparticles sputtered on silica for 5 seconds.

4. Conclusion

Magnetron sputtering appears to be a very potent technology to produce nanoparticles on surfaces. Size and concentration of nanoparticles can easily be controlled by plasma energy and sputter time as shown in this study.

The experiments conducted here also show that AgNPs and CuNPs have the capacity to clearly delay the attachment of albumin of the coated surfaces. However, in case of AgNPs, it is obvious that attachment of albumin cannot be completely prevented after prolonged exposure to albumin solution for 24 h. In case of CuNPs, although a very minor

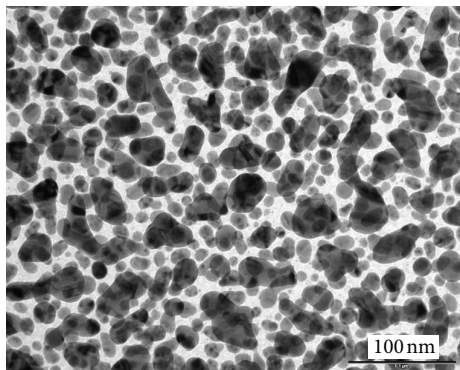


FIGURE 6: Ag nanoparticles sputtered on silica for 10 seconds.

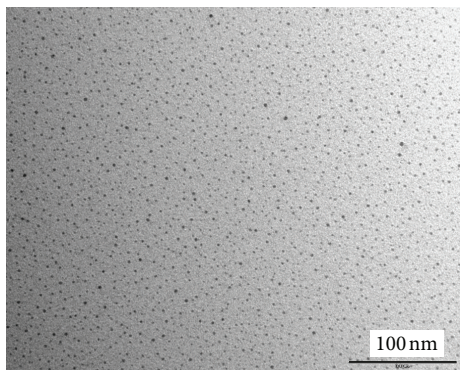


FIGURE 7: Cu nanoparticles sputtered on silica for 10 seconds.

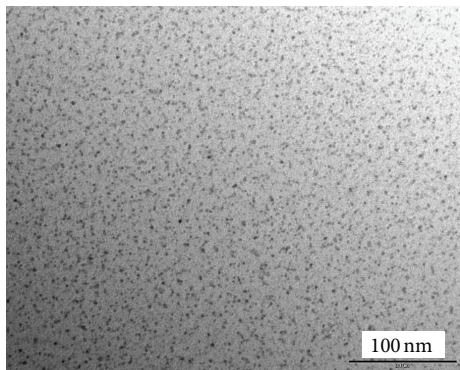


FIGURE 8: Cu nanoparticles sputtered on silica for 20 seconds.

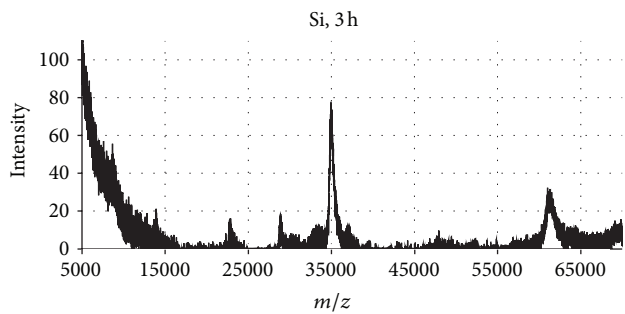
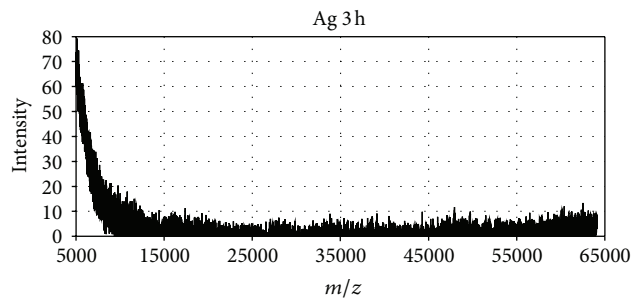
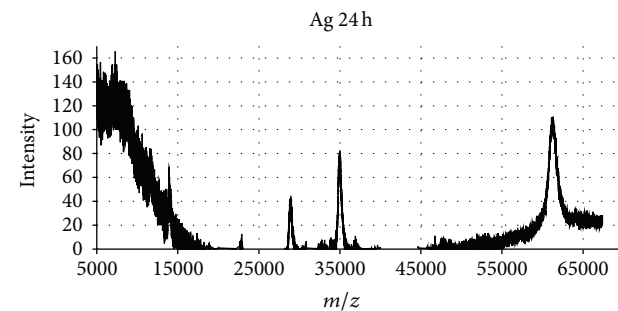


FIGURE 9: MALDI-MS spectrum of pure silica after 3 h of contact with MSA solution.

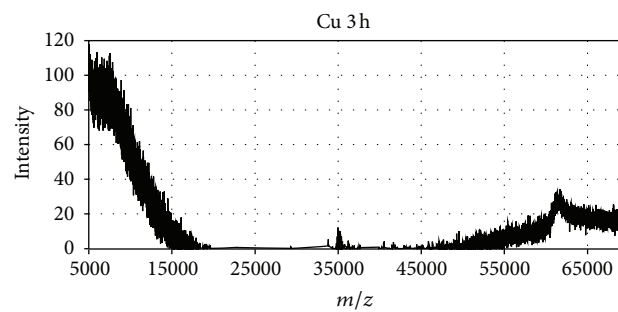


(a)

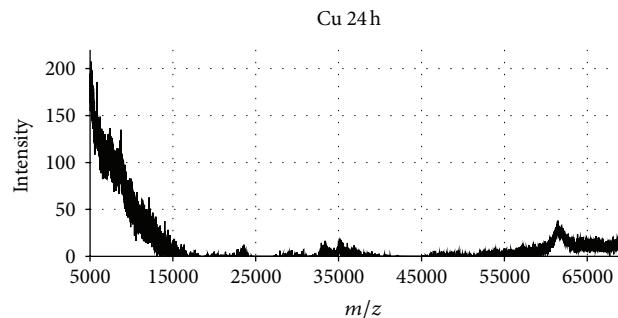


(b)

FIGURE 10: MALDI-MS spectrum of silica with Ag nanoparticles after 3 h (a) and 24 h (b), respectively, of contact with MSA solution.



(a)



(b)

FIGURE 11: MALDI-MS spectrum of silica with Cu nanoparticles after 3 h (a) and 24 h (b), respectively, of contact with MSA solution.

albumin attachment is detectable after exposure for only 3 h, no further increase of albumin attachment was observed within 24 h of exposure. This observation may indicate that the size of the nanoparticles may play a role in the albumin attachment. Very small nanoparticles like those in case of the CuNPs (1 to 5 nm) may not completely prevent albumin attachment, as the albumin molecule has a size of about 8 to 10 nm, whereas nanoparticles in the size range of 10 to 20 nm like AgNPs observed on the glass slides are able to prevent albumin attachment.

The fact that albumin attachment can be delayed by coatings of AgNPs and CuNPs is of some significance, as biomedical tools are often used only once after removing them from sterile packaging and are then used only for short time, for example, during surgery. If protein attachment can be prevented during that time period, as shown for surfaces coated with AgNPs, the chance of infection is clearly reduced.

Conflict of Interests

The authors declare that they have no conflict of interests.

References

- [1] D. Mack, H. Rohde, L. G. Harris, A. P. Davies, M. A. Horstkotte, and J. K.-M. Knobloch, "Biofilm formation in medical device-related infection," *International Journal of Artificial Organs*, vol. 29, no. 4, pp. 343–359, 2006.
- [2] S. Noimark, C. W. Dunnill, M. Wilson, and I. P. Parkin, "The role of surfaces in catheter-associated infections," *Chemical Society Reviews*, vol. 38, no. 12, pp. 3435–3448, 2009.
- [3] K. Vasilev, J. Cook, and H. J. Griesser, "Antibacterial surfaces for biomedical devices," *Expert Review of Medical Devices*, vol. 6, no. 5, pp. 553–567, 2009.
- [4] J. C. Tiller, C.-J. Liao, K. Lewis, and A. M. Klibanov, "Designing surfaces that kill bacteria on contact," *Proceedings of the National Academy of Sciences of the United States of America*, vol. 98, no. 11, pp. 5981–5985, 2001.
- [5] M. S. Kim, G. Khang, and H. B. Lee, "Gradient polymer surfaces for biomedical applications," *Progress in Polymer Science*, vol. 33, no. 1, pp. 138–164, 2008.
- [6] I. Banerjee, R. C. Pangule, and R. S. Kane, "Antifouling coatings: recent developments in the design of surfaces that prevent fouling by proteins, bacteria, and marine organisms," *Advanced Materials*, vol. 23, no. 6, pp. 690–718, 2011.
- [7] F. Costa, I. F. Carvalho, R. C. Montelaro, P. Gomes, and M. C. L. Martins, "Covalent immobilization of antimicrobial peptides (AMPs) onto biomaterial surfaces," *Acta Biomaterialia*, vol. 7, no. 4, pp. 1431–1440, 2011.
- [8] W. C. E. Schofield and J. P. S. Badyal, "A substrate-independent approach for bactericidal surfaces," *ACS Applied Materials and Interfaces*, vol. 1, no. 12, pp. 2763–2767, 2009.
- [9] A. Simchi, E. Tamjid, F. Pishbin, and A. R. Boccaccini, "Recent progress in inorganic and composite coatings with bactericidal capability for orthopaedic applications," *Nanomedicine*, vol. 7, no. 1, pp. 22–39, 2011.
- [10] H. de Lencastre, D. Oliveira, and A. Tomasz, "Antibiotic resistant *Staphylococcus aureus*: a paradigm of adaptive power," *Current Opinion in Microbiology*, vol. 10, no. 5, pp. 428–435, 2007.
- [11] H. Nikaido, "Multidrug resistance in bacteria," *Annual Review of Biochemistry*, vol. 78, pp. 119–146, 2009.
- [12] I. M. Gould, "Antibiotics, skin and soft tissue infection and meticillin-resistant *Staphylococcus aureus*: cause and effect," *International Journal of Antimicrobial Agents*, vol. 34, supplement 1, pp. S8–S11, 2009.
- [13] M. L. W. Knetsch and L. H. Koole, "New strategies in the development of antimicrobial coatings: the example of increasing usage of silver and silver nanoparticles," *Polymers*, vol. 3, no. 1, pp. 340–366, 2011.
- [14] K. Senior, S. Muller, V. J. Schacht, and M. Bunge, "Antimicrobial precious-metal nanoparticles and their use in novel materials," *Recent Patents on Food, Nutrition & Agriculture*, vol. 4, pp. 200–209, 2012.
- [15] V. K. Sharma, R. A. Yngard, and Y. Lin, "Silver nanoparticles: green synthesis and their antimicrobial activities," *Advances in Colloid and Interface Science*, vol. 145, no. 1–2, pp. 83–96, 2009.
- [16] J. S. Kim, E. Kuk, K. N. Yu et al., "Antimicrobial effects of silver nanoparticles," *Nanomedicine*, vol. 3, no. 1, pp. 95–101, 2007.
- [17] M. Rai, A. Yadav, and A. Gade, "Silver nanoparticles as a new generation of antimicrobials," *Biotechnology Advances*, vol. 27, no. 1, pp. 76–83, 2009.
- [18] S. Galdiero, A. Falanga, M. Vitiello, M. Cantisani, V. Marra, and M. Galdiero, "Silver nanoparticles as potential antiviral agents," *Molecules*, vol. 16, no. 10, pp. 8894–8918, 2011.
- [19] H. H. Lara, E. N. Garza-Treviño, L. Ixtepan-Turrent, and D. K. Singh, "Silver nanoparticles are broad-spectrum bactericidal and virucidal compounds," *Journal of Nanobiotechnology*, vol. 9, article 30, 2011.
- [20] A. Panáček, M. Kolář, R. Večeřová et al., "Antifungal activity of silver nanoparticles against *Candida* spp," *Biomaterials*, vol. 30, no. 31, pp. 6333–6340, 2009.
- [21] L. S. Acosta-Torres, I. Mendieta, R. E. Nuñez-Anita, M. Cajero-Juárez, and V. M. Castaño, "Cytocompatible antifungal acrylic resin containing silver nanoparticles for dentures," *Internat J Nanomedicine*, vol. 7, pp. 4777–4786, 2012.
- [22] J. R. Morones, J. L. Elechiguerra, A. Camacho et al., "The bactericidal effect of silver nanoparticles," *Nanotechnology*, vol. 16, no. 10, pp. 2346–2353, 2005.
- [23] Q. L. Feng, J. Wu, G. Q. Chen, F. Z. Cui, T. N. Kim, and J. Q. Kim, "A mechanistic study of the antibacterial effect of silver ions on *Escherichia coli* and *Staphylococcus aureus*," *Journal of Biomedical Materials*, vol. 52, pp. 662–668, 2000.
- [24] I. Sondi and B. Salopek-Sondi, "Silver nanoparticles as antimicrobial agent: a case study on *E. coli* as a model for Gram-negative bacteria," *Journal of Colloid and Interface Science*, vol. 275, no. 1, pp. 177–182, 2004.
- [25] H. Y. Song, K. K. Ko, L. H. Oh, and B. T. Lee, "Fabrication of silver nanoparticles and their antimicrobial mechanisms," *European Cells and Materials*, vol. 11, pp. 58–60, 2006.
- [26] I.-W. Shim, W.-T. Noh, J. Kwon, J. Y. Cho, K.-S. Kim, and D. H. Kang, "Preparation of copper nanoparticles in cellulose acetate polymer and the reaction chemistry of copper complexes in the polymer," *Bulletin of the Korean Chemical Society*, vol. 23, no. 4, pp. 563–568, 2002.
- [27] H. H. Huang, F. Q. Yan, Y. M. Kek et al., "Synthesis, characterization, and nonlinear optical properties of copper nanoparticles," *Langmuir*, vol. 13, no. 2, pp. 172–179, 1997.
- [28] C. Latasa, C. Solano, J. R. Penadés, and I. Lasa, "Biofilm-associated proteins," *Comptes Rendus*, vol. 329, no. 11, pp. 849–857, 2006.

- [29] Y. Schmitt, H. Hähl, C. Gilow et al., “Structural evolution of protein-biofilms: simulations and experiments,” *Biomicrofluidics*, vol. 4, no. 3, Article ID 032201, 2010.
- [30] J. Kimling, M. Maier, B. Okenve, V. Kotaidis, H. Ballot, and A. Plech, “Turkevich method for gold nanoparticle synthesis revisited,” *Journal of Physical Chemistry B*, vol. 110, no. 32, pp. 15700–15707, 2006.
- [31] P. Wagener, S. Barcikowski, and N. Baersch, “Fabrication of nanoparticles and nanomaterials using laser ablation in liquids,” *Photonik International*, vol. 1, pp. 20–23, 2011.
- [32] V. Amendola, O. M. Bakr, and F. Stellacci, “A study of the surface plasmon resonance of silver nanoparticles by the discrete dipole approximation method: effect of shape, size, structure, and assembly,” *Plasmonics*, vol. 5, no. 1, pp. 85–97, 2010.
- [33] P. K. Khanna, S. Gaikwad, P. V. Adhyapak, N. Singh, and R. Marimuthu, “Synthesis and characterization of copper nanoparticles,” *Materials Letters*, vol. 61, no. 25, pp. 4711–4714, 2007.
- [34] Y. Liu, R. G. Jordan, and S. L. Qiu, “Electronic structures of ordered Ag-Mg alloys,” *Physical Review B*, vol. 49, no. 7, pp. 4478–4484, 1994.
- [35] L. H. Tjeng, M. B. J. Meinders, J. Van Elp, J. Ghijsen, G. A. Sawatzky, and R. L. Johnson, “Electronic structure of Ag_2O ,” *Physical Review B*, vol. 41, no. 5, pp. 3190–3199, 1990.
- [36] M. P. Seah, G. C. Smith, and M. T. Anthony, “AES. Energy calibration of electron spectrometers. I. An absolute, traceable energy calibration and the provision of atomic reference line energies,” *Surface and Interface Analysis*, vol. 15, no. 5, pp. 293–308, 1990.
- [37] M. P. Seah, I. S. Gilmore, and G. Beamson, “XPS: binding energy calibration of electron spectrometers 5—Re-evaluation of the reference energies,” *Surface and Interface Analysis*, vol. 26, no. 9, pp. 642–649, 1998.
- [38] F. Parmigiani, G. Pacchioni, F. Illas, and P. S. Bagus, “Studies of the CuO bond in cupric oxide by X-ray photoelectron spectroscopy and ab initio electronic structure models,” *Journal of Electron Spectroscopy and Related Phenomena*, vol. 59, no. 3, pp. 255–269, 1992.
- [39] A. N. Mansour, “Gold Mg K_{α} XPS spectra from the physical electronics model 5400 spectrometer,” *Surface Science Spectra*, vol. 3, no. 3, 5 pages, 1994.
- [40] J. G. Jolley, G. G. Geesey, M. R. Haukins, R. B. Write, and P. L. Wichlacz, “Auger electron and X-ray photoelectron spectroscopic study of the biocorrosion of copper by alginate polysaccharide,” *Applied Surface Science*, vol. 37, no. 4, pp. 469–480, 1989.
- [41] J. A. Thornton, “The microstructure of sputter-deposited coatings,” *Journal of Vacuum Science & Technology A*, vol. 4, pp. 3059–3065, 1986.
- [42] R. Spares, C. Franco, E. Pires et al., “Mass spectrometry and animal science: protein identification strategies and particularities of farm animal species,” *Journal of Proteomics*, vol. 75, pp. 4190–4206, 2012.
- [43] C. Dass, *Principles and Practice of Biological Mass Spectrometry*, John Wiley, New York, USA, 2001.
- [44] M. A. Kiselev, I. A. Gryzunov, G. E. Dobretsov, and M. N. Komarova, “Size of a human serum albumin molecule in solution,” *Biofizika*, vol. 46, no. 3, pp. 423–427, 2001.

Review Article

Nanoscaffolds for Guided Cardiac Repair: The New Therapeutic Challenge of Regenerative Medicine

**Letizia Ventrelli,^{1,2} Leonardo Ricotti,² Arianna Menciassi,²
Barbara Mazzolai,¹ and Virgilio Mattoli¹**

¹ Center for Micro-BioRobotics @SSSA, Istituto Italiano di Tecnologia, Viale Rinaldo Piaggio 34, 56025 Pontedera, Italy

² The BioRobotics Institute, Scuola Superiore Sant'Anna, Polo Sant'Anna Valdera, Viale Rinaldo Piaggio 34, 56025 Pontedera, Italy

Correspondence should be addressed to Letizia Ventrelli; l.ventrelli@sssup.it

Received 15 March 2013; Accepted 12 May 2013

Academic Editor: Mohamed Bououdina

Copyright © 2013 Letizia Ventrelli et al. This is an open access article distributed under the Creative Commons Attribution License, which permits unrestricted use, distribution, and reproduction in any medium, provided the original work is properly cited.

Cardiovascular diseases represent the leading cause of death and disability in the world. At the end-stage of heart failure, heart transplantation remains the ultimate option. Therefore, due to the numerous drawbacks associated with this procedure, new alternative strategies to repair the wounded heart are required. Cell therapy is a potential option to regenerate functional myocardial tissue. The characteristics of the ideal cardiac cell therapy include the use of the proper cell type and delivery methods as well as the choice of a suitable biomaterial acting as a cellular vehicle. Since traditional delivery methods are characterized by several counter backs, among which low cell survival, new engineered micro- and nanostructured materials are today extensively studied to provide a good cardiac therapy. In this review, we report the most recent achievements in the field of cell therapy for myocardial infarction treatment and heart regeneration, focusing on the most commonly used cell sources, the traditional approaches used to deliver cells at the damaged site, and a series of novel technologies based on recent advancements of bioengineering, highlighting the tremendous potential that nanoscaffolds have in this framework.

1. Introduction

According to the World Health Organization (WHO), cardiovascular diseases (CVDs) represent the leading causes of death and disability in the world. Ischemic heart diseases such as myocardial infarction (MI), in particular, represent widely spread pathologies, producing significant morbidity [1]. MI is characterized by a decrease of blood supply to the cardiac tissue with a consequent death of cardiomyocytes and loss of contractile function. As a further consequence, the resulting nonfunctional tissue, which is still subjected to mechanical loads, generates abnormal stresses at the infarct and peri-infarct zone, with an expansion of the left ventricle [2]. The mechanical and biological stresses imply continuous changes at the structural, mechanical, and molecular levels, known as postinfarct left ventricle remodeling [3] (Figure 1). This process is highly dynamic and time dependent, comprising (i) an acute inflammatory phase, evolving to (ii) a granulation stage and then to (iii) chronic fibrosis. This degeneration progress often culminates in heart failure and death.

At the end-stage of heart failure, heart transplantation remains the ultimate option. However, the procedure of replacing the failed heart with a healthy one raises several limitations such as lack of organ donors, immune rejection, and many other complications. Because of these restrictions, researchers are still looking for new alternative strategies to repair the wounded heart and permanently restore its function. Among all approaches, cell therapy is a potential option to regenerate functional myocardial tissue. Stem or nonstem cell-based procedures are of great interest at present, and they hold great promises for a significant recovery of cardiac function. As known, the therapeutic effect of exogenous stem cells is due to four main general mechanisms: (i) differentiation of the administered cells into the cellular constituents of the regenerating myocardium; (ii) release of factors capable of paracrine signaling (a form of cell signaling in which the targeted cell is close to the signal-releasing one) from the administered cells; (iii) fusion of the administered cells with the existing constituents of the target organ; (iv)

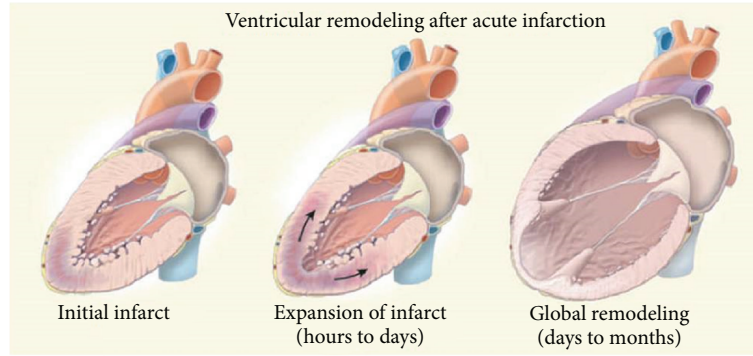


FIGURE 1: Ventricular dilation associated with progressive heart failure. After the initial insult, infarct expansion and ventricular wall thinning contribute to further ventricular remodeling, ultimately causing increased intraventricular pressure and decreased cardiac output. Reproduced with permission of Elsevier.

restoration of endogenous stem cell niches in the target organ, stimulated by exogenous cell delivery [4]. However, nonstem cells have been also used for therapeutic purposes, such as autologous or heterologous myoblasts.

The characteristics of the ideal “cardiac-therapeutic” cell type include quantitative and temporal availability, safety of administration, effectiveness of its engraftment, differentiation ability, and (most importantly) cardiac repair capability [5]. However, cell activity is not the only concern within this picture; delivery methods and properly engineered biomaterials actually represent other two key aspects to consider. As discussed in Section 3, all traditional delivery methods lead towards low cell survival and/or limited therapeutic efficacy [6]. Conversely, engineered micro- and nanostructured materials are widely studied at present to permit a suitable cell differentiation and integration with the host tissue as well as to release active compounds or to directly or indirectly perform physical therapy. Cells in general and stem cells in particular are strongly affected by extracellular stimuli, such as soluble and adhesive factors, which bind to cell-surface receptors. However, mechanical properties of the extracellular matrix, especially rigidity, also play a key role in cell signaling, proliferation, differentiation, and migration [7, 8]. Similarly, topography is able to trigger specific behaviors and/or to inhibit certain pathways [9]. The development of properly engineered substrates mimicking natural stem cell environment is therefore a crucial research field. In addition, new active materials and highly technological integrated devices are emerging, with the aim of providing injured heart with locally delivered drugs and indirect or direct physical stimulation [10–13]. Despite such synergistic joint efforts of engineers, biologists, and material scientists, a number of scientific and technological issues remain to be addressed and solved before fully exploiting the potential of cell-based regenerative therapies for heart-related pathologies. This will be probably possible in a near future by means of even more pronounced interdisciplinary research efforts [14].

This review aims to report the most recent achievements in the field of cell therapy for MI treatment and heart regeneration and to highlight the tremendous potential that nanoscaffolds have within this challenge. Firstly, the most

common cell sources used in the last decades for cardiac repair will be described showing also the most recent clinical studies on humans. Then, the traditional approaches used to deliver cells at the damaged site will be reported, discussing their safety and their efficacy in inducing cardiac remodeling and healing. A series of novel technologies, based on recent advancements of bioengineering will be then exposed, including patches, fragments, active scaffolds, composite biomaterials, and so forth. Finally, an original strategy for cardiac repair based on magnetic nanosheets will be highlighted and discussed, before drawing conclusions about the promises of these new systems in the therapeutic challenge of heart regeneration.

2. Sources of Cells for Cardiac Remodeling

Different cell sources and types determine different therapeutic outcomes. Cell-based treatment of cardiac pathologies can be carried out by using either stem or nonstem cell types. Concerning stem cells, their level of commitment is strongly related to the therapeutic potential but also to possible drawbacks, such as teratoma formation [15]. Based on the differentiating potential, stem cells can be classified into three categories. Pluripotent stem cells, such as induced pluripotent stem cells (iPSCs) and human embryonic stem cells (hESCs), show the greater healing potential thanks to their ability to differentiate into cells of all three embryonal layers (ectodermal, endodermal, and mesodermal). Multipotent stem cells, such as mesenchymal stem cells (MSCs), can generate many cell types (e.g., muscle cells, hepatocytes, blood cells, etc.) within a specific organ. Finally, oligopotent stem cells (such as myeloid or lymphoid precursors) can generate only few cell types (e.g., monocytes, macrophages, etc.), and they are generally not taken into consideration for cardiac repair.

Consistent differences can be also found between stem cells of the same type but deriving from different sources. For example, a comparative analysis between MSCs of different origin revealed that those deriving from umbilical cord blood show a limited isolation success rate and are not able to differentiate in adipose tissue; however, they can be cultured

for long periods and show a high proliferation capacity. On the contrary, MSCs from bone marrow show high isolation success rate and good differentiation capacity but very low proliferation ability. Finally, MSCs from adipose tissue show the highest colony frequency and good differentiation ability [16].

hESCs and iPSCs have not been used in clinical studies yet for the treatment of myocardial disease, due to a lack of knowledge about their tendency to form tumor tissues when used *in vivo* and to strong ethical issues related to the use of human embryos (concerning hESCs) and to epigenetic memory and other partly unknown phenomena related to the use of iPSCs. However, the therapeutic potential of these cells has been evidenced by many studies both *in vitro* [17–20] and *in vivo* [21, 22], which highlighted the possibility of efficiently differentiating pluripotent cells into cardiomyocytes and, in general, of triggering cardiac regeneration.

Adult MSCs showed good promises not for their capability of directly differentiating into cardiac-like tissue, but rather for their ability to induce “trophic effects” [23]. These effects include secretion of cytokines and growth factors, inhibition of fibrosis (and therefore prevention of scar formation) and apoptosis, angiogenesis enhancement, and stimulation of tissue-intrinsic reparative processes. Encouraging results were obtained by using adipose tissue-deriving MSCs in rat myocardial infarct models [24] and bone marrow-derived MSCs in pig with damaged myocardium [25]. Concerning MSC application to humans, the outcomes obtained in eighteen clinical studies in which bone marrow-derived cells (BMCs) were used for cardiac repair were reviewed and meta-analyzed in 2007 [26]. The results highlighted that BMC transplantation is associated with modest improvements in physiologic and anatomic parameters in patients with both acute myocardial infarction and chronic ischemic heart disease. However, research is still focused on the translation of MSCs to the clinics by focusing on specific heart defects or impairments [27].

Cardiac progenitor cells (CPCs) have been studied in postnatal hearts, and specific surface markers expressed by these cells have been identified. The most studied are the CPCs expressing the tyrosine kinase receptor c-KIT [28]. Endogenous c-KIT⁺ cells (such as interstitial cells of Cajal, thymic epithelium cells, and mast cells) are therefore under study, in order to identify their regeneration potential. CPCs from adult myocardium have been already reported to give rise to cardiomyocytes *in vitro* and *in vivo* after transplantation and to enhance cardiac function after infarction [29]. The “stemness” of CPCs has recently been questioned, and it has been suggested that they are principally cardiac fibroblasts, while CPC-derived cardiomyocytes are contaminants derived from the original tissue [30].

Concerning other cells used for cardiac repair, the literature reports heterologous epicardium-derived cells [31], skeletal myoblasts derived from skeletal muscle satellite cells [32–34], fetal cardiomyocytes [35], fibroblasts, and smooth muscle cells [36, 37]. In all these cases, even if some beneficial effects were found to the infarcted heart (mainly due to paracrine effects), the overall regeneration outcomes were rather poor.

Another interesting possibility has been recently highlighted by Song and colleagues [38], who reprogrammed cardiac fibroblasts into myocardial cells by using cardiac transcription factors (GATA4, HAND2, MEF2C, and TBX5) in mice.

In general, many years of *in vitro* and *in vivo* experiments and clinical trials have permitted to draw some conclusions [39]. Cell therapy is overall safe, with the caveat of ventricular arrhythmias which still require careful scrutinization; the cell type needs to be tailored to the primary clinical indication, whereas the paracrine effects of bone marrow cells may be therapeutically efficacious for limitation of remodeling or relief of angina. Only cells endowed with a true cardiomyogenic differentiation potential are likely to affect regeneration of chronic scars; autologous cells are primarily limited by their variable and unpredictable functionality, thereby calling attention to banked, consistent, and readily available allogeneic cell products. Regardless of the cell type, a meaningful and sustained therapeutic benefit is unlikely to occur until cell transfer and survival techniques are improved to allow greater engraftment rates. Furthermore, trial end points probably need to be reassessed to focus on mechanistic issues or hard end points depending on whether new or already extensively used cells are investigated.

3. Traditional Approaches for the Delivery of Cells in the Injured Heart

In addition to the cell type to be transplanted, another key factor concerns the adoption of an efficient method for cell delivery. The main objectives are (i) to ensure a safe transplantation, (ii) to transplant a sufficient amount of cells into the cardiac region of interest, (iii) to obtain maximum retention of cells within the target area, and (iv) a sufficient local engraftment [40]. Although there is a number of available options to direct cells to the heart, in this section, we focus on three basic strategies, namely, systemic therapy, focused coronary infusion and direct myocardial injection.

3.1. Systemic Therapy. Systemic administration of cells can be achieved through both growth factors mobilization and peripheral venous injection [40].

In the growth factor treatment [41], myocardial regeneration via stem cells mobilization and migration from tissues to injured myocardium is favoured by using specific growth factors like stromal cell-derived factor-1 (SDF-1) and stem cell factor (SCF). In particular, when the natural cell processes are not sufficient for MI healing, these phenomena are artificially induced and accelerated by supra doses of such chemical agents. Askari et al. [42] investigated the expression of SDF-1 by the myocardium after MI, finding a significant upregulation immediately after infarction and a downregulation within 7 days; the results suggested that SDF-1 is sufficient to induce therapeutic stem-cell homing to MI. Finally, though some findings showed general enhancement of cardiac performance *per se*, the efficacy of the growth factor therapy is improved when the treatment is combined with standard cellular transplantation [43].

Compared with invasive delivery methods such as direct intramyocardial injection, intravenous (IV) injection of cells [44, 45] is the simplest and noninvasive delivery strategy to treat myocardial diseases in humans. Moreover, the administration of a large numbers of cells can be easily repeated. Peripheral infusion of stem cells (by the jugular vein, the femoral vein, the scalp vein, etc.) is also used in small animal (e.g., rats) and porcine models of MI showing limited myocardial infarct size, reduced remodeling, and improvement of cardiac function [46–48]. However, entrapment of cells to noncardiac organs such as the lungs [45], lowering the selectivity and efficiency of this approach, limits its applicability.

3.2. Intracoronary Infusion. Selective intracoronary infusion of cells in the proximity of ischemic myocardial areas allows the delivery of a higher cell concentration in comparison with systemic therapies. Successful experimental [49] and clinical [50] studies have recently showed that BMCs and MSCs delivered by the intracoronary route regenerated damaged myocardium in acute MI. Chen et al. [51] investigated the efficacy of intracoronary injection of BMCs in patient with acute MI, confirming significant improvement on cardiac function and on left ventricle remodeling. The infusion of cells to the injured myocardium carried out in these studies is technically simple to perform: cells are injected through the central lumen of an over-the-wire balloon catheter during transient balloon inflations in order to maximize the exposure time of cells with the microcirculation of the infarct-related vessel. Moreover, clinical trials also demonstrated the feasibility, safety, and efficacy of this method [52]. However, possible drawbacks may be the nonselective distribution of the injected cells and, depending on the delivered cell type, their ability to migrate from coronary vessels and to infiltrate into the infarcted site without causing obstruction.

3.3. Direct Intramyocardial Injection. Direct myocardial injection is suitable to deliver cells in patients with chronic myocardial diseases, such as chronic ischemia [53], or other advanced coronary artery diseases [54], but it could be also used to treat acute MI. Direct injection can be realized transeptically, transendocardially, or via the coronary venous system [40].

Transeptical cell injection can be performed during open heart surgery, allowing for a direct visualization of the myocardium. Due to its invasiveness, this technique is commonly used in animal studies, whereas its clinical application is limited to patients undergoing sternotomy for different cardiac surgery. Menasché et al. [55] transplanted autologous skeletal myoblasts in patients undergoing coronary artery bypass grafting operations via multiple epicardial echo-guided needle injections. Even if this first clinical trial failed and no improvements in regional or global LV function were found, the increased number of early postoperative arrhythmic events after cell injection and LV remodeling for high-dose injection laid the groundwork for future investigations.

Another possible strategy for direct cell injection is the less invasive transendocardial delivery via a percutaneous

catheter-based approach [56]. To date, a multiplicity of catheter systems are available for transendocardial injection such as the Stiletto [57] or MyoStar [58] catheters. Basically, all these systems are made up of multicomponent catheters consisting of an injection needle for cell delivery and a support catheter to direct the needle to the desired site. Therefore, by passing the catheter retrogradely across the aortic valve, it is placed against the endocardial surface, thus allowing intramyocardial cell injection into the left ventricular (LV) wall. Moreover, some of the catheter systems described before integrate additional navigation capability to facilitate the selection of target areas. Perin et al. [59] performed an electromechanical mapping (EMM) of the endocardial surface by integrating the MyoStar catheter with the NOGA system; this study demonstrated the safety of intramyocardial injection of bone marrow-derived stem cells in patients with severe LV dysfunction and an improvement in both perfusion and myocardial contractility.

The last emerging technique for direct cell repopulation is transcatheter coronary vein injection. In this approach, cells can be intramyocardially injected through the coronary veins by using a catheter placed inside the coronary vein itself. In particular, Thompson et al. [60] reported a study in which the coronary venous system of pigs was used as a road map for direct cell injection. For this purpose, a special catheter system incorporating an intravascular phased array ultrasound tip for guidance and a preshaped extendable nitinol needle for transvascular myocardial access were used. While they demonstrated the feasibility (e.g., the widespread intramyocardial access from the anterior interventricular coronary vein) and safety (e.g., no death, no ventricular arrhythmia, or other procedural complications) of percutaneous intramyocardial access, the efficiency of cell grafting or functional properties of the myocardium after the injection were not assessed. Nevertheless, the study carried out by Thompson is an important step regarding the treatment of myocardium via the coronary venous system.

In contrast to peripheral venous injection and intracoronary infusion, where the specificity of the delivery is very low, direct intramyocardial injection of cells represents a more attractive route. This is due to the specific regions of the myocardium that can be targeted (noncardiac entrapment of the cells is reduced) and, as a consequence, to a highest local tissue concentration that can be reached.

Finally, based on both the advantages and drawbacks of the delivery methods previously reported, it is possible to conclude that the choice of the more suitable strategy depends on several factors, such as the specific disease the patient is affected by and the type of cells to be transplanted. For this reason, and as a consequence of the fast and sophisticated technological improvements we are witnessing, further studies and more clinical trials should be performed in the near future.

4. New Approaches: Cell Sheet Engineering, Fragments, and Patches

This section aims to report tissue engineering technologies recently developed for the treatment of MI. The most

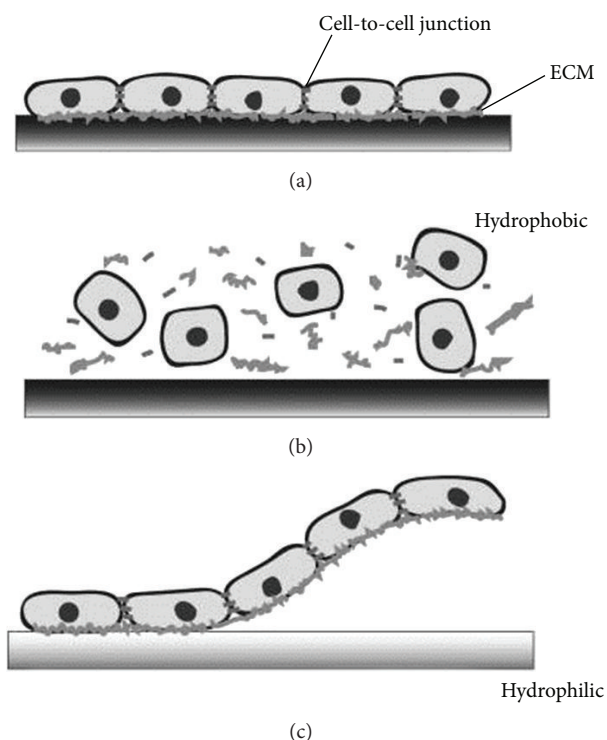


FIGURE 2: Cell sheet detachment from temperature-responsive culture surfaces. (a) ECM assures cell attachment to hydrophobic surfaces, and cell-to-cell junction proteins keep cells packed together; (b) enzymatic digestion causes ECM, and junctions are disrupted, and cells are released separately; (c) thermoresponsive culture surfaces allow the release of cell sheets by lowering temperature. Reproduced with permission of Wiley & Sons.

important features of these techniques are summarized in Table 1.

In the nineties, Okano's group developed an innovative tissue engineering method named "cell sheet technology" [61, 62]. Such technology is based on thermoresponsive culture dishes designed by using a temperature-responsive polymer, poly(*N*-isopropylacrylamide) (PNIPAAm), covalently immobilized onto common tissue culture polystyrene surfaces (TCPSs). By controlling the hydrophobicity of the dish through temperature, it is possible to switch on and off cell adhesion (Figure 2).

Through this method the seeded cells detach spontaneously and can be harvested in a noninvasive way as an intact sheet together with their deposited extracellular matrix (ECM). In comparison with conventional tissue engineering methodologies, cell sheet engineering shows several advantages. Firstly, there is the possibility to harvest cells as an entire sheet without using proteolytic enzymes such as trypsin, which causes the breaking of adhesive proteins and membrane receptors; furthermore, the presence of ECM on the sheet allows the sheet to be directly transplanted into host tissues without any mediators. Another important point is the elimination of biodegradable scaffolds, thus reducing the inflammatory response after implantation. Finally, the ability to harvest cell sheets as both single layers and multilayers

(thus creating three-dimensional structures) paves the way to advanced regenerative therapies, not only for the treatment of MI. As regards myocardial reconstruction, cell sheets obtained from PNIPAAm-grafted TCPS have been used with different sources of cells [61, 63–66] and with cardiomyocyte sheets layered in different numbers (from two up to four). *In vitro* histological analyses showed an integration of the single sheets, resulting in a homogeneous, continuous, and cell-dense structure; moreover, thanks to the formation of gap junctions after the layering, electrically synchronized cell pulses were observed. *In vivo*, spontaneous beatings were macroscopically noticed, and typical heart-like structures were found out.

Sung's group proposed an alternative approach, relying on the same philosophy of cell sheet engineering [67–69]. A continuous cell sheet was harvested by using a thermoresponsive methylcellulose (MC) hydrogel coated on TCPS dishes; then, fragmented cell sheets were obtained by means of a stainless screen. Finally, the collected fragments were transplanted by injection through a needle (Figure 3).

In these studies, different cell types were used. Chen et al. [67] and Wang et al. [68] reported fragmented sheets of rat bone marrow MSCs, transplanted via intramyocardial injection directly into the periinfarct area using a needle. After sheet preparation, both studies confirmed the preservation of endogenous ECM; subsequent to injection, the MSC sheet fragments showed the maintenance of their activity. In comparison with traditional delivery methods, a higher number of MSCs were retained in the interested area, thus resulting in a higher heart recovery. In a more recent work, Yeh et al. [69] used human amniotic fluid stem cells (hAFSCs), known to have angiogenic capability and cardiomyogenic potential. After hAFSC isolation and expansion, cell sheet fragments were prepared and transplanted into the peri-ischemic area of a rat model. Again, the fragments preserved the endogenous ECM, thus leading to enhanced cell retention in the area of interest, and significant improvements in the cardiac function were also observed.

Cardiac patches represent another interesting approach for the treatment of heart pathologies [70–73]. Although heart patches can be developed in different ways, they are basically developed starting from both biological and synthetic scaffolds laden with cells. Figure 4 shows an example of cardiac patch.

Therefore, the two most important features being addressed during the development of cardiac patches are (i) the choice of biomaterials to be used as scaffolds (showing suitable mechanical properties, such as sufficiently strength to resist the movement of myocardial tissue, adjustable biodegradation times, and ability to both carry and preserve cells) and (ii) the choice of proper cell sources for myocardial repair. Based on these assumptions, several studies can be found in the literature. Piao et al. [70] used rat bone marrow-derived mononuclear cells (BMMNCs) seeded onto a poly-glycolide-*co*-caprolactone (PGCL) scaffold; its implantation into the epicardial surface of a rat MI model produced migration and differentiation of these cells towards cardiomyocyte-related phenotypes. Chen et al. [73] also fabricated a hybrid heart patch, demonstrating its capability

TABLE 1: Summary of recent tissue engineering technologies in cardiac failure.

Approach	Authors and year	Applications	Cell types	Materials	Delivery routes	Reference
Cell sheet engineering	Kikuchi and Okano, 2005	Severe heart failure, myocardial tissue reconstruction	(i) Chick embryo cardiomyocytes	Temperature-responsive culture dishes: PNIPAAm grafted to TCPS	(i) Transplantation into dorsal subcutaneous tissues (ii) Direct transplantation into host damaged heart	[61–66]
	Matsuda et al., 2007		(ii) Neonatal rat cardiomyocytes			
	Shimizu et al., 2003		(iii) Skeletal myoblasts			
	Masuda et al., 2008		(iv) MSCs			
	Yang et al., 2007		(v) Coculture of cardiomyocytes and endothelial cells			
Cell sheet fragments	Chen et al., 2007	MI	(i) Rat bone marrow MSCs	Thermoresponsive MC hydrogel coated on TCPS dishes	Transplantation via direct intramyocardial injection	[67–69]
	Wang et al., 2008		(ii) hAFSCs			
	Yeh et al., 2010					
Tissue-bioengineered cardiac patches: scaffolds (biological or synthetic) laden with cell culture system	Piao et al., 2007	Heart failure associated with MI	(i) Rat BMMNCs	(i) Porous acellular bovine pericardia (ii) PGCL (iii) PGS (iv) Thermoresponsive MC hydrogel system coated on TCPS dishes	Implantation and suture over different infarcted areas	[70–73]
	Wei et al., 2008		(ii) Rat bone marrow MSCs			
	Huang et al., 2010		(iii) Cardiomyocytes differentiated from hESCs			
	Chen et al., 2010		(iv) Murine ESCs			
(i) Cell sheets (ii) Bioengineered patches (iii) Hydrogels	Scudellari, 2009	Heart diseases	(i) Skeletal myoblasts	(i) Biomaterials (ii) Biological constructs	(i) Direct injection into the heart muscle (ii) Percutaneous injection catheter-based delivery	[74]
			(ii) BMCs			
			(iii) MSCs			
			(iv) Cardiac stem cells			
			(v) ESCs			
			(vi) iPS			

MSCs: mesenchymal stem cells; PNIPAAm: poly(N-isopropylacrylamide); TCPS: tissue culture polystyrene; MI: myocardial infarction; hAFSCs: human amniotic fluid stem cells; MC: methylcellulose; BMMNCs: bone marrow-derived mononuclear cells; hESCs: human embryonic stem cells; ESCs: embryonic stem cells; PGCL: poly-glycolide-co-caprolactone; PGS: poly(glycerol sebacate); BMCs: bone marrow cells; iPS: induced pluripotent stem cells.

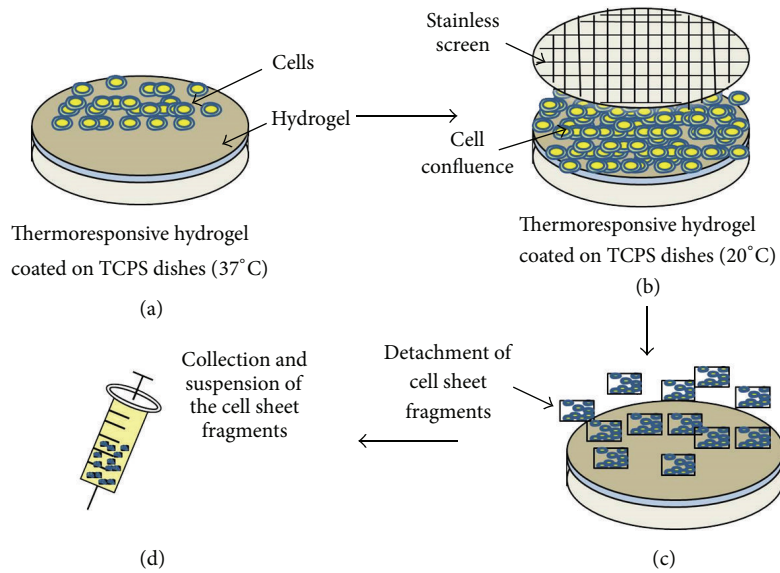


FIGURE 3: Representation of cell sheet fragments preparation and suspension. Cells cultured on a thermoresponsive hydrogel (a) are allowed to reach confluence and then fragmented by means of a stainless screen (b). Fragments are detached (c), suspended, and collected in a syringe (d) to be injected in the host organ.

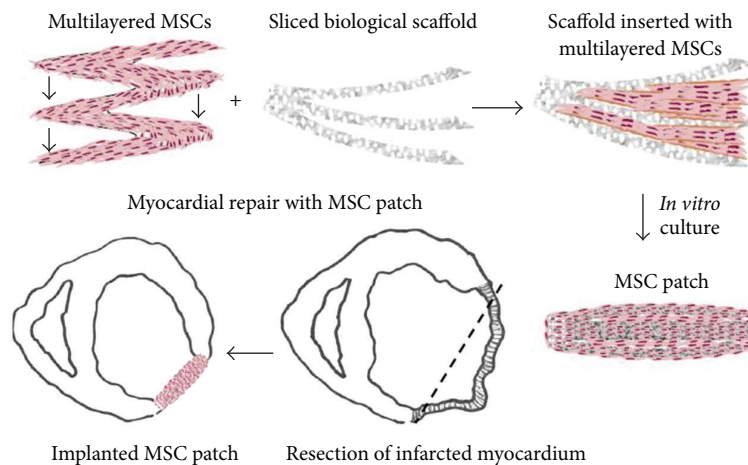


FIGURE 4: Scheme of preparation of a MSC-based therapeutic cardiac patch. Reproduced with permission of Elsevier.

to sustain cell viability and attachment as well as active cell beating for long periods; moreover, *in vivo* tests showed that the implanted patch remained undamaged over two weeks without affecting ventricular function. In this case, the cardiac patch was fabricated using again a synthetic scaffold made of poly(glycerol sebacate) (PGS), seeded with different cell types. In addition to synthetic scaffolds, biological materials can also be used to fabricate cardiac patches. Wei et al. [71] and Huang et al. [72] used sliced porous biological scaffolds (e.g., acellular bovine pericardia) and thermoresponsive MC hydrogels coated on TCPS dishes and seeded with rat bone marrow MSCs and murine ESCs, respectively. In both studies, *in vitro* tests showed high cell viability and adhesion, whereas a good integration into the host and an improvement of heart functions were observed during *in vivo* test.

Since all these bioengineering-based components have to be implanted into the human body, their future clinical applications will firstly require an eligible candidate and proven safety of both cell sources and biomaterials. A good outline of several newly developed tissue engineering techniques for the treatment of heart diseases is reported in [74].

A deep inside analysis of both traditional methods of cell delivery and the new bioengineering-based ones highlight that, despite the direct cell injection should be an inefficient route of delivery because of a high loss or death (more than 90% [75]) of cells, the combination of these approaches could prevent cell loss augmenting the cell transfer efficiency and giving a site-directed repair.

Finally, special attention has to be paid to biomaterials because, if the cell sheet engineering avoids the use of

TABLE 2: Advantages and disadvantages of novel tissue engineering technologies for the treatment of heart diseases.

Approach	Advantages	Disadvantages
Cell sheet engineering	<ul style="list-style-type: none"> (i) Elimination of the use of biodegradable scaffolds, increased cell-to-cell connections, and reduced inflammatory responses (ii) Noninvasive cells harvesting as intact monolayer sheets: cultured cells detach spontaneously by lowering temperature, thus avoiding the use of proteolytic enzymes (iii) Harvested cell sheets can be easily transferred and directly attached to the host tissue (iv) Ability to layer the harvested cell sheets: rapid cell-to-cell connections between the layers 	<ul style="list-style-type: none"> (i) Transplantation of cell sheets alone cannot provide the proper mechanical strength necessary for replacing the infarcted myocardium (ii) Need to rely on open surgery
Cell sheet fragments	<ul style="list-style-type: none"> (i) No use of proteolytic enzymes when harvesting cells (ii) Injectable without open surgical methods (iii) Good ability on cell attachment and proliferation when transferred to other surfaces (iv) High cell retention in the infarcted myocardium 	<ul style="list-style-type: none"> (i) Lack of a controlled delivery inside vessels (ii) Risk of thrombosis inside vessels
Bioengineered cardiac patches	<ul style="list-style-type: none"> (i) Integration of the advantages of tissue-engineered scaffolds and cell sheets (ii) Ability to provide the required mechanical strength to support seeded cell sheet systems (iii) Prevention of cell loss to augment cell transfer efficiency, thus allowing a site-directed repair 	<ul style="list-style-type: none"> (i) Immunogenicity caused by residual degraded scaffolds (ii) Invasive open chest surgery (iii) Materials should be optimized according to the cell source

biodegradable scaffolds reducing inflammatory responses, they are used to develop cardiac patches involving the choice of the more suitable material up to the cell source. Table 2 aims at resuming an exhaustive overview of the main advantages and disadvantages of the above described novel tissue engineering technologies.

5. Advanced Biomaterials for Heart-Related Applications

As mentioned, the achievement of effective MI treatments depends not only on the choice of the most suitable cell source but also on the employed biomaterials. Since a biomaterial, especially if used for clinical trials, interacts with biological structures, the following main requirements are demanded [76]: (i) biocompatibility with human body in general and cardiac tissues in particular; (ii) safe biodegradability; (iii) specific mechanical properties resembling those of the native heart, such as strength and flexibility; and (iv) contraction capability. An exhaustive list of biomaterials used in the last decade for MI treatment is reported in Table 3, while Figure 5 shows, for some of them, their chemical structure, their degradation times, and representative images of 2D or 3D scaffolds.

The source of the material (i.e., natural, synthetic, or composite-derived) marks several differences between its properties and possible applications [76–81]. Furthermore, its delivery strategies should be also taken into account (i.e., injection, 3-D scaffolds, or patches) [77, 79, 81].

Concerning naturally derived materials, such as alginate, chitosan, collagen, and fibrin are the most used ones. Alginate is an anionic polysaccharide found in the cell walls of brown seaweed and, thanks to its biocompatibility and gelation with divalent cations (such as Ca^{++}) of the myocardial tissue,

it shows good potential for MI treatment. Leor et al. [82] prepared an alginate-calcium solution that was intracoronary injected into a swine model of MI: the solution diffused into the infarcted zone and replaced the damaged ECM, thus preventing LV dilation. Chitosan is another linear (cationic) polysaccharide. Because of its biocompatibility and biodegradability, it is often used in biomedical applications ranging from drug delivery to tissue engineering. Wang et al. [83] intramyocardially injected a temperature-responsive chitosan hydrogel provided with specific growth factors into rat infarction models, obtaining significant improvements in cardiac functions. Fibrin glue, a biomaterial made up of fibrinogen and thrombin, can be also used for controlled release of growth factors. Nie et al. [84] demonstrated an enhancement in myocardial perfusion and cardiac functions in a canine infarct model by means of fibrin glue incorporating basic fibroblast growth factors. As described previously, all these materials can be either injected or used as delivery vehicles. An in-depth description of biological materials (concerning structure and mechanical properties) can be found in [85].

Synthetic materials represent another category of bioscaffolds used for heart regeneration. Widely used biodegradable and biocompatible polymers are poly(lactic acid) (PLA), poly(glycolic acid) (PGA), and their copolymers, for example, poly(lactic-co-glycolic acid) (PLGA) [76, 77, 80]. Caspi et al. [86] reported the achievement of an engineered human cardiac tissue showing good contracting ability, thus demonstrating the capability of developing a highly vascularized tissue with specific cardiac structures and functions. The 3D biodegradable polymeric scaffold used in this study was half made of PLGA and the other half of another widely used polymer, poly(L-lactic acid) (PLLA). This substrate was subsequently seeded with different cell culture combinations,

TABLE 3: Biomaterials for MI treatment reported in literature, in the last decade.

Biomaterial	Delivery strategies	Reference
Naturally derived materials		
Alginate	Injectable	[80]
	3D scaffold	[76–79]
Chitosan	Injectable	[77]
	Patches	[78, 79]
Collagen	Injectable	[80]
	3D scaffold	[76]
Extracellular matrix	Patches	[77, 78]
	Injectable	[76]
Fibrin and fibrin glue	Patches	[79]
	Injectable	[76]
Gelatin	3D scaffold	[77–79]
	Injectable	[76, 77]
Silk fibroin	Patches	[77]
Synthetic materials		
PEG	Injectable	[76]
	Films	[78]
PLA	3D scaffold	[76, 77, 80]
PGA	3D scaffold	[76, 77, 80]
PLGA	3D scaffold	[76, 77, 80]
PU	3D sheet	[76, 77]
PEU	3D scaffold	[77]
PEUU	3D scaffold	[76]
	Patches	[77]
TMC	Films	[76]
PTMC	Films	[77]
DLLA	Films	[76]
PNIPAAm	Cell sheet	[76]
	Injectable	[78]
PGCL	Patches	[76]
PGS	3D scaffold	[77]
PCL	Patches	[77]
Self-assembling peptides	Injectable	[78, 79]
Other synthetic hydrogels	Injectable	[79]
Composites materials		
ϵ -Caprolactone- <i>co</i> -L-lactide reinforced with PCLA, gelatin or PGA	Patches	[80]
PEUU with type I collagen	3D scaffold	[76]
Poly(caprolactone) with type I collagen	3D scaffold	[76]
Decellularized materials		
Urinary bladder matrix, SIS	Injectable	[78]
Porcine ventricular and pericardial tissue	Patches	[78]

MTE: myocardial tissue engineering; 3D: three dimensional; PEG: poly(ethylene glycol); PLA: poly(lactic acid); PGA: poly(glycolic acid); PLGA: poly(lactic-*co*-glycolic acid); PU: polyurethane; PEU: polyester urethane; PEUU: Poly(ester urethane) urea; TMC: 1,3-trimethylene carbonate; PTMC: poly(1,3-trimethylene carbonate); DLLA: D,L-lactide; PNIPAAm: poly(N-isopropylacrylamide); PGCL: poly-*co*-caprolactone; PGS: poly(glycerol sebacate); PCL: poly(ϵ -caprolactone); PCLA: poly(L-lactide); SIS: small intestine submucosa.

each one based on the use of hESCs; by adding endothelial cells (ECs) and embryonic fibroblasts (EmFs), vascularization

was finally encouraged. Such triculture system (composed of fibroblasts, endothelial cells, and cardiomyocytes) was also reported by Iyer and Radisic [76, 87], who used poly(ethylene glycol) (PEG) scaffolds as substrates for cell seeding.

Poly(ϵ -caprolactone) (PCL) [76, 77] is a biodegradable polyester which is degraded, in physiological conditions, by hydrolysis of its ester linkages; for this reason, it has been approved by the Food and Drug Administration (FDA) and, today, is widely used in several biomedical applications. PCL is often copolymerized with glycolide, resulting in poly(glycolide-*co*-caprolactone) (PGCL). Piao et al. [70, 76] fabricated cardiac patches made of PGCL and seeded them with BMMNCs; therefore, implants in rat MI models were performed, and a reduced LV remodeling and systolic dysfunction were achieved.

A recently developed biodegradable material for soft tissue engineering purposes is a special elastomer, named poly(glycerol sebacate) (PGS) [73, 77]. Thanks to its mechanical properties, comparable to those of the heart tissue, it has been used as cardiac patch by Chen et al. as previously mentioned [73]. Finally, another interesting synthetic material is poly(N-isopropylacrylamide) (PNIPAAm), a temperature-sensitive polymer that switches its surface properties from hydrophobic to hydrophilic below physiological temperature. As already mentioned, this property has been used for cell sheet engineering approaches.

The combination of natural and synthetic materials allows the preparation of composite scaffolds. Some examples are represented by poly(ester urethane) urea (PEUU) blended with type I collagen [76], and ϵ -caprolactone-*co*-L-lactide reinforced with poly(L-lactide) (PCLA), gelatin, or PGA [80] (see Table 3).

Finally, decellularized materials (tissues and organs) have been also used as bioscaffolds for tissue engineering and regenerative medicine applications [71, 72, 78, 88]. Decellularization consists of the removal (by means of physical, chemical or enzymatic methods) of cells from a tissue or an organ, maintaining only its ECM. Even if the native source tissue/organ and the decellularization methods affect the structure of the ECM scaffold and therefore its response before and after the implantation in the body, this could represent a good way to provide cells with the best environment in which they can grow, proliferate, migrate, and differentiate. Furthermore, decellularization is helpful because the removal of antigens could avoid inflammations and, consequently, a transplant rejection. Singelyn and Christman [78] reported some examples of decellularized materials used for cardiac applications such as decellularized small intestine submucosa (SIS), intact rat and porcine hearts, and decellularized ventricular and pericardial ECM. In particular, Christman's group [78, 89] carried out *in vitro* and *in vivo* studies on an injectable decellularized myocardial matrix, made of porcine ventricular tissue, in order to characterize its composition and structure. The experiments showed the capability of myocardial matrix to gel both *in vitro* and *in vivo* upon epicardial injection, to self-assemble in nanofibrous scaffolds, and to promote both *in vitro* and *in vivo* migration of endothelial and smooth muscle cells within the structure.

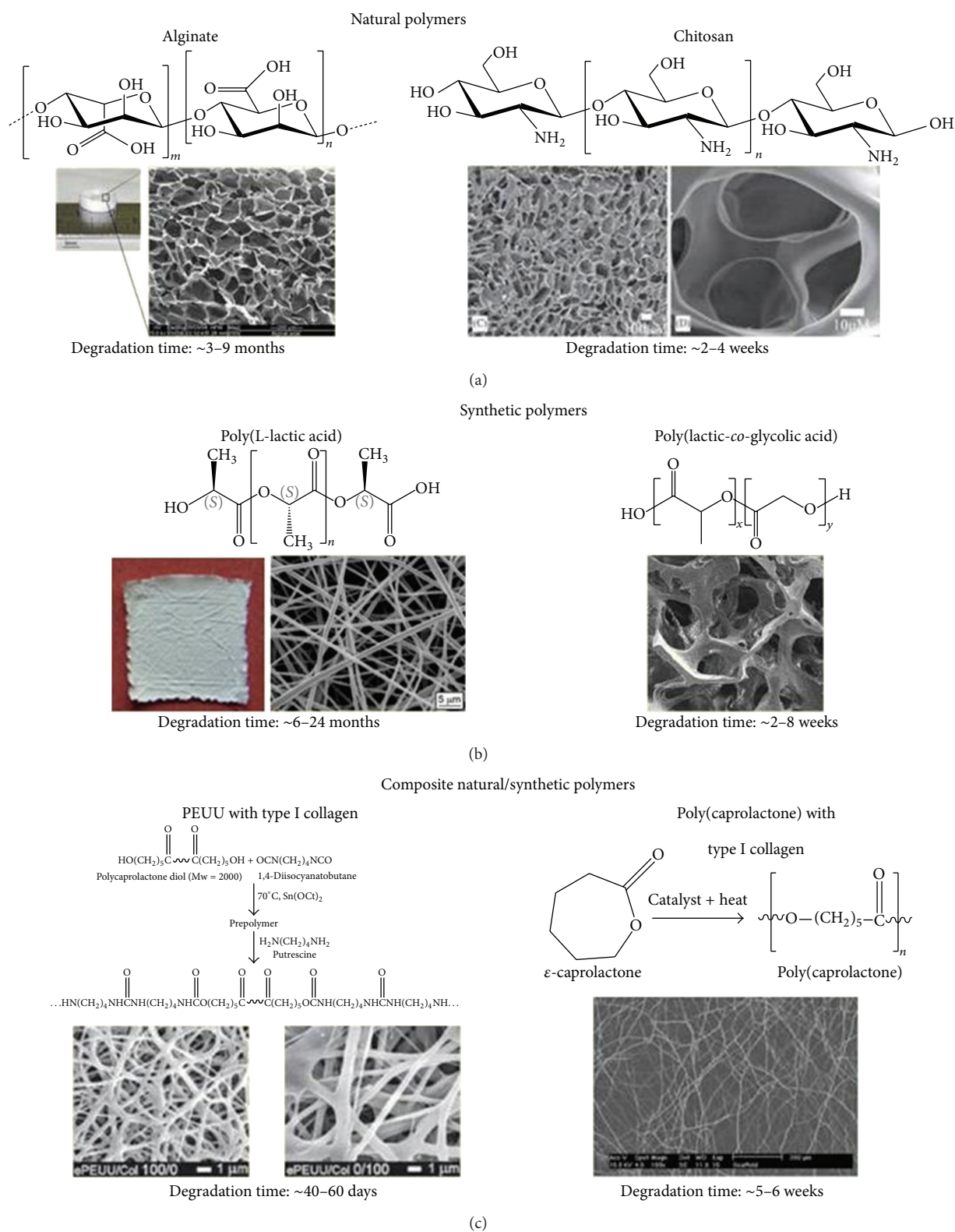


FIGURE 5: Biomaterials widely used for MI treatment. For each of them, the chemical structure (top), representative images of the scaffold (middle) and the degradation time (bottom) are reported. Reproduced with permission of Elsevier and Wiley & Sons.

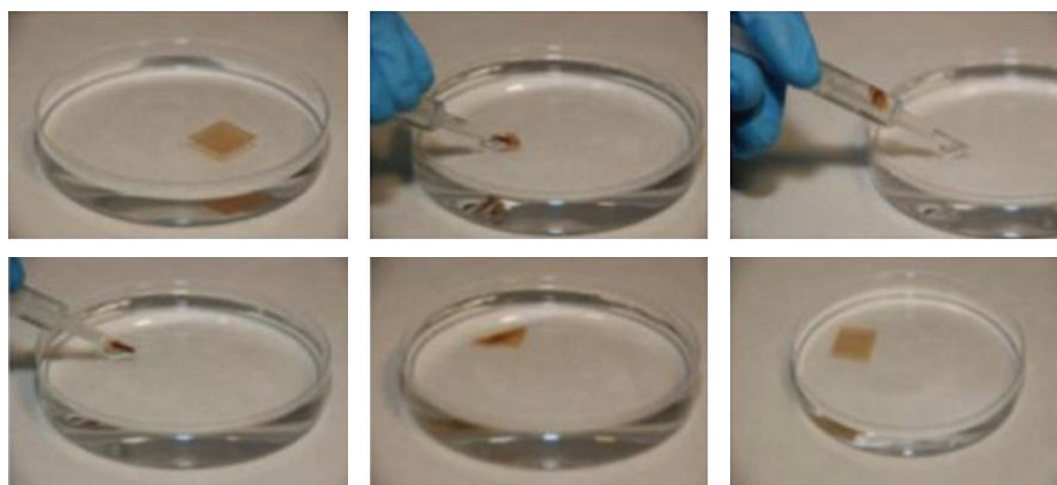
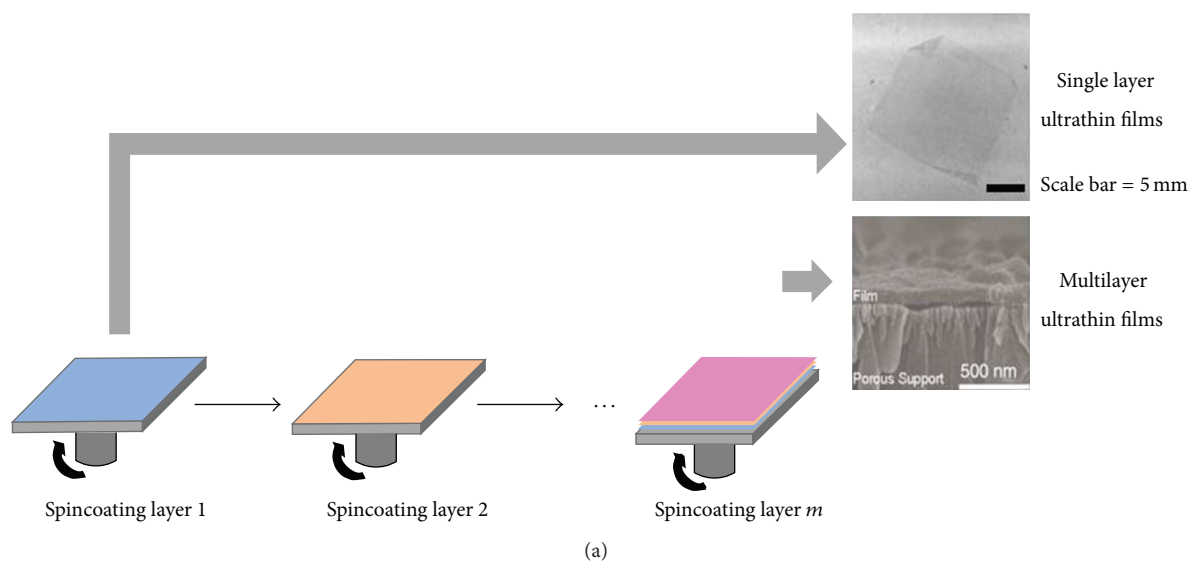


FIGURE 6: Polymeric nanofilms. (a) Scheme of single and multilayer nanofilm fabrication process; (b) magnetic nanofilms: injection (top) and ejection (bottom) sequence. Reproduced with permission of Elsevier, Springer, and Wiley & Sons.

6. Cells on Magnetic Nanosheets and Their Guidance

In addition to the already described technologies, an original approach based on polymeric nanofilms recently emerged, and it holds great promises for the treatment of heart diseases.

Nanofilms are polymeric films showing a relatively large area ($\sim 100 \text{ cm}^2$) and a nanometric thickness (10–100 nm), which leads to define them as “quasi 2D structures”. Their flexibility, associated with robustness and high biocompatibility as well as the possibility to use numerous polymers to fabricate them, opens the way to several applications in the biomedical field, ranging from biochemical or physical sensors, drug delivery systems, or substrates for tissue engineering [90, 91]. Concerning their fabrication, polymeric nanofilms can be prepared both as single and multilayer films by means of a simple method firstly proposed by Takeoka’s group, namely, spin coated assisted deposition [90]. In Figure 6(a), a simple scheme of the spin coating process

is shown. This technique is used as a single or a multistep process, according to the required number of layers [92–94]. Two different approaches are exploited in order to produce ultrathin nanosheets [95, 96]. The former uses a water-soluble polymer as a sacrificial layer, which is directly spun onto a substrate via spin coating; subsequently, another layer of the desired polymer is deposited on top. In the latter, a polymeric layer is firstly deposited onto the substrate, followed by the spinning of the polymeric supporting layer.

Since one of the key purposes of ultrathin films concerns their use as drug or cell carriers (as discussed below), the handling, control, and positioning of nanofilms inside the human body represent crucial requirements. A possibility that recently emerged consists of the development of magnetic nanofilms, specifically nanosheets containing magnetic elements. This feature allows an external and noninvasive approach, based on the use of an outer magnetic field, which can be adopted for an accurate displacement of the film within the body. A recent study performed by Mattoli’s group

TABLE 4: Novel approach based on ultrathin nanofilms.

Authors	Technology	Methods	Cell types	Materials	Possible applications	Reference
Pensabene et al., 2009 Mattoli et al., 2009	Polymer nanosheets bearing magnetic nanoparticles	Spin coating method		(i) PVA (ii) PLLA (iii) NPs	Biomedical field as free-standing carriers or as plasters	[95, 96]
Ricotti et al., 2010	Polymer nanosheets bearing cells	Spin coating method	C2C12 mouse myoblast cell line	(i) PVA (ii) PLA	(i) Regenerative medicine (ii) Muscle tissue engineering (iii) Drug delivery	[101]
Fujie et al., 2010	Polymer nanosheets bearing cells	Layer-by-layer assembly method	NIH-3T3 mouse fibroblast cell line	(i) COL (ii) HA	(i) Regenerative medicine (ii) Cell biology	[97]
Fujie et al., 2011	Polymer nanosheets bearing cells	Spin coating method	H9c2 embryonic myocardium rat cell line	(i) PVA (ii) PLLA	Building of specific cell culture environments	[99]

PVA: poly(vinyl alcohol); PLLA: poly(L-lactic acid); NPs: iron oxide nanoparticles; PLA: poly(lactic acid); COL: collagen; HA: hyaluronic acid.

[96] was based on the fabrication of nanofilms functionalized with paramagnetic nanoparticles (NPs). The magnetic behavior of the nanosheet, floating in water, was evaluated by using an external permanent magnet (field intensity $B_r = 350$ mT): results showed a fine film controllability and highlighted that velocities were strictly correlated to the concentration of the loaded NPs. A practical application of magnetic nanofilms was described by Pensabene et al. [95]. In this work, magnetic nanofilms were developed and evaluated as both drug carriers and nanoplasters. Magnetic nanosheet manipulation was tested by using a micropipette (Figure 6(b)); adhesion to the gastric mucosa was also assessed. Furthermore, the control and positioning of the films in a liquid environment (water) were finally addressed, showing their ability to reach and attach on the tissue. These outcomes allowed to conclude that the use of magnetic nanofilms constitutes a feasible strategy for bringing and releasing in a controlled way drugs or cells in different areas of the human body. Of course, further studies will be required in order to assess both the proper concentration of magnetic components and the appropriate values of external magnetic fields.

As previously mentioned, free-standing polymeric ultrathin films can be also used as novel cell culture systems and cell carriers, in order to be applied to several biomedical applications (e.g., cell biology, tissue engineering and regenerative medicine applications, and included MI therapy). The most recent studies focusing on the adhesion and proliferation properties of cells seeded onto single layer or multilayer nanofilms are summarized in Table 4.

In [97], Fujie et al. reported the fabrication of two types (i.e., fibril and nonfibril) of free-standing ECM-like multilayer nanosheets made of biopolymers such as type I collagen (COL) and hyaluronic acid (HA). Both layer-by-layer (LbL) assembly method [98] and supporting technique [95, 96] were used. Subsequently, the morphological and mechanical features of the ECM-like nanosheets as well as their mechanical effects on the adhesive properties of NIH-3T3 mouse fibroblasts seeded on it were studied. Results showed that the elongation of cells increased on the

fibril-based nanofilms, whereas it decreased on the nonfibril-based ones. This study demonstrated that cell adhesion properties were tuned by simply varying the structural ECM components of the nanosheets (e.g., the content of HA and COL fibrils). The mechanical effects of freely suspended polymeric nanofilms on cell adhesion properties have been also assessed by studying how nanosheet stiffness affects biological responses. Fujie et al. [99] synthesized ultrathin films, composed of PLLA and showing different stiffnesses, obtained by changing their thickness; H9c2 cells (an embryonic myocardium rat cell line) were then cultured onto these substrates. The adhesion properties of H9c2 on these nanofilms were valued by estimating adhesion area and elongation ratio of cells, highlighting similar results to previously reported ones [97]: cells preferentially adhered on rigid substrates in comparison to soft ones. Pensabene et al. [100] used single similar nanosheets to sustain human mesenchymal stem cell adhesion, proliferation, and differentiation, thus highlighting the possibility of using nanosheets as smart carriers of therapeutic cells. Finally, another example in which nanosheets were used as cell culture systems was reported by Ricotti et al. [101]. Here, the development of free-standing single layer PLA nanofilms as cellular scaffolds was described. After their characterization in terms of thickness and roughness, viability, adhesion, and proliferation properties of C2C12 mouse myoblasts cultured onto these substrates were assessed. Early differentiation was also verified.

In conclusion, cell adhesive properties can be tuned by changing both the structural components and the mechanical properties of polymeric nanosheets. Furthermore, the use of suitable biocompatible polymers as well as the choice of the proper cell line should allow the development of novel ultrathin films acting like cell-based matrices to be transplanted in human bodies for the treatment of several heart diseases (such as MI). Such results also suggested the possibility of using polymeric ultra-thin films as structural components for the development of bio-hybrid actuators, opening different and parallel applicative routes with respect to those related to pure regenerative medicine [102].

7. Conclusions

At present, researchers are looking for new alternative strategies to repair the wounded heart and restore its function. Among the several approaches pursued, cell-based treatment is a promising option for cardiac pathologies. In this review, we reported the most recent achievements in the field of cell therapy for MI treatment and heart regeneration. The most common cell sources used in the last decades for cardiac repair and the traditional approaches employed to delivery cells at the damaged site have been described. Then, a series of novel technologies based on recent advancements of bioengineering and tissue engineering have been illustrated, including patches, fragments, and biomaterials. Finally, an original strategy for cardiac repair based on magnetic nanosheets has been discussed, highlighting the tremendous potential and promises that nanoscaffolds have within the therapeutic challenge related to heart regeneration.

On the basis of the findings reported in this last section, the magnetic nanofilm-based approach looks really promising. This therapeutic philosophy implies that the injection of cell-seeded nanosheets inside the body and its guidance up to the damaged heart site can deeply improve MI therapeutic outcomes. Furthermore, the possibility of loading the nanofilm with specific growth factors or drugs makes this new bioengineering approach even more appealing and promising.

Conflict of Interests

Letizia Ventrelli attests to the fact that all authors listed do not have any financial relation with the commercial identity mentioned in this paper, and there is no conflict of interests.

References

- [1] D. Lloyd-Jones, R. J. Adams, T. M. Brown et al., “Executive summary: heart disease and stroke statistics—2010 update: a report from the American Heart Association,” *Circulation*, vol. 121, no. 7, pp. 948–954, 2010.
- [2] L. W. Eaton, J. L. Weiss, B. H. Bulkley, J. B. Garrison, and M. L. Weisfeldt, “Regional cardiac dilatation after acute myocardial infarction. Recognition by two-dimensional echocardiography,” *The New England Journal of Medicine*, vol. 300, no. 2, pp. 57–62, 1979.
- [3] B. I. Jugdutt, “Ventricular remodeling after infarction and the extracellular collagen matrix: when is enough enough?” *Circulation*, vol. 108, no. 11, pp. 1395–1403, 2003.
- [4] R. Mazhari and J. M. Hare, “Mechanisms of action of mesenchymal stem cells in cardiac repair: potential influences on the cardiac stem cell niche,” *Nature Clinical Practice Cardiovascular Medicine*, vol. 4, no. 1, pp. S21–S26, 2007.
- [5] A. W. Heldman, J. P. Zambrano, and J. M. Hare, “Cell therapy for heart disease: where are we in 2011?” *Journal of the American College of Cardiology*, vol. 57, no. 4, pp. 466–468, 2011.
- [6] N. Dib, H. Khawaja, S. Varner, M. McCarthy, and A. Campbell, “Cell therapy for cardiovascular disease: a comparison of methods of delivery,” *Journal of Cardiovascular Translational Research*, vol. 4, no. 2, pp. 177–181, 2011.
- [7] D. E. Discher, D. J. Mooney, and P. W. Zandstra, “Growth factors, matrices, and forces combine and control stem cells,” *Science*, vol. 324, no. 5935, pp. 1673–1677, 2009.
- [8] J. Fu, Y.-K. Wang, M. T. Yang et al., “Mechanical regulation of cell function with geometrically modulated elastomeric substrates,” *Nature Methods*, vol. 7, no. 9, pp. 733–736, 2010.
- [9] C. J. Bettinger, R. Langer, and J. T. Borenstein, “Engineering substrate topography at the Micro- and nanoscale to control cell function,” *Angewandte Chemie—International Edition*, vol. 48, no. 30, pp. 5406–5415, 2009.
- [10] M. Goldberg, R. Langer, and X. Jia, “Nanostructured materials for applications in drug delivery and tissue engineering,” *Journal of Biomaterials Science, Polymer Edition*, vol. 18, no. 3, pp. 241–268, 2007.
- [11] S. Ganta, H. Devalapally, A. Shahiwala, and M. Amiji, “A review of stimuli-responsive nanocarriers for drug and gene delivery,” *Journal of Controlled Release*, vol. 126, no. 3, pp. 187–204, 2008.
- [12] T. Dvir, B. P. Timko, M. D. Brigham et al., “Nanowired three-dimensional cardiac patches,” *Nature Nanotechnology*, vol. 6, no. 11, pp. 720–725, 2011.
- [13] B. Tian, J. Liu, T. Dvir et al., “Macroporous nanowire nanoelectronic scaffolds for synthetic tissues,” *Nature Materials*, vol. 11, no. 11, pp. 986–994, 2012.
- [14] L. Ricotti and A. Menciassi, “Engineering stem cells for future medicine,” *IEEE Transactions on Biomedical Engineering*, vol. 60, no. 3, pp. 727–734, 2013.
- [15] M. Baker, “Why hES cells make teratomas,” *Nature Reports Stem Cells*, 2009.
- [16] S. Kern, H. Eichler, J. Stoeve, H. Klüter, and K. Bieback, “Comparative analysis of mesenchymal stem cells from bone marrow, umbilical cord blood, or adipose tissue,” *Stem Cells*, vol. 24, no. 5, pp. 1294–1301, 2006.
- [17] P. Dierickx, P. A. Doevendans, N. Geijsen, and L. W. van Laake, “Embryonic template-based generation and purification of pluripotent stem cell-derived cardiomyocytes for heart repair,” *Journal of Cardiovascular Translational Research*, vol. 5, no. 5, pp. 566–580, 2012.
- [18] P. Menasché, “Embryonic stem cells for severe heart failure: why and how?” *Journal of Cardiovascular Translational Research*, vol. 5, no. 5, pp. 555–565, 2012.
- [19] H. Uosaki, P. Andersen, L. T. Shenje et al., “Direct contact with endoderm-like cells efficiently induces cardiac progenitors from mouse and human pluripotent stem cells,” *PLoS One*, vol. 7, no. 10, Article ID e46413, 2012.
- [20] K. Matsuura, M. Wada, K. Konishi et al., “Fabrication of mouse embryonic stem cell-derived layered cardiac cell sheets using a bioreactor culture system,” *PLoS One*, vol. 7, no. 12, Article ID e52176, 2012.
- [21] J. P. Vallée, M. Hauwel, M. Lepetit-Coiffé et al., “Embryonic stem cell-based cardiopatches improve cardiac function in infarcted rats,” *Stem Cells Translational Medicine*, vol. 1, no. 3, pp. 248–260, 2012.
- [22] C. Mauritz, A. Martens, S. V. Rojas et al., “Induced pluripotent stem cell (iPSC)-derived Flk-1 progenitor cells engraft, differentiate, and improve heart function in a mouse model of acute myocardial infarction,” *European Heart Journal*, vol. 32, no. 21, pp. 2634–2641, 2011.
- [23] A. I. Caplan and J. E. Dennis, “Mesenchymal stem cells as trophic mediators,” *Journal of Cellular Biochemistry*, vol. 98, no. 5, pp. 1076–1084, 2006.

- [24] Y. Miyahara, N. Nagaya, M. Kataoka et al., "Monolayered mesenchymal stem cells repair scarred myocardium after myocardial infarction," *Nature Medicine*, vol. 12, no. 4, pp. 459–465, 2006.
- [25] L. C. Amado, A. P. Saliaris, K. H. Schuleri et al., "Cardiac repair with intramyocardial injection of allogeneic mesenchymal stem cells after myocardial infarction," *Proceedings of the National Academy of Sciences of the United States of America*, vol. 102, no. 32, pp. 11474–11479, 2005.
- [26] A. Abdel-Latif, R. Bolli, I. M. Tleyjeh et al., "Adult bone marrow-derived cells for cardiac repair: a systematic review and meta-analysis," *Archives of Internal Medicine*, vol. 167, no. 10, pp. 989–997, 2007.
- [27] A. R. Williams and J. M. Hare, "Mesenchymal stem cells: biology, pathophysiology, translational findings, and therapeutic implications for cardiac disease," *Circulation Research*, vol. 109, no. 8, pp. 923–940, 2011.
- [28] M. A. Laflamme and C. E. Murry, "Heart regeneration," *Nature*, vol. 473, no. 7347, pp. 326–335, 2011.
- [29] I. Chimenti, R. R. Smith, T.-S. Li et al., "Relative roles of direct regeneration versus paracrine effects of human cardiosphere-derived cells transplanted into infarcted mice," *Circulation Research*, vol. 106, no. 5, pp. 971–980, 2010.
- [30] D. C. Andersen, P. Andersen, M. Schneider, H. B. Jensen, and S. P. Sheikh, "Murine "cardiospheres" are not a source of stem cells with cardiomyogenic potential," *Stem Cells*, vol. 27, no. 7, pp. 1571–1581, 2009.
- [31] A. Ruiz-Villalba and J. M. Pérez-Pomares, "The expanding role of the epicardium and epicardial-derived cells in cardiac development and disease," *Current Opinion in Pediatrics*, vol. 24, no. 5, pp. 569–576, 2012.
- [32] D. Marelli, C. Desrosiers, M. El-Alfy, R. L. Kao, and R. C.-J. Chiu, "Cell transplantation for myocardial repair: an experimental approach," *Cell Transplantation*, vol. 1, no. 6, pp. 383–390, 1992.
- [33] R. C.-J. Chiu, A. Zibaitis, and R. L. Kao, "Cellular cardiomyoplasty: myocardial regeneration with satellite cell implantation," *Annals of Thoracic Surgery*, vol. 60, no. 1, pp. 12–18, 1995.
- [34] G. Y. Koh, M. G. Klug, M. H. Soonpaa, and L. J. Field, "Differentiation and long-term survival of C2C12 myoblast grafts in heart," *Journal of Clinical Investigation*, vol. 92, no. 3, pp. 1548–1554, 1993.
- [35] M. H. Soonpaa, G. Y. Koh, M. G. Klug, and L. J. Field, "Formation of nascent intercalated disks between grafted fetal cardiomyocytes and host myocardium," *Science*, vol. 264, no. 5155, pp. 98–101, 1994.
- [36] K. A. Hutcheson, B. Z. Atkins, M. T. Hume, M. B. Hopkins, D. D. Glower, and D. A. Taylor, "Comparison of benefits on myocardial performance of cellular cardiomyoplasty with skeletal myoblasts and fibroblasts," *Cell Transplantation*, vol. 9, no. 3, pp. 359–368, 2000.
- [37] T. Fujii, T. M. Yau, R. D. Weisel et al., "Cell transplantation to prevent heart failure: a comparison of cell types," *Annals of Thoracic Surgery*, vol. 76, no. 6, pp. 2062–2070, 2003.
- [38] K. Song, Y. J. Nam, X. Luo et al., "Heart repair by reprogramming non-myocytes with cardiac transcription factors," *Nature*, vol. 485, no. 7400, pp. 599–604, 2012.
- [39] P. Menasche, "Cardiac cell therapy: lessons from clinical trials," *Journal of Molecular and Cellular Cardiology*, vol. 50, no. 2, pp. 258–265, 2011.
- [40] P. J. Psaltis, A. C. W. Zannettino, S. Gronthos, and S. G. Worthley, "Intramyocardial navigation and mapping for stem cell delivery," *Journal of Cardiovascular Translational Research*, vol. 3, no. 2, pp. 135–146, 2010.
- [41] P. J. Psaltis, S. Gronthos, S. G. Worthley, and A. C. W. Zannettino, "Cellular therapy for cardiovascular disease—part 2: delivery of cells and clinical experience," *Clinical Medicine Insights: Cardiology*, vol. 2, part 2, pp. 139–151, 2008.
- [42] A. T. Askari, S. Unzek, Z. B. Popovic et al., "Effect of stromal-cell-derived factor 1 on stem-cell homing and tissue regeneration in ischaemic cardiomyopathy," *The Lancet*, vol. 362, no. 9385, pp. 697–703, 2003.
- [43] H. Kondoh, Y. Sawa, N. Fukushima et al., "Combined strategy using myoblasts and hepatocyte growth factor in dilated cardiomyopathic hamsters," *Annals of Thoracic Surgery*, vol. 84, no. 1, pp. 134–141, 2007.
- [44] Q. Zhang, R. Madonna, W. Shen et al., "Stem cells and cardiovascular tissue repair: mechanism, methods, and clinical applications," *Journal of Cardiothoracic-Renal Research*, vol. 1, no. 1, pp. 3–14, 2006.
- [45] I. M. Barbash, P. Chouraqui, J. Baron et al., "Systemic delivery of bone marrow-derived mesenchymal stem cells to the infarcted myocardium: feasibility, cell migration, and body distribution," *Circulation*, vol. 108, no. 7, pp. 863–868, 2003.
- [46] M. J. Price, C.-C. Chou, M. Frantzen et al., "Intravenous mesenchymal stem cell therapy early after reperfused acute myocardial infarction improves left ventricular function and alters electrophysiologic properties," *International Journal of Cardiology*, vol. 111, no. 2, pp. 231–239, 2006.
- [47] B. Bittira, D. Shum-Tim, A. Al-Khalidi, and R. C.-J. Chiu, "Mobilization and homing of bone marrow stromal cells in myocardial infarction," *European Journal of Cardio-Thoracic Surgery*, vol. 24, no. 3, pp. 393–398, 2003.
- [48] K. C. Wollert and H. Drexler, "Clinical applications of stem cells for the heart," *Circulation Research*, vol. 96, no. 2, pp. 151–163, 2005.
- [49] D. Orlic, J. Kajstura, S. Chimenti et al., "Bone marrow cells regenerate infarcted myocardium," *Nature*, vol. 410, no. 6829, pp. 701–705, 2001.
- [50] B. E. Strauer, M. Brehm, T. Zeus et al., "Repair of infarcted myocardium by autologous intracoronary mononuclear bone marrow cell transplantation in humans," *Circulation*, vol. 106, no. 15, pp. 1913–1918, 2002.
- [51] S.-L. Chen, W.-W. Fang, F. Ye et al., "Effect on left ventricular function of intracoronary transplantation of autologous bone marrow mesenchymal stem cell in patients with acute myocardial infarction," *American Journal of Cardiology*, vol. 94, no. 1, pp. 92–95, 2004.
- [52] B. E. Strauer, M. Brehm, T. Zeus et al., "Myocardial regeneration after intracoronary transplantation of human autologous stem cells following acute myocardial infarction," *Deutsche Medizinische Wochenschrift*, vol. 126, no. 34–35, pp. 932–938, 2001.
- [53] C. A. Thompson, V. K. Reddy, A. Srinivasan et al., "Left ventricular functional recovery with percutaneous, transvascular direct myocardial delivery of bone marrow-derived cells," *Journal of Heart and Lung Transplantation*, vol. 24, no. 9, pp. 1385–1392, 2005.
- [54] S. Fuchs, L. F. Satler, R. Kornowski et al., "Catheter-based autologous bone marrow myocardial injection in no-option patients with advanced coronary artery disease: a feasibility study," *Journal of the American College of Cardiology*, vol. 41, no. 10, pp. 1721–1724, 2003.

- [55] P. Menasché, O. Alfieri, S. Janssens et al., “The myoblast autologous grafting in ischemic cardiomyopathy (MAGIC) trial: first randomized placebo-controlled study of myoblast transplantation,” *Circulation*, vol. 117, no. 9, pp. 1189–1200, 2008.
- [56] H.-F. Tse, Y.-L. Kwong, J. K. F. Chan, G. Lo, C.-L. Ho, and C.-P. Lau, “Angiogenesis in ischaemic myocardium by intramyocardial autologous bone marrow mononuclear cell implantation,” *The Lancet*, vol. 361, no. 9351, pp. 47–49, 2003.
- [57] P. M. Grossman, Z. Han, M. Palasis, J. J. Barry, and R. J. Lederman, “Incomplete retention after direct myocardial injection,” *Catheterization and Cardiovascular Interventions*, vol. 55, no. 3, pp. 392–397, 2002.
- [58] N. Dib, J. Dinsmore, Z. Lababidi et al., “One-year follow-up of feasibility and safety of the first U.S., randomized, controlled study using 3-dimensional guided catheter-based delivery of autologous skeletal myoblasts for ischemic cardiomyopathy (CAuSMIC study),” *JACC: Cardiovascular Interventions*, vol. 2, no. 1, pp. 9–16, 2009.
- [59] E. C. Perin, H. F. R. Dohmann, R. Borojevic et al., “Transendocardial, autologous bone marrow cell transplantation for severe, chronic ischemic heart failure,” *Circulation*, vol. 107, no. 18, pp. 2294–2302, 2003.
- [60] C. A. Thompson, B. A. Nasser, J. Makower et al., “Percutaneous transvenous cellular cardiomyoplasty: a novel nonsurgical approach for myocardial cell transplantation,” *Journal of the American College of Cardiology*, vol. 41, no. 11, pp. 1964–1971, 2003.
- [61] A. Kikuchi and T. Okano, “Nanostructured designs of biomedical materials: applications of cell sheet engineering to functional regenerative tissues and organs,” *Journal of Controlled Release*, vol. 101, no. 1–3, pp. 69–84, 2005.
- [62] N. Matsuda, T. Shimizu, M. Yamato, and T. Okano, “Tissue engineering based on cell sheet technology,” *Advanced Materials*, vol. 19, no. 20, pp. 3089–3099, 2007.
- [63] T. Shimizu, M. Yamato, A. Kikuchi, and T. Okano, “Cell sheet engineering for myocardial tissue reconstruction,” *Biomaterials*, vol. 24, no. 13, pp. 2309–2316, 2003.
- [64] S. Masuda, T. Shimizu, M. Yamato, and T. Okano, “Cell sheet engineering for heart tissue repair,” *Advanced Drug Delivery Reviews*, vol. 60, no. 2, pp. 277–285, 2008.
- [65] J. Yang, M. Yamato, T. Shimizu et al., “Reconstruction of functional tissues with cell sheet engineering,” *Biomaterials*, vol. 28, no. 34, pp. 5033–5043, 2007.
- [66] J. Yang, M. Yamato, K. Nishida et al., “Cell delivery in regenerative medicine: the cell sheet engineering approach,” *Journal of Controlled Release*, vol. 116, no. 2, pp. 193–203, 2006.
- [67] C.-H. Chen, Y. Chang, C.-C. Wang et al., “Construction and characterization of fragmented mesenchymal-stem-cell sheets for intramuscular injection,” *Biomaterials*, vol. 28, no. 31, pp. 4643–4651, 2007.
- [68] C.-C. Wang, C.-H. Chen, W.-W. Lin et al., “Direct intramyocardial injection of mesenchymal stem cell sheet fragments improves cardiac functions after infarction,” *Cardiovascular Research*, vol. 77, no. 3, pp. 515–524, 2008.
- [69] Y.-C. Yeh, W.-Y. Lee, C.-L. Yu et al., “Cardiac repair with injectable cell sheet fragments of human amniotic fluid stem cells in an immune-suppressed rat model,” *Biomaterials*, vol. 31, no. 25, pp. 6444–6453, 2010.
- [70] H. Piao, J.-S. Kwon, S. Piao et al., “Effects of cardiac patches engineered with bone marrow-derived mononuclear cells and PGCL scaffolds in a rat myocardial infarction model,” *Biomaterials*, vol. 28, no. 4, pp. 641–649, 2007.
- [71] H.-J. Wei, C.-H. Chen, W.-Y. Lee et al., “Bioengineered cardiac patch constructed from multilayered mesenchymal stem cells for myocardial repair,” *Biomaterials*, vol. 29, no. 26, pp. 3547–3556, 2008.
- [72] C.-C. Huang, C.-K. Liao, M.-J. Yang et al., “A strategy for fabrication of a three-dimensional tissue construct containing uniformly distributed embryoid body-derived cells as a cardiac patch,” *Biomaterials*, vol. 31, no. 24, pp. 6218–6227, 2010.
- [73] Q.-Z. Chen, H. Ishii, G. A. Thouas et al., “An elastomeric patch derived from poly(glycerol sebacate) for delivery of embryonic stem cells to the heart,” *Biomaterials*, vol. 31, no. 14, pp. 3885–3893, 2010.
- [74] M. Scudellari, “The delivery dilemma,” *Nature Reports Stem Cells*, 2009.
- [75] T. E. Robey, M. K. Saiget, H. Reinecke, and C. E. Murry, “Systems approaches to preventing transplanted cell death in cardiac repair,” *Journal of Molecular and Cellular Cardiology*, vol. 45, no. 4, pp. 567–581, 2008.
- [76] H. Jawad, N. N. Ali, A. R. Lyon, Q. Z. Chen, S. E. Harding, and A. R. Boccaccini, “Myocardial tissue engineering: a review,” *Journal of Tissue Engineering and Regenerative Medicine*, vol. 1, no. 5, pp. 327–342, 2007.
- [77] S. Mukherjee, J. R. Venugopal, R. Ravichandran, S. Ramakrishna, and M. Raghunath, “Multimodal biomaterial strategies for regeneration of infarcted myocardium,” *Journal of Materials Chemistry*, vol. 20, no. 40, pp. 8819–8831, 2010.
- [78] J. M. Singelyn and K. L. Christman, “Injectable materials for the treatment of myocardial infarction and heart failure: the promise of decellularized matrices,” *Journal of Cardiovascular Translational Research*, vol. 3, no. 5, pp. 478–486, 2010.
- [79] D. M. Nelson, Z. Ma, K. L. Fujimoto, R. Hashizume, and W. R. Wagner, “Intra-myocardial biomaterial injection therapy in the treatment of heart failure: materials, outcomes and challenges,” *Acta Biomaterialia*, vol. 7, no. 1, pp. 1–15, 2011.
- [80] P. Zammaretti and M. Jaconi, “Cardiac tissue engineering: regeneration of the wounded heart,” *Current Opinion in Biotechnology*, vol. 15, no. 5, pp. 430–434, 2004.
- [81] K. L. Christman and R. J. Lee, “Biomaterials for the treatment of myocardial infarction,” *Journal of the American College of Cardiology*, vol. 48, no. 5, pp. 907–913, 2006.
- [82] J. Leor, S. Tuvia, V. Guetta et al., “Intracoronary injection of in situ forming alginate hydrogel reverses left ventricular remodeling after myocardial infarction in Swine,” *Journal of the American College of Cardiology*, vol. 54, no. 11, pp. 1014–1023, 2009.
- [83] H. Wang, X. Zhang, Y. Li et al., “Improved myocardial performance in infarcted rat heart by co-injection of basic fibroblast growth factor with temperature-responsive Chitosan hydrogel,” *Journal of Heart and Lung Transplantation*, vol. 29, no. 8, pp. 881–887, 2010.
- [84] S.-P. Nie, X. Wang, S.-B. Qiao et al., “Improved myocardial perfusion and cardiac function by controlled-release basic fibroblast growth factor using fibrin glue in a canine infarct model,” *Journal of Zhejiang University: Science B*, vol. 11, no. 12, pp. 895–904, 2010.
- [85] M. A. Meyers, P.-Y. Chen, A. Y.-M. Lin, and Y. Seki, “Biological materials: structure and mechanical properties,” *Progress in Materials Science*, vol. 53, no. 1, pp. 1–206, 2008.
- [86] O. Caspi, A. Lesman, Y. Basevitch et al., “Tissue engineering of vascularized cardiac muscle from human embryonic stem cells,” *Circulation Research*, vol. 100, no. 2, pp. 263–272, 2007.

- [87] R. K. Iyer and M. Radisic, "Microfabricated poly(ethylene glycol) templates for cell Tri-culture in cardiac tissue engineering," *Journal of Molecular and Cellular Cardiology*, vol. 40, no. 6, p. 877, 2006.
- [88] T. W. Gilbert, T. L. Sellaro, and S. F. Badylak, "Decellularization of tissues and organs," *Biomaterials*, vol. 27, no. 19, pp. 3675–3683, 2006.
- [89] J. M. Singelyn, J. A. DeQuach, S. B. Seif-Naraghi, R. B. Littlefield, P. J. Schup-Magoffin, and K. L. Christman, "Naturally derived myocardial matrix as an injectable scaffold for cardiac tissue engineering," *Biomaterials*, vol. 30, no. 29, pp. 5409–5416, 2009.
- [90] T. Fujie, Y. Okamura, and S. Takeoka, "Ubiquitous transference of a free-standing polysaccharide nanosheet with the development of a nano-adhesive plaster," *Advanced Materials*, vol. 19, no. 21, pp. 3549–3553, 2007.
- [91] Z. Tang, Y. Wang, P. Podsiadlo, and N. A. Kotov, "Biomedical applications of layer-by-layer assembly: from biomimetics to tissue engineering," *Advanced Materials*, vol. 18, no. 24, pp. 3203–3224, 2006.
- [92] T. Boudou, T. Crouzier, K. Ren, G. Blin, and C. Picart, "Multiple functionalities of polyelectrolyte multilayer films: new biomedical applications," *Advanced Materials*, vol. 22, no. 4, pp. 441–467, 2010.
- [93] V. Mattoli, F. Greco, T. Fujie, S. Taccola, A. Menciassi, and P. Dario, "Freestanding functionalized nanofilms for biomedical applications," *Procedia Computer Science*, vol. 7, pp. 337–339, 2011.
- [94] L. Ricotti, S. Taccola, I. Bernardeschi, V. Pensabene, P. Dario, and A. Menciassi, "Quantification of growth and differentiation of C2C12 skeletal muscle cells on PSS-PAH-based polyelectrolyte layer-by-layer nanofilms," *Biomedical Materials*, vol. 6, no. 3, Article ID 031001, 2011.
- [95] V. Pensabene, V. Mattoli, A. Menciassi, P. Dario, T. Fujie, and S. Takeoka, "Magnetic nanosheet adhesion to mucosal tissue," in *Proceedings of the 9th IEEE Conference on Nanotechnology (NANO '09)*, pp. 403–407, July 2009.
- [96] V. Mattoli, V. Pensabene, T. Fujie et al., "Fabrication and characterization of ultra-thin magnetic films for biomedical applications," in *Proceedings of the 23rd Eurosensors Conference*, J. Brugger and D. Briand, Eds., pp. 28–31, Elsevier Science, Amsterdam, The Netherlands, 2009.
- [97] T. Fujie, S. Furutate, D. Niwa, and S. Takeoka, "A nano-fibrous assembly of collagen-hyaluronic acid for controlling cell-adhesive properties," *Soft Matter*, vol. 6, no. 19, pp. 4672–4676, 2010.
- [98] C. Jiang and V. V. Tsukruk, "Freestanding nanostructures via layer-by-layer assembly," *Advanced Materials*, vol. 18, no. 7, pp. 829–840, 2006.
- [99] T. Fujie, L. Ricotti, A. Desii, A. Menciassi, P. Dario, and V. Mattoli, "Evaluation of substrata effect on cell adhesion properties using freestanding poly(l-lactic acid) nanosheets," *Langmuir*, vol. 27, no. 21, pp. 13173–13182, 2011.
- [100] V. Pensabene, S. Taccola, L. Ricotti et al., "Flexible polymeric ultrathin film for mesenchymal stem cell differentiation," *Acta Biomaterialia*, vol. 7, no. 7, pp. 2883–2891, 2011.
- [101] L. Ricotti, S. Taccola, V. Pensabene et al., "Adhesion and proliferation of skeletal muscle cells on single layer poly(lactic acid) ultra-thin films," *Biomedical Microdevices*, vol. 12, no. 5, pp. 809–819, 2010.
- [102] L. Ricotti and A. Menciassi, "Bio-hybrid muscle cell-based actuators," *Biomedical Microdevices*, vol. 14, no. 6, pp. 987–998, 2012.

Research Article

Fabrication, Characterization, and Antimicrobial Activity, Evaluation of Low Silver Concentrations in Silver-Doped Hydroxyapatite Nanoparticles

A. Costescu,¹ C. S. Ciobanu,² S. L. Iconaru,^{1,2} R. V. Ghita,² C. M. Chifiriuc,³
L. G. Marutescu,³ and D. Predoi²

¹ Faculty of Physics, University of Bucharest, 405 Atomistilor, P.O. Box MG-1, 077125 Magurele, Romania

² National Institute of Materials Physics, 105 Bis Atomistilor, P.O. Box MG 07, 077125 Magurele, Romania

³ Microbiology Department, Faculty of Biology, University of Bucharest, Aleea Portocalelor 1-3, 60101 Bucharest, Romania

Correspondence should be addressed to D. Predoi; dpredoi@gmail.com

Received 14 February 2013; Accepted 18 April 2013

Academic Editor: Suad Rashdan

Copyright © 2013 A. Costescu et al. This is an open access article distributed under the Creative Commons Attribution License, which permits unrestricted use, distribution, and reproduction in any medium, provided the original work is properly cited.

The aim of this study was the evaluation of $(\text{Ca}_{10-x}\text{Ag}_x)(\text{PO}_4)_6(\text{OH})_2$ nanoparticles (Ag:HAp-NPs) for their antibacterial and antifungal activity. Resistance to antimicrobial agents by pathogenic bacteria has emerged in the recent years as a major public health problem worldwide. In this paper, we report a comparison of the antimicrobial activity of low concentrations silver-doped hydroxyapatite nanoparticles. The silver-doped nanocrystalline hydroxyapatite powder was synthesized at 100°C in deionised water. The as-prepared Ag:Hap nanoparticles were characterized by X-ray diffraction (XRD), transmission electron microscopy (TEM), FT-IR, and FT-Raman spectroscopy. X-ray diffraction (XRD) studies demonstrate that powders obtained by coprecipitation at 100°C exhibit the apatite characteristics with good crystal structure, without any new phase or impurities found. FT-IR and FT-Raman spectroscopy revealed the presence of the various vibrational modes corresponding to phosphates and hydroxyl groups and the absence of any band characteristic to silver. The specific microbiological assays demonstrated that Ag:HAp-NPs exhibited antimicrobial features, but interacted differently with the Gram-positive, Gram-negative bacterial and fungal tested strains.

1. Introduction

Nanotechnology is at the base of recent and future developments in technological and industrial applications. In last years, the progress made in the area of engineered nanomaterials allowed us to have spectacular inside knowledge about materials at an atomic and molecular scale. Recently, biomaterials are emerging as the most studied area of materials science [1–6]. Biomaterials could be defined as “implantable materials that perform their function in contact with living tissues” [7]. This is a new interdisciplinary branch set to achieve new and improved materials with biological properties for use in clinical applications. The aim of this research direction is to study, facilitate, and improve the biological interactions between materials and organisms. The inorganic materials with good biological properties are intensively studied for this purpose. The most studied biomaterials

are those based on calcium phosphate, which belongs to the so-called apatite's family. An important representative of the apatite's family is hydroxyapatite with the general formula $\text{Ca}_{10}(\text{PO}_4)_6(\text{OH})_2$. Due to its outstanding properties such as biocompatibility, osteoconductivity, and bioactivity, the hydroxyapatite (HAp) has been extensively investigated [8, 9]. It is found naturally in the human body as one of the major constituents of bones and teeth. HAp nanoparticles have been investigated as coatings of medical implants for use in dentistry and orthopaedics as prosthesis due to their excellent properties [10]. Even though these nanoparticles have excellent biocompatibility, one of the most significant problems nowadays when using implants is the risk of infections. The development of surgical infections is common and widely spread amongst patients despite the hospitals tremendous efforts to avoid them. Due to the high costs and mortality rates, the research towards developing new

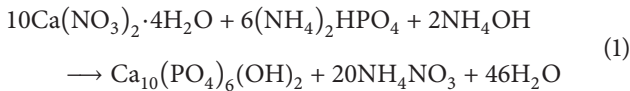
compounds with high biocompatibility and antimicrobial properties is a hot topic at global scale. Silver has been used since ancient times as an efficient antimicrobial agent, being active against a wide range of microorganisms [11]. In agreement with Clement and Jarrett [12], the understanding of silver toxicity to bacteria and of bacterial resistance mechanisms has a long way to go. Silver binds to many cellular components, the interaction with the membrane components probably being more important than that with the nucleic acids [12]. Hydroxyapatite has the ability to achieve the substitution of Ca^{2+} ions with other metal ions such as Cu^{2+} , Zn^{2+} , and Ag^{2+} , without changing its initial structure and properties.

In this paper, we report a novel compound based on low silver concentrations in silver doped hydroxyapatite nanoparticles with high biocompatibility, synthesized at low temperature using the coprecipitation method. Characterization of the Ag:Hap ($0 \leq x_{\text{Ag}} \leq 0.1$) using X-ray diffraction (XRD) and transmission electron microscopy (TEM) confirmed that the product consists of pure HAp ellipsometric nanoparticles. The antimicrobial properties of $(\text{Ca}_{10-x}\text{Ag}_x)(\text{PO}_4)_6(\text{OH})_2$, with $0 \leq x_{\text{Ag}} \leq 0.1$ nanoparticles were evaluated on Gram-negative (*Escherichia coli* ATCC 25922, *E. coli* 714, *K. pneumoniae* 2968) and Gram-positive (*Bacillus subtilis*) bacterial strains as well as *Candida krusei* 963 yeast.

2. Experimental Section

2.1. Sample Preparation. The reagents used for the synthesis of silver doped hydroxyapatite were ammonium dihydrogen phosphate $[(\text{NH}_4)_2\text{HPO}_4]$ (Alpha Aesare, Germany, 99.99% purity), calcium nitrate $[\text{Ca}(\text{NO}_3)_2 \cdot 4\text{H}_2\text{O}]$ (Alpha Aesare, Germany, 99.99% purity), silver nitrate AgNO_3 (Alpha Aesare, Germany, 99.99% purity), and ammonium hydroxide NH_4OH (Alpha Aesare, Germany, 99.99% purity).

The synthesis of $(\text{Ca}_{10-x}\text{Ag}_x)(\text{PO}_4)_6(\text{OH})_2$, with $x_{\text{Ag}} = 0$, $x_{\text{Ag}} = 0.02$, $x_{\text{Ag}} = 0.05$, $x_{\text{Ag}} = 0.07$, and $x_{\text{Ag}} = 0.1$ was carried out as reported [13, 14]. The synthesis of Ag:HAp with $x_{\text{Ag}} = 0$ was carried out as reported [13, 14] by the following reaction [15]:



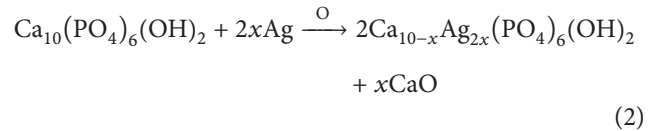
The pH of solution was adjusted to 10 with ammonium hydroxide (NH_4OH) in accord with [16]. Nanocrystalline hydroxyapatite doped with Ag was performed by setting the x_{Ag} from 0 to 0.1 ($0 \leq x_{\text{Ag}} \leq 0.1$) and $[\text{Ca}+\text{Ag}]/\text{P}$ as 1.67. The AgNO_3 and $\text{Ca}(\text{NO}_3)_2 \cdot 4\text{H}_2\text{O}$ were dissolved in deionised water to obtain 300 mL $[\text{Ca}+\text{Ag}]$ -containing solution. On the other hand, the $(\text{NH}_4)_2\text{HPO}_4$ was dissolved in deionised water to make 300 mL P-containing solution. The $[\text{Ca}+\text{Ag}]$ -containing solution was stirred at 100°C for 30 minutes. Meanwhile the pH of P-containing solution was adjusted to 10 with ammonium hydroxide (NH_4OH) and stirred continuously for 30 minutes. The P-containing solution was added drop by drop into the $[\text{Ca}+\text{Ag}]$ -containing solution and stirred for 2 h and the pH was constantly adjusted

and kept at 10 during the reaction. When the reaction was complete, the deposited mixtures were washed several times with deionised water. The resulting material (Ag:HAp) was dried at 100°C for 72 h.

Silver doped hydroxyapatite powders (Ag:HAp) with $x_{\text{Ag}} \neq 0$, setting the x_{Ag} from 0.02 to 0.1 ($0.02 \leq x_{\text{Ag}} \leq 0.1$), were prepared assuming that silver ions would substitute for the calcium site in the HAp lattice.

According to Nath et al. [17], it is important to note that the acceptable reason for this phenomenon is that the radius of silver ion is bigger than that of the strontium ion (11.5%) with fewer valence electrons. It is also important to note that Ma et al. [18] and Corami et al. [19] in two separate research studies suggested some reactions for ion exchange between heavy metals and apatite particles.

The diffusion of Ag in HAp lattice can be characterized by the following equation [17]:



This equation indicates that Ag can be incorporated into the lattice of HAp, which is schematically shown by [17]. According to Nath et al., the complex crystal structure of HAp is described by Ca triangle around the OH column. It is worth mentioning that, in the presence of Ag, one of the Ca^{2+} sites can be substituted by Ag. Nath et al. also confirmed this substitution mechanism using Raman spectroscopy by confirming the presence of Ag–O bond. Nath et al. [17] and Nazari et al. [20] showed that because of valency difference between Ca and Ag ions, a vacancy will be created in the anion site, as per the following defect reaction:



As shown by Nath et al. and Nazari et al., it can be perceived that the creation of oxygen vacancy will enable the proton of OH-bond to be attracted towards Ag-defect in the HAp structure.

2.2. Sample Characterization. The X-ray diffraction measurements for the Ag:HAp samples were recorded using a Bruker D8 Advance diffractometer, with nickel filtered Cu K_α ($\lambda = 1.5418 \text{ \AA}$) radiation with a high efficiency one-dimensional detector (Lynx Eye type) operated in integration mode. The diffraction patterns were collected in the 2θ range 20° – 70° , with a step of 0.02° and 34 s measuring time per step. Transmission electron microscopy (TEM) studies were carried out using a FEI Tecnai 12 equipped with a low dose Gatan digital camera. The specimen for TEM imaging was prepared by ultra microtomy in order to obtain thin section of about 60 nm. The powder was embedded in an epoxy resin (polaron 612) before microtomy. TEM modes used were bright field (BF) and selected area diffraction (SAD). The functional groups present in the prepared nanoparticles and thin films were identified by FTIR using a Spectrum BX spectrometer. In order to obtain the nanoparticles spectra,

1% of the nanopowder was mixed and ground with 99% KBr. Tablets of 10 mm diameter were prepared by pressing the powder mixture at a load of 5 tons for 2 min. The spectrum was recorded in the range of 500 to 4000 cm^{-1} with 4 cm^{-1} resolution. Micro-Raman spectra on powders were performed in a backscattering geometry at room temperature and in ambient air, under a laser excitation wavelength of 514 nm, using a Jobin Yvon T64000 Raman spectrophotometer under a microscope. Chemical analyses of samples were performed by HITACHI Z-8100 Polarized Zeeman Atomic Spectrophotometer performed at the Fonctionnement et Evolution des Biogéosystèmes Continentaux (Institut des Sciences de la Terre d'Orléans, France).

For the antimicrobial assays, microbial suspensions of 1.5×10^8 CFU/mL corresponding to 0.5 McFarland density obtained from 15 to 18 h bacterial cultures developed on solid media were used. The tested substances were solubilised in DMSO and the starting stock solution was of 5000 $\mu\text{g}/\text{mL}$ concentration. The quantitative assay was performed by liquid microdilution method [21–27].

3. Results and Discussions

Figure 1 shows the XRD patterns of pure HAp ($x_{\text{Ag}} = 0$), Ag:HAp ($x_{\text{Ag}} = 0.02$, $x_{\text{Ag}} = 0.05$, $x_{\text{Ag}} = 0.07$, and $x_{\text{Ag}} = 0.1$) and the standard data for the hexagonal hydroxyapatite. For pure HAp ($x_{\text{Ag}} = 0$) and Ag:HAp ($x_{\text{Ag}} = 0.02$, $x_{\text{Ag}} = 0.05$, $x_{\text{Ag}} = 0.07$, and $x_{\text{Ag}} = 0.1$), the diffraction peaks can be well indexed to the hexagonal $\text{Ca}_{10}(\text{PO}_4)_6(\text{OH})_2$ in $P6_3m$ space group (ICDD-PDF No. 9-432). The XRD analysis of Ag:HAp nanoparticles did not give the characteristic peak for silver or other phases. The XRD patterns of HAp and Ag:HAp also demonstrate that powders made by coprecipitation at 100°C with low silver concentrations in silver doped hydroxyapatite nanoparticles exhibit the apatite characteristics with good crystal structure and no new phase or impurity is found in good accord with our previous studies [13, 14, 28, 29].

The absence of other phases in XRD pattern of Ag:HAp samples demonstrates that the Ag^+ ions have successfully substituted Ca^{2+} ions without affecting the crystal structure of the original HAp. This result is in agreement with previous studies conducted by Ravindran et al., in 2010 [29], and Shirkhazadeh et al., in 1995 [30].

The morphology and particle size of nanopowders were determined by TEM observation. Figure 2 shows TEM images of Ag:HAp ($x_{\text{Ag}} = 0$). As shown in Figure 1, Ag:HAp nanoparticles exhibited an ellipsoidal morphology which is consistent with the SEM results [13].

Figure 3 exhibits the TEM images of Ag:HAp ($x_{\text{Ag}} = 0.02$, $x_{\text{Ag}} = 0.05$, $x_{\text{Ag}} = 0.07$, and $x_{\text{Ag}} = 0.1$) at low resolution. No obvious morphological changes are observed between the initial HAp and the corresponding Ag:HAp ($x_{\text{Ag}} = 0.02$, $x_{\text{Ag}} = 0.05$, $x_{\text{Ag}} = 0.07$, and $x_{\text{Ag}} = 0.1$), and new fine particles were formed. The Ag:HAp nanoparticles preserve the morphology of pure HAp prepared by coprecipitation method [14, 28]. The long axis corresponded to the c -axis of the hexagonal HAp structure.

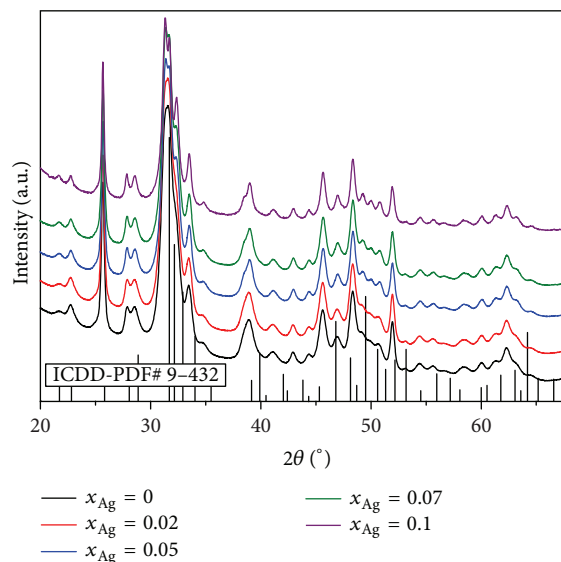


FIGURE 1: Comparative representation of the experimental XRD patterns of the Ag:HAp samples synthesized $x_{\text{Ag}} = 0$, $x_{\text{Ag}} = 0.02$, $x_{\text{Ag}} = 0.05$, $x_{\text{Ag}} = 0.07$, and $x_{\text{Ag}} = 0.1$, and the characteristic lines of hydroxyapatite according to the ICDD-PDF number 9-432.

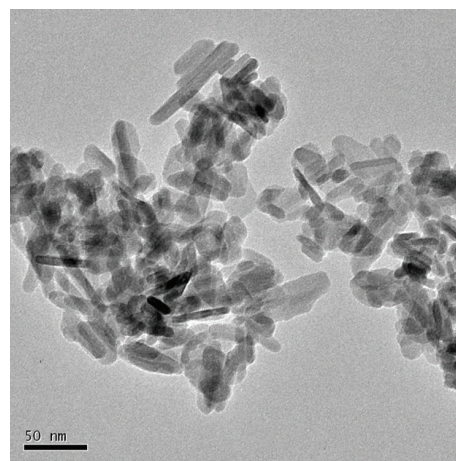


FIGURE 2: The TEM images of Ag:HAp ($x_{\text{Ag}} = 0$) at low resolution.

It can be seen from the HRTEM image of Ag:HAp (Figure 4(a)) the crystalline phase of hydroxyapatite with well-resolved lattice fringes. The distances between the adjacent lattice fringes (2.81 Å and 1.94 Å) agree well with the d_{211} and d_{222} spacing values from the literature (ICDD-PDF no. 9-432). All the samples exhibit a uniform ellipsoidal morphology with particles from 5 nm to 15 nm. Figure 4(b) shows a selected area electron diffraction (SAED) pattern recorded from an area containing a large number of ellipsometric nanoparticles. The rings in the SAED pattern can be indexed as (002), (210), (211), (310), (222), (213), (004), and (304) reflections of the hexagonal HAp, in agreement with the XRD results. No extra reflections are observed and we can therefore conclude that the product consists of pure HAp ellipsometric nanoparticles.

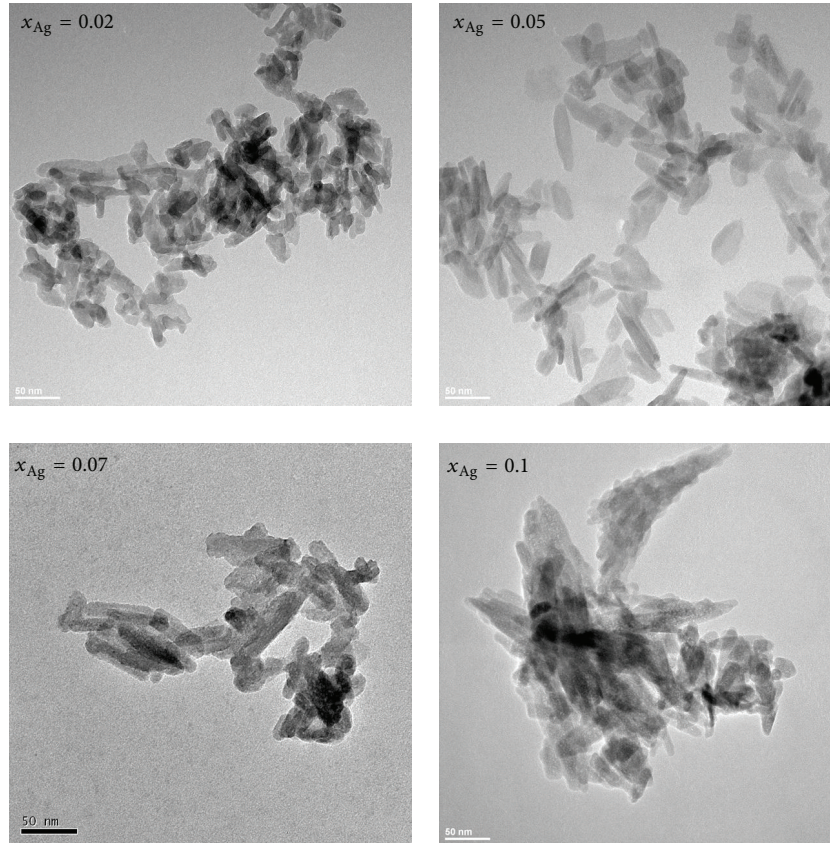


FIGURE 3: The TEM images of Ag:HAp ($x_{\text{Ag}} = 0.02$, $x_{\text{Ag}} = 0.05$, $x_{\text{Ag}} = 0.07$, and $x_{\text{Ag}} = 0.1$) at low resolution.

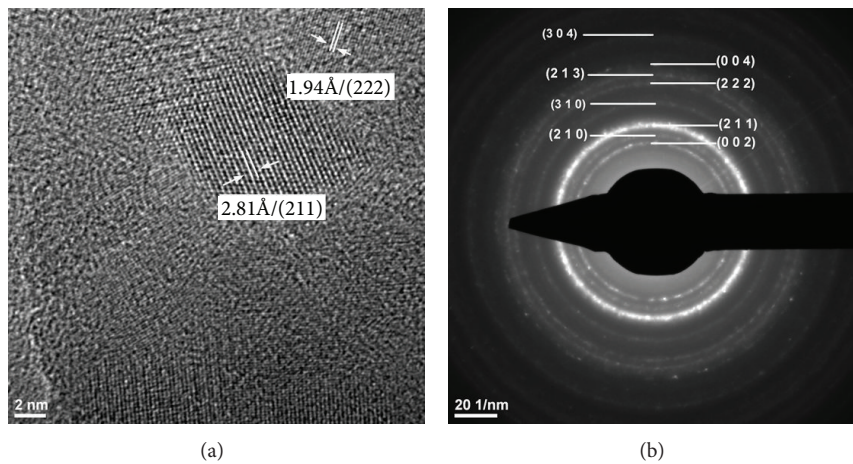


FIGURE 4: HRTEM image and SAED analysis of Ag:HAp with $x_{\text{Ag}} = 0.05$.

These results are well consistent with the XRD results revealing that the doping components have little influence on the surface morphology of the samples. The morphology identifications indicated that the nanoparticles with good crystal structure could be made by coprecipitation method at low temperature.

FT-IR spectroscopy was performed in order to investigate the functional groups present in nanohydroxyapatite, $\text{Ca}_{10-x}\text{Ag}_x(\text{PO}_4)_6(\text{OH})_2$, ($x_{\text{Ag}} = 0$, $x_{\text{Ag}} = 0.02$, $x_{\text{Ag}} = 0.05$,

$x_{\text{Ag}} = 0.07$, and $x_{\text{Ag}} = 0.1$) synthesized at 100°C by coprecipitation method. Figure 5 shows the FT-IR results obtained from Ag:HAp-NPs when the x_{Ag} increases from 0.05 to 0.3. The absorption peak in the region of $1600\text{--}1700\text{ cm}^{-1}$ ascribed to O–H bending mode is evidence of the presence of absorbed water in the synthesized products [31, 32].

The data clearly reveals the presence of various vibrational modes corresponding to phosphate and hydroxyl groups. For all the samples, the presence of strong OH vibration

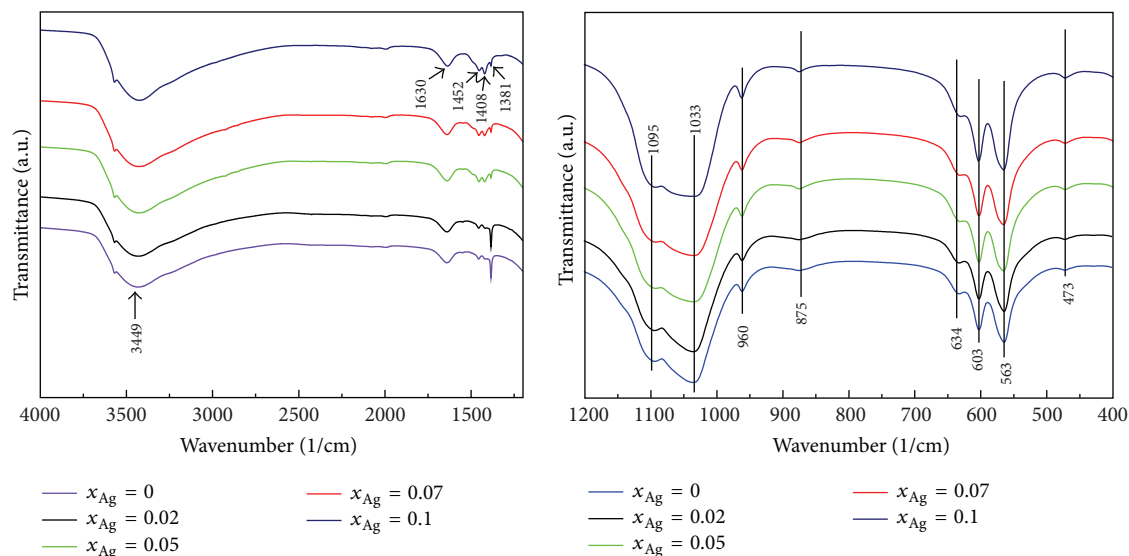


FIGURE 5: Transmittance infrared spectra of the Ag:HAP samples synthesized with $x_{\text{Ag}} = 0$, $x_{\text{Ag}} = 0.02$, $x_{\text{Ag}} = 0.05$, $x_{\text{Ag}} = 0.07$, and $x_{\text{Ag}} = 0.1$.

peak could be noticed. The peak observed at 634 cm^{-1} is attributed to the characteristic stretching and vibrational modes of structural OH groups [33]. The band at 1630 cm^{-1} corresponds to the adsorbed H_2O [33]. The broad bands in the regions $1600\text{--}1700\text{ cm}^{-1}$ and $3200\text{--}3600\text{ cm}^{-1}$ correspond to H–O–H bands of water lattice [34].

Bands characteristics of PO_4^{3-} tetrahedral apatite's structure are clearly observed at 473 cm^{-1} , 563 cm^{-1} , 603 cm^{-1} , 960 cm^{-1} , and $1095\text{--}1033\text{ cm}^{-1}$ [35, 36]. The peak at 473 cm^{-1} is attributed to $\text{PO}_4 \nu_2$. The peaks at 563 cm^{-1} and 603 cm^{-1} belong to $\text{PO}_4 \nu_4$. The peak at 960 cm^{-1} is attributed to $\text{PO}_4 \nu_1$ and the peaks at $1095\text{--}1033\text{ cm}^{-1}$, to $\text{PO}_4 \nu_3$. A CO_3^{2-} band occurred in the spectra at 1452 and 1400 cm^{-1} . The bands at 875 cm^{-1} are attributed to HPO_4^{2-} ions [37, 38].

Complementary information can be obtained from Raman spectroscopy. Raman spectra of Ag:HAP from 1200 cm^{-1} to 400 cm^{-1} is shown in Figure 6. The OH^- vibrational bands expected in the region of 630 cm^{-1} are not clearly detected. This behavior is in good accord with the previous studies [39].

We assigned the bands present at 1026 cm^{-1} (ν_3), 1047 cm^{-1} (ν_3), and 1074 cm^{-1} (ν_3) to the asymmetric ν_3 (P–O) stretching. The internal modes of the PO_4^{3-} tetrahedral ν_1 frequency (960 cm^{-1}) correspond to the symmetric stretching of P–O bonds. The 616 cm^{-1} , 590 cm^{-1} , and 576 cm^{-1} bands arise from ν_4 PO_4 [37]. The vibrational bands at 429 cm^{-1} (ν_2) and 449 cm^{-1} (ν_2) are attributed to the O–P–O bending modes. The band at 1070 cm^{-1} (ν_1) attributed to CO_3^{2-} impurity was obscured by the intensity of PO_4 band at 1074 cm^{-1} . The other CO_3 modes ν_3 , ν_4 , and ν_2 have band positions not obscured by the PO_4 bands, but they have weak intensities and were not detected [40]. Water vibrational modes give rise to weak intensity stretching and bending bands in Raman spectra. These water bands,

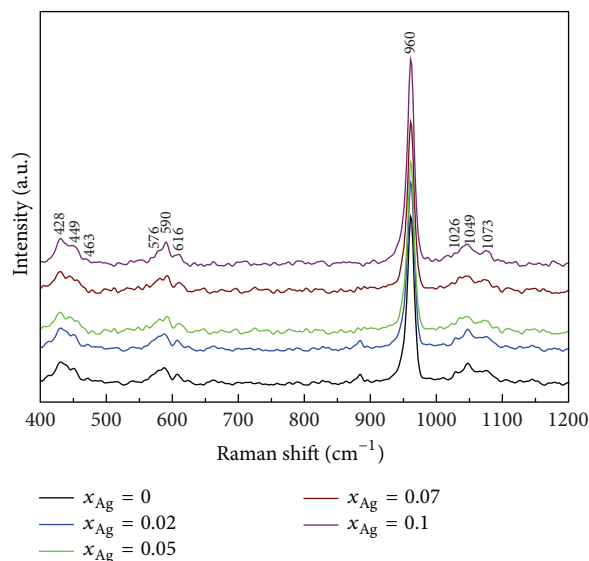


FIGURE 6: Raman spectra of the Ag:HAP samples synthesized with $x_{\text{Ag}} = 0$, $x_{\text{Ag}} = 0.02$, $x_{\text{Ag}} = 0.05$, $x_{\text{Ag}} = 0.07$, and $x_{\text{Ag}} = 0.1$.

expected at about the same wave number in FTIR spectra, were not observed in Raman spectra.

The results on chemical analyses of samples are reported in Table 1. The synthesis allowed a good control over the chemical composition of Ag:HAP powders ($x_{\text{Ag}} = 0$, $x_{\text{Ag}} = 0.02$, $x_{\text{Ag}} = 0.05$, $x_{\text{Ag}} = 0.07$, and $x_{\text{Ag}} = 0.1$), with the Ca/P and (Ca+Ag)/P atomic ratios being close to the stoichiometric value of 1.67.

The antimicrobial activity of Ag:HAP ($0 \leq x_{\text{Ag}} \leq 0.1$) nanoparticles was tested using strains belonging to the most commonly encountered pathogens: *E. coli* ATCC 25922, *E. coli* 714, *K. pneumoniae* 2968, *B. subtilis*, and *C. krusei* 963.

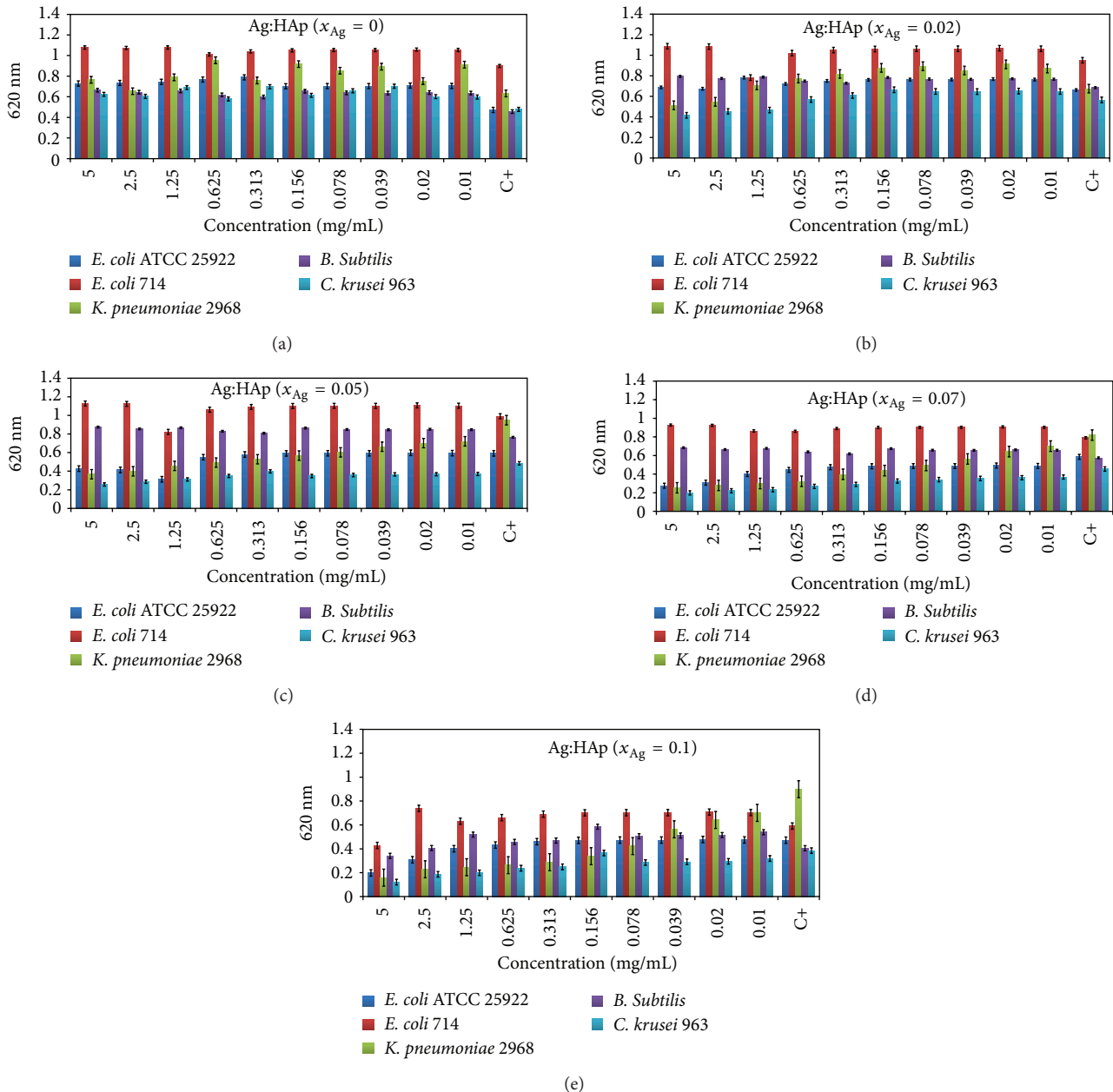


FIGURE 7: Antibacterial activity of Ag:HAp-NPs ($x_{Ag} = 0, 0.02, 0.05, 0.07,$ and 0.1) on *E. coli* ATCC 25922, *E. coli* 714, *K. pneumoniae* 2968, *B. subtilis*, and *C. krusei* strains.

The results of microbiological assays of Ag:HAp ($0 \leq x_{Ag} \leq 0.1$) nanoparticles are shown in Figures 7(a)–7(e). The Ag:HAp ($x_{Ag} = 0$) nanoparticles exhibited no inhibitory effect on the microbial growth as compared to the positive growth control (C+) (Figure 7(a)). The Ag:HAp nanoparticles with $x_{Ag} = 0.02$ exhibited an inhibitory effect on the growth of *K. pneumoniae* at the first two tested concentrations and of *C. krusei* 963 at the first three tested concentrations (Figure 7(b)). The Ag:HAp nanoparticles with higher concentrations of Ag ($x_{Ag} = 0.05; 0.07$ and 0.1) showed an improved antimicrobial activity against the same two pathogens, that is, *K. pneumoniae* and *C. krusei*, but maintained for the entire

range of the tested concentrations, from 5 to 0.01 mg/mL (Figures 7(c), 7(d), and 7(e)). Starting with the $x_{Ag} = 0.05$, the tested nanoparticles started to exhibit also an inhibitory effect against one of the two *E. coli* tested strains, that is, *E. coli* ATCC 25922, which is totally susceptible to antibiotics, being recommended as a reference strain for performing susceptibility testing. In exchange, the second *E. coli* 714 strain, which is a clinical strain, resistant to beta-lactam antibiotics, proved to be resistant to almost all tested nanoparticles, irrespective to the silver ions concentration, except the Ag:HAp nanoparticles doped $x_{Ag} = 0.1$, demonstrating that a potential cross-resistance mechanism could be responsible

TABLE I: Chemical analyses of samples.

Samples	Ca/P (molar ratio)	Ag (%)	(Ca+Ag)/P (molar ratio)
$x_{\text{Ag}} = 0$	1.668	—	—
$x_{\text{Ag}} = 0.02$	1.673	1.89	1.675
$x_{\text{Ag}} = 0.05$	1.668	4.91	1.673
$x_{\text{Ag}} = 0.07$	1.666	6.97	1.669
$x_{\text{Ag}} = 0.1$	1.665	9.98	1.667

for the concomitant resistance to antibiotics and silver ions in this strain. As for *B. subtilis* strain, only the nanoparticles doped with the highest concentration of silver exhibited an inhibitory effect. These results are clearly demonstrating that the antimicrobial effect of the silver doped nanoparticles is dependent on the structure of the microbial cell wall.

Kreibig and Vollmer [40], Morones et al. [41], and Pal et al. [42] demonstrated that the nanosize of the nanoparticles assures a large surface contact area with the microbial cells and, hence, a better interaction with the microbial target will occur. Raimondi et al. [43] and Bai et al. [36], studying the inhibition of bacterial growth by differentially shaped nanoparticles, showed that the antibacterial efficacy of the nanoparticles depends on the shape of nanoparticles. In their studies, Pal et al. [42] show that, in the case of spherical nanoparticles, total silver content of 12.5 μg is needed while the rod shaped particles need a total of 50 to 100 μg of silver content. Our study demonstrates that the antibacterial activity of Ag:HAp nanoparticles is dependent on the silver concentration, with the intensity of the inhibitory effect increasing proportionally from 0.01 mg/mL to 5 mg/mL. In order to obtain a large and effective antimicrobial spectrum, including the Gram-negative, Gram-positive bacterial and fungal strains, a higher Ag:HAp concentration of 5 mg/mL is required for this type of nanoparticles. However, further studies are needed to evaluate the cytotoxicity of the nanoparticles doped with this silver concentration, before recommending them for *in vivo* clinical applications.

4. Conclusions

The Ag:HAp nanoparticles obtained by coprecipitation method at low temperature have good crystal structure and doping components have little influence on the surface morphology of the samples. The DRX analysis of Ag:HAp did not exhibit the characteristic peak for silver. Low silver concentrations are required to be effective against Gram-negative bacterial and fungal strains, but, however, the intensity of the antimicrobial effect against these strains is increasing with the silver ions concentration. Only high Ag:HAp concentration of 5 mg/mL was effective against the Gram-positive bacterial strains. The antimicrobial properties of Ag:HAp nanoparticles are supporting their potential use for various medical applications, for example, textile dressings, orthopedic and dental prostheses, or implants with improved resistance to microbial colonization.

Acknowledgments

The financial and encouragement support was provided by the Ministry of Education of Romania, project no: C2-06 under program CEA-IFA, Programul Nucleu PN 45, program 94/PN2/PCCA (2012–2014) (AntiBioTube). The authors gratefully acknowledge the support given to this work by Dr. F. Massuyeau from the Institut des Matériaux-Jean Rouxel, France.

References

- [1] M. Vallet-Regí, “Evolution of bioceramics within the field of biomaterials,” *Comptes Rendus Chimie*, vol. 13, no. 1-2, pp. 174–185, 2010.
- [2] Z. Shi, X. Huang, Y. Cai, R. Tang, and D. Yang, “Size effect of hydroxyapatite nanoparticles on proliferation and apoptosis of osteoblast-like cells,” *Acta Biomaterialia*, vol. 5, no. 1, pp. 338–345, 2009.
- [3] J. Baier, R. Strumberger, F. Berger, P. Atanasova, U. Welzel, and J. Bill, “Mineralization and particle growth kinetics of ZnO in the presence of gelatin,” *Biointerface Research in Applied Chemistry*, vol. 2, no. 3, pp. 339–349, 2012.
- [4] J. Baier, T. Naumburg, N. J. Blumenstein et al., “Bio-inspired mineralization of zinc oxide in presence of ZnO-binding peptides,” *Biointerface Research in Applied Chemistry*, vol. 2, no. 3, pp. 380–391, 2012.
- [5] A. M. Grumezescu, E. Andronescu, A. Ficaï, C. Bleotu, and M. C. Chifiriuc, “Chitin based biomaterial for antimicrobial therapy: fabrication, characterization and in vitro profile based interaction with eukaryotic and prokaryotic cells,” *Biointerface Research in Applied Chemistry*, vol. 2, no. 5, pp. 438–445, 2012.
- [6] A. M. Grumezescu, E. Andronescu, A. Ficaï et al., “Water soluble magnetic biocomposite with pontential applications for the antimicrobial therapy,” *Biointerface Research in Applied Chemistry*, vol. 2, no. 6, pp. 469–475, 2012.
- [7] C. S. Ciobanu, S. L. Iconaru, E. Gyorgy et al., “Biomedical properties and preparation of iron oxide-dextran nanostructures by maple technique,” *Chemistry Central Journal*, vol. 6, article 17, 2012.
- [8] S. L. Iconaru, E. Andronescu, C. S. Ciobanu, A. M. Prodan, P. Le Coustumer, and D. Predoi, “Biocompatible magnetic iron oxide nanoparticles doped dextran thin films produced by spin coating deposition solution,” *Digest Journal of Nanomaterials and Biostructures*, vol. 7, no. 1, pp. 399–409, 2012.
- [9] S. L. Iconaru, A. M. Prodan, P. Le Coustumer, and D. Predoi, “Synthesis, antibacterial and antibiofilm activity of iron oxide glycerol nanoparticles obtained by co-precipitation method,” *Journal of Chemistry*, vol. 2013, Article ID 412079, 6 pages, 2013.
- [10] Habraken WJEM, J. G. C. Wolke, and J. A. Jansen, “Ceramic composites as matrices and scaffolds for drug delivery in tissue engineering,” *Advanced Drug Delivery Reviews*, vol. 59, article 234, 2007.
- [11] A. D. Russell and W. B. Hugo, “7 antimicrobial activity and action of silver,” *Progress in Medicinal Chemistry*, vol. 31, pp. 351–370, 1994.
- [12] J. L. Clement and P. S. Jarrett, “Antibacterial silver,” *Metal-Based Drugs*, vol. 1, article 467, 1994.
- [13] C. S. Ciobanu, F. Massuyeau, L. V. Constantin, and D. Predoi, “Structural and physical properties of antibacterial Ag-doped nano-hydroxyapatite synthesized at 100°C,” *Nanoscale Research Letters*, vol. 6, article 613, 2011.

- [14] C. S. Ciobanu, S. L. Iconaru, P. Le Coustumer, L. V. Constantin, and D. Predoi, "Antibacterial activity of silver-doped hydroxyapatite nanoparticles against gram-positive and gram-negative bacteria," *Nanoscale Research Letters*, vol. 7, article 324, 2012.
- [15] I. Cacciotti, A. Bianco, M. Lombardi, and L. Montanaro, "Mg-substituted hydroxyapatite nanopowders: synthesis, thermal stability and sintering behaviour," *Journal of the European Ceramic Society*, vol. 29, no. 14, pp. 2969–2978, 2009.
- [16] A. Bianco, I. Cacciotti, M. Lombardi, L. Montanaro, and G. Gusmano, "Thermal stability and sintering behaviour of hydroxyapatite nanopowders," *Journal of Thermal Analysis and Calorimetry*, vol. 88, no. 1, pp. 237–243, 2007.
- [17] S. Nath, S. Kalmodia, and B. Basu, "Densification, phase stability and in vitro biocompatibility property of hydroxyapatite-10 wt% silver composites," *Journal of Materials Science: Materials in Medicine*, vol. 21, no. 4, pp. 1273–1287, 2010.
- [18] Q. Y. Ma, S. J. Tralna, T. J. Logan, and J. A. Ryan, "Effects of aqueous Al, Cd, Cu, Fe(II), Ni, and Zn on Pb immobilization by hydroxyapatite," *Environmental Science and Technology*, vol. 28, no. 7, pp. 1219–1228, 1994.
- [19] A. Corami, S. Mignardi, and V. Ferrini, "Cadmium removal from single- and multi-metal (Cd + Pb + Zn + Cu) solutions by sorption on hydroxyapatite," *Journal of Colloid and Interface Science*, vol. 317, no. 2, pp. 402–408, 2008.
- [20] A. G. Nazari, A. Tahari, F. Moztaazadeh, M. Mozafari, and M. E. Bahrololoom, "Ion exchange behaviour of silver-doped apatite micro- and nanoparticles as antibacterial biomaterial," *Micro and Nano Letters*, vol. 6, no. 8, pp. 713–717, 2011.
- [21] M. C. Chifiriuc, R. Palade, and A. M. Israil, "Comparative analysis of disk diffusion and liquid medium microdilution methods for testing the antibiotic susceptibility patterns of anaerobic bacterial strains isolated from intrabdominal infections," *Biointerface Research in Applied Chemistry*, vol. 1, no. 6, pp. 209–220, 2011.
- [22] P. B. Mohite, R. B. Pandhare, and S. G. Khanage, "Synthesis, characterization and antimicrobial activity of some new pyrimidines containing tetrazole," vol. 1, pp. 258–263, 2012.
- [23] L. Marutescu, C. Limban, M. C. Chifiriuc, A. V. Missir, I. C. Chirita, and M. T. Caproiu, "Studies on the antimicrobial activity of new compounds containing thiourea function," *Biointerface Research in Applied Chemistry*, vol. 1, no. 6, article 236, 2011.
- [24] S. G. Khanage, P. B. Mohite, R. B. Pandhare, and S. Raju, "Investigation of pyrazole and tetrazole derivatives containing 3,5-disubstituted-4H-1,2,4-triazole as a potential antitubercular and antifungal agent," *Biointerface Research in Applied Chemistry*, vol. 2, no. 2, pp. 277–283, 2012.
- [25] A. P. Mishra, H. Purwar, and R. K. Jain, "Microwave synthesis, spectral, thermal and antimicrobial activities of Co(II), Ni(II) and Cu(II) metal complexes with Schiff base ligand," *Biointerface Research in Applied Chemistry*, vol. 2, no. 2, pp. 291–299, 2012.
- [26] S. G. Khanage, P. B. Mohite, R. B. Pandhare, and S. A. Raju, "Synthesis, characterization and antimicrobial evaluation of 3,5-diphenyl-1H-1,2,4-triazole containing pyrazole function," *Biointerface Research in Applied Chemistry*, vol. 2, no. 3, pp. 313–319, 2012.
- [27] A. I. Shah and D. S. Raj, "Design, synthesis and in vitro evaluation of the antibacterial and antifungal activity of some new dihydropyrano[3,2-c]chromene derivatives," *Biointerface Research in Applied Chemistry*, vol. 2, no. 3, pp. 320–331, 2012.
- [28] C. S. Ciobanu, S. L. Iconaru, M. C. Chifiriuc, A. Costescu, P. Le Coustumer, and D. Predoi, "Synthesis and antimicrobial activity of silver-doped hydroxyapatite nanoparticles," *BioMed Research International*, vol. 2013, Article ID 916218, 10 pages, 2013.
- [29] A. Ravindran, A. Singh, A. M. Raichur, N. Chandrasekaran, and A. Mukherjee, "Studies on interaction of colloidal Ag nanoparticles with bovine serum albumin (BSA)," *Colloids and Surfaces B*, vol. 76, no. 1, pp. 32–37, 2010.
- [30] M. Shirkhazadeh, M. Azadegan, and G. Q. Liu, "Bioactive delivery systems for the slow release of antibiotics: incorporation of Ag⁺ ions into micro-porous hydroxyapatite coatings," *Materials Letters*, vol. 24, no. 1–3, pp. 7–12, 1995.
- [31] D. Predoi, R. V. Ghita, F. Ungureanu, C. C. Negrila, R. A. Vatasescu-Balcan, and M. Costache, "Characteristics of hydroxyapatite thin films," *Journal of Optoelectronics and Advanced Materials*, vol. 9, no. 12, pp. 3827–3831, 2007.
- [32] D. Predoi, M. Barsan, E. Andronescu, R. A. Vatasescu-Balcan, and M. Costache, "Hydroxyapatite-iron oxide bioceramic prepared using nano-size powders," *Journal of Optoelectronics and Advanced Materials*, vol. 9, no. 11, pp. 3609–3613, 2007.
- [33] J. Qian, Y. Kang, W. Zhang, and Z. Li, "Fabrication, chemical composition change and phase evolution of biomorphic hydroxyapatite," *Journal of Materials Science: Materials in Medicine*, vol. 19, no. 11, pp. 3373–3383, 2008.
- [34] C. S. Ciobanu, S. L. Iconaru, F. Massuyeau, L. V. Constantin, and D. Predoi, "Synthesis, structure, and luminescent properties of europium-doped hydroxyapatite nanocrystalline powders," *Journal of Nanomaterials*, vol. 2012, Article ID 942801, 9 pages, 2012.
- [35] C. S. Ciobanu, S. L. Iconaru, P. Le Coustumer, and D. Predoi, "Vibrational investigations of silver-doped hydroxyapatite with antibacterial properties," *Journal of Spectroscopy*, vol. 2013, Article ID 471061, 5 pages, 2013.
- [36] X. Bai, K. More, C. M. Rouleau, and A. Rabiei, "Functionally graded hydroxyapatite coatings doped with antibacterial components," *Acta Biomaterialia*, vol. 6, no. 6, pp. 2264–2273, 2010.
- [37] A. Mortier, J. Lemaitre, and P. G. Rouxhet, "Temperature-programmed characterization of synthetic calcium-deficient phosphate apatites," *Thermochimica Acta*, vol. 143, pp. 265–282, 1989.
- [38] S. Koutsopoulos, "Preparation of calcium aluminate cement for hard tissue repair: effects of lithium fluoride and maleic acid on setting behavior, compressive strength, and biocompatibility," *Journal of Biomedical Materials Research*, vol. 62, no. 4, pp. 593–599, 2002.
- [39] B. O. Fowler, "Infrared studies of apatites. I. Vibrational assignments for calcium, strontium, and barium hydroxyapatites utilizing isotopic substitution," *Inorganic Chemistry*, vol. 13, no. 1, pp. 194–207, 1974.
- [40] U. Kreibitz and M. Vollmer, *Optical Properties of Metal Clusters*, Springer, Berlin, Germany, 1995.
- [41] J. R. Morones, J. L. Elechiguerra, A. Camacho et al., "The bactericidal effect of silver nanoparticles," *Nanotechnology*, vol. 16, no. 10, pp. 2346–2353, 2005.
- [42] S. Pal, Y. K. Tak, and J. M. Song, "Does the antibacterial activity of silver nanoparticles depend on the shape of the nanoparticle? A study of the gram-negative bacterium *Escherichia coli*," *Applied and Environmental Microbiology*, vol. 73, no. 6, pp. 1712–1720, 2007.

- [43] F. Raimondi, G. G. Scherer, R. Kötz, and A. Wokaun, "Nanoparticles in energy technology: examples from electrochemistry and catalysis," *Angewandte Chemie—International Edition*, vol. 44, no. 15, pp. 2190–2209, 2005.

Research Article

Facile and Sensitive Epifluorescent Silica Nanoparticles for the Rapid Screening of *EHEC*

Pravate Tuitemwong,¹ Nut Songvorawit,² and Kooranee Tuitemwong²

¹ Department of Microbiology, Food Safety Center, Faculty of Science, King Mongkut's University of Technology Thonburi, Bangkok 10140, Thailand

² Department of Microbiology, Kasetsart University, Bangkok 10900, Thailand

Correspondence should be addressed to Kooranee Tuitemwong; fscikrt@ku.ac.th

Received 3 January 2013; Accepted 21 April 2013

Academic Editor: Mohamed Bououdina

Copyright © 2013 Pravate Tuitemwong et al. This is an open access article distributed under the Creative Commons Attribution License, which permits unrestricted use, distribution, and reproduction in any medium, provided the original work is properly cited.

This study was to develop antibodies conjugated fluorescent dye-doped silica nanoparticles (FDS-NPs) aiming to increase signals for the rapid detection of *Escherichia coli* O157:H7 with glass slide method. The FDS-NPs were produced with microemulsion/sol-gel techniques resulting in spherical in shape with 47 ± 6 nm in diameter. The particles showed high intensity and stable orange color Rubpy luminescent dye. The XRD spectrum showed a broad diffraction peak in the range of $18-30^\circ$ (centered at 22°) indicating an amorphous structure. Surface modifications for bioconjugation with affinity chromatography purified (IgGs) antibodies were successful. The properties were evident from FTIR spectra at 1631.7 cm^{-1} . Results indicated that nanoparticles could attach onto cells of *E. coli* O157:H7 coated on a glass slide, and give distinctively bright color under epifluorescence microscope (400x). It was shown that FDS-NPs could detect a very low amount of cells of *E. coli* O157:H7 (16 CFU in 10 ml) in 60 min. The phosphate buffered saline (PBS) with ionic strength of 1.70 gave zeta potential of good particle dispersion (-40 mV). This work demonstrated that highly sensitive bioconjugated *E. coli* O157:H7 FDS-NPs were successfully developed with a potential to be used for the rapid detection of *E. coli* O157:H7 in foods.

1. Introduction

Rapid detection and identification of pathogens are of great importance for medical and food analyses. Traditional microbiological methods of detecting and enumerating bacteria require several days to yield reliable results. In many cases, the products have already been used by the consumers before the analyses are completed. Alternative and rapid assays based on different microbiological methods are constantly developed [1]. The effective testing of bacteria requires methods of analysis that meet a number of challenging criteria. Time and sensitivity of analysis are the most important limitations related to the usefulness of microbiological testing. The detection methods must give rapid results and highly sensitive since the presence of even a single pathogenic organism in the body or food may be an infectious dose [2]. To achieve good detections, fluorescent labeling probes are among the most popular methods. However, the traditional fluorophore such as fluorescein isothiocyanate (FITC) is not photostable in

addition to the problem of relatively low fluorescence intensity [3]. Fluorescent-doped silica nanoparticles (FDS-NPs) have been developed [4]. The advantages of these particles are high intensity of the fluorescent signal, high photostability, high solubility, no toxicity, and efficient conjugation with various biomolecules because the silica surface is simple to modify. In this experiment, we synthesized, characterized and performed amine modification the FDS-NPs for the rapid detection of *E. coli* O157:H7. The aim was to increase the fluorescent signals surrounding *E. coli* O157:H7 cells to the detection level rather than increasing cell numbers which requires much longer time for growth, thereby significantly reduces the detection time.

2. Materials and Methods

2.1. Preparation of Purified IgGs. Purified IgGs against *E. coli* O157:H7 was prepared from concentrated *E. coli* O157:H7

rabbit polyclonal antiserum using affinity chromatography method. Slide agglutination test was used to confirm efficiency of the antiserum against *E. coli* O157:H7.

2.1.1. Preparation of Antiserum. *E. coli* O157:H7 polyclonal antiserum was obtained from S&N Laboratory, Bangkok, Thailand. It was diluted with 0.85% NaCl (ratio 1:1). Tris-HCl (pH 8.0) was added to maintain pH, and then the antiserum solution was precipitated with saturated $(\text{NH}_4)_2\text{SO}_4$. The sample was centrifuged at $8000 \times g$, 4°C , for 30 min to collect the precipitate of mixed protein. The precipitate was dissolved in 1x PBS, pH 7.2 to remove salt or other small molecules, and then the sample was further desalted using centrifugal ultrafiltration (Vivaspin 20; 30,000 MWCO) for 3 wash cycles. The product was filtered through a $0.20 \mu\text{m}$ filter before purification step.

2.1.2. Purification of IgGs. The mixed protein solution was purified using protein A-sepharose affinity column (HiTrap Protein A HP, 5 mL). The column was equilibrated with 5 column volumes of binding buffer (20 mM sodium phosphate buffer, pH 7.0). Then, the antiserum was applied and washed with 5–10 column volumes of binding buffer to remove impurities and unbound materials. The 1 mL fractions were collected and determined for amount of protein by UV absorption at 280 nm. After that, the column was eluted with 5 column volumes of elution buffer (0.1M citric acid, pH 3.0). The fractions of IgGs were neutralized with tris-HCl (pH 9.0) and pooled together. It was desalted using Vivaspin 20 ultracentrifugation. The purified IgGs was further determined for protein concentration with Lowry method [5] and for purity using sodium dodecyl sulfate polyacrylamide gel electrophoresis (SDS-PAGE).

2.2. Preparation of Test Organisms. In this study, *E. coli* O157:H7 was used as a target organism for the detection with FDS-NPs and MNPs, while *E. coli* ATCC 8739, *E. aerogenes*, *P. mirabilis*, *S. Typhimurium* DMST 16809, *B. cereus* ATCC 11778, and *S. aureus* ATCC 25923 were used as challenge organisms to study the specificity of the nanoparticles. All test bacteria were grown in TSB at 37°C for 24 h before experiment. The bacterial inoculum was spreaded on PCA plate using sterile swab. Then, sterile glass slide was placed on the surface of that agar medium and incubated at 37°C for 8 h to allow the bacteria to grow and attach on the glass slide. After incubation, the slide was gently washed to remove unbound cells before detection with FDS-NPs.

2.3. Fluorescent Dye-Doped Silica Nanoparticles

2.3.1. Preparation of FDS-NPs. The method was modified from that described by Tansub et al. [6]. Briefly, cyclohexane, 1-hexanol, Triton X-100, 20 mM Rubpy dye solution, TEOS, and 30% NH_4OH were mixed together and stirred (1500 rpm) in a 50 mL flask for 24 h. After the reaction was completed, FDS-NPs were separated from the solution with acetone precipitation. FDS-NPs were then washed with 95% ethanol and distilled water several times to remove the solvent and

surfactant. The nanoparticles were dried in hot air oven at 100°C for 48 h. After that, the nanoparticles were ground and stored in dark bottles.

2.3.2. Characterization of FDS-NPs. Characterization of FDS-NPs was carried out as described by Tansub et al. [6]. Size and morphology of FDS-NPs were examined under TEM. Elemental components were analyzed by using scanning electron microscope with SEM-EDS. Particle structure was analyzed by using XRD (40 kV, angle 4–45 degree, increment 0.02 degree/step, and scan speed 0.3 sec/step). Optical properties, excitation, and emission spectra of Rubpy dye and the FDS-NPs were obtained using the spectrofluorometer for investigation. The photostability was obtained from the fluorescence intensity measured with spectrofluorometer every 5 min.

2.3.3. Surface Modification and Coating of IgGs onto FDS-NPs

Surface Modification. Amino group modification of FDS-NPs was carried out before coating with IgGs. FDS-NPs of 2 mg/mL was suspended in 1 mM acetic acid containing 5% APTES and stirred at room temperature (30°C) for 3 h. Then, the amino-functionalized FDS-NPs were washed with distilled water. The nanoparticles were stored in a dark bottle at 4°C . They were characterized by FT-IR spectrometer to confirm the existence of free amino group on the particle surface. The sample was prepared by milling the FDS-NPs with KBr (ratio 1:100) to form a very fine powder. The powder was then compressed to a thin pellet before it was analyzed with FT-IR spectrometer at midinfrared wave (wave number $4000\text{--}400 \text{ cm}^{-1}$) with resolution of 4.0 cm^{-1} and number of scan of 32.

Coating of IgGs onto FDS-NPs. The suspension of amino-functionalized FDS-NPs in 1x PBS (2 mg/mL, pH 7.4) with 2.5% glutaraldehyde was stirred at room temperature for 2 h. The particles were separated by centrifugation and washed with PBS to remove free glutaraldehyde. After that, they were redispersed into 1x PBS. The glutaraldehyde treated FDS-NPs were then incubated with purified IgGs against *E. coli* O157:H7 by adjusting the final concentration of FDS-NPs and IgGs to 2 and 0.1 mg/mL, respectively. The suspension was divided to two portions. One was incubated at 4°C and the other at 37°C to study the effects of temperature. The amount of protein on the particles at 3, 6, 12, and 24 h of incubation was determined by Lowry method [5]. Noncovalent binding of IgGs on particles was also studied using unmodified FDS-NPs incubated with IgG solution at the same conditions as described above.

2.3.4. Zeta Potential Measurement. Effect of ionic strength on aggregations of FDS-NPs in terms of zeta potential was investigated. Uncoated and IgG-coated FDS-NPs were dispersed in 0.1x PBS (0.2 mg/mL), pH 7.4 (a standard solution), and that containing different NaCl concentrations. FDS-NP

suspension was analyzed for zeta potential with zeta meter. The ionic strength (I) of a solution was calculated by (1):

$$I = \frac{1}{2} \sum_{i=1}^n c_i z_i^2, \quad (1)$$

where c_i is a molar concentration of i th ion present in the solution and z_i is its charge.

Stability and dispersibility of particles at each zeta potential (in the unit of mV) can be interpreted as follows. The values from -30 to $+30$ are considered unstable and tend to aggregate, from -40 to -30 and $+40$ to $+30$ are moderately stable, -60 to -40 and $+60$ to $+40$ are good stability, and the values beyond -60 or $+60$ indicated excellent stability [7].

2.3.5. Testing with Bacteria. FDS-NPs were tested with targets on the effects of incubation time and particle concentration and with nontarget bacteria in terms of specificity. All samples were stained with DAPI (a fluorescent dye which binds to DNA of organisms and exhibits blue luminescence when it is excited with UV light) before observation to easily distinguish between particle bound and unbound cells. The samples were observed under epifluorescence microscope with UV and blue light excitation. Each treatment of all experiments was performed in triplicate.

Effect of Incubation Time. Glass slide with *E. coli* O157:H7 was flooded with 0.5 mL of IgG-coated FDS-NPs (0.2 mg/mL) and incubated at room temperature at various reaction times (15, 30, 60, 120, and 180 min). After the incubation, the slide was washed to remove unbound particles and then was stained with DAPI solution. The slide was observed under epifluorescence microscope. Capture efficiency of FDS-NPs at each incubation time was assessed as the percentage of bacterial cells attached by particles to the total bacterial cells in the slide in the same field for 3–5 fields. Capture efficiency was calculated by (2):

$$\text{Capture efficiency (\%)} = \left(\frac{N_a}{N_0} \right) \times 100, \quad (2)$$

where N_a is number of bright orange dots (FDS-NPs bound cells) and N_0 is the sum of bright orange and blue dots (total cells) which were found in the microscopic field.

Effect of FDS-NP Concentration. IgG-coated FDS-NPs were dispersed and diluted to 0.2, 0.5, and 1.0 mg/mL in 1x PBS (pH 7.4). Then, glass slide with *E. coli* O157:H7 was flooded with 0.5 mL of particle suspension and incubated for 60 min at room temperature. Then, it was washed with distilled water to remove unbound particles. The slide was stained with DAPI solution and observed under epifluorescence microscope. Capture efficiency of FDS-NPs at each concentration was calculated by (2). Nonspecific binding of FDS-NPs was also

observed using uncoated FDS-NPs incubated with *E. coli* O157:H7.

Specificity. The specificity was tested using the same glass slide method but using non-*E. coli* O157:H7 bacteria with IgG-coated FDS-NPs. The attachment was considered nonspecific binding of the FDS-NPs.

3. Results and Discussion

3.1. Purification of Antiserum. *E. coli* O157:H7 polyclonal antiserum purchased from S&A Reagent Lab was tested with suspension of *E. coli* O157:H7 and other bacteria. Positive result which refers to agglutination was obtained from *E. coli* O157:H7, while negative results were observed with *E. coli* ATCC 8739, *E. aerogenes*, *P. mirabilis*, *S. typhimurium* DMST 16809, *B. cereus* ATCC 11778, and *S. aureus* ATCC 25923. Results indicated that *E. coli* O157:H7 antiserum had adequate efficiency to use for further experiments.

3.2. Purification of IgGs. The antiserum had protein content of 56 mg/mL. Because total protein of antiserum was 280 mg (56 mg/mL, 5 mL) that was greater than the binding capacity of the protein-A sepharose affinity column (about 100 mg IgGs), the *E. coli* O157:H7 antiserum was prior divided into 4 portions. Each portion was applied into column for 2 cycles. The target IgGs were obtained only from the first cycle of purification. None was detected from portions from the second cycle. Figure 1 shows amount of protein and IgGs of each fraction. For portions 1, 2, 3, and 4, IgG was collected from fractions 22 to 33, from 29 to 40, from 29 to 42, and from 34 to 40, respectively. The purified IgG was further examined for the purity by SDS-PAGE. The results confirmed its purity by showing two bands of heavy chain, 50 kDa, and light chain, 25 kDa (Figure 2).

For this research, an *E. coli* O157:H7 antiserum from a rabbit was purified with protein A-sepharose affinity column. Protein A is a surface protein found in cell wall of *Staphylococcus aureus*. Protein A consists of six different regions, five of which show strong, specific binding for the Fc-part of IgG, leaving the antigen-binding sites free. Immobilized protein A can bind at least two molecules of IgG per molecule. When an antiserum was applied into a column, IgG will bind to protein A-sepharose, while other proteins do not. The binding of IgG and protein A can be broken by acidity of elution buffer.

3.3. Synthesis and Characterization of FDS-NPs. FDS-NPs were successfully synthesized by modified sol-gel reaction via water-in-oil microemulsion method. At the early step, the mixture was a homogeneous solution with clear orange color. After the reaction had passed 24 h, there was no change in the mixture. But when acetone was added to isolate NPs, the mixture changed from clear orange solution to precipitate like a gel indicating that the formation of FDS-NPs has completed. The FDS-NPs were washed, dried, and ground. The obtained product was fine orange powder. The FDS-NPs were quite uniform in spherical shape with average sizes of 47 ± 6 and

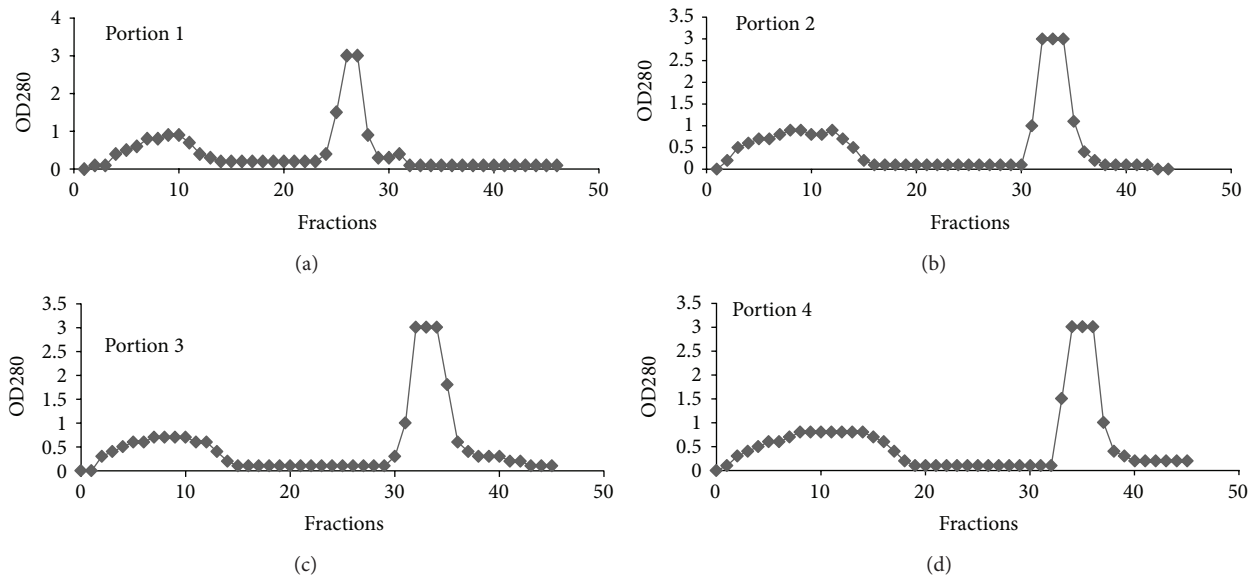


FIGURE 1: Purification of IgGs from *E. coli* O157:H7 antiserum.

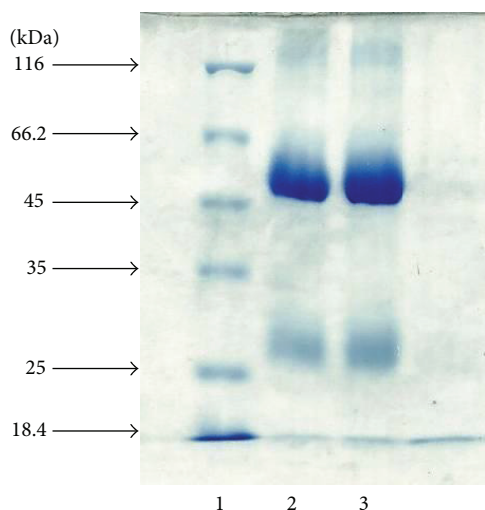


FIGURE 2: SDS-PAGE of the purified IgGs. Lane 1 is protein standard (ladder). Lanes 2 and 3 are IgGs from *E. coli* O157:H7 antiserum.

mode of 50 nm (Figure 3). The TEM image shows that FDS-NPs were quite uniform in spherical shape.

In the synthesis of FDS-NPs, TEOS, as a precursor, reacts with water to form polymer of SiO_2 or silica by sol-gel process [4]. A polymerization reaction is initiated by NH_4OH . In water-in-oil microemulsion, the aqueous phase is dispersed as microdroplets surrounded by a monolayer of surfactant and cosurfactant molecules (Triton X-100 and 1-hexanol) in the continuous hydrocarbon phase (cyclohexane). The aqueous cores of microemulsion systems can serve as compartmentalized media for chemical reactions, as a microreactor for the synthesis of NPs [8]. In addition, the size of the NPs can be manipulated as needed, by changing the water-to-surfactant molar ratio [6, 9]. While this reaction is

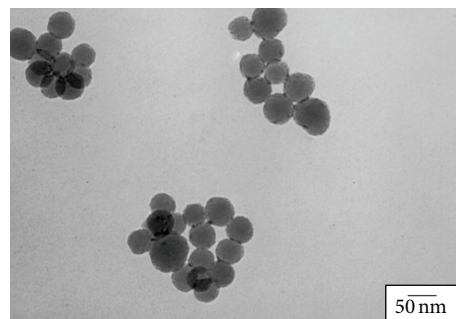


FIGURE 3: The TEM image of FDS-NPs at 160000x.

proceeding, a lot of Rubpy dye molecules, which are dissolved in water phase, are trapped inside a silica matrix. That makes this particles have a luminescence property.

3.4. Structure of FDS-NPs Using X-Ray Diffraction. The SiO_2 materials can be divided into two states: the crystalline and amorphous. XRD measurement to characterize the structure of FDS-NPs was performed. The XRD spectrum (Figure 4) shows a broad diffraction peak in the range of $18\text{--}30^\circ$ (center at 22°), which indicates an amorphous structure [10–12]. In this study, XRD spectrum of FDS-NPs did not match with any standard XRD pattern in the database of *Inorganic Crystal Structure Database* (ICSD). It is also reported that silicon dioxide is an amorphous solid which does not have a characteristic X-ray diffraction pattern (<http://www.ltschem.com/sio2.htm>).

3.5. Optical Properties of FDS-NPs: Excitation and Emission Spectra. The study of luminescence properties showed that both FDS-NPs and pure Rubpy had an excitation band in the range of UV light to blue light maximum with

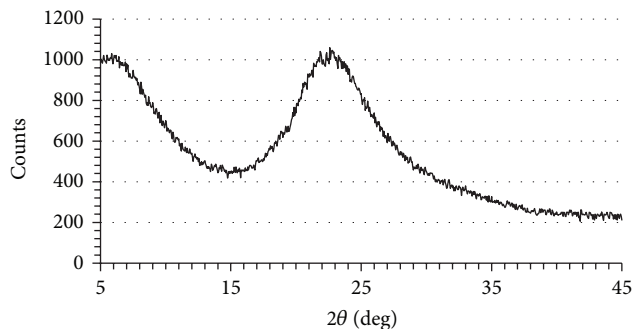


FIGURE 4: XRD spectrum of FDS-NPs.

the maximum excitation wavelength at 455 nm (Figure 6). Emission spectrum of FDS-NPs was the same as that of pure Rubpy dye, which had a maximum emission wavelength at 606 nm (the range of orange light) (Figure 7). These results indicated that the structure of silica did not change optical properties of fluorescent dye.

3.6. Photostability. The FDS-NPs were excited with UV light (365 nm) of mercury lamp (8 W) for 60 min (Figure 6). After excitation for 60 min, the FDS-NPs showed a slight decrease (1.5%) of the emission intensity, while the emission intensity of pure Rubpy dye was decreased by 6%. This study chose high hydrophilic Rubpy dye as an inorganic fluorescent dye. Therefore, it can dissolve in water and hence suit to be applied with FDS-NPs synthesis using water in oil microemulsion. The dye molecules appear to be more stable and well protected by FDS-NPs structure from photobleaching and photodegradation that often affect conventional dyes. Moreover, a large number of dye molecules incorporated inside a very small volume of silica particle made FDS-NPs a very bright luminescence when excited (Figure 7). The maximum fluorescent intensity of dyes in the particles appears to be higher than that of the pure form because a large number of molecules were trapped in the FDS-NPs particles.

3.7. Elemental Components and Surface Modification of FDS-NPs Particles. Elemental components of FDS-NPs product were characterized by SEM-EDS. The results showed that the elements of FDS-NPs comprised of Si (11.31% atomic), O (64.43% atomic), Ru (0.15% atomic), and C (24.11% atomic). The existence of Ru confirmed that Rubpy dye was doped inside the particles. Carbon was also detected. Three possible presumptions for the existence of carbon in FDS-NPs could be from either Rubpy dye molecules, alcohol from condensation reaction, or organic components which bound tightly with FDS-NPs. A large amount of oxygen higher than a general 1:2 atomic ratio of SiO₂ was found in FDS-NPs. This suggested that the extra oxygen molecule was from H₂O molecules which bound to the particles. This result was confirmed by the FT-IR spectra (data not shown), where the appearance of H₂O was confirmed.

Based on the FTIR spectra of FDS-NPs with amino-functionalized surface modification, it was found that the

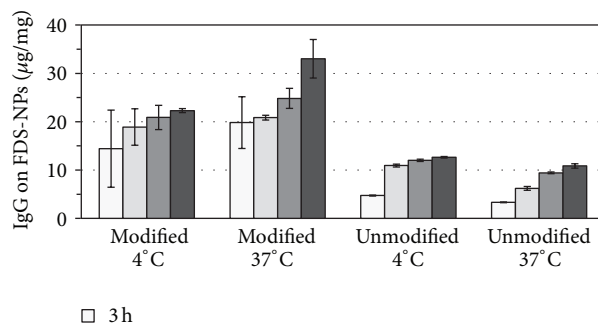


FIGURE 5: Amount of IgGs on FDS-NPs after incubation at various conditions.

amine group was successfully attached onto the particle surface. The wave numbers from 3400 to 3280 cm⁻¹ represent -NH₂ asymmetric and symmetric stretching vibrations. The wave numbers from 1650 to 1600 cm⁻¹ represent N-H bending vibration. Since IR bands that refer to N-H bending vibration and -NH₂ stretching vibration overlap with the IR bands of -OH groups and C-N stretching vibration was overlapped with the absorption peak of Si-O-Si stretching vibration, it is difficult to distinguish between modified and unmodified FDS-NPs.

There were two points that were quite different between them. First, a broad IR band in the range from 3600 to 3000 cm⁻¹ generally refers to O-H stretching vibrations of Si-OH and adsorbed H₂O [13–15]. This range also overlaps with the asymmetric and symmetric stretching vibrations of the -NH₂ groups. From the result, this band of modified FDS-NPs was wider than unmodified one. This can be explained by the absorption of amino group which was added into modified particles. Second, a band around the range from 1630 to 1600 cm⁻¹ of modified particles was also wider than that of the unmodified particles [13, 14]. Tansub et al. [6] found similar overlapping. The authors successfully confirmed the existence of amino group on particle surface by FT Raman.

3.8. Antibodies Conjugation (IgGs) with FDS-NPs. Effects of reaction temperature and time on coating IgG on FDS-NPs were determined from amount of immobilized protein on FDS-NPs. The high concentration of IgG solution (100 µg/mL) was incubated with amino-modified FDS-NPs to obtain the maximum IgG loading capacity of FDS-NPs. Protein assay by Lowry method was used for determining the remaining protein. The total protein concentration subtracted by the remaining protein yields the protein attached on FDS-NPs particles.

Results that showed average amount of immobilized IgGs on amino-modified FDS-NPs at 4°C for 3, 6, 12, and 24 h were 14.20, 18.90, 20.89, and 22.30 µg/mg, respectively (Figure 5). Whereas at 37°C, the immobilized IgGs on FDS-NPs were 19.83, 20.85, 24.83, and 33.02 µg/mg, respectively (Figure 5). The longer incubation time resulted in higher immobilized IgGs on FDS-NPs. Higher rates of immobilization were obtained from incubation at 37°C compared with that of 4°C. Thus, condition of 37°C and 24 h was used as an appropriate

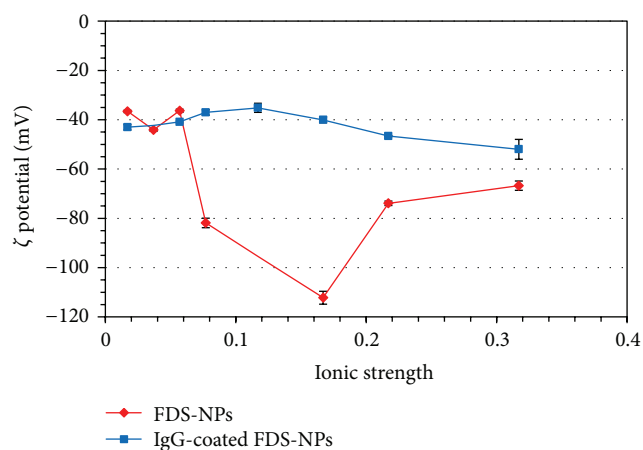


FIGURE 6: Zeta potential at various ionic strength of FDS-NPs (uncoated FDS-NPs) and IgG-coated FDS-NPs.

condition for IgG coating for subsequent experiments. The attachments were not significant at 4°C, but the incubation at 37°C gave a significant increase of bound protein on FDS-NPs. At 3 h incubation, for example, IgGs on particles were detected at much lower concentrations (3.43 µg/kg) than the IgGs on amino-modified FDS-NPs (20 µg/kg).

Since the immobilization of protein onto particles can occur via both physical and chemical approaches, noncovalent binding was also observed using unmodified FDS-NPs. The amount of IgGs after incubation for 3, 6, 12, and 24 h were 4.74, 10.94, 12.01, and 12.65 µg/mg for incubation at 4°C and were 3.34, 6.20, 9.43, and 10.86 µg/mg for incubation at 37°C. It indicated that noncovalent binding may occur in this procedure due to electrostatic force, van der Waals interaction, or hydrogen bonding.

There are numerous techniques to choose to immobilize protein onto nanoparticle, depending on functional groups on the nanoparticle surface and biomolecules. In this case, FDS-NPs were modified to have amino groups on their surface that facilitate the bioconjugation with the target antibodies. Thus, glutaraldehyde, which is well known as a crosslinking reagent between two amino groups of protein, was used for FDS-NPs-IgGs conjugation. Two aldehyde groups at both sides of glutaraldehyde molecule are reactive groups that can bind to amino group via covalent bonding. This allowed IgGs to be immobilized on FDS-NPs. From the experiment, this technique is easy to manipulate, does not require many reagents, and has short time consumption with high efficiency.

3.9. Zeta Potential of FDS-NPs. Zeta potential is an electric potential in colloidal system. It is useful for prediction of dispersion stability of particles in solution since many factors, such as pH, conductivity, type of ion, and ionic strength in a medium have an effect on this value. However, pH 7.4 is the favorable pH for antigen-antibody interaction. Thus, only an effect of ionic strength to the zeta potential of FDS-NPs was studied.

Generally, zeta potential particles in the range from 30 to -30 mV will be unstable and tend to aggregate, that is,

undesirable to any application, and they are more stable when the value is far from zero point. From the results, zeta potential of uncoated FDS-NPs at all ionic strengths was well below -30 mV (Figure 6), indicating that the FDS-NPs were well dispersed and stable when ionic strength was 0.167. However, after FDS-NPs were coated with IgGs, the zeta potential of each ionic strength has changed, suggesting that these changes derived from an effect of IgGs coated on particle surface. The zeta potentials of IgG-coated FDS-NPs at all ion concentrations were about -40 mV and slightly decreased when ionic strength increased. This means the FDS-NPs are, moderately to well, dispersed in all conditions of this experiment. Although at high ion concentration, coated FDS-NPs had more stability. However, high ionic strength can cause the antibody to denaturalize, thereby decrease the efficiency of antigen-antibody interaction. Thus, ionic strength of 0.167 was considered as an appropriate condition for further experiment. However, the ionic strength (0.167) is approximate to the ionic strength of 1x PBS (ionic strength 0.17). Therefore, 1x PBS (pH 7.4) was used as a solution for further experiment.

3.10. Testing with Bacteria. The antibody conjugated FDS-NPs were tested for their capturing ability of the target *E. coli* O157:H7 cells using glass slide method. The target cells exhibit bright orange color under epifluorescence microscope (Figure 7).

3.10.1. Effect of Incubation Time. Effects of incubation time were observed under epifluorescence microscope (Figure 7), and the targets were excited with both blue and UV lights to compare the ratio of bound and free cells. It was found that, the FDS-NPs gave distinctively bright color under epifluorescence microscope that facilitated the detection of target bacteria by increasing the signals not the cell numbers. The signals increment requires only 15–60 min to reach the detection level, while the cell growth requires 24–48 h to reach the detectable level from 10^5 to 10^8 cfu/g.

The capture efficiency of FDS-NPs was 58.17%, 74.48%, 87.83%, 85.23%, and 90.91% for 15, 30, 60, 120, and 180 min, respectively. The longer incubation time resulted in the greater capture efficiency. However, when the incubation time had passed 120 min, the amount of bacteria which were bound with FDS-NPs was not different from that of the 60 min. This indicated that it reached to the maximum binding capacity of FDS-NPs. Thus, 60 min were assumed optimal incubation time for this experiment.

3.10.2. Effects of FDS-NP Concentration. *E. coli* O157:H7 cells were incubated with various concentrations of FDS-NPs. Capture efficiency of 0.2 mg/mL FDS-NPs was 87.31%, while 0.5 mg/mL and 1.0 mg/mL FDS-NPs were 87.77% and 88.77% because 0.2 mg/mL FDS-NPs gave a percent capture closed to that of 1.0 mg/mL FDS-NPs. Hence, 0.2 mg/mL was used as the concentration of FDS-NPs in the subsequent experiments. Moreover, to ensure whether *E. coli* O157:H7 cells were captured by FDS-NPs via antigen-antibody interaction, uncoated FDS-NPs were incubated with the target bacteria

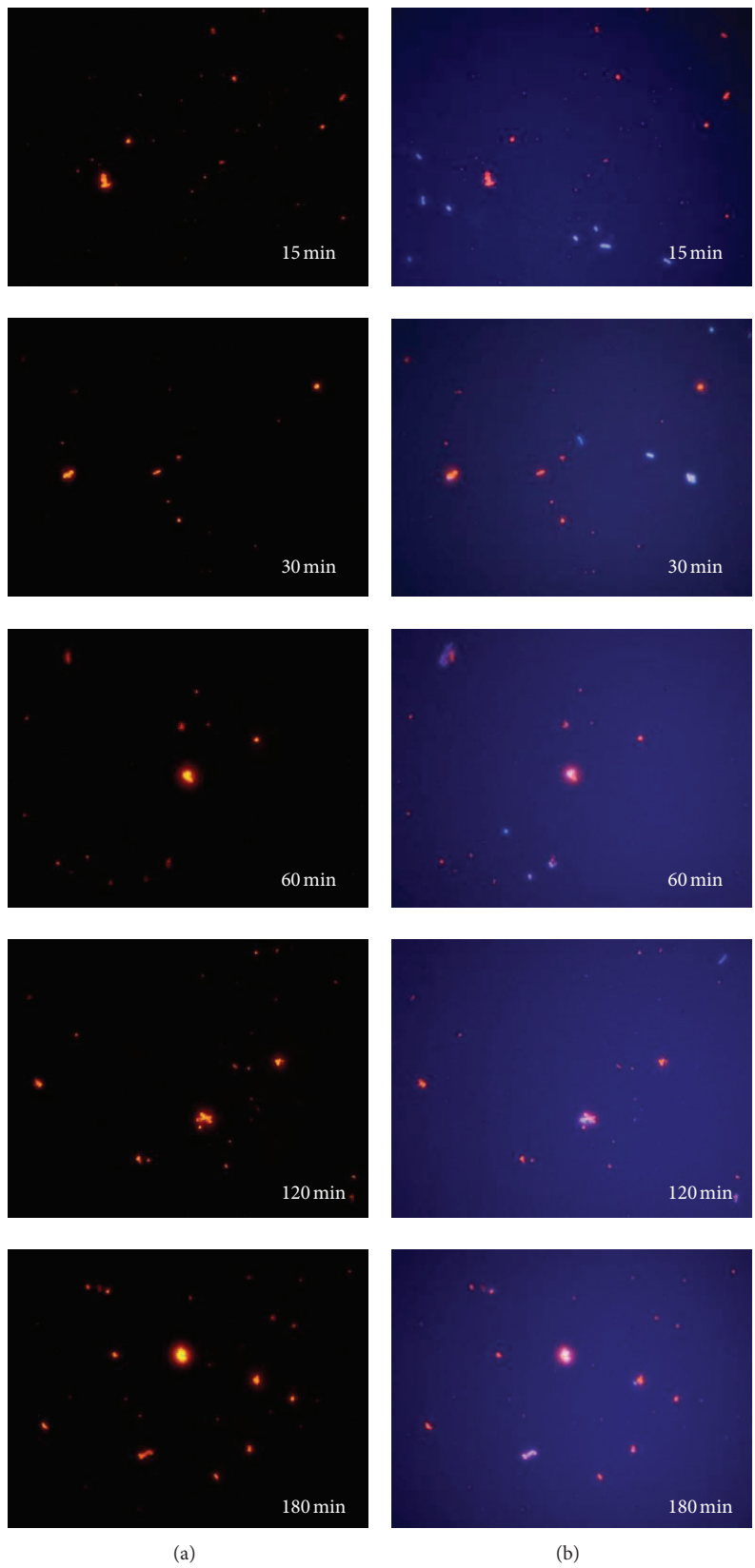


FIGURE 7: Fluorescence images at 1000x of *E. coli* O157:H7 incubated with IgG-coated FDS-NPs at various incubation times: (a) excited with blue light and (b) excited with UV light.

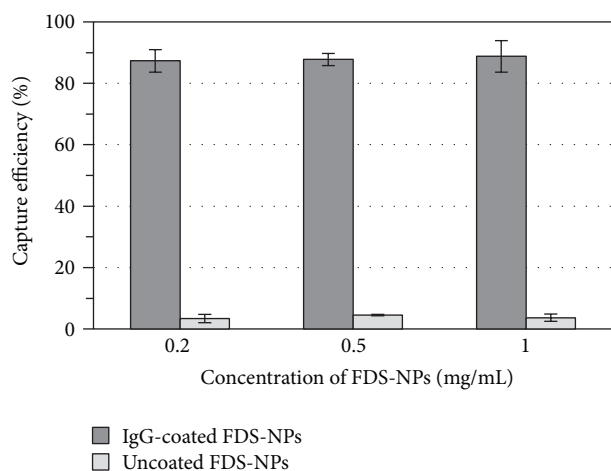


FIGURE 8: Effects of concentration of FDS-NPs on the binding efficiency of IgG-coated FDS-NPs with *E. coli* O157:H7.

as a control. The results showed that the capture efficiency of all trials were about 3%–5% indicating that few cells were captured by uncoated FDS-NPs (Figure 8). This capture was nonspecific binding and could occur by weak interaction between surface of bacterial cells and surface of FDS-NPs such as electrostatic force. However, for this experiment, it was confirmed that the bacterial cells were captured by IgGs on FDS-NP surface rather than other unspecific interactions.

4. Conclusion

This study demonstrated that the FDS-NPs nanoparticles prepared by microemulsion combined with sol-gel techniques were successful having spherical shape with nanosize (40–50 nm) with high photostability of luminescence (1.5% decrease when excited with 8 W UV light for 60 min). The nanoparticles were modified to add functional group (amino group) on their surface using APTES. Glutaraldehyde was used as crosslinker between IgGs and particle surface that allowed IgGs to coat on FDS-NPs. Loading capacity of IgGs on particle surface was about 33 $\mu\text{g}/\text{mg}$ when incubated with IgGs at 37°C for 24 h. IgG-coated FDS-NPs tended to create aggregates in the detection of targeted bacteria, while the detection of *E. coli* O157:H7 on glass slide was successful. FDS-NPs could attach onto target organism and give distinctively bright color under fluorescence microscope. The detection of bacteria with this nanoparticle is very promising, though at low levels of the cells, due to their ability of amplify light signal in the detection step. Capture efficiency at 0.2 mg/mL FDS-NPs and 60 min incubation was 87.31%. IgG-coated FDS-NPs had low cross-reaction to nontarget bacteria despite using polyclonal antibody with affinity purification.

References

[1] L. Vanne, M. Karwoski, S. Karppinen, and A. M. Sjöberg, “HACCP-based food quality control and rapid detection methods for microorganisms,” *Food Control*, vol. 7, no. 6, pp. 263–276, 1996.

[2] D. Ivnitiski, I. Abdel-Hamid, P. Atanasov, and E. Wilkins, “Biosensors for detection of pathogenic bacteria,” *Biosensors and Bioelectronics*, vol. 14, no. 7, pp. 599–624, 1999.

[3] W. Lian, S. A. Litherland, H. Badrane et al., “Ultrasensitive detection of biomolecules with fluorescent dye-doped nanoparticles,” *Analytical Biochemistry*, vol. 334, no. 1, pp. 135–144, 2004.

[4] S. Santra, P. Zhang, K. Wang, R. Tapeç, and W. Tan, “Conjugation of biomolecules with luminophore-doped silica nanoparticles for photostable biomarkers,” *Analytical Chemistry*, vol. 73, no. 20, pp. 4988–4993, 2001.

[5] O. H. Lowry, N. J. Rosebrough, A. L. Farr, and R. J. Randall, “Protein measurement with the Folin phenol reagent,” *The Journal of Biological Chemistry*, vol. 193, no. 1, pp. 265–275, 1951.

[6] W. Tansub, K. Tuitemwong, S. Thepwiwat, P. Limsuwan, and P. Tuitemwong, “Synthesis of antibodies-conjugated fluorescent dye-doped silica nanoparticles for a rapid single step detection of *Campylobacter jejuni* in live poultry,” *Journal of Nanomaterials*, vol. 2012, Article ID 865186, 7 pages, 2012.

[7] Malvern Instruments Ltd, *Zeta Potential Measurement Using Laser Doppler Electrophoresis (LDE)*, Innovative Solutions in Material Characterization, Malvern, UK, 2011, http://www.malvern.com/LabEng/technology/zeta_potential/zeta_potential_LDE.htm.

[8] X. Zhao, L. R. Hilliard, S. J. Mechery et al., “A rapid bioassay for single bacterial cell quantitation using bioconjugated nanoparticles,” *Proceedings of the National Academy of Sciences of the United States of America*, vol. 101, no. 42, pp. 15027–15032, 2004.

[9] I. Abarcan, T. Doussineau, and M. Smaïhi, “Tailored macro/microstructural properties of colloidal silica nanoparticles via microemulsion preparation,” *Polyhedron*, vol. 25, no. 8, pp. 1763–1770, 2006.

[10] H. Zhao, Y. Li, R. Liu, F. Zhao, and Y. Hu, “Synthesis method for silica needle-shaped nano-hollow structure,” *Materials Letters*, vol. 62, no. 19, pp. 3401–3403, 2008.

[11] M. Zhao, L. Zheng, X. Bai, N. Li, and L. Yu, “Fabrication of silica nanoparticles and hollow spheres using ionic liquid microemulsion droplets as templates,” *Colloids and Surfaces A*, vol. 346, no. 1–3, pp. 229–236, 2009.

[12] J. T. Park, J. A. Seo, S. H. Ahn, J. H. Kim, and S. W. Kang, “Surface modification of silica nanoparticles with hydrophilic polymers,” *Journal of Industrial and Engineering Chemistry*, vol. 16, no. 4, pp. 517–522, 2010.

[13] D. D. Asouhidou, K. S. Triantafyllidis, N. K. Lazaridis, and K. A. Matis, “Adsorption of Remazol Red 3BS from aqueous solutions using APTES- and cyclodextrin-modified HMS-type mesoporous silicas,” *Colloids and Surfaces A*, vol. 346, no. 1–3, pp. 83–90, 2009.

[14] B. Shi, Y. Wang, Y. Guo et al., “Aminopropyl-functionalized silicas synthesized by W/O microemulsion for immobilization of penicillin G acylase,” *Catalysis Today*, vol. 148, no. 1–2, pp. 184–188, 2010.

[15] L. D. White and C. P. Tripp, “Reaction of (3-aminopropyl) dimethylethoxysilane with amine catalysts on silica surfaces,” *Journal of Colloid and Interface Science*, vol. 232, no. 2, pp. 400–407, 2000.

Research Article

Retinoic Acid Decorated Albumin-Chitosan Nanoparticles for Targeted Delivery of Doxorubicin Hydrochloride in Hepatocellular Carcinoma

Jaleh Varshosaz,¹ Farshid Hassanzadeh,² Hojjat Sadeghi,³
Zahra Ghelich Khan,¹ and Mahboobeh Rostami²

¹ Department of Pharmaceutics, School of Pharmacy and Novel Drug Delivery Systems Research Centre, Isfahan University of Medical Sciences, P.O. Box 81745-359, Isfahan, Iran

² Department of Medicinal Chemistry, School of Pharmacy, Isfahan University of Medical Sciences, Isfahan, Iran

³ Department of Biotechnology, School of Pharmacy, Isfahan University of Medical Sciences, Isfahan, Iran

Correspondence should be addressed to Jaleh Varshosaz; varshosaz@pharm.mui.ac.ir

Received 9 February 2013; Accepted 1 April 2013

Academic Editor: Mohamed Bououdina

Copyright © 2013 Jaleh Varshosaz et al. This is an open access article distributed under the Creative Commons Attribution License, which permits unrestricted use, distribution, and reproduction in any medium, provided the original work is properly cited.

Retinoic acid (R) grafted chitosan (C) copolymers with different degree of substitution of retinoic acid on the chitosan were synthesized. Retinoic acid targeted chitosan-albumin nanoparticles were prepared for targeted delivery of doxorubicin in hepatocellular carcinoma by coacervation method. Physical properties of nanoparticles including particle size, zeta potential, drug loading efficiency, and drug release profiles were studied. TEM micrographs were taken to see the morphology of nanoparticles. The cytotoxicity of doxorubicin-loaded nanoparticles was studied on HepG2 cells using MTT assay and their cellular uptake by fluorescence microscopy. FTIR and ¹HNMR spectra confirmed successful production of RC conjugate which was used in production of the targeted RC-albumin nanoparticles. IC₅₀ of drug loaded in these nanoparticles reduced to half and one-third compared to nontargeted nanoparticles and free drug, respectively.

1. Introduction

Hepatocellular carcinoma (HCC) is the fifth most common malignancy in the world, the most common primary malignancy of the liver, and the third most common cause of cancer deaths [1, 2]. The data from epidemiological surveys show that the incidence is rising in North America, Oceania, and central Europe [1]. Unfortunately, the 5-year survival rate of the disease is very low (<5%), and about 600,000 lives are lost each year because of HCC [3]. Important risk factors for HCC include hepatitis B and chronic hepatitis C infection, alcoholic cirrhosis, and nonalcoholic steatohepatitis [4].

Patients diagnosed at early stage benefit from surgical resection, percutaneous ablation, and liver transplant, but more than 80% of patients are diagnosed at intermediate stage [5–9]. Even after curative treatments like resection or percutaneous ablation the recurrence rate is high [10]. The other problem is poor sensitivity to radiotherapy and high

resistance to available anticancer drugs [11, 12]. In addition, side effects of chemotherapeutic agents are one of major limitations in cancer treatment; for example, cardio toxicity is one of most important risks of anthracyclines which are used in different types of malignancies including: leukemias, lymphomas, breast, uterine, ovarian, and lung cancers. Suggested mechanisms of action for anthracyclines are three mechanisms: (1) inhibition of DNA and RNA synthesis by intercalating between base pairs of the DNA/RNA strand, thus preventing the replication of rapidly growing cancer cells, (2) inhibition of topoisomerase II enzyme, preventing the relaxing of supercoiled DNA and thus blocking DNA transcription and replication, and (3) creation of iron-mediated free oxygen radicals that damage the DNA and cell membranes [13, 14]. The most important reported side effects of these drugs include cardiotoxicity and vomiting which considerably limit their usefulness. Considering these facts,

designing a drug delivery system with minimum possible side effects appears to be reasonable.

Nanoparticulate drug carriers require more considerations in HCC, because Kupffer cells in liver sinusoids take up the nanoparticles and make the drug delivery difficult [15–17]. If the nanoparticle is targeted somehow to release the drug almost only into HCC affected liver cells, the cytotoxic activity will be less than nontargeted ones as was shown with doxorubicin [18]. Vascular endothelial growth factor, growth factor receptor, galactose, transferrin, folate, and retinoic acid can be used as potential targeting agents in HCC [19–23]. Among them retinoic acid would be one of the best choices since the retinoic acid receptor- α is reported as the dominant receptor in HCC, and its mRNA has been shown to be at low levels in normal liver but at high levels in HCC [22, 24].

Retinoic acid (R) is a derivative of vitamin A with an important role in regulation of cell proliferation and differentiation [25], and its inhibitory effect on cancer cell growth is well established [26–30].

Chitosan (C) a chitin derivative is the second biomass found in huge amounts on earth and along with its derivatives is known as a low-toxic, biocompatible, biodegradable, mucoadhesive, and low production cost material [31, 32] which has been used as a delivery system for proteins, nutraceuticals, gene, and drugs [33–37]. Because of its positively charged nature at low pH values, chitosan can associate with anions to form polyelectrolytes in solution [31].

Albumin, a versatile protein carrier for drug delivery, has been shown to be nontoxic, nonimmunogenic, biocompatible and biodegradable. Therefore, it is ideal material to fabricate nanoparticles for drug delivery. Albumin nanoparticles have gained considerable attention owing to their high binding capacity of various drugs and being well tolerated without any serious sideeffects [38].

Ionic coacervation method is a suitable preferred technique for production of nanoparticles as colloidal drug carriers which have the capability of being decorated with the specific receptor binding ligands. Since there is no organic solvent used in this method and nanoparticles are prepared without involving toxic cross linking agents like glutaraldehyde, the resulting nano-dispersion has no toxic residue to be removed which, in turn reduces production costs, and a safer drug delivery system will be resulted.

The aim of the present study was designing a targeted delivery system of doxorubicin to hepatocellular carcinoma by anchoring retinoic acid to chitosan-albumin nanoparticles. Epirubicin is the anticancer agent of choice used in HCC [23], but as there is no evidence suggesting any survival or response difference between epirubicin and its isomer, doxorubicin, at similar doses [39], doxorubicin was used in the present study due to its lower cost.

2. Materials and Methods

2.1. Materials. Doxorubicin HCl was provided from Hangzhou ICH Biopharm Co., Ltd. (Zhejiang, China), retinoic acid from Solmag (Italy), and chitosan oligosaccharide (90% deacetylated, Mw = 8.6 kDa) was supplied by Yuhuan Marine Biochemistry Co., Ltd. (Zhejiang, China).

N-hydroxysuccinimide (NHS), N, N'-Dicyclohexylcarbodiimide (DCC), and 3-[4, 5-dimethylthiazol-2-yl]-2, 5-diphenyl tetrazolium bromide (MTT) were from Sigma (USA). Egg albumin, anhydrous dimethylsulfoxide (DMSO), and acetic acid were from Merck Chemical Company (Germany). RPMI-1640 culture medium was from PAA (Austria) and antibiotic mixtures were from GIBCO Laboratories (Scotland). HepG2 cell line was supplied by Pasteur Institute (Iran).

2.2. Preparation of Retinoic Acid Anchored Chitosan (RC). The coupling reaction of retinoic acid and chitosan was done as reported in our previous work [40] with little change. Briefly, chitosan (2 g) was dissolved in acetate buffer (0.1 M, pH 4.7). Retinoic acid (calculated amounts for substituting 2 and 4 amine groups), DCC, and NHS (each in 1.5-fold of R) were dissolved in 12 mL of anhydrous DMSO, and after 24 hr of stirring under nitrogen flush, this solution was added drop wise to chitosan solution and was left to be stirred overnight in darkness at room temperature. After completion of the reaction, diluted aqueous solution of NaOH was added drop wise to adjust the pH of reaction flask to 9. The product was then dialyzed (Mw cutoff 2000, Membra-Cel, Viskase, USA) against phosphate buffer at pH 7.4 and water (each for 2 days) and finally lyophilized for maximum purification (Freeze-dryer, Christ, α -2-4 LDPlus, Germany). Chitosan with 2 or 4 groups substituted was tagged as R2 or R4, respectively.

2.3. Preparation of RC-Albumin Nanoparticles. To fabricate RC-albumin nanoparticles, an aqueous coacervation technique was used. Different amounts of each type of synthesized RC (6.66–66.6 mg of R4 or R2) were dissolved by levigating with a few drops of water and acetic acid. Then enough water was added, and the pH was adjusted to 2.49. The solution was then sonicated using probe sonicator (HD 3200, Bandeline, Germany) for 4 min with the power of 40 w for amounts less than 50 mg and 60 w for 50 mg and more. The drug (2.6–50 mg) was then added to this solution while being stirred. The albumin solution was prepared simply by dissolving egg albumin (3.34–50 mg) in deionized water. In the next step, albumin solution was added drop wise to the solution of RC while being stirred at 600 rpm.

2.3.1. Experimental Design. To evaluate the effect of processing variables on the responses of particle size, zeta potential, encapsulation efficiency (EE%), and drug release efficiency (RE%) and to screen the most effective ones, an irregular factorial design was used. Four different variables including total polymer, polymer type, albumin amount, and drug content were studied each in two levels. Table 1 shows the four control factors selected in the optimization study.

An overview of the formulations investigated is presented in Table 2.

A run involved the corresponding combination of levels to which the factors in the experiment were set. All experiments were done in triplicate. The effects of the studied variables on the responses were then analyzed by the Design Expert software (Version 7.1, USA) to obtain

TABLE 1: Description and trial levels of studied factors in irregular factorial design used in preparation of doxorubicin loaded in RC-albumin nanoparticles.

Studied variables	Levels	
	I	II
Total mass of RC-albumin (mg)	10	100
Polymer type	R2	R4
Albumin/RC	0.5	1
Drug/RC-albumin	0.25	0.5

TABLE 2: Composition of different formulations investigated in preparation of doxorubicin loaded in RC-albumin nanoparticles using irregular factorial design.

Formulation code	Total mass of RC-albumin (mg) (A)	Albumin/RC (B)	Drug/RC-albumin (C)	Polymer type (D)
A ₁₀₀ B ₁ C _{0.5} R2	100	1	0.5	R2
A ₁₀ B _{0.5} C _{0.5} R2	10	0.5	0.5	R2
A ₁₀ B _{0.5} C _{0.25} R2	10	0.5	0.25	R2
A ₁₀₀ B _{0.5} C _{0.5} R4	100	0.5	0.5	R4
A ₁₀₀ B _{0.5} C _{0.5} R2	100	0.5	0.5	R2
A ₁₀ B ₁ C _{0.5} R2	10	1	0.5	R2
A ₁₀₀ B ₁ C _{0.25} R2	100	1	0.25	R2
A ₁₀₀ B _{0.5} C _{0.25} R4	100	0.5	0.25	R4
A ₁₀ B ₁ C _{0.5} R4	10	1	0.5	R4
A ₁₀₀ B ₁ C _{0.25} R4	100	1	0.25	R4
A ₁₀ B _{0.5} C _{0.25} R4	10	0.5	0.25	R4
A ₁₀ B ₁ C _{0.25} R4	10	1	0.25	R4

independently the main effects of these factors, followed by the analysis of variance (ANOVA) to determine which factors were statistically significant. The optimum conditions were determined by the optimization method to yield a heightened performance.

2.4. Particle Size and Zeta Potential Measurements. The mean particle size and zeta potential of RC-albumin nanoparticles were measured by photon correlation spectroscopy (PCS) at a fixed angle of 90° (Zetasizer, ZEN 3600, Malvern Instrumental, UK). Nanodispersion was suitably diluted to measure mean particle size and polydispersity index.

2.5. Entrapment Efficiency. A 600 μ L of RC-albumin nano-dispersion was centrifuged (Microcentrifuge Sigma 30 k, UK) at 10000 rpm for 5 min in eppendorf tubes (cut-off 10000 Da). The supernatant, containing the free drug, was diluted 1:7 with deionized water, and the UV absorbance of resulting solution was evaluated spectrophotometrically (UV-mini 1240, Shimadzu, Kyoto, Japan) at $\lambda_{\max} = 247$ nm. The solution contained all components but the drug was used as the blank. The amount of entrapped drug was determined through the difference between the total and the free

drug. The entrapment efficiency (EE) of doxorubicin in RC-albumin nanoparticles was calculated using the following:

$$EE (\%) = \frac{\text{entrapped drug in nanoparticles}}{\text{total amount of drug added}} \times 100. \quad (1)$$

2.6. Drug Release Studies. Two ml of each nanoparticle dispersion was transferred to a dialysis bag (Mw cutoff 12000, Membra-Cel, Viskase, USA), and the bag was placed in phosphate buffer solution (pH 7.4) containing 2% Tween 20 while stirred at $37 \pm 1^\circ\text{C}$. 700 μ L samples were taken and doxorubicin absorbance of each sample was measured at $\lambda_{\max} = 499.4$ nm at specific time intervals until 70% of entrapped drug was released into the media. The parameter of release efficiency within 60 min ($RE_{60}\%$) was used to compare the release profiles:

$$RE_{60}\% = \frac{\int_0^t y \cdot dt}{y_{100} \cdot t} \times 100. \quad (2)$$

2.7. Optimization of the RC-Albumin Nanoparticle Formulations. Data processing was done using Design Expert software and the effects of each independent variable on the studied responses were, determined. All responses fitted in the linear model.

The constraints of particle size was $148.0 \leq Y_1 \leq 472.2$ nm with particle size targeted on minimum, for zeta potential it was $29.3 \leq Y_2 \leq 46.8$ mV while it was desired to be in range of obtained results, for loading efficiency the constraints were $7.3 \leq Y_3 \leq 58.0\%$ with the goal set at the maximum and $RE_{60}\%$ had constraints of $41.5 \leq Y_4 \leq 76.8\%$ with desired target set at the maximum.

2.8. Transmission Electron Microscopy (TEM). Samples of well-dispersed optimum formulation of nanoparticles were placed on a 300 mesh carbon coated copper grid, and the grid was left to dry in room temperature. Micrographs were taken with different levels of magnification with an accelerating voltage of 80 kv using a transmission electron microscope (Zeiss, EM10C, Germany).

2.9. Cell Culture. HepG2 cells (purchased from the Pasteur Institute, Iran) were maintained in tissue culture flask in 5% CO₂, 95% humidified atmosphere at 37° in RPMI-1640 medium containing 10% (v/v) of FBS (Fetal Bovine Serum), and 1% of antibiotics mixture (penicillin/streptomycin 50 IU/mL).

2.10. Cell Proliferation Assay (MTT Assay). HepG2 cells in logarithmic phase of growth were plated in 96-well plates at 2×10^4 cells/mL and grown for 24 hr. The cells were then treated with doxorubicin-loaded RC-albumin nanoparticles, chitosan-albumin nontargeted nanoparticles, and free doxorubicin all at 0.25, 0.5, and 1 μ g/mL concentrations at 37°C for 48 hr. In each case blank nanoparticles with the same concentration were used for comparison. After this period, each well was exposed to 20 μ L of MTT, and plates were

incubated for an additional 3 hr. Then in each well, the culture medium was removed and blue-violet formazan crystals were dissolved by adding 150 μL of DMSO. The absorbance of each well was measured at wavelength of 570 nm using an ELISA plate reader (Awareness, USA). Untreated cells and cells treated with doxorubicin were used as negative and positive controls, respectively.

2.11. Cellular Uptake Studies. The cellular uptake tests on HepG2 cells were performed after 24 hr culturing the cells. The nanoparticles were loaded with sodium fluorescein as the fluorescent probe marker. The remained free marker was removed by dialyzing against deionized water, and then the washed loaded nanoparticles were used for the cellular uptake test. Then sodium fluorescein-labeled nanoparticles of RC-albumin nanoparticles, nontargeted chitosan-albumin nanoparticles, and also the solution of sodium fluorescein were incubated with the cells for 1 and 4 hr, and then micrographs were taken using visible or fluorescent light using a fluorescent microscope (Olympus, IX71, Japan).

3. Results and Discussion

3.1. Synthesis of RC Copolymer. The synthesis of RC copolymer was confirmed by ^1H NMR and FT-IR spectra. The results are shown in Figures 1 and 2.

^1H NMR spectra (400 MHz, DMSO-d_6) of R, C, and RC copolymer are shown in Figure 1. Absence of the acidic proton of R in the area of 12 ppm with the downfield shift of the (g) proton of retinoic acid accompanying with the presence of other reference peaks of chitosan and R led us to conclude that the chemical bonding between chitosan and R has occurred.

FT-IR spectra of these substances are shown in Figure 2. The absorption band at 1635 cm^{-1} in spectra of chitosan (Figure 2(a)) was attributed to the carbonyl of $\text{O}=\text{C}-\text{NHR}$ of chitosan, and the absorption band at 1521 cm^{-1} was assigned to the amino groups of chitosan with high deacetylation degrees. The absorption band at 1680 cm^{-1} in spectra of R (Figure 2(b)) was assigned to the carbonyl group of R, and the absorption band around 2931 cm^{-1} was attributed to its aliphatic alkanes. In the spectra of RC (Figure 2(c)) additional absorption band that has appeared at 1736 cm^{-1} demonstrated conjugation between R and chitosan; furthermore, the presence of other reference bands of R and chitosan indicates the occurrence of conjugation between R and chitosan.

3.2. Particle Size. Twelve different formulations of RC-albumin nanoparticles loaded with doxorubicin (Table 1) were prepared, and their physical properties were measured as shown in Table 3.

As it can be seen in Figure 3, mean diameter of nanoparticles is dependent mainly on the interaction between polymer type and drug content. Statistical analysis of the results showed that increase in degree of substitution of R in copolymer led to decrease in particle size. The total mass of copolymer and albumin also had a significant impact on particle diameter. Comparing the contribution percentage

of total mass of copolymer and albumin with the ratio of albumin/RC on the particle size of nanoparticles (Figure 3), it can be concluded that the albumin part of the total amount of RC-albumin plays a quite less significant role than the chitosan part.

Retinoic acid is a hydrophobic molecule, so the more retinoic acid is attached to chitosan the less water soluble it will be, and this causes enhancement in hydrophobic interactions which make the particle decrease its surface, and more packed nanoparticles will be formed [40].

On the other hand, doxorubicin is protonated in nano dispersion and is a water soluble drug [41], so the drug entrapped in particles naturally tends to leave them and enter the water. When hydrophobic interactions were less significant (R2 compared to R4) the particles could swell. The total mass of copolymer and albumin also had a significant impact on particle diameter. From previous studies [42–44] it was expected that increased chitosan concentration led to increase in size.

Comparing the contribution percentage of total mass of copolymer-albumin with the ratio of albumin/RC on the particle size of nanoparticles (Figure 3), it can be concluded that the albumin part of the total amount of copolymer and albumin plays a quite less significant role than the chitosan part. Even statistical analysis of the effect of each variable on the particle size showed that albumin/RC caused decrease in the particle size of nanoparticles. The increase in albumin concentration induced more negative charge in nanodispersion, and the positively charged chitosan molecules formed more ionic bonds which made the particles wall to form tighter surface leading to the shrinkage and decrease in the surface of the particles, so in higher amounts of albumin, the effect of chitosan in increasing the size is somewhat attenuated.

3.3. Zeta Potential. As Figure 4 indicates the zeta potential of nanoparticles depended mostly on the amount of total mass of RC-albumin and the interaction between the drug content and albumin. Statistical analysis showed that in drug content level of 0.25 increasing the albumin to RC ratio had a slim effect on zeta potential but, as the albumin concentration was increased, switching to higher level of drug content had quite significant impact on zeta potential.

Zeta potential is often a key factor in the stability of colloidal dispersions. Table 3 indicates that the changes of zeta potential were between 39.5 ± 1.8 to 46.8 ± 3.2 mV. This demonstrates that the nanoparticles dispersion obtained by coacervation method in an aqueous system is a physically stable system. As Figure 4 indicates the zeta potential of nanoparticles depended mostly on the amount of total mass of RC-albumin and the interaction between the drug content and albumin. As was mentioned before, albumin imparts negative charge to the nanoparticles, and the higher albumin concentration resulted in less positively charged nanoparticles. This reducing impact on zeta potential is more profound than the increasing effect of chitosan on zeta potential (Figure 4).

Freitas and Müller [45] have shown that the increased drug content could reduce the charge density and absolute

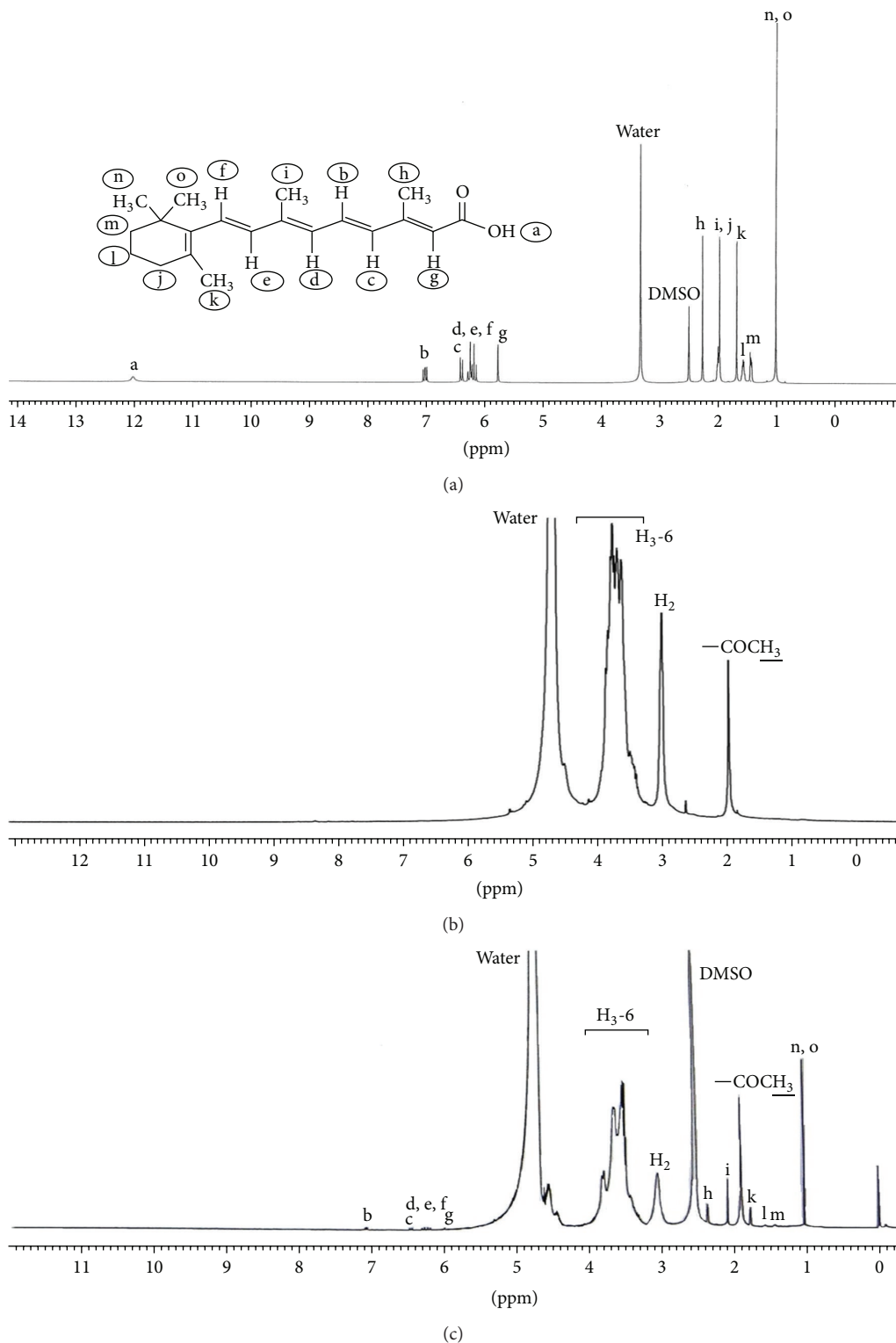


FIGURE 1: ¹H NMR spectra: (a) retinoic acid, (b) chitosan, and (c) retinoic acid-chitosan conjugate.

values of zeta potential. Statistical analysis of our results revealed that in drug content level of 0.25 increasing the albumin to RC ratio had slim effect on zeta potential, but as the albumin concentration was increased, switching to higher level of drug content had quite significant impact on zeta potential.

3.4. Entrapment Efficiency. As it can be seen in Figure 5, the amount of total RC and albumin was the most important factor affecting the entrapment efficiency, while the role of albumin alone was negligible. Therefore, it may be concluded that the main factor was the amount of RC. Increased drug content resulted in lower entrapment efficiency (Table 3).

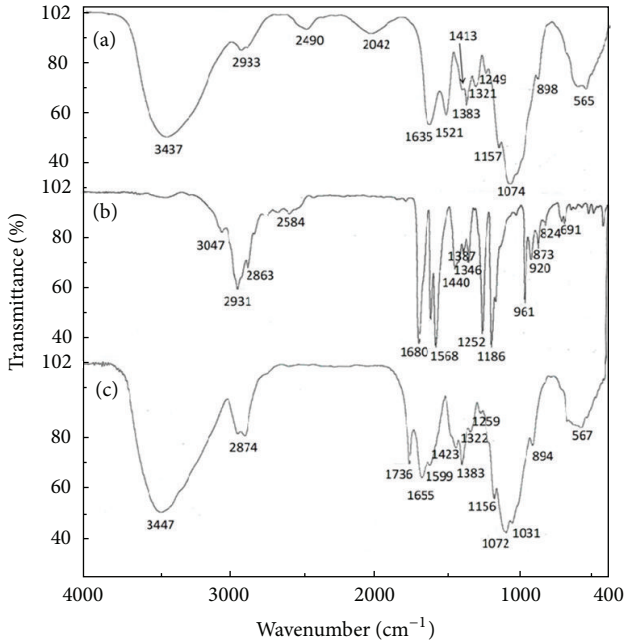


FIGURE 2: FT-IR spectra: (a) chitosan, (b) retinoic acid, (c) retinoic acid-chitosan conjugate.

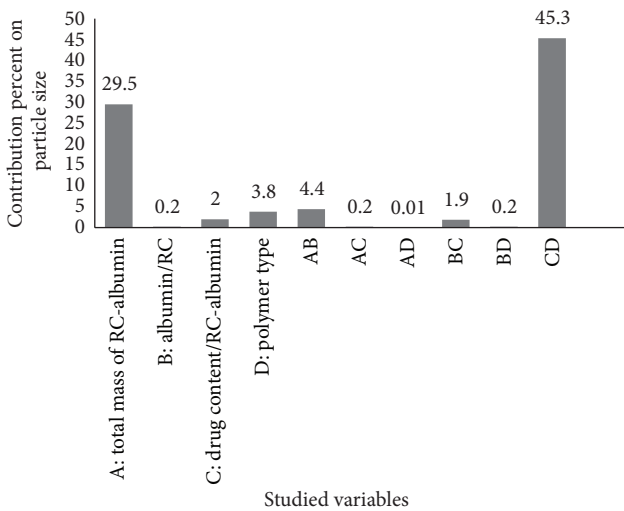


FIGURE 3: Contribution percent of studied variables on the particle size of RC-albumin nanoparticles loaded with doxorubicin.

The interaction of albumin/RC with drug content/albumin-RC was also another effective parameter on doxorubicin entrapment efficiency.

Many factors have been reported to affect the entrapment efficiency of drugs in nanoparticles with chitosan structures such as drug to polymer ratio, chitosan concentration, the properties of the drug itself, and the stirring rate. In present study the stirring rate was set to be the same for all tests so its effect did not interfere in entrapment efficiency.

As mentioned earlier, Figure 5 indicates that the amount of total RC and albumin was the most important factor

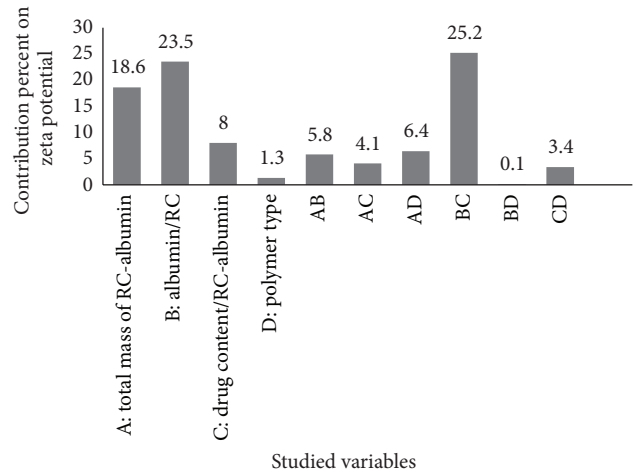


FIGURE 4: Contribution percent of studied variables on the zeta potential of RC-albumin nanoparticles loaded with doxorubicin.

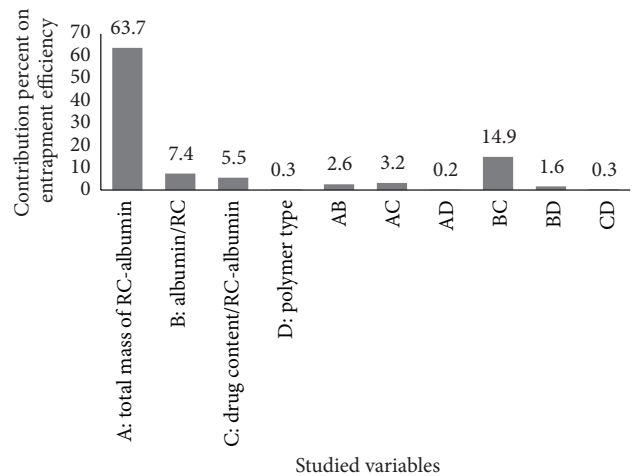


FIGURE 5: Contribution percent of studied variables on entrapment efficiency of RC-albumin nanoparticles loaded with doxorubicin.

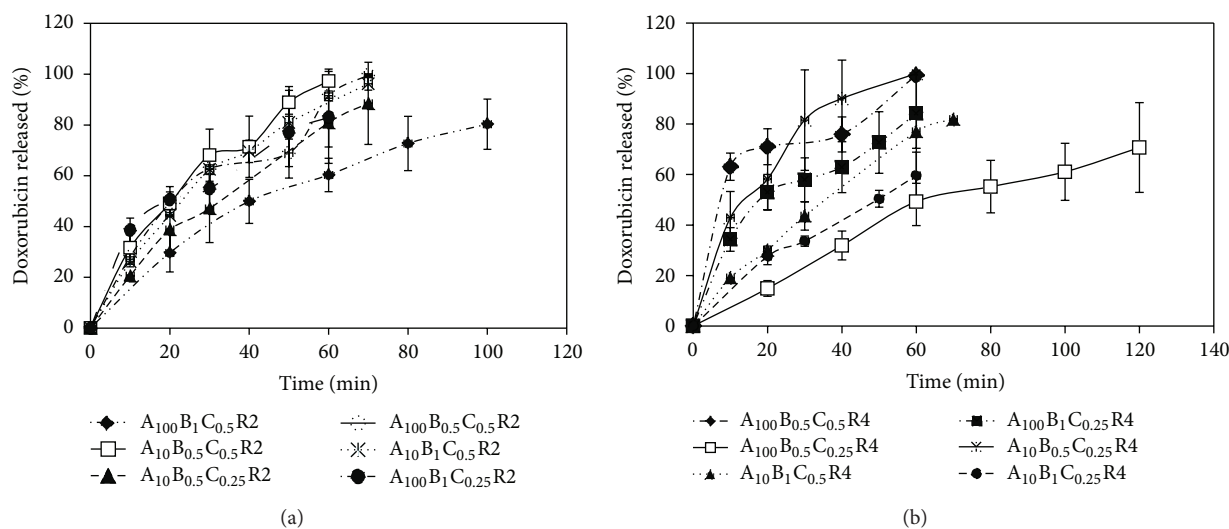
affecting the entrapment efficiency, while the role of albumin alone was negligible. Therefore, it may be concluded that the main factor was the amount of RC. Bayomi [37] observed that high concentration of albumin solution and accordingly the increase of albumin-to-chitosan weight ratio were accompanied with increase in particle size and incorporation efficiency of indomethacin in albumin-chitosan microspheres, while a slow drug release was observed.

In another study reported by Bayomi et al. [44], they prepared casein-chitosan microspheres using an aqueous coacervation method to encapsulate diltiazem hydrochloride and reported the amount of protein (casein) as the major variable affecting the entrapment efficiency of the drug.

Although some reports from previous studies [46, 47] showed that with higher levels of chitosan concentration used in production of chitosan nanoparticles entrapment efficiency had increased, in the present study statistical analysis of data showed that increase in RC concentration

TABLE 3: Physicochemical properties of different doxorubicin-loaded RC-albumin nanoparticles.

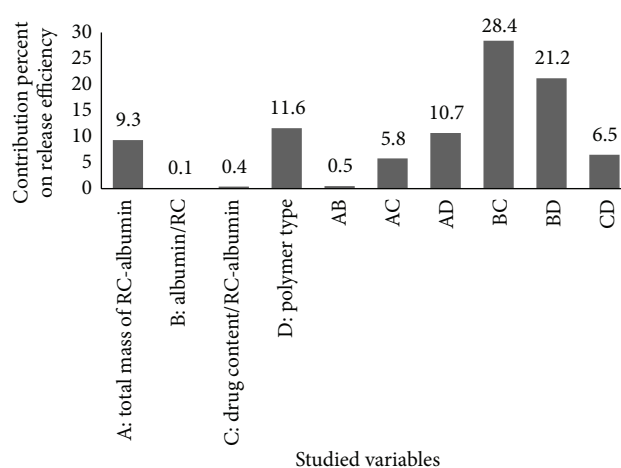
Formulation code	Particle size (nm)	PdI	Zeta potential (mv)	Loading efficiency%	RE ₆₀ %
A ₁₀₀ B ₁ C _{0.5} R2	357.0 ± 39.8	0.53	39.5 ± 1.8	33.3 ± 7.2	41.5 ± 1.2
A ₁₀ B _{0.5} C _{0.5} R2	232.4 ± 19.3	0.31	43.7 ± 1.2	40.6 ± 14.5	66.6 ± 128
A ₁₀ B _{0.5} C _{0.25} R2	148.0 ± 16.0	0.44	41.3 ± 3.8	56.8 ± 13.4	50.5 ± 9.4
A ₁₀₀ B _{0.5} C _{0.5} R4	264.5 ± 86.7	0.77	46.8 ± 3.2	8.3 ± 2.8	76.8 ± 2.4
A ₁₀₀ B _{0.5} C _{0.5} R2	472.2 ± 78.9	0.94	44.8 ± 1.9	7.3 ± 6.3	55.6 ± 3.1
A ₁₀ B ₁ C _{0.5} R2	370.0 ± 51.9	0.93	29.3 ± 6.9	50.7 ± 4.7	52.6 ± 7.8
A ₁₀₀ B ₁ C _{0.25} R2	234.0 ± 8.0	0.86	45.0 ± 2.2	28.9 ± 9.9	54.8 ± 10.6
A ₁₀₀ B _{0.5} C _{0.25} R4	340.7 ± 64.6	0.76	41.2 ± 4.7	32.5 ± 6.8	32.2 ± 4.2
A ₁₀ B ₁ C _{0.5} R4	188.0 ± 65.8	0.94	37.4 ± 6.6	57.7 ± 7.1	43.4 ± 3.6
A ₁₀₀ B ₁ C _{0.25} R4	349.0 ± 65.3	0.70	42.3 ± 2.3	34.2 ± 5.1	53.8 ± 8.1
A ₁₀ B _{0.5} C _{0.25} R4	248.2 ± 59.3	0.65	43.3 ± 4.2	48.7 ± 8.0	72 ± 8.7
A ₁₀ B ₁ C _{0.25} R4	186.4 ± 18.3	0.74	42.5 ± 0.3	41.1 ± 26.2	46.4 ± 5.4

FIGURE 6: Doxorubicin HCl release profile from different formulations of RC-albumin nanoparticles prepared from (a) R2 or (b) R4 copolymer with different studied variables (mean ± SD, $n = 3$).

significantly decreased the entrapment efficiency. This might be due to higher viscosity of RC solution in higher concentrations and less chance of the drug to be entrapped into the particles [46]. Moreover, as was mentioned before, doxorubicin has positive charge, so when it came in contact with positively charged RC electrical repulsion inhibited the drug to enter into the nanoparticles, and as the albumin ratio was increased, its negative charge neutralized the total positive charge and entrapment efficiency of doxorubicin was enhanced (Table 3). Increased drug content resulted in lower entrapment efficiency (Table 3), and this effect agreed with what was reported by Sinha et al. [46].

3.5. In Vitro Drug Release Studies. Generally, a fast release profile for doxorubicin was observed in all formulations (Figure 6).

Figure 7 shows the most effective factors that determine release behavior. Some of these variables are the total mass

FIGURE 7: Contribution percent of studied variables on release efficiency (RE₆₀%) of RC-albumin nanoparticles loaded with doxorubicin.

of RC and albumin, polymer type, the interaction of these two variables, the interaction effect of the drug and albumin content, and also the interaction of albumin and polymer type. Statistical analysis of release data showed that increasing the total mass of RC and albumin significantly decreased the RE. Albumin content had low effect on release behavior of doxorubicin from the nanoparticles.

Doxorubicin release profiles from the most of nanoparticle formulations showed a near zero order process (Figure 6). However, some of the nanoparticles especially those prepared with R4 polymer like $A_{100}B_{0.5}C_{0.5}R4$, $A_{100}B_1C_{0.25}R4$, and $A_{10}B_{0.5}C_{0.25}R4$ showed a biphasic release pattern for doxorubicin so that at first, a quick release and then a slow phase were observed. The initial rapid release is probably caused by drug release which is dissolved in the surface of nanoparticles that leaks promptly into the release medium, and the next slow release phase is due to the drug diffusion through the core of the nanoparticles matrix.

Statistical analysis of release data showed that increasing the total mass of RC and albumin significantly decreased the RE. Albumin content had low effect on release behavior of doxorubicin from the nanoparticles this effect agrees well with what Nishioka et al. [47] have reported. In the study reported by Bayomi [37] on the release of indomethacin from chitosan-albumin microspheres, they found that higher drug loading around 40% w/w or higher started to interfere with the coacervation process and increased the rate of drug release. Similar results were obtained with coacervation of chitosan with gumkaraya [48], and it was concluded that this effect may be due to an increase in the number of drug particles, which reduced the amount of coacervated phase within the microspheres and might have interfered with cohesion of coacervate. In spite of the reported effect of drug loading (more than 40%) on the release rate of drug from chitosan-albumin microspheres [37], in our work the drug to polymer ratio was set at 0.5 or 0.25 (Table 2), but still at these high loading its effect on drug release efficiency was negligible (Figure 7). This may be attributed to the different drug solubility of indomethacin (as a low water soluble drug) used in previous studies and doxorubicin HCl (a quite water soluble drug) used in the present study that does not interfere with coacervation process.

3.6. Optimization. In many formulations, not just pharmaceutical in nature, it is necessary to balance several different measures of quality (i.e., properties) in order to find the best overall product. Changes to the formulation to improve one property may have a deleterious impact on another property. The process of finding the best compromise has been more rigorous by the process of desirability optimization, to produce numerical value of a desirability function.

Computer optimization of the results from irregular factorial design will allow the estimation of a specific combination of the variables that will optimize the individual responses and will yield a product with desirable qualities. The criteria for the optimization of all studied factors are shown in Table 1. Twelve different formulations were designed with Design Expert software by an irregular factorial design. Then considering the results of the

experiments done on these formulations (Table 3), optimization was done using Design Expert software, and $A_{10}B_1C_{0.37}R2$ was suggested as the optimum formulation which showed a good particle size of 286 nm, zeta potential was 30.5 mV, an acceptable entrapment efficiency of 43.6%, and relatively high release efficiency of 56.17%.

Comparing the results predicted by this software for the optimum formulation of nanoparticles with the actual values showed that the error percent was -33%, 12%, 3.11%, and 13% for particle size, zeta potential, entrapment efficiency, and release efficiency, respectively.

3.7. Transmission Electron Microscopy (TEM) of the Nanoparticles. The morphology of the prepared nanoparticles is shown in Figure 8. The nanoparticles are obviously discrete; some spherical and some irregular shapes and the scale bar of the graphs confirm the particle size of the nanoparticles obtained by PCS method (Table 3).

The results of particle size of the nanoparticles obtained by PCS method (Table 3) were confirmed by the TEM pictures as seen in Figure 8. Although the pH of the solution was adjusted at 2.49 in all formulations, but some irregularity was seen in the particles. After preliminary studies the, pH of 2.49 was selected as the cross-linking interaction was initiated at acidic pH in the presence of amino groups. It was expected as the pH of solution was increased, the efficiency of cross-linking reaction was decreased and the particles became less rigid, resulting in irregular particles. This trend of changes was maximum at pH 4.52, which is close to the isoelectric point of egg albumin where the molecules are nearly overall electroneutral, and incomplete coacervation (if any) and/or incomplete cross linking of the nanoparticles is possible [38].

3.8. Cell Proliferation Assay. Cell survival percentage of HepG2 cells is shown in Figure 9. Doxorubicin-loaded nanoparticles targeted with retinoic acid (RC-albumin) were compared with nontargeted ones (chitosan-albumin) and free doxorubicin. As can be seen from Figure 9, the IC_{50} is decreased in both targeted and nontargeted nanoparticles compared to free doxorubicin. The retinoic acid targeted nanoparticles had the lowest IC_{50} . The highest growth inhibitory effect was observed in cells treated with RC-albumin nanoparticles at $0.5 \mu\text{g/mL}$ concentration that is approximately two and three times greater than the effect observed with nontargeted and free doxorubicin at the same concentration, respectively.

However, the cell survival percentage shows an increase in doxorubicin-loaded RC-albumin nanoparticles-treated group at $1 \mu\text{g/mL}$ concentration and its blank nanoparticles. Antonyak et al. [49] reported that retinoic acid and its various synthetic analogs affected mammalian cell growth, differentiation, and apoptosis. Whereas treatment of the human leukemia cell line HL60 with retinoic acid resulted in cellular differentiation, addition of the synthetic retinoid, N-(4-hydroxyphenyl) retinamide (HPR), and induced HL60 cells to undergo apoptosis. Moreover, pretreatment of HL60 cells as well as other cell lines (i.e., NIH3T3 cells) with retinoic acid blocked HPR-induced cell death. Therefore,

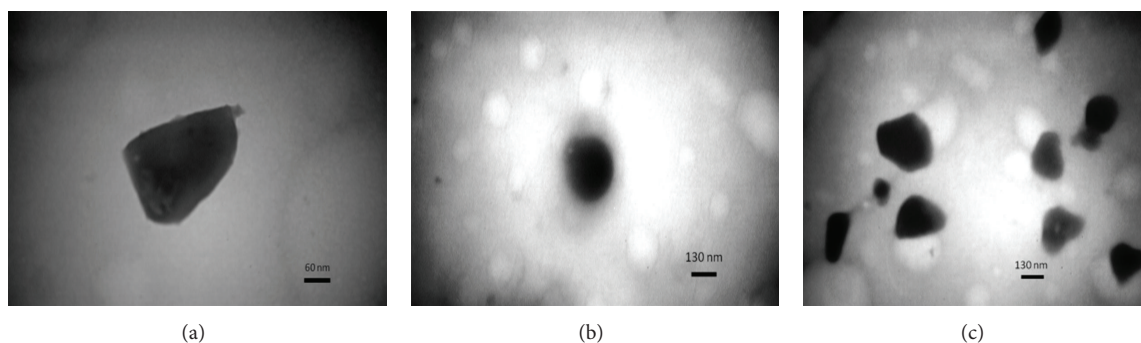


FIGURE 8: TEM micrographs of RC-albumin nanoparticles loaded with doxorubicin with different magnifications.

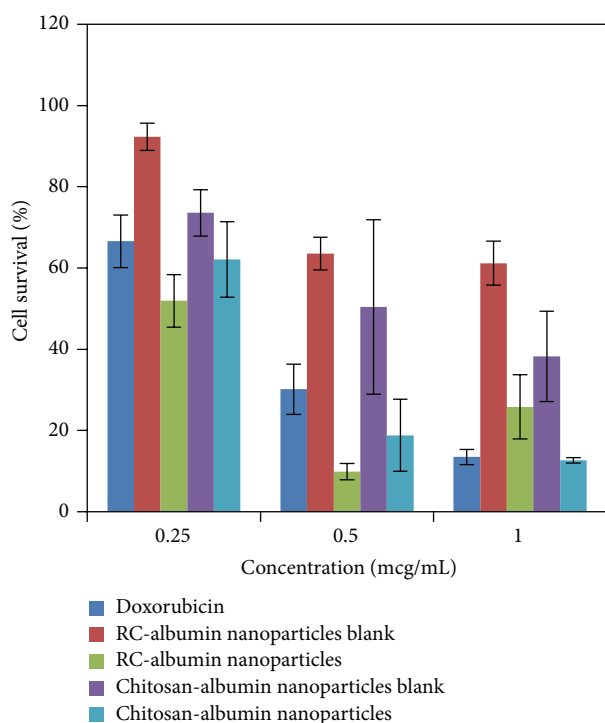


FIGURE 9: Viability of HepG2 cells after treatment with different concentrations of doxorubicin-loaded nanoparticles of chitosan-albumin with or without retinoic acid conjugate in comparison with free doxorubicin by MTT assay ($n = 3$).

it may be concluded that the growth inhibitory effect of retinoic acid on HepG2 cells that is exerted via α -receptors over expressed in hepatocellular carcinoma may be dose dependent. When the concentration of nanoparticles was increased to deliver $1\mu\text{g}/\text{mL}$ of doxorubicin to the cells, the concentration of carrier itself, that is, RC-albumin, was increased too, and the increased retinoic acid may have blocked cell death induced by doxorubicin that is loaded in RC-albumin nanoparticles. Consequently the viable cells had increased at $1\mu\text{g}/\text{mL}$ concentration.

3.9. Cellular Uptake Study. The results are represented in Figure 10. As this figure shows after 1 hr of incubation just

RC-albumin nanoparticles show a brief accumulation of fluorescence in the cells. After 4 hr, the green fluorescence is sighted more significantly in cells that are incubated with sodium fluorescein loaded in RC-albumin nanoparticles than nontargeted chitosan-albumin nanoparticles, and there is no significant fluorescence in cells that are incubated with solution of sodium fluorescein. It should be reminded that after loading the nanoparticles with the fluorescein solution, the free fluorescein was removed from the solution by dialysis method, and just the washed loaded nanoparticles were exposed to the cells.

These results depict robust uptake of the nanoparticles in HepG2 cells. Control cells incubated with free solution of fluorescein did not show any fluorescence. The cells incubated with nontargeted nanoparticles (chitosan-albumin) loaded with fluorescein exhibited a brief green fluorescence compared to rapid internalization and accumulation of retinoic acid targeted nanoparticles (RC-albumin) by the cancer cells (Figure 10). Further investigation on the mechanism of retinoic acid targeted nanoparticles uptake, and the kinetics of drug uptake and retention in the HepG2 cells compared to a free drug *in vivo* will be useful to establish the efficacy of nanoparticles for various therapeutic applications.

4. Conclusions

Chitosan-albumin nanoparticles targeted with R were prepared for targeted delivery of doxorubicin to hepatocellular carcinoma. R was grafted to chitosan by DCC-NHS chemistry, and RC copolymer was synthesized successfully. An aqueous coacervation method was used to attach albumin to RC copolymer. Preparation of the targeted nanoparticles of RC-albumin containing doxorubicin was optimized statistically by an irregular factorial design. The best formulation of the RC-albumin nanoparticles was $A_{10}B_1C_{0.37}R_2$ which was prepared by copolymer of chitosan and retinoic acid in which 2 amine groups were substituted, 10 mg of RC-albumin was used in its preparation, the ratio of albumin/RC was 1 and the ratio of drug/RC-albumin was 0.37. The particle size of these nanoparticles was 286 nm, zeta potential of 30.5 mV, an acceptable entrapment efficiency of 43.6%, and relatively high release efficiency of 56.17% until 1 hr of release test. The highest growth inhibitory effect was observed in HepG2 cells treated with RC-albumin

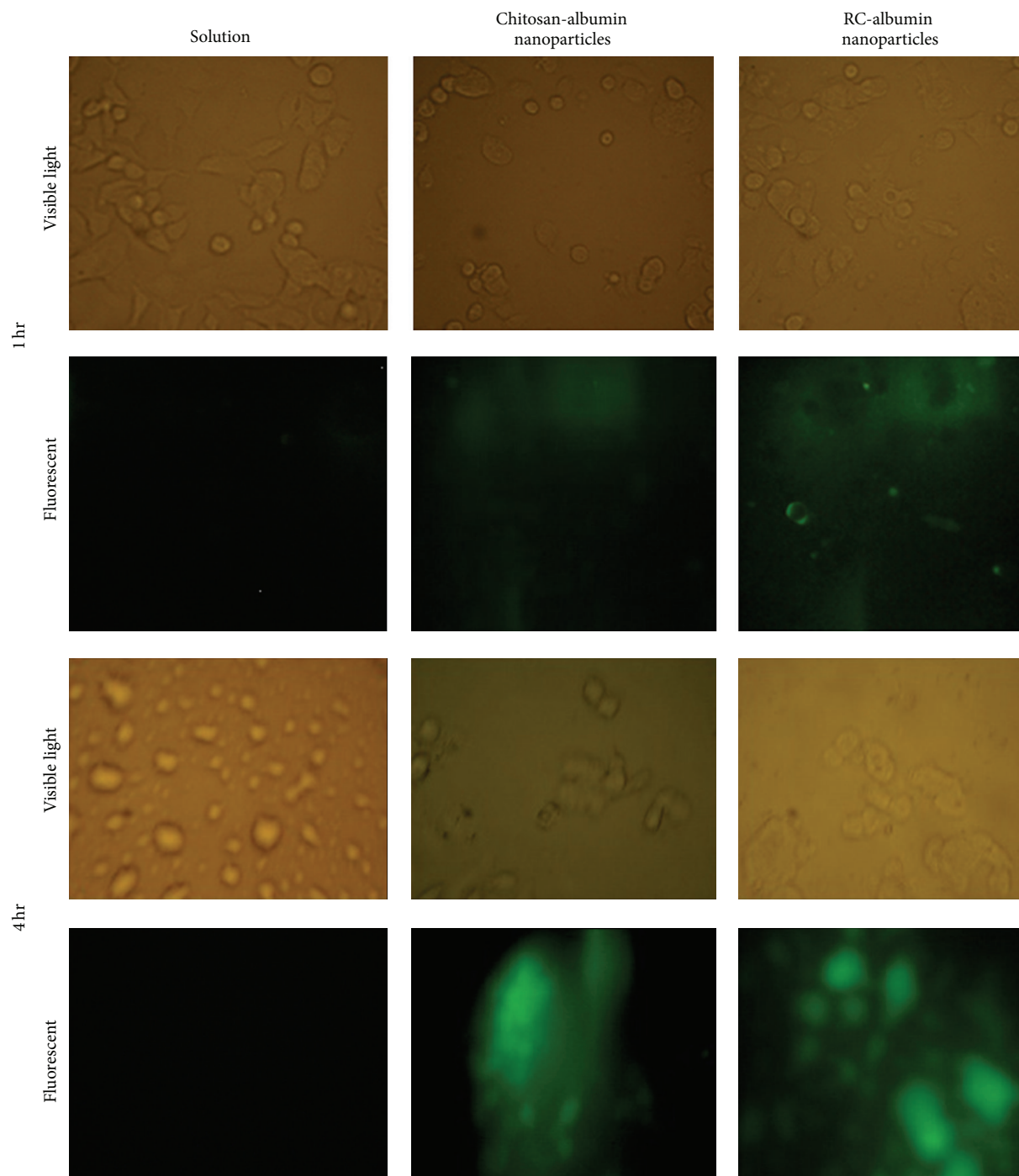


FIGURE 10: Fluorescent and visible light microscopic images of HepG2 cells after incubation with fluorescein loaded in nanoparticles of RC-albumin and chitosan-albumin or as free fluorescein solution for 1 and 4 hr.

nanoparticles at $0.5 \mu\text{g}/\text{mL}$ concentration that is approximately two and three times greater than the effect observed by nontargeted and free doxorubicin at the same concentration, respectively. This may reduce needed dose of doxorubicin and consequently reduces the required doses which in turn reduces the cardiotoxicity of this drug. The results should be checked *in vivo* to confirm the promising results on the cell culture.

Conflict of Interests

There is not any conflict of interests.

Acknowledgments

The authors acknowledge the financial support of Isfahan University of Medical Sciences. This paper is extracted from the dissertation of Zahra Ghelich Khan the PharmD student

of Faculty of Pharmacy of Isfahan University of Medical Sciences.

References

- [1] H. B. El-Serag, "Hepatocellular carcinoma: an epidemiologic view," *Journal of Clinical Gastroenterology*, vol. 35, supplement 5, pp. S27–S28, 2002.
- [2] J. M. Llovet, S. Ricci, V. Mazzaferro et al., "Sorafenib in advanced hepatocellular carcinoma," *The New England Journal of Medicine*, vol. 359, no. 4, pp. 378–390, 2008.
- [3] D. M. Parkin, F. Bray, J. Ferlay, and P. Pisani, "Global cancer statistics, 2002," *Ca: A Cancer Journal for Clinicians*, vol. 55, no. 2, pp. 74–108, 2005.
- [4] H. B. El-Serag and K. L. Rudolph, "Hepatocellular carcinoma: epidemiology and molecular carcinogenesis," *Gastroenterology*, vol. 132, no. 7, pp. 2557–2576, 2007.
- [5] V. K. Rustgi, "Epidemiology of hepatocellular carcinoma," *Gastroenterology Clinics of North America*, vol. 16, no. 4, pp. 545–551, 1987.
- [6] W. T. London, "Primary hepatocellular carcinoma—etiology, pathogenesis, and prevention," *Human Pathology*, vol. 12, no. 12, pp. 1085–1097, 1981.
- [7] C. L. Lai, P. B. Gregory, P. C. Wu, A. S. F. Lok, K. P. Wong, and M. M. T. Ng, "Hepatocellular carcinoma in Chinese males and females. Possible causes for the male predominance," *Cancer*, vol. 66, no. 5, pp. 1107–1110, 1987.
- [8] C. Muir, J. Waterhouse, J. Powell, T. Mack, and S. Whelan, *Cancer Incidence in Five Continents, Volume 5*, Oxford University Press, New York, NY, USA, 1987.
- [9] S. R. Nerenstone, D. C. Ihde, and M. A. Friedman, "Clinical trials in primary hepatocellular carcinoma: current status and future directions," *Cancer Treatment Reviews*, vol. 15, no. 1, pp. 1–31, 1988.
- [10] M. A. Avila, C. Berasain, B. Sangro, and J. Prieto, "New therapies for hepatocellular carcinoma," *Oncogene*, vol. 25, no. 27, pp. 3866–3884, 2006.
- [11] M. Huang and G. Liu, "The study of innate drug resistance of human hepatocellular carcinoma Bel₇₄₀₂ cell line," *Cancer Letters*, vol. 135, no. 1, pp. 97–107, 1999.
- [12] J. M. Llovet, A. Burroughs, and J. Bruix, "Hepatocellular carcinoma," *The Lancet*, vol. 362, no. 9399, pp. 1907–1917, 2003.
- [13] P. B. Jensen, B. S. Sorensen, M. Sehested et al., "Different modes of anthracycline interaction with topoisomerase II. Separate structures critical for DNA-cleavage, and for overcoming topoisomerase II-related drug resistance," *Biochemical Pharmacology*, vol. 45, no. 10, pp. 2025–2035, 1993.
- [14] K. Shan, A. Michael Lincoff, and J. B. Young, "Anthracycline-induced cardiotoxicity," *Annals of Internal Medicine*, vol. 125, no. 1, pp. 47–58, 1996.
- [15] E. Ruoslahti, S. N. Bhatia, and M. J. Sailor, "Targeting of drugs and nanoparticles to tumors," *Journal of Cell Biology*, vol. 188, no. 6, pp. 759–768, 2010.
- [16] T. J. Harris, G. von Maltzahn, M. E. Lord et al., "Protease-triggered unveiling of bioactive nanoparticles," *Small*, vol. 4, pp. 1307–1312, 2008.
- [17] S. M. Moghimi, A. C. Hunter, and J. C. Murray, "Long-circulating and target-specific nanoparticles: theory to practice," *Pharmacological Reviews*, vol. 53, no. 2, pp. 283–318, 2001.
- [18] S. Wagner, F. Rothweiler, M. G. Anhorn et al., "Enhanced drug targeting by attachment of an anti αv integrin antibody to doxorubicin loaded human serum albumin nanoparticles," *Biomaterials*, vol. 31, no. 8, pp. 2388–2398, 2010.
- [19] J. Chen, H. Wu, D. Han, and C. Xie, "Using anti-VEGF McAb and magnetic nanoparticles as double-targeting vector for the radioimmunotherapy of liver cancer," *Cancer Letters*, vol. 231, no. 2, pp. 169–175, 2006.
- [20] P. Liu, Z. Li, M. Zhu et al., "Preparation of EGFR monoclonal antibody conjugated nanoparticles and targeting to hepatocellular carcinoma," *Journal of Materials Science*, vol. 21, no. 2, pp. 551–556, 2010.
- [21] T. H. Kim, I. K. Park, J. W. Nah, Y. J. Choi, and C. S. Cho, "Galactosylated chitosan/DNA nanoparticles prepared using water-soluble chitosan as a gene carrier," *Biomaterials*, vol. 25, no. 17, pp. 3783–3792, 2004.
- [22] K. Sano, T. Takayama, K. Murakami, I. Saiki, and M. Makuuchi, "Overexpression of retinoic acid receptor α in hepatocellular carcinoma," *Clinical Cancer Research*, vol. 9, no. 10 I, pp. 3679–3683, 2003.
- [23] J. Edeline, J. L. Raoul, E. Vauleon, A. Guillygomac'h, K. Boudjema, and E. Boucher, "Systemic chemotherapy for hepatocellular carcinoma in non-cirrhotic liver: a retrospective study," *World Journal of Gastroenterology*, vol. 15, no. 6, pp. 713–716, 2009.
- [24] C. E. Sever and J. Locker, "Expression of retinoic acid α and β receptor genes in liver and hepatocellular carcinoma," *Molecular Carcinogenesis*, vol. 4, no. 2, pp. 138–144, 1991.
- [25] T. T. Schug, D. C. Berry, N. S. Shaw, S. N. Travis, and N. Noy, "Opposing effects of retinoic acid on cell growth result from alternate activation of two different nuclear receptors," *Cell*, vol. 129, no. 4, pp. 723–733, 2007.
- [26] F. Recchia, G. Saggio, A. Cesta et al., "Phase II study of interleukin-2 and 13-cis-retinoic acid as maintenance therapy in metastatic colorectal cancer," *Cancer Immunology, Immunotherapy*, vol. 56, no. 5, pp. 699–708, 2007.
- [27] J. Guo, B. Xiao, Y. Lou et al., "Antitumor effects of all-trans-retinoic acid on cultured human pancreatic cancer cells," *Journal of Gastroenterology and Hepatology*, vol. 21, no. 2, pp. 443–448, 2006.
- [28] A. M. Tsimberidou, M. Tirado-Gomez, M. Andreeff et al., "Single-agent liposomal all-trans retinoic acid can cure some patients with untreated acute promyelocytic leukemia: an update of The University of Texas M. D. Anderson Cancer Center Series," *Leukemia and Lymphoma*, vol. 47, no. 6, pp. 1062–1068, 2006.
- [29] B. Singh, R. F. Murphy, X. Z. Ding, A. B. Roginsky, R. H. Bell Jr., and T. E. Adrian, "On the role of transforming growth factor- β in the growth inhibitory effects of retinoic acid in human pancreatic cancer cells," *Molecular Cancer*, vol. 6, article no. 82, 2007.
- [30] L. Altucci and H. Gronemeyer, "The promise of retinoids to fight against cancer," *Nature Reviews Cancer*, vol. 1, no. 3, pp. 181–193, 2001.
- [31] M. P. Patel, R. R. Patel, and J. K. Patel, "Chitosan mediated targeted drug delivery system: a review," *Journal of Pharmacy and Pharmaceutical Sciences*, vol. 13, no. 4, pp. 536–557, 2010.
- [32] S. Hirano, H. Seino, Y. Akiyama, and I. Nonaka, "Chitosan: a biocompatible material for oral and intravenous administration," in *Progress in Biomedical Polymers*, C. G. Gebelein and R. L. Dunn, Eds., Plenum Press, New York, NY, USA, 1990.
- [33] Y. Zheng, Z. Cai, X. Song et al., "Preparation and characterization of folate conjugated N-trimethyl chitosan nanoparticles

- as protein carrier targeting folate receptor: in vitro studies," *Journal of Drug Targeting*, vol. 17, no. 4, pp. 294–303, 2009.
- [34] K. Y. Lee, I. C. Kwon, Y. H. Kim, W. H. Jo, and S. Y. Jeong, "Preparation of chitosan self-aggregates as a gene delivery system," *Journal of Controlled Release*, vol. 51, no. 2-3, pp. 213–220, 1998.
- [35] L. Chen and M. Subirade, "Chitosan/ β -lactoglobulin core-shell nanoparticles as nutraceutical carriers," *Biomaterials*, vol. 26, no. 30, pp. 6041–6053, 2005.
- [36] T. W. Wang, Q. Xu, Y. Wu, A. J. Zeng, M. Li, and H. Gao, "Quaternized chitosan (QCS)/poly (aspartic acid) nanoparticles as a protein drug-delivery system," *Carbohydrate Research*, vol. 344, no. 7, pp. 908–914, 2009.
- [37] M. A. Bayomi, "Aqueous preparation and evaluation of albumin-chitosan microspheres containing indomethacin," *Drug Development and Industrial Pharmacy*, vol. 30, no. 4, pp. 329–339, 2004.
- [38] A. O. Elzoghby, W. M. Samy, and N. A. Elgindy, "Albumin-based nanoparticles as potential controlled release drug delivery systems," *Journal of Controlled Release*, vol. 157, no. 2, pp. 168–182, 2012.
- [39] E. C. van Dalen, E. M. Michiels, H. N. Caron, and L. C. Kremer, "Different anthracycline derivatives for reducing cardiotoxicity in cancer patients," *Cochrane Database of Systematic Reviews*, vol. 3, Article ID CD005006, 2010.
- [40] A. Fattahi, M. A. Golozar, J. Varshosaz, M. H. Sadeghi, and M. Fathi, "Preparation and characterization of micelles of oligomeric chitosan linked to all trans retinoic acid," *Carbohydrate Polymers*, vol. 87, pp. 1176–1184, 2012.
- [41] J. Qi, P. Yao, F. He, C. Yu, and C. Huang, "Nanoparticles with dextran/chitosan shell and BSA/chitosan core—doxorubicin loading and delivery," *International Journal of Pharmaceutics*, vol. 393, no. 1-2, pp. 176–184, 2010.
- [42] E. B. Denkbaş, E. Kiliçay, C. Birlikseven, and E. Öztürk, "Magnetic chitosan microspheres: preparation and characterization," *Reactive and Functional Polymers*, vol. 50, pp. 225–232, 2002.
- [43] Y. B. Ge, D. W. Chen, L. P. Xie, and R. Q. Zhang, "Optimized preparation of daidzein-loaded chitosan microspheres and in vivo evaluation after intramuscular injection in rats," *International Journal of Pharmaceutics*, vol. 338, no. 1-2, pp. 142–151, 2007.
- [44] M. A. Bayomi, S. A. Al-Suwayeh, A. M. El-Helw, and A. F. Mesnad, "Preparation of casein-chitosan microspheres containing diltiazem hydrochloride by an aqueous coacervation technique," *Pharmaceutica Acta Helveticae*, vol. 73, no. 4, pp. 187–192, 1998.
- [45] C. Freitas and R. H. Müller, "Effect of light and temperature on zeta potential and physical stability in solid lipid nanoparticle (SLN) dispersions," *International Journal of Pharmaceutics*, vol. 168, no. 2, pp. 221–229, 1998.
- [46] V. R. Sinha, A. K. Singla, S. Wadhawan et al., "Chitosan microspheres as a potential carrier for drugs," *International Journal of Pharmaceutics*, vol. 274, no. 1-2, pp. 1–33, 2004.
- [47] Y. Nishioka, S. Kyotani, H. Masui et al., "Preparation and release characteristics of cisplatin albumin microspheres containing chitin and treated with chitosan," *Chemical and Pharmaceutical Bulletin*, vol. 37, no. 11, pp. 3074–3077, 1989.
- [48] G. V. M. M. Babu, C. D. S. Prasad, C. P. S. Narayan, and K. V. R. Murthy, "New system for microencapsulation of diclofenac sodium using gum karaya and chitosan," *Saudi Pharmaceutical Journal*, vol. 9, no. 3-4, pp. 169–178, 2001.
- [49] M. A. Antonyak, U. S. Singh, D. A. Lee et al., "Effects of tissue trans glutaminase on retinoic acid-induced cellular differentiation and protection against apoptosis," *The Journal of Biological Chemistry*, vol. 276, no. 36, pp. 33582–33587, 2001.

Research Article

Electrodeposition, Characterization, and Corrosion Stability of Nanostructured Anodic Oxides on New Ti-15Zr-5Nb Alloy Surface

Jose M. Calderon Moreno, Cora Vasilescu, Silviu Iulian Drob, Monica Popa, Paula Drob, and Ecaterina Vasilescu

Romanian Academy, Institute of Physical Chemistry "Ilie Murgulescu," Splaiul Independentei 202, 060021 Bucharest, Romania

Correspondence should be addressed to Cora Vasilescu; cvasilescu@chimfiz.icf.ro

Received 11 February 2013; Accepted 20 March 2013

Academic Editor: Mohamed Bououdina

Copyright © 2013 Jose M. Calderon Moreno et al. This is an open access article distributed under the Creative Commons Attribution License, which permits unrestricted use, distribution, and reproduction in any medium, provided the original work is properly cited.

A new Ti-15Zr-5Nb alloy with suitable microstructure and mechanical properties was processed by galvanostatic anodization in 0.3 M H_3PO_4 solution and a continuous nanostructured layer of protective TiO_2 oxide was electrodeposited. The obtained anatase oxide layer has a nanotubes-like porosity (SEM observations) and contains significant amount of phosphorus in phosphotitanate compound embedded in the oxide lattice (Raman, FT-IR, SEM, and EDX analysis). This layer composition can stimulate the formation of the bone and its porosity can offer a good scaffold for bone cell adhesion. The electrochemical behaviour, corrosion stability, and variations of the open circuit potentials, E_{oc} , and corresponding open circuit potential gradients, ΔE_{oc} , for 1500 soaking hours in Ringer solutions of 3.21, 7.58, and 8.91 pH values were studied. The anodized layer was more resistant, stable (from EIS spectra), and was formed from an inner barrier insulating layer that assures the very good alloy corrosion resistance and an outer porous layer that provides the good conditions for cell development. The nanostructured alloy has higher corrosion stability, namely, a more reduced quantity of ions released and a lower toxicity than that of the bare one. The monitoring of E_{oc} and ΔE_{oc} showed the enhancement and stabilizing of the long-term passive state of the anodized alloy and, respectively, no possibility at galvanic corrosion.

1. Introduction

Titanium and its alloys are used as orthopaedic and dental implants due to their good mechanical and anticorrosive properties and biocompatibility. However, it is an increasing necessity to obtain new alloys with a low elastic modulus, close to that of the human bone (10–40 GPa) [1], and based only on nontoxic, nonallergic, biocompatible elements as Zr, Nb, and Ta [2, 3]. Titanium alloys containing these biocompatible metals are relatively bioinert and the implant-bone integration is a longer process than that of the bone healing.

The alloy bioactivity depends on its surface chemistry, topography, porosity, and roughness; a rough surface enhances the contact with the bone and improves the bioactive bone-binding activity. Thus, surface treatments that form thin or thick, uniform, resistant, porous, rough layers

on the implant surface and also incorporate constituent elements of the human bone (calcium and phosphorus) or protective compounds (phosphates, hydroxyapatite) are applied in the last time [4–7]. Electrochemical anodic or cathodic deposition of the oxide layers is an important, cheap, efficient method to increase the protective and osseointegrative properties of the titanium alloys; oxide nanotubes are formed on the alloy surface being a good matrix for bone cell colonization [8].

Electrochemical potentiostatic anodization technique was performed on Ti and its alloys in different solutions, and controlling the polarization parameters, the bioactive TiO_2 nanotubes were obtained enhancing the alloy biocompatibility [9–14].

Electrochemical galvanostatic anodization method was accomplished on Ti and some of its binary, ternary, and

quaternary alloy surfaces using especially acidic solutions; varying solution composition, pH, temperature, and anodizing parameters, biofunctionalized surfaces were realized [15–17].

To obtain a biocompatible surface is a complex problem because must be an alloy containing only nontoxic, nonallergic, biocompatible elements, having very good mechanical properties and then must be taken into consideration the most favorable method adapted for the improvement of its bioactivity.

In this paper, a new Ti-15Zr-5Nb alloy was elaborated to satisfy the most important requirements of an implant material; this alloy (containing only nontoxic and nonallergic elements) has an $\alpha + \beta$ microstructure, type Widmanstätten, a low Young's modulus (82.69 GPa), and a good correlation between its mechanical properties and corrosion resistance. Its biocompatibility and anticorrosive properties were enhanced by galvanostatic anodization in 0.3 M H_3PO_4 (orthophosphoric acid) solution assuring the formation of a continuous nanostructured layer of protective TiO_2 oxide; this layer incorporated phosphorus as phosphotitanate ($\text{P}_2\text{O}_5^{2-}$) ions, increasing the alloy bioactivity.

2. Experimental Details

2.1. Materials. The new Ti-15Zr-5Nb alloy was obtained by vacuum, cold-crucible, semilevitation melting; alloy composition is (%wt.) 0.011% H_2 ; 0.02% N_2 ; 0.12% O_2 ; 0.052% Mg; 0.00235% Ca; 0.00831% Cr; 0.02048% Fe; 0.0077% Ni; 0.0181% Ta; 14.97% Zr; 5.11% Nb; balance Ti. From as-cast ingots were cut cylindrical samples for experiments.

2.2. Electrodeposition of the Nanostructured Oxide Layer. Before the anodic galvanostatic processing, the samples were ground with metallographic paper till 2000 grade to eliminate any surface defects and then were ground with metallographic paper of 600 grades to assure the necessary roughness and were washed with bidistilled water. Then, the samples were ultrasonically degreased in acetone and bidistilled water (for 15 min), dried in air, and fixed in a Stern-Makrides mount system. The anodic galvanostatic polarization was applied by a DC power source (MATRIX, China) that supplied current densities of 5 mA/cm^2 and 10 mA/cm^2 between the working electrode (Ti-15Zr-5Nb alloy) and auxiliary electrode (Pt); these current densities were constantly maintained for different time periods of 15, 30, 45, and 60 min. The anodization solution was orthophosphoric acid (H_3PO_4) of 0.3 M and 1 M concentrations; three processing parameters were varied: the solution concentration, current density, and time; different oxide layers were obtained and the nanostructured surface with the most favorable structural and morphological properties was selected and its electrochemical behaviour, corrosion stability, and long-term behaviour in different simulated physiological solutions were studied.

2.3. Characterization of the Nanostructured Oxide Layer. Composition of the obtained layers was verified by Raman microscopy and Fourier transform infrared (FT-IR) analysis.

Raman spectra were measured at room temperature using a LABRam Jobin Yvon (Japan) equipment. Acquisition time was 40 s; the green line ($\lambda = 514.5 \text{ nm}$) of Ar^+ laser was used to excite Raman spectra at a power of $\sim 20 \text{ mW}$. Measurements were carried out under a microscope, with a 90x microscope objective; the laser spot size was around $1\text{--}2 \mu\text{m}$. Raman measurements covered the range between 100 and 1100 cm^{-1} .

FT-IR spectra were registered as a resolution of 4 cm^{-1} , over the frequency range from 1400 to 600 cm^{-1} , using a spectrophotometer model Nicolet 6700 FTIR (USA). The spectra were taken from thin transparent ($\sim 20 \text{ mg/cm}^2$) KBr pellets containing approximately 0.5% wt samples. Pellets were prepared by compacting and vacuum pressing of an intimate mixture obtained by grinding 1 mg of substance in 200 mg KBr.

The morphology, microstructure, and elemental composition of the nanostructured electrodeposited layer were analyzed by scanning electron microscopy (SEM) using a Quanta 3D FEG apparatus (The Nederland) working at an accelerating voltage of 20 kV and equipped with an energy dispersive X-ray (EDX) spectrometer.

2.4. Electrochemical Behaviour of Bare and Anodized Ti-15Zr-5Nb Alloys. The electrochemical behaviour of the anodized Ti-15Zr-5Nb alloy was examined in comparison with the bare alloy in Ringer solution of different pH values (acid pH = 3.21, obtained by HCl addition; neutral pH = 7.58, normal; alkaline pH = 8.91, obtained by KOH addition) that simulate the severe functional conditions from the human body: in the case of surgery, the pH decreases till 3–4 value [18, 19] and must long time to come back to 7.4 value; in the case of inflammations or infections, the pH can increase till 9 value [20]. Ringer solution composition was (g/L) NaCl—6.8; KCl—0.4; CaCl_2 —0.2; $\text{MgSO}_4 \cdot 7\text{H}_2\text{O}$ —0.2048; $\text{NaH}_2\text{PO}_4 \cdot \text{H}_2\text{O}$ —0.1438; NaHCO_3 —1.1; glucose—1. The working temperature was $37^\circ \pm 1^\circ \text{C}$.

The electrochemical behaviour was studied by cyclic potentiodynamic polarization method and electrochemical impedance spectroscopy (EIS).

The cyclic potentiodynamic measurements were applied beginning from -0.5 V till $+2 \text{ V}$ (versus saturated calomel electrode, SCE) at a scan rate of 1 mV/s . Voltalab 80 equipment (Radiometer, France) with its VoltaMaster 4 program was used. From voltammograms, the main electrochemical parameters that characterize the bare and anodized Ti-15Zr-5Nb alloy behaviour were determined: E_{corr} —corrosion potential (like zero current potential); E_p —passivation potential (the potential value at which the current becomes constant); $|E_{\text{corr}} - E_p|$ —tendency to passivation (low values show a rapid, easy passivation); ΔE_p —passive potential range (potential range for constant current, plateau range; larger potential range proves a more resistant material); i_p —passive current density (lower values indicate a more protective passive layer).

EIS measurements were carried out at open circuit potential- E_{oc} with the same VoltaLab 80 equipment; Nyquist and Bode spectra were recorded applying sine wave of 5 mHz in the frequency range from 100 mHz to 100 kHz, with 7

points per decade. The electric equivalent circuit was fitted using nonlinear least square ZVIEW program.

2.5. Corrosion Stability of Bare and Anodized Ti-15Zr-5Nb Alloys. Linear polarization measurements were performed for ± 50 mV around the open circuit potential at a scan rate of 1 mV/s, using the same Voltalab 80 equipment. From Tafel representation, the VoltaMaster 4 program directly supplied the values of the corrosion current density— i_{corr} , corrosion rate— V_{corr} , and polarization resistance— R_p ; the total quantity (ng/cm^2) of ions released in biofluid was calculated [21, 22] as

$$\text{Ion release} = 1.016 \cdot V_{\text{corr}} \cdot 10^5, \quad (1)$$

where V_{corr} = corrosion rate in mm/year.

2.6. Long-Term Behaviour of Bare and Anodized Ti-15Zr-5Nb Alloys. The long-term behaviour of bare and anodized alloys was monitored by the measurements of the open circuit potentials— E_{oc} (with a performing Hewlett-Packard multimeter) at regular time periods, till 1500 soaking hours in Ringer solutions. The shift of E_{oc} to more positive values shows the increase of the thickness of oxide passive film and lower corrosion rate [23]. The decrease of E_{oc} value suggests dissolution processes at the interface and its subsequent increase, the formation of new oxide layer [23]. Also, taking into consideration that the human biofluid pH can vary from acid to alkaline values, different pH values can appear along the implant surface; thus, E_{oc} will have various values on different zones of the implant, producing potential gradients— ΔE_{oc} —that can initiate galvanic cells and can accelerate the implant corrosion; simulating these conditions, the following gradients were calculated [24–26]:

$$\begin{aligned} \Delta E_{\text{oc1}}(\text{pH}) &= E_{\text{oc}}^{\text{pH} = 3.21} - E_{\text{oc}}^{\text{pH} = 7.58}, \\ \Delta E_{\text{oc2}}(\text{pH}) &= E_{\text{oc}}^{\text{pH} = 3.21} - E_{\text{oc}}^{\text{pH} = 8.91}, \\ \Delta E_{\text{oc3}}(\text{pH}) &= E_{\text{oc}}^{\text{pH} = 7.58} - E_{\text{oc}}^{\text{pH} = 8.91}. \end{aligned} \quad (2)$$

Also, the time variations of ΔE_{oc} values were registered with the aim of evaluating the possible susceptibility to galvanic or local corrosion.

3. Results and Discussion

3.1. Characterization of the Alloy Nanostructured Surface. Composition of the electrodeposited layer was determined from Raman spectra and FT-IR analysis. The morphology, microstructure, and elemental composition of the surface layer were analyzed by SEM and EDX methods.

3.1.1. Characterization of the Alloy Surface Galvanostatically Anodized in 0.3 M H_3PO_4 for 45 min. at a Current Density of 10 mA/cm². SEM observations of the alloy surface after galvanostatic anodization (Figure 1) revealed the formation of a layer showing two hierarchical features: hill-like protuberances with a typical width between 5 and 10 μm (Figure 1(a)),

where the layer is locally thicker, and nanotube-like porosity with diameters in the one to a few hundred nanometers (Figure 1(b)). The chemical analysis by EDX determined that the nanostructured layer contains significant amount of P and O, as well as the constituent alloy elements (Figure 2).

Raman microspectroscopy is especially suitable for the analysis of the presence of oxides [27, 28] and/or phosphates, [29–31] even if present as nanocrystalline or secondary phases in surface layers, difficult to detect by other methods. Raman measurements (Figure 3) clearly showed the existence of titanium oxide with anatase-like structure, indicated by the existence of a strong band at 149 cm^{-1} , coincident with the main E_g vibrational band of anatase. The significant shift from reported values at $\sim 142\text{--}145 \text{ cm}^{-1}$ [27, 28] of different anatase nanoparticles with dimensions between 12 and 30 nm and the width of the main band clearly indicate smaller dimensions of the anatase nanocrystallites nucleated in the anodized surface layer. Besides, the additional spectral features reveal a substantial modification of the crystalline structure of anatase during anodization in H_3PO_4 : the wide bands centered at $\sim 400 \text{ cm}^{-1}$ and at $\sim 600 \text{ cm}^{-1}$ cannot be unambiguously matched with the secondary features of anatase at 395 cm^{-1} (B_{1g}) and 638 cm^{-1} (E_g) [27, 28], while the (A_{1g}) band at 515 cm^{-1} is not present and the E_g band at 195 cm^{-1} is masked by the wide main band. Different authors have reported similar wide Raman bands in titania modified layers containing phosphorus, either as phosphate (PO_4^{3-}) or as pyrophosphate ($\text{P}_2\text{O}_7^{4-}$) groups, embedded in the O–Ti(Nb)–O oxidized surface layer [32, 33] and caused by modification of Ti–O–Ti bonds into P–O–Ti and P–O–P bonds in the oxide lattice. Raman analysis of the anodized surface, on the other hand, found no evidence of the presence of the PO_4^{3-} group characteristic main vibrational band at $\sim 1000 \text{ cm}^{-1}$ [29–31].

Because the sensitivity of Raman method for Ti–O bonding is significantly higher than that for phosphate bonds, we used FT-IR vibrational spectroscopy to investigate the presence of phosphate groups, in order to complete the compositional analysis of the electrodeposited films. The two wide bands, centered at $\sim 800 \text{ cm}^{-1}$ and 1100 cm^{-1} , detected by FT-IR (Figure 4) can only be attributed to the ν_3 bending mode of the P–O–P bonds in phosphotitanate glass oxide, due to the incorporation of P^{5+} ions [33, 34] into the oxide coating, promoted by the acidic conditions.

We can conclude that the layer electrodeposited in 0.3 M H_3PO_4 solution is formed by anatase oxide that contains phosphorus as $\text{P}_2\text{O}_7^{4-}$ ion in phosphotitanate compound, phosphorus being the main inorganic component of the human bone thus stimulating the formation of bone [35]. Also, this nanolayer has a nanotube-like porosity that can provide a good scaffold for the bone cell development [35].

3.1.2. Characterization of the Alloy Surface Galvanostatically Anodized in 1 M H_3PO_4 for 45 min. at a Current Density of 10 mA/cm². The analysis of the galvanostatic anodization Ti-15Zr-5Nb alloy surface by vibrational Raman (Figure 5) and

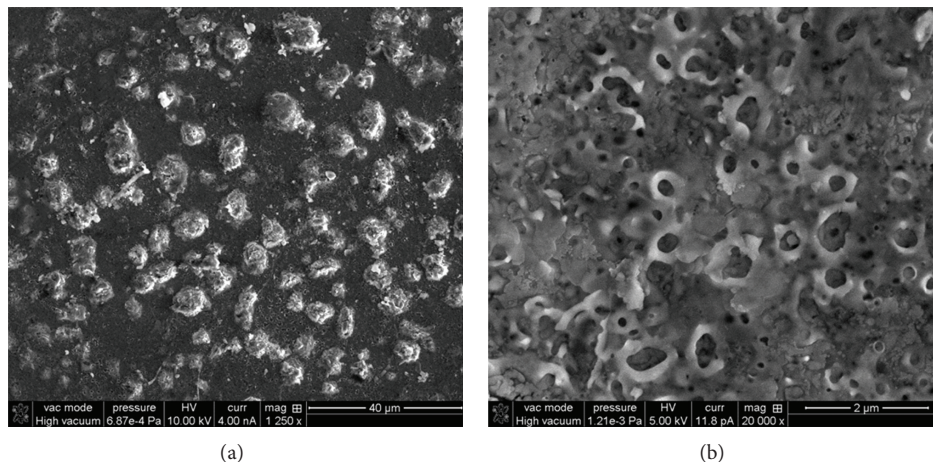


FIGURE 1: SEM micrographs of Ti-15Zr-5Nb alloy surface galvanostatically anodized in 0.3 M H_3PO_4 solution for 45 min. at 10 mA/cm^2 : (a) hill-like protuberances; (b) nanotube-like porosity.

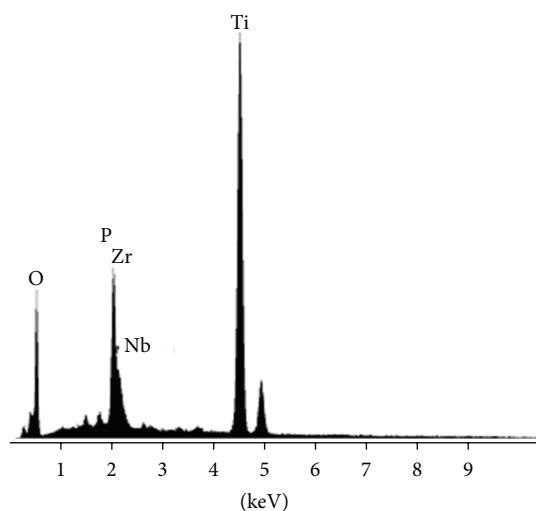


FIGURE 2: EDX spectrum of Ti-15Zr-5Nb alloy surface galvanostatically anodized in 0.3 M H_3PO_4 solution for 45 min. at 10 mA/cm^2 .

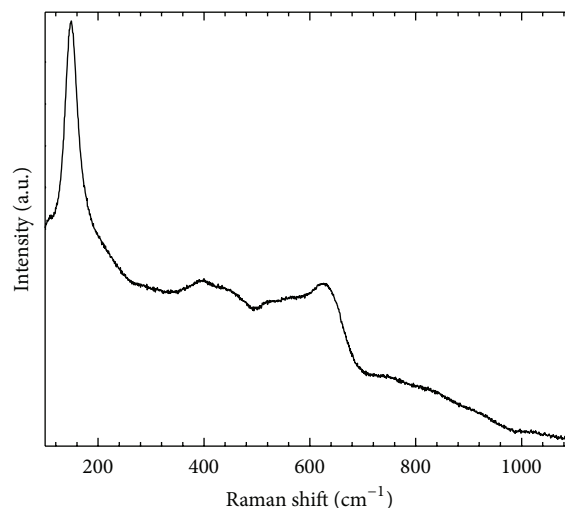


FIGURE 3: Raman spectrum of Ti-15Zr-5Nb alloy surface galvanostatically anodized in 0.3 M H_3PO_4 solution for 45 min. at 10 mA/cm^2 .

FT-IR (Figure 6) spectroscopies detected the same composition of the electrodeposited layer, namely, TiO_2 anatase oxide, modified with phosphorus as pyrophosphate bonds in titania-based oxide.

SEM micrographs (Figure 7) of the sample processed electrochemically in 1 M H_3PO_4 showed the deposition of loose aggregates (Figure 7(b)) of submicron sized particles on top of the porous layer (Figure 7(a)). The additional features have the same composition of the continuous passivating layer, as determined from the EDX analysis (Figure 8). It results in the fact that in 1 M H_3PO_4 solution was obtained a nanolayer with lower microstructural properties.

From the previous experimental results, it appears that the most favorable properties of Ti-15Zr-5Nb alloy surface were obtained by the galvanostatic anodization in 0.3 M H_3PO_4 solution for 45 min. at 10 mA/cm^2 . The electrochemical behaviour, corrosion stability, and long-term behaviour

of the alloy surface processed by this method will be studied later on (named anodized alloy).

3.2. Electrochemical Behaviour of the Bare and Anodized Alloys in Ringer Solutions of Different pH Values. Electrochemical behaviour of the bare and anodized alloys in Ringer solutions of 3.21, 7.58, and 8.91 pH values was determined from cyclic potentiodynamic and EIS measurements.

3.2.1. Electrochemical Behaviour from Cyclic Potentiodynamic Measurements. Cyclic potentiodynamic curves from Figure 9 make evident a nobler behaviour of the anodized alloy than that of the bare one, because all the electrochemical parameters (Table 1) have more favorable values [10, 15]:

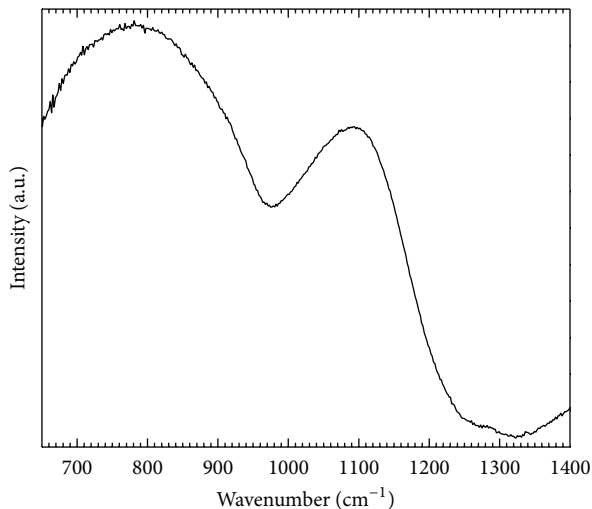


FIGURE 4: FT-IR spectrum of Ti-15Zr-5Nb alloy surface galvanostatically anodized in 0.3 M H_3PO_4 solution for 45 min. at 10 mA/cm^2 .

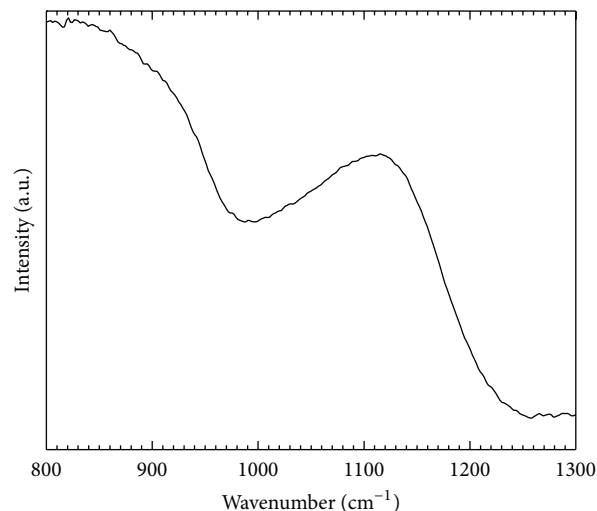


FIGURE 6: FT-IR spectrum of Ti-15Zr-5Nb alloy surface galvanostatically anodized in 1 M H_3PO_4 solution for 45 min. at 10 mA/cm^2 .

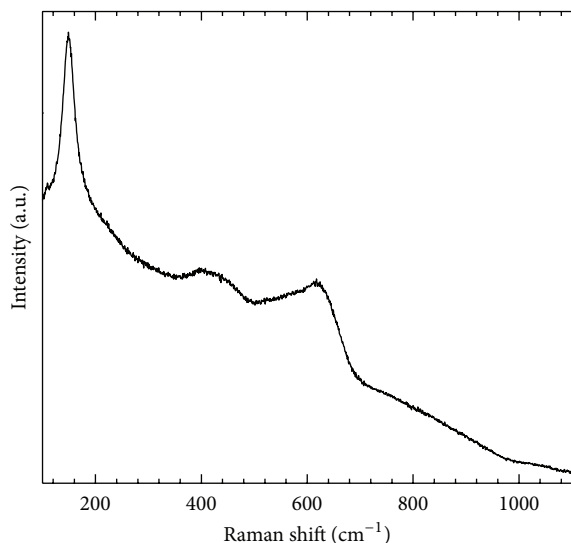


FIGURE 5: Raman spectrum of Ti-15Zr-5Nb alloy surface galvanostatically anodized in 1 M H_3PO_4 solution for 45 min. at 10 mA/cm^2 .

- (i) corrosion, E_{corr} and passivation, E_p potentials have more electropositive values and passive current densities, i_p are lower, showing a more protective, more resistant nanostructured layer on the anodized alloy surface [23],
- (ii) tendency to passivation, $|E_{\text{corr}} - E_p|$, has lower values indicating that the processed alloy is more easily, more rapidly passivated, as a result of the existence of the electrodeposited nanolayer that improves the protective properties of the native passive layer by its thickening [23, 25].

In acid and alkaline Ringer solutions, the main electrochemical parameters presented slightly more unfavorable values both for the bare and the anodized alloys due to the

slight higher aggressivity of these solutions; nevertheless, the anodized alloy revealed a very good passive behaviour.

3.2.2. Electrochemical Behaviour from EIS Measurements.

Nyquist spectra (Z_{real} versus Z_{imag}) exhibited semicircles with large curvature radii (Figure 10) that describe a capacitive behaviour, a resistant passive film [15, 36, 37]. Because the curvature radii have higher values for the anodized alloy, it results in the fact that its passive film is more resistant. The impedance values for the electrochemical anodized alloy exceed two times the values for the bare alloy; these results indicate a very protective nanostructured layer [15, 36, 37].

Bode spectra (phase angle versus $\log f$) displayed both for bare and anodized alloys (Figure 11) phase angles around the value of -90° that represent a capacitive behaviour, a passive film like an electric insulator [16]. Same better behaviour of the anodized alloy than that of the bare one resulted:

- (i) in Ringer solution of $\text{pH} = 3.21$; the bare alloy presents two phase angles at -81° and -79° , and the anodized one higher values at -83° and -81° that denote a better capacitive behaviour for the nanostructured alloy;
- (ii) in Ringer solution of $\text{pH} = 7.58$; the phase angles have values of -84° and -80° for the bare alloy and of -86° and -82° for the anodized alloy, namely, a more insulating passive film existing on the nanostructured alloy surface;
- (iii) in Ringer solution of $\text{pH} = 8.91$; values of -79° and -76° were registered for the bare alloy and of -81° and -78° for the anodized alloy.

Those two phase angles indicate a protective film formed by two layers: an inner barrier insulating layer characterized by the higher phase angle in the low frequency range and an outer porous layer represented by the lower phase angle in the intermediate frequency range; through this porous

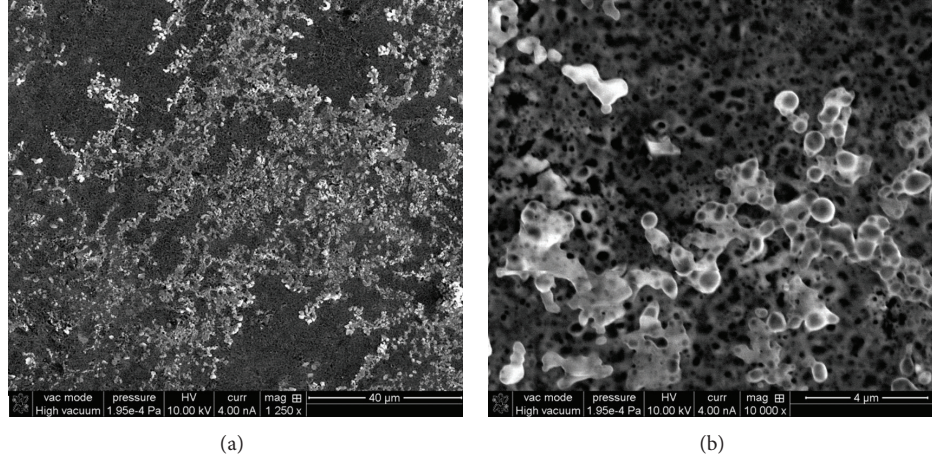


FIGURE 7: SEM micrographs of Ti-15Zr-5Nb alloy surface galvanostatically anodized in 1 M H_3PO_4 solution for 45 min. at 10 mA/cm^2 .

TABLE 1: Main electrochemical parameters for bare and anodized Ti-15Zr-5Nb alloys obtained in Ringer solutions at 37°C .

Ti-15Zr-5Nb	E_{corr} (mV)	E_p (mV)	ΔE_p (mV)	$ E_{\text{corr}} - E_p $ (mV)	i_p ($\mu\text{A/cm}^2$)
Ringer pH = 3.21					
Bare	-350	-200	>2000	150	3.9
Anodized	-250	-150	>2000	100	1.9
Ringer pH = 7.58					
Bare	-200	0	>2000	200	1.0
Anodized	-100	0	>2000	100	0.9
Ringer pH = 8.91					
Bare	-350	-200	>2000	150	4.1
Anodized	-200	-100	>2000	100	2.0

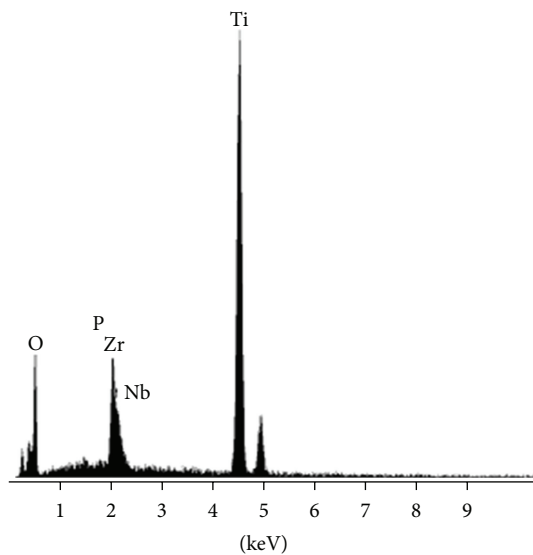


FIGURE 8: EDX spectrum of Ti-15Zr-5Nb alloy surface galvanostatically anodized in 1 M H_3PO_4 solution for 45 min.

layer can penetrate the aggressive ions from the physiological solutions and can corrode the inner compact layer, but, in

the same time, in these pores can be incorporated calcium and phosphorous ions from biofluid that can provide a good scaffold for the bone cell adhesion [38].

According to the literature [39, 40], an electric equivalent circuit with two time constants (Figure 12) was modeled: the first time constant illustrates the inner barrier layer by its resistance, R_b , and capacitance, CPE_b ; the second time constant refers to the outer porous layer by its resistance, R_p , and capacitance, CPE_p .

The inner barrier layer resistances, R_b , and the porous layer resistances, R_p , of the anodized alloy are higher than those of the bare one (Table 2), showing that the galvanostatic processing generated a more resistant nanolayer; this fact is confirmed by the values of the frequency independent parameters n_1 and n_2 which are bigger for the processed alloy, indicating a better capacitor ($n = 1$ represents an ideal capacitor), namely, superior protective properties [39]. Barrier layer resistances, R_b , for both bare and anodized alloys have values of about 100 times higher than those of the porous layer, R_p , proving that the barrier layer assures the alloy good resistance against the physiological solution aggressivity [41, 42]; on the other hand, lower values of R_p denote that the porous layer has inferior protective properties, permitting the diffusion and incorporation of the ions from the biofluid through and into this layer [36, 43]; thus, this porous layer

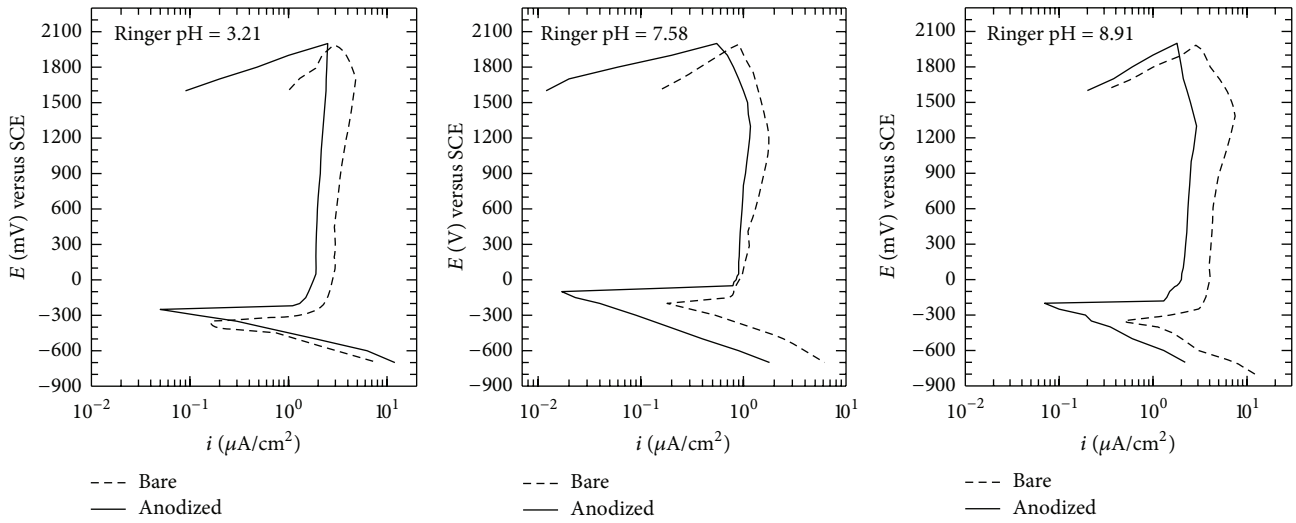


FIGURE 9: Cyclic potentiodynamic curves for bare and anodized Ti-15Zr-5Nb alloys recorded in Ringer solutions at 37°C.

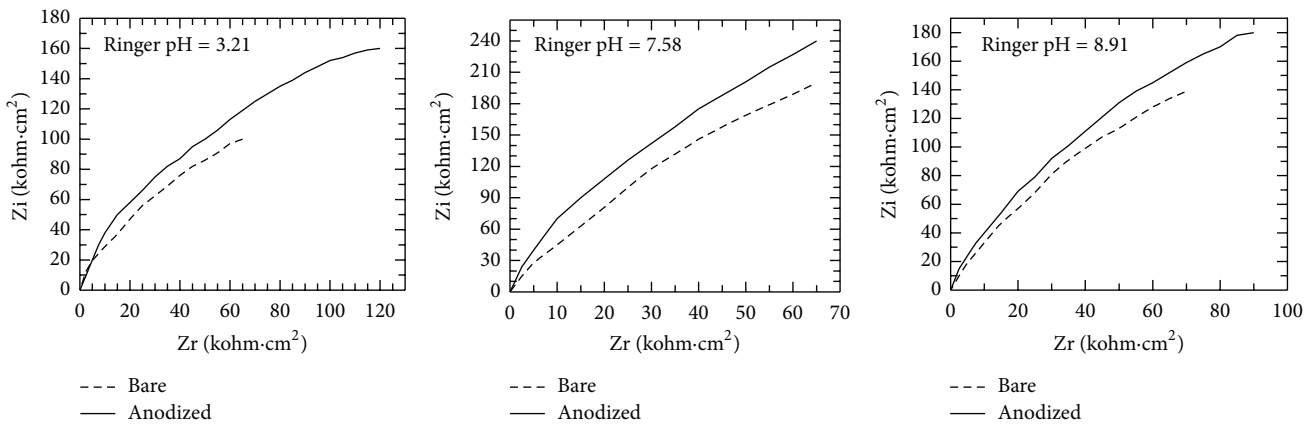


FIGURE 10: Nyquist spectra for bare and anodized Ti-15Zr-5Nb alloys recorded in Ringer solutions at 37°C.

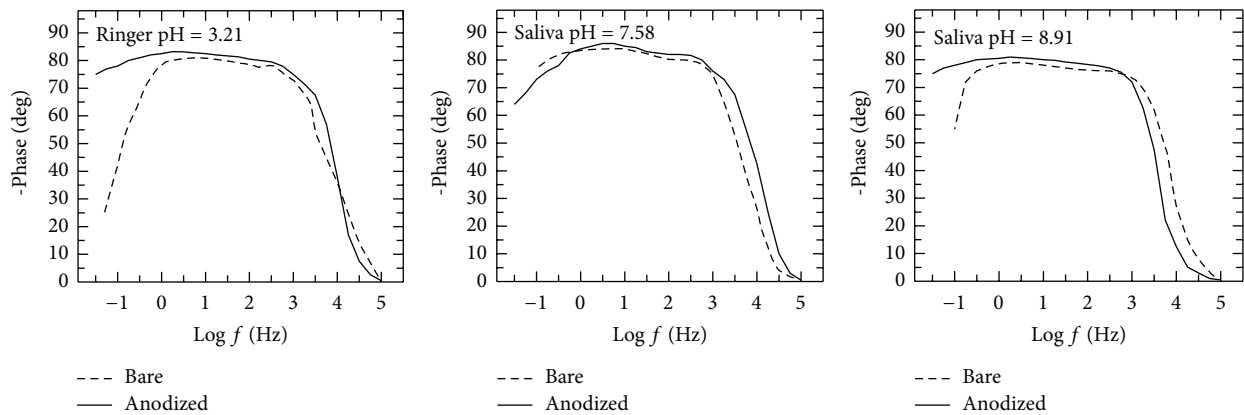


FIGURE 11: Bode spectra for bare and anodized Ti-15Zr-5Nb alloys recorded in Ringer solutions at 37°C.

TABLE 2: Fitting parameters of the two time constants electric equivalent circuit.

Ti-15Zr-5Nb	R_{sol} ($\Omega \cdot \text{cm}^2$)	R_b ($\Omega \cdot \text{cm}^2$)	CPE_b ($S \cdot s^n \cdot \text{cm}^{-2}$)	$n1$	R_p ($\Omega \cdot \text{cm}^2$)	CPE_p ($S \cdot s^n \cdot \text{cm}^{-2}$)	$n2$
Ringer pH = 3.21							
Bare	14.2	7.3×10^6	2.2×10^{-6}	0.96	1.2×10^4	2.5×10^{-5}	0.90
Anodized	14.8	8.7×10^6	1.8×10^{-6}	0.98	1.5×10^4	2.6×10^{-5}	0.91
Ringer pH = 7.58							
Bare	13.6	8.1×10^6	2.0×10^{-6}	0.97	1.8×10^4	2.1×10^{-5}	0.91
Anodized	15.1	9.9×10^6	1.6×10^{-6}	0.99	1.9×10^4	2.3×10^{-5}	0.93
Ringer pH = 8.91							
Bare	14.5	6.2×10^6	2.3×10^{-6}	0.95	1.6×10^4	2.6×10^{-5}	0.90
Anodized	14.9	8.3×10^6	1.9×10^{-6}	0.97	1.7×10^4	2.7×10^{-5}	0.92

TABLE 3: Main corrosion parameters for bare and anodized Ti-15Zr-5Nb alloys obtained in Ringer solutions at 37°C.

Ti-15Zr-5Nb	i_{corr} ($\mu\text{A}/\text{cm}^2$)	V_{corr} ($\mu\text{m}/\text{Y}$)	Resistance class	Ion release (ng/cm^2)	R_p ($\text{k}\Omega \cdot \text{cm}^2$)
Ringer pH = 3.21					
Bare	0.081	0.751	PS	76.3	330
Anodized	0.029	0.269	PS	27.33	1295
Ringer pH = 7.58					
Bare	0.039	0.358	PS	36.4	397
Anodized	0.0054	0.050	PS	5.08	3020
Ringer pH = 8.91					
Bare	0.071	0.657	PS	66.75	305
Anodized	0.019	0.175	PS	17.78	1380

PS: perfect stable.

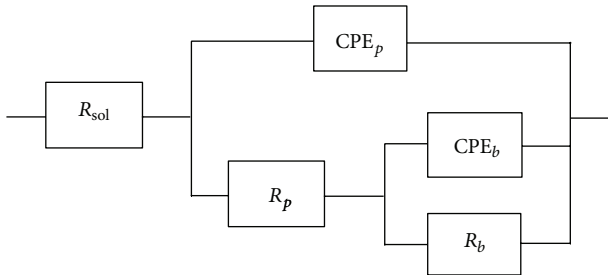


FIGURE 12: Electric equivalent circuit with two time constants.

provides the necessary conditions for the interactions of the alloy with human fluid, namely, the bioactivity of the surface layer [43].

3.3. Corrosion Stability of the Bare and Anodized Alloys in Ringer Solutions of Different pH Values. The corrosion stability of the bare and anodized alloys was appreciated from the values of the corrosion current densities, i_{corr} , corrosion, V_{corr} , and ion release rates and polarization resistances, R_p (Table 3), obtained from Tafel representations. The main corrosion parameters have better values for the anodized alloy than those for the bare one:

- (i) corrosion current densities, i_{corr} , corrosion, V_{corr} , and ion release rates have lower values that show a better resistance to corrosion and implicitly a more reduced

quantity of ions released in biofluid, namely, a lower toxicity [21, 22];

- (ii) polarization resistance, R_p , has higher values (of about 10 times, order $\text{M}\Omega \cdot \text{cm}^2$) that prove a more resistant layer [23, 25].

Though, in acid and alkaline Ringer solutions, both the bare and the anodized alloys have a little higher corrosion rates, their values are placed in the “Perfect Stable” resistance class, indicating a very good anticorrosive resistance. The best corrosion resistance for the processed alloy resulted in neutral Ringer solution, normal conditions from the human body.

3.4. Long-Term Behaviour of the Bare and Anodized Alloys in Ringer Solutions of Different pH Values. The long-term behaviour of the bare and anodized alloys was determined from the monitoring of the open circuit potentials, E_{oc} , and corresponding open circuit potential gradients, ΔE_{oc} , for 1500 soaking hours in Ringer solutions of acid (3.21), neutral (7.58), and alkaline (8.91) pH values (Figure 13).

The open circuit potentials for the anodized alloy shifted to more positive values in time, showing the increase of its protective nanolayer thickness [23]. E_{oc} had more electropositive values for the anodized alloy than those for the bare one, which reveal more protective nanolayers [15, 16, 23]. Also, these potentials reached almost constant values after about 700 h, demonstrating more resistant, stable state [23].

The open circuit potential gradients, ΔE_{oc} , have very low values (Table 4) that cannot generate galvanic corrosion.

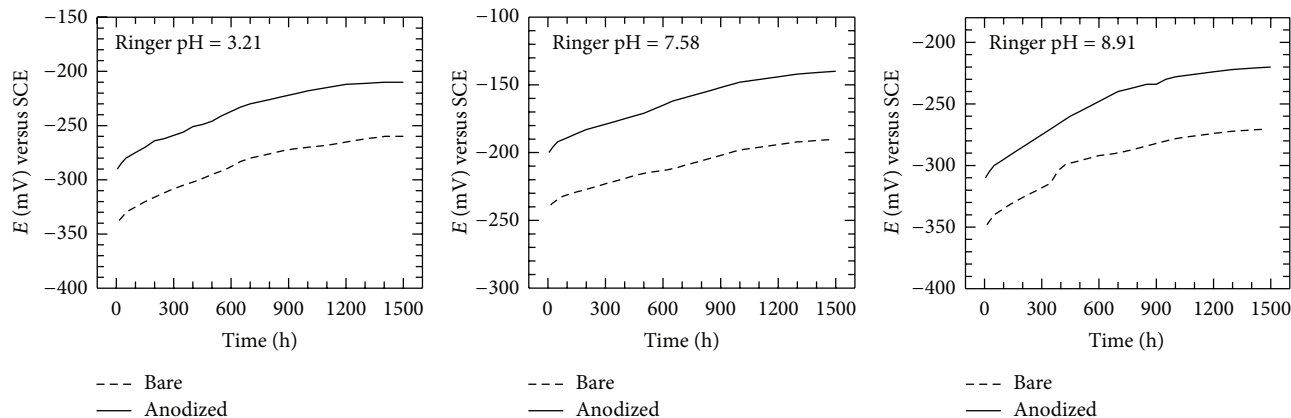


FIGURE 13: Monitoring of the open circuit potentials for bare and anodized Ti-15Zr-5Nb alloy in Ringer solutions at 37°C.

TABLE 4: Potential gradients for bare and anodized Ti-15Zr-5Nb alloys obtained in Ringer solutions at 37°C.

Ti-15Zr-5Nb	Time (h)	ΔE_{oc1} (mV)	ΔE_{oc2} (mV)	ΔE_{oc3} (mV)
Bare	24	-98	+10	+108
	500	-80	+10	+81
	1000	-72	+8	+80
	1500	-70	+10	+80
Anodized	24	-89	+20	+20
	500	-75	+10	+41
	1000	-70	+10	+80
	1500	-70	+10	+80

Many authors [44, 45] showed that only differences of 600–700 mV can initiate and maintain galvanic cells; therefore, both the bare and the anodized alloys cannot corrode by galvanic corrosion, even in the case of large differences in the biofluid pH values between 3.21 and 8.91 (ΔE_{oc2}) that could appear on the alloy surface in its long-term “working life” as implant.

4. Conclusions

The new Ti-15Zr-5Nb alloy surface was nanostructured by galvanostatic anodization in 0.3 M H_3PO_4 solution. The obtained layer has a nanotube-like porosity, revealed by SEM, and it is formed of anatase-like small crystallites, with added phosphorus as phosphotitanate, determined by Raman spectroscopy, FT-IR, and EDX analyses; this composition can stimulate the formation of the bone and the porosity can offer a good scaffold for the bone cell attachment. Cyclic potentiodynamic curves make evident a nobler behaviour of the anodized alloy than that of the bare one, as a result of the existence of the nanostructured layer that improves the protective properties of the native passive film by its thickening. EIS spectra revealed a better capacitive behaviour, a more insulating protective film electrodeposited on the alloy surface; the nanostructured film is formed by two layers: an inner barrier layer that assures the alloy very good

anticorrosive resistance and an outer porous layer that can provide the good conditions for the bone cell adhesion. Corrosion and ion release rates have lower values showing a better resistance to corrosion and implicitly a more reduced quantity of ions released in biofluid, namely, a lower toxicity of the anodized alloy. The open circuit potentials for the nanostructured alloy shifted to more positive values in time, indicating the increase of its protective layer thickness. The open circuit potential gradients have very low values that cannot generate galvanic corrosion.

Acknowledgments

This work was supported by Romanian UEFISCDI, Project no. IDEI 278/2010. Also, support of the EU (ERDF) and Romanian Government Infrastructure POS-CCE O 2.2.1 project INFRANANOCHEM no. 19/2009 is gratefully acknowledged.

References

- [1] P. K. Zysset, X. E. Guo, C. E. Hoffler, K. E. Moore, and S. A. Goldstein, “Mechanical properties of human trabecular bone lamellae quantified by nanoindentation,” *Technology and Health Care*, vol. 6, no. 5-6, pp. 429–432, 1998.
- [2] E. Eisenbarth, D. Velten, M. Müller, R. Thull, and J. Brems, “Biocompatibility of β -stabilizing elements of titanium alloys,” *Biomaterials*, vol. 25, no. 26, pp. 5705–5713, 2004.
- [3] P. Thomsen, C. Larsson, L. E. Ericson, L. Sennerby, J. Lausmaa, and B. Kasemo, “Structure of the interface between rabbit cortical bone and implants of gold, zirconium and titanium,” *Journal of Materials Science: Materials in Medicine*, vol. 8, no. 11, pp. 653–665, 1997.
- [4] S. Tanaka, H. Tobimatsu, Y. Maruyama, T. Tanaki, and G. Jerkiewicz, “Preparation and characterization of microporous layers on titanium,” *ACS Applied Materials & Interfaces*, vol. 1, no. 9, pp. 2312–2319, 2009.
- [5] A. Zeller, A. Musyanovych, M. Kappl et al., “Nanostructured coatings by adhesion of phosphonated polystyrene particles onto titanium surface for implant material applications,” *ACS Applied Materials & Interfaces*, vol. 2, no. 8, pp. 2421–2428, 2010.

- [6] A. Nakahira, T. Kubo, and C. Numako, "TiO₂-derived titanate nanotubes by hydrothermal process with acid treatments and their microstructural evaluation," *ACS Applied Materials & Interfaces*, vol. 2, no. 9, pp. 2611–2616, 2010.
- [7] P. He, J. Tao, J. Xue, and Y. Chen, "Cytotoxicity property of nano-TiO₂ sol and nano-TiO₂ powder," *Journal of Nanomaterials*, vol. 2011, Article ID 261605, 8 pages, 2011.
- [8] J. Park, S. Bauer, K. Von Der Mark, and P. Schmuki, "Nanosize and vitality: TiO₂ nanotube diameter directs cell fate," *Nano Letters*, vol. 7, no. 6, pp. 1686–1691, 2007.
- [9] T. Dey, P. Roy, B. Fabry, and P. Schmuki, "Anodic mesoporous TiO₂ layer on Ti for enhanced formation of biomimetic hydroxyapatite," *Acta Biomaterialia*, vol. 7, no. 4, pp. 1873–1879, 2011.
- [10] H. H. Park, I. S. Park, K. S. Kim et al., "Bioactive and electrochemical characterization of TiO₂ nanotubes on titanium via anodic oxidation," *Electrochimica Acta*, vol. 55, no. 20, pp. 6109–6114, 2010.
- [11] Y. Shibata, D. Suzuki, S. Omori et al., "The characteristics of in vitro biological activity of titanium surfaces anodically oxidized in chloride solutions," *Biomaterials*, vol. 31, no. 33, pp. 8546–8555, 2010.
- [12] F. M. B. Hassan, H. Nanjo, S. Venkatachalam, M. Kanakubo, and T. Ebina, "Effect of the solvent on growth of titania nanotubes prepared by anodization of Ti in HCl," *Electrochimica Acta*, vol. 55, no. 9, pp. 3130–3137, 2010.
- [13] E. Peláez-Abellán, L. Rocha-Sousa, W. D. Müller, and A. C. Guastaldi, "Electrochemical stability of anodic titanium oxide films grown at potentials higher than 3 V in a simulated physiological solution," *Corrosion Science*, vol. 49, no. 3, pp. 1645–1655, 2007.
- [14] J. C. Mirza Rosca, M. V. Popa, E. Vasilescu, P. Drob, C. Vasilescu, and S. I. Drob, "Effects of electrochemical and thermal oxidation on the behaviour of some biomaterials in simulated body fluids," *Revue Roumaine de Chimie*, vol. 55, no. 10, pp. 639–646, 2010.
- [15] R. Narayanan and S. K. Seshadri, "Phosphoric acid anodization of Ti-6Al-4V—structural and corrosion aspects," *Corrosion Science*, vol. 49, no. 2, pp. 542–558, 2007.
- [16] S. K. Poznyak, A. D. Lisenkov, M. G. S. Ferreira, A. I. Kulak, and M. L. Zheludkevich, "Impedance behaviour of anodic TiO₂ films prepared by galvanostatic anodisation and powerful pulsed discharge in electrolyte," *Electrochimica Acta*, vol. 76, pp. 453–461, 2012.
- [17] Z. Li, C. Ning, D. Ding, H. Liu, and L. Huang, "Biological properties of Ti-Nb-Zr-O nanostructures grown on Ti₃₅Nb₅Zr alloy," *Journal of Nanomaterials*, vol. 2012, Article ID 834042, 7 pages, 2012.
- [18] T. Hanawa, "In vivo metallic biomaterials and surface modification," *Materials Science and Engineering A*, vol. 267, no. 2, pp. 260–266, 1999.
- [19] Z. Cai, H. Nakajima, M. Woldu, A. Berglund, M. Bergman, and T. Okabe, "In vitro corrosion resistance of titanium made using different fabrication methods," *Biomaterials*, vol. 20, no. 2, pp. 183–190, 1999.
- [20] R. Van Noort, "Titanium: the implant material of today," *Journal of Materials Science*, vol. 22, no. 11, pp. 3801–3811, 1987.
- [21] E. Vasilescu, P. Drob, D. Raducanu et al., "Effect of thermo-mechanical processing on the corrosion resistance of Ti6Al4V alloys in biofluids," *Corrosion Science*, vol. 51, no. 12, pp. 2885–2896, 2009.
- [22] E. Vasilescu, P. Drob, D. Raducanu et al., "In vitro biocompatibility and corrosion resistance of a new implant titanium base alloy," *Journal of Materials Science: Materials in Medicine*, vol. 21, no. 6, pp. 1959–1968, 2010.
- [23] D. J. Blackwood, A. W. C. Chua, K. H. W. Seah, R. Thampuran, and S. H. Teoh, "Corrosion behaviour of porous titanium-graphite composites designed for surgical implants," *Corrosion Science*, vol. 42, no. 3, pp. 481–503, 2000.
- [24] M. V. Popa, I. Demetrescu, E. Vasilescu et al., "Corrosion susceptibility of implant materials Ti-5Al-4V and Ti-6Al-4Fe in artificial extra-cellular fluids," *Electrochimica Acta*, vol. 49, no. 13, pp. 2113–2121, 2004.
- [25] V. D. Cojocaru, D. Raducanu, I. Cinca et al., "Improvement of the corrosion resistance and structural and mechanical properties of a titanium base alloy by thermo-mechanical processing," *Materials and Corrosion*, 2012.
- [26] M. V. Popa, I. Demetrescu, S. H. Suh et al., "Monitoring of titanium base alloys-biofluids interface," *Bioelectrochemistry*, vol. 71, no. 2, pp. 126–134, 2007.
- [27] V. G. Pol, S. H. Kang, J. M. Calderon-Moreno, C. S. Johnson, and M. M. Thackeray, "Autogenic reactions for preparing carbon-encapsulated, nanoparticulate TiO₂ electrodes for lithium-ion batteries," *Journal of Power Sources*, vol. 195, no. 15, pp. 5039–5043, 2010.
- [28] H. C. Choi, Y. M. Jung, and S. B. Kim, "Size effects in the Raman spectra of TiO₂ nanoparticles," *Vibrational Spectroscopy*, vol. 37, no. 1, pp. 33–38, 2005.
- [29] M. V. Popa, J. M. C. Moreno, M. Popa et al., "Electrochemical deposition of bioactive coatings on Ti and Ti-6Al-4V surfaces," *Surface and Coatings Technology*, vol. 205, no. 20, pp. 4776–4783, 2011.
- [30] M. Popa, E. Vasilescu, P. Drob et al., "Biomimetic deposition of nanocrystalline hydroxyapatite coatings on non-allergic Ti-20Nb-10Zr-5Ta and stability of the coated alloy in body fluids," *Journal of American Ceramic Society*, vol. 95, no. 12, pp. 3807–3814, 2012.
- [31] P. N. de Aza, F. Guitian, C. Santos, S. de Aza, R. Cusco, and L. Artus, "Vibrational properties of calcium phosphate compounds. 2. Comparison between hydroxyapatite and β -tricalcium phosphate," *Chemistry of Materials*, vol. 9, no. 4, pp. 916–922, 1997.
- [32] Y. Zhao, G. Zhu, X. Jiao, W. Liu, and W. Pang, "Template synthesis and characterization of a new 2-D layered titanium phosphate," *Journal of Materials Chemistry*, vol. 10, no. 2, pp. 463–467, 2000.
- [33] T. Masui, H. Hirai, N. Imanaka, and G. Y. Adachi, "New sunscreen materials based on amorphous cerium and titanium phosphate," *Journal of Alloys and Compounds*, vol. 408–412, pp. 1141–1144, 2006.
- [34] H. J. De Jager and L. C. Prinsloo, "The dehydration of phosphates monitored by DSC/TGA and in situ Raman spectroscopy," *Thermochimica Acta*, vol. 376, no. 2, pp. 187–196, 2001.
- [35] M. P. Neupane, Y. K. Kim, I. S. Park, S. J. Lee, M. H. Lee, and T. S. Bae, "Effect of electrolyte pH on the structure and in vitro osteoblasts response to anodic titanium oxide," *Metals and Materials International*, vol. 14, no. 5, pp. 607–613, 2008.
- [36] S. L. Assis, S. Wolynec, and I. Costa, "The electrochemical behaviour of Ti-13Nb-13Zr alloy in various solutions," *Materials and Corrosion*, vol. 59, no. 9, pp. 739–743, 2008.
- [37] A. Robin, O. A. S. Carvalho, S. G. Schneider, and S. Schneider, "Corrosion behavior of Ti-xNb-13Zr alloys in Ringer's solution," *Materials and Corrosion*, vol. 59, no. 12, pp. 929–933, 2008.

- [38] R. Z. Legeros, S. Lin, R. Rohanizadeh, D. Mijares, and J. P. Legeros, "Biphasic calcium phosphate bioceramics: preparation, properties and applications," *Journal of Materials Science: Materials in Medicine*, vol. 14, no. 3, pp. 201–209, 2003.
- [39] Y.-H. Jeong, H.-C. Choe, and W. A. Brantley, "Electrochemical and surface behavior of hydroxyapatite/Ti film on nanotubular Ti-35Nb-xZr alloys," *Applied Surface Science*, vol. 258, no. 6, pp. 2129–2136, 2012.
- [40] M. T. Woldemedhin, D. Raabe, and A. W. Hassel, "Characterization of thin anodic oxides of Ti-Nb alloys by electrochemical impedance spectroscopy," *Electrochimica Acta*, vol. 82, pp. 324–332, 2012.
- [41] I. Milošev, T. Kosec, and H. H. Strehblow, "XPS and EIS study of the passive film formed on orthopaedic Ti-6Al-7Nb alloy in Hank's physiological solution," *Electrochimica Acta*, vol. 53, no. 9, pp. 3547–3558, 2008.
- [42] V. A. Alves, R. Q. Reis, I. C. B. Santos et al., "In situ impedance spectroscopy study of the electrochemical corrosion of Ti and Ti-6Al-4V in simulated body fluid at 25°C and 37°C," *Corrosion Science*, vol. 51, no. 10, pp. 2473–2482, 2009.
- [43] S. Tamilselvi and N. Rajendran, "In vitro corrosion behaviour of Ti-5Al-2Nb-1Ta alloy in Hanks solution," *Materials and Corrosion*, vol. 58, no. 4, pp. 285–289, 2007.
- [44] E. Blasco-Tamarit, A. Igual-Muñoz, J. G. Antón, and D. M. García-García, "Galvanic corrosion of titanium coupled to welded titanium in LiBr solutions at different temperatures," *Corrosion Science*, vol. 51, no. 5, pp. 1095–1102, 2009.
- [45] G. Sheela, M. Ramasamy, C. R. K. Rao, and M. Pushpanam, "Electrochemical assessment on corrosion behaviour of electrochemically joined dissimilar metal joints," *Bulletin of Electrochemistry*, vol. 17, no. 8, pp. 347–350, 2001.

Research Article

Effect of SPIO Nanoparticle Concentrations on Temperature Changes for Hyperthermia via MRI

Alsayed A. M. Elsherbini¹ and Ahmed El-Shahawy²

¹ Photochemistry and Nanochemistry, National Institute of Laser Enhanced Science (NILES), Cairo University, P.O. Box 12613, Giza, Egypt

² Children's Cancer Hospital, Cairo 57357, Egypt

Correspondence should be addressed to Alsayed A. M. Elsherbini; elsayed@niles.edu.eg

Received 25 November 2012; Accepted 23 February 2013

Academic Editor: Mohamed Bououdina

Copyright © 2013 A. A. M. Elsherbini and A. El-Shahawy. This is an open access article distributed under the Creative Commons Attribution License, which permits unrestricted use, distribution, and reproduction in any medium, provided the original work is properly cited.

Magnetic nanoparticles (MNPs) are being developed for a wide range of biomedical applications. In particular, hyperthermia involves heating the MNPs through exposure to an alternating magnetic field (AMF). These materials offer the potential for selectively heating cancer tissue locally and at the cellular level. This may be a successful method if there are enough particles in a tumor possessing sufficiently high specific absorption rate (SAR) to deposit heat quickly while minimizing thermal damage to surrounding tissue. The current research aim is to study the influence of super paramagnetic iron oxides Fe₃O₄ (SPIO) NPs concentration on the total heat energy dose and the rate of temperature change in AMF to induce hyperthermia in *Ehrlich* carcinoma cells implanted in female mice. The results demonstrated a linearly increasing trend between these two factors.

1. Introduction

Hyperthermia offers an attractive approach for the treatment of cancer as a local therapy. It is associated with fewer side effects in comparison to chemotherapy and radiotherapy, and it can be used in combination with all conventional treatment modalities. But hyperthermia has not yet been established in clinical routine; this is mostly not due to a general lack of efficacy but rather to the limitations of the currently available techniques with respect to selectively targeting the tumor region and homogeneously distributing the heat within the tumor [1].

Magnetic induced interstitial hyperthermia addresses these shortcomings, especially for deep-seated and poorly accessible tumors. For this application, MNPs exhibiting super paramagnetic behavior at room temperature are preferred because they do not retain any magnetism after removal of the magnetic field. Furthermore, the particles must have combined properties of high magnetic saturation, biocompatibility, and interactive functions at the surfaces. Among them, iron oxide particles such as magnetite (Fe₃O₄)

or its oxidized form maghemite (γ -Fe₂O₃) are by far the most commonly employed in biomedical applications, since their biocompatibility has already been proven by Schwertmann, 1991 [2]. Highly magnetic materials such as cobalt and nickel are toxic, susceptible to oxidation and hence are of little interest.

Ideally, in hyperthermia treatment, one would optimize the temperature pattern. However, temperature profiles in biological tissues during hyperthermia depend on the combined influences of applied power and several cooling mechanisms. These mechanisms are difficult to predict, since cooling depends heavily on thermal parameters that vary in time. Therefore, hyperthermia treatment limits to SAR predictions and assumed that a high SAR level will correlate with a high temperature [3].

Previous studies showed that the heating capacity of MNPs can be influenced by many factors; for example, the heating effect of magnetic particles depended strongly on the particles size [4]. The magnetic anisotropy constant can influence the heating mechanism of MNPs [5, 6]. The strength of the applied AMF [7]. On the other hand Portet et al.

demonstrated that the type of surfactant coats the MNPs has influence on the heating capacity of MNPs [8]. The influence of MNPs concentration on the heat energy and hence the temperature change was the interest in this study.

2. Materials and Methods

2.1. Materials. All chemicals used in this study were analytical grade reagents and were used without further purification.

2.2. Methods

2.2.1. Preparation of SPIO NPs Fe_3O_4 . A photochemical method was carried out by dissolving a mixture of ferrioxalate with $FeCl_3 \cdot 6H_2O$ in predetermined concentration ratio in 100 mL of 10% aqueous hydrogen peroxide solution. The pH of the solution was adjusted to 13 by the addition of 1 mL of NaOH. The black precipitates appeared just after the mixing of iron hydroxide with the base solution. These precipitates were collected by magnet, and the product was washed several times with distilled water and finally dried in the air. To increase the stability of SPIO NPs especially *in vivo* conditions, the prepared SPIO NPs were suspended in glycerin medium.

2.2.2. Characterizations

(1) **Transmission Electron Microscopy (TEM).** Transmission electron microscopy of the produced samples was formed by drying a drop of the solution on a carbon-coated copper grid. Particles sizes were determined from the micrographs of the Joel-100S transmission electron microscope of resolution of 0.3 nm.

(2) **X-Ray Diffraction Analysis.** Crystallographic study was performed on iron oxide powder by Rotating Anode X-ray Diffractometer (Rigaku, Japan) using Cu K α radiation. The inter-planer distances (d) were calculated according to Scherrer's equation and were compared to the JCPDS file 2.532X-ray diffraction data in order to deduce the crystal structure.

2.2.3. Preparation of Tumor Bearing Mice. 6–8-week old female Swiss albino mice (20.0 to 29.2 g, median, 26.3 g) were injected with Ehrlich Carcinoma (EAC) from the breeding unit of the Egyptian National Cancer Institute (ENCI). 1×10^6 (EAC) cells/mL were implanted by subcutaneous inoculation to obtain a single grafted tumor. Ehrlich carcinoma cells were implanted in all mice at the same day and under the same conditions. During implantation mice were anesthetized by Fentanyl-dihydrochloride (Fentanyl; Janssen-Cilag, Neuss, Germany) 50 mg/kg body weight. The tumors started to appear within seven days after the day of implantation. Twenty days from the day of implantation, all tumors volumes for all mice were measured by digital caliper in three orthogonal diameters (D_1 , D_2 , and D_3):

$$\text{Tumor Volume} = (D_1 D_2 D_3) \left(\frac{\pi}{6} \right). \quad (1)$$

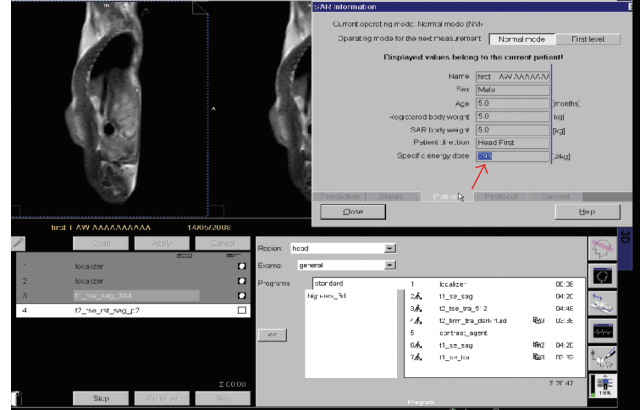


FIGURE 1: Typical photograph of Syngo software: the red arrow refer to SAR value by J/kg.

2.2.4. Experimental Design. After four weeks from the day of tumor implantation and when a grossly visible and palpable mass of the tumor was obtained, the experiments started. The tumors volumes measurements of the selected mice ($n = 60$) revealed no significant difference $P > 0.3$ and the mean initial value of the tumors volumes was $72.5 \pm 3.2 \text{ mm}^3$. The selected mice were classified into two groups as follow.

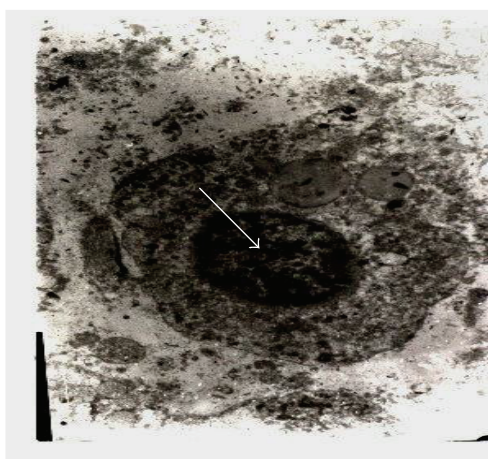
- (i) The 1st group: the mice were not injected by SPIO NPs but subjected to AMF, that is, considered as baseline (control group $n = 10$).
- (ii) The 2nd group: the mice were subjected to AMF after direct injection by SPIO NPs with different concentrations into the region of interest (ROI). This group (SPIO + AMF) in turn was classified into (5 subgroups): the mice in the 1st subgroup ($n = 10$) were injected by 1 mL from magnetic suspension containing $200 \mu\text{g Fe}_3\text{O}_4/\text{kg}$ body weight, the 2nd ($n = 10$) by $400 \mu\text{g}$, the 3rd ($n = 10$) by $600 \mu\text{g}$, the 4th ($n = 10$) by $800 \mu\text{g}$, and the 5th ($n = 10$) by $103 \mu\text{g}$.

Each mouse in these subgroups was subjected to AMF three times at 7, 14, and 21 days from the starting date of the experiment. All factors were fixed in all experiments (field strength, frequency, amplitude, size, and even shape of NPs). The values of total heat energy dose or in other words specific energy dose (SED jg^{-1}) for each concentration in the Ehrlich tumor were monitoring directly during the magnetic resonance imaging (MRI) via highly advanced software (Syngo. NUMARIS/4, Siemens, German) (Figure 1) and consequently the heat deposition rate (HDR $\text{jg}^{-1}\text{s}^{-1}$), maximum temperature achieved in the tumor and the time to maximum temperature (TMT). It is worth mentioning that the injected SPIO NPs were identified inside the tumor by electron microscopic image comparing with the control sample Figure 2. All experiments were approved by the regional animal care committee.

2.2.5. In Vivo Experiment. Four weeks after tumors implantations, mice were anesthetized with 2% to 3% isoflurane



(a)



(b)

FIGURE 2: Transmission electron microscope image of (a) the control sample and (b) the injected SPIO NPs inside the tumor.

through an MR-compatible mobile inhalation system (DRE, Inc., Louisville, KY, USA). Three fiber optical temperature probes which are not RF sensitive (FISO, Inc., Quebec, Canada): the first probe was inserted in the center of the tumor, the second probe was placed immediately adjacent to the tumor periphery, and the third probe was inserted 1 cm inside the rectum. The optical fiber positions were monitored by radiography (Figure 3). After placing the probes, each mouse was centered inside the magnetic field for MRI. To focus the AMF on the region of interest, a surface transmit and receiver radiofrequency (RF) induction coil (inner diameter 7 cm; length 7 cm) specially designed for small animal imaging was placed on the center of tumor area in all experiments. All imaging studies were performed at the Children's Cancer Hospital (CCH), department of radiology, using 1.5-Tesla high field MR scanner (Magnetom, Espree, Siemens, Germany) equipped with high-performance gradients (23 mT/m maximum amplitude 120 T per m per sec maximum slew rate) and fast receiver hardware (bandwidth

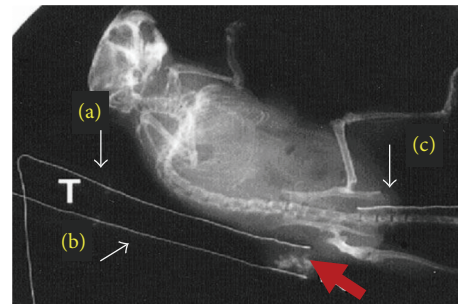


FIGURE 3: X-ray image (top view), T optical fiber thermocouples with measuring junctions located at tumor (a), tumor periphery (b), and at the rectum (c). The tumor was loaded with SPIO nanoparticles (red arrow).

± 500 MHz). All imaging parameters were optimized for all experiments as follow.

Slice thickness = 2 mm; interspaces = 1 mm. Field of view (FOV) = 160 mm, average = 15, matrix = 256×256 , slices = 12 for an acquisition, power = 25 kW, duty = 100%, bandwidth = 9.62 kHz, and the variable factor was only the duration of exposure which was limited between 30 to 40 mins or until the rectal temperature of the mouse reached 41.5°C to prevent unnecessary mortality in the mice due to exposure to excessively high temperatures. All mice were subjected to AMF after 15 minutes from localized injection with SPIO NPs which were directly injected into the central portion of the tumors over a 5 min period; the slow injection rate was necessary because of the high interstitial tumor tissue pressure. The NPs were injected at more than one site to obtain a homogenous distribution. At the end of each experiment, mice were placed on their backs on a warm recovery bed. Each mouse was left until the core (rectal) temperature began to decrease and the probe was removed. When the righting reflex returned, mice were returned to their cages and observed for 48 hours for signs of morbidity. Dead mice were sent to necropsy for examination.

3. Results

3.1. Characterization of MNPs

3.1.1. *Transmission Electron Micrograph (TEM)*. Transmission electron microscopy for the prepared SPIO NPs showed that particles have \sim spherical shapes and their sizes were in the range of $\sim 54 \pm 3$ nm (Figure 4).

3.1.2. *X-Ray Diffraction Analysis*. The XRD spectrum of the prepared SPIO NPs shows six characteristic peaks for Fe_3O_4 ($2\theta = 30.1^\circ, 35.5^\circ, 43.1^\circ, 53.4^\circ, 57.0^\circ, \text{ and } 62.6^\circ$) marked by their indices (220, 311, 400, 422, 511, and 440), respectively (Figure 5).

3.1.3. Heating Capacity of MNPs

(1) *Monitoring SED and HDR*. The mean values reported of the total heat energy dose were $[282.1 \pm 13.8 \text{ Jg}^{-1}]$ for (200 μg),

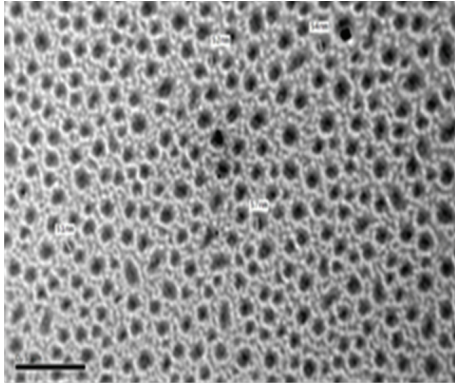


FIGURE 4: Transmission electron microscope of prepared SPIO NPs.

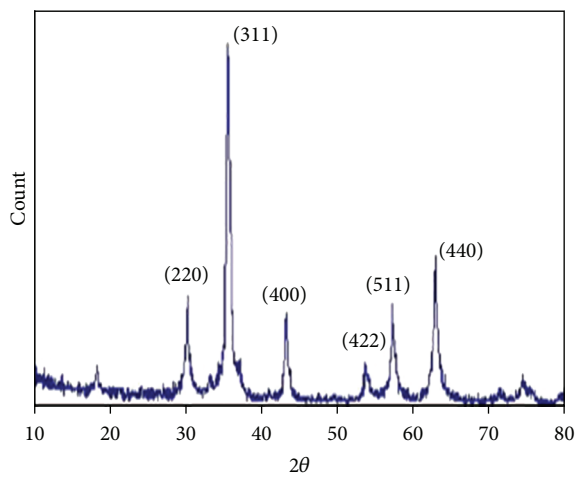


FIGURE 5: XRD patterns of prepared SPIO NPs.

462.7 ± 10.0 for ($400 \mu\text{g}$), 663.7 ± 13.0 for ($600 \mu\text{g}$), 864.1 ± 16.6 for ($800 \mu\text{g}$), and 1087 ± 18 for ($10^3 \mu\text{g}$).

The quantitative statistical analysis using *Kruskal-Wallis* test for comparison between more than two groups not only revealed that the SED values were directly proportional to the concentrations of the injected nanoparticles inside the tumors but also varied considerably between the different concentrations with highly significant *P* values, at 7 days $P < .001$, at 14 days $P < .001$, and at 21 days $P < .007$, but the variations in the SED values of each concentration between the (7, 14, 21) days were insignificant and, $P < .7$ as shown in Figure 6.

The results of HDR revealed that the mean values of HDR in the tumors were [0.157 for ($200 \mu\text{g}$), 0.259 for ($400 \mu\text{g}$), 0.367 for ($600 \mu\text{g}$), 0.478 for ($800 \mu\text{g}$), and 0.604 for ($10^3 \mu\text{g}$)]. These values varied considerably between the different concentrations of SPIO NPs with highly significant *P* values, at 7 days $P < .001$, at 14 days $P < .001$, and at 21 days $P < .007$. Also, the variations in the HDR values of each concentration between the (7, 14, and 21) days were insignificant $P < .7$ (Figure 7).

(2) *Monitoring Maximum Temperature and TMT.* The maximum temperatures achieved inside the tumor were [$40.11 \pm$

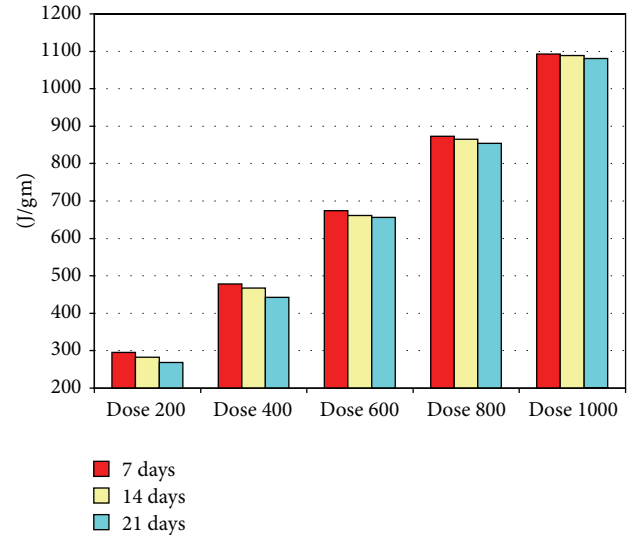


FIGURE 6: Shows Mean of SAR by jg m^{-1} dependent on SPIO NPs concentrations in three sessions (at 7, 14 and 21 days from starting the experiments).

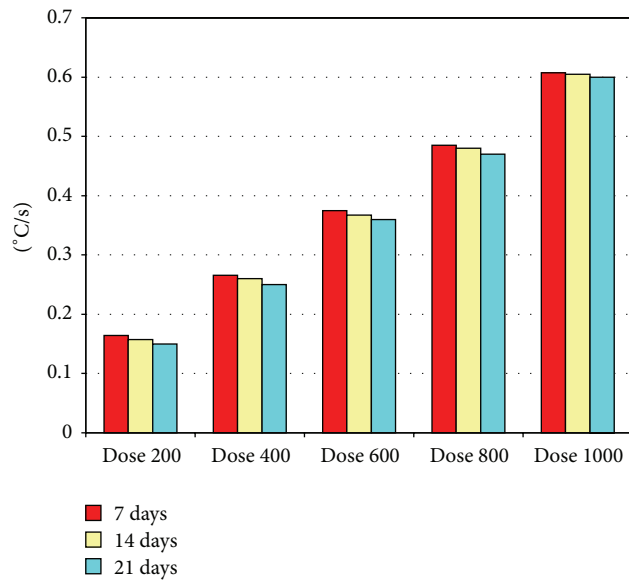


FIGURE 7: Mean values of HDR by ($\text{jg}^{-1}\text{s}^{-1}$) dependent on SPIO NPs concentrations in three sessions (at 7, 14, and 21 days from starting the experiments).

1.52°C for ($200 \mu\text{g}$), $42.36 \pm 1.54^{\circ}\text{C}$ for ($400 \mu\text{g}$), $44.43 \pm 2.0^{\circ}\text{C}$ for ($600 \mu\text{g}$), $46.8 \pm 1.5^{\circ}\text{C}$ for ($800 \mu\text{g}$), and $48.6 \pm 1.0^{\circ}\text{C}$ for ($10^3 \mu\text{g}$) (Figure 8). The TMT recorded as (40 ± 2.5 min for 200 and $400 \mu\text{g}$, 30 ± 2.0 min for $600 \mu\text{g}$, 25 ± 5.0 min for $800 \mu\text{g}$ and 20 ± 5.0 min for $10^3 \mu\text{g}$) (Figure 9). It is worthwhile to mention that there was no substantial temperature elevation observed in the control group.

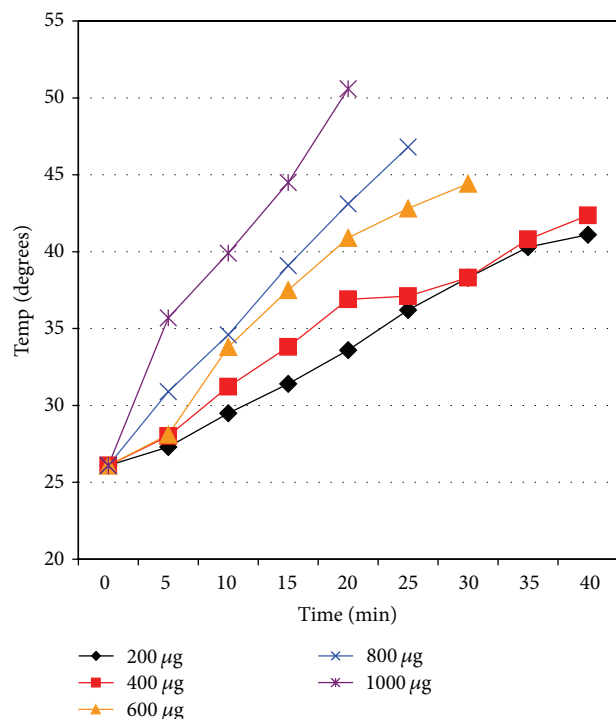


FIGURE 8: The maximum temperature achieved inside the Ehrlich tumors related with the concentrations of the injected SPIO NPs versus time. Data reported represents the mean values in the three sessions (7, 14, and 21 days from starting the experiments).

4. Discussion

In the current study, the SPIO NPs (Fe_3O_4) were synthesized in solution under controlled conditions by wet chemical method. The size, morphology, uniformity, and crystal structure of the prepared SPIO NPs were determined using two techniques TEM and XRD which have been widely employed for this purpose. The TEM images revealed the quasispherical uncoated SPIO NPs with size changes in the range of $\sim 54 \pm 3$ nm. X-ray diffraction spectrum gave further information about the structure of the SPIO NPs. The positions and relative intensities of all diffraction peaks matched well with those from the JCPDS card (no. 85-1436) for Fe_3O_4 magnetite.

The heating ability of MNPs in the presence of AMF is usually expressed by the SAR, also called specific power loss (SPL) which can be defined as the amount of heat generated per unit gram per unit time. The reported SED value on Syngo represents the total heat dose and reflects a cumulative effect which differs according to the SAR of each MNPs concentration.

It is important therefore to understand the underlying physical mechanisms by which heat is generated. The heat generated by MNP via AMF may be due to three major mechanisms which depend greatly on the particle size and their magnetic properties. Large multidomain ferro- or ferrimagnetic materials contain several subdomains each having their own specific magnetization direction. When these materials are exposed to the AMF, the subdomain with magnetization

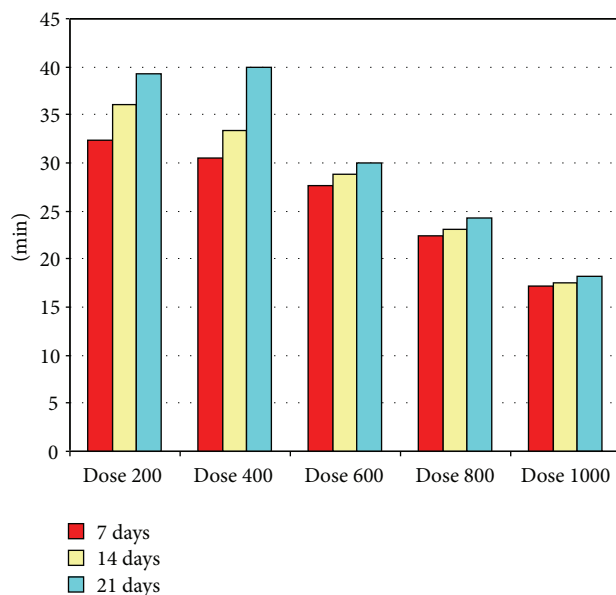


FIGURE 9: Mean values of TMT in the three sessions of treatment (7, 14, and 21 days from starting the experiments).

direction along the magnetic field axis elongates and the other ones shrink. This leads to “domain wall displacements.” Since the magnetization curves for increasing and decreasing magnetic field amplitudes do not coincide, the material demonstrates “hysteresis behavior” and produces heat. In small particles such as SPIO NPs, there is no domain wall, and therefore, hysteresis losses cannot occur. However, the external AMF energy helps magnetic moments to rotate and overcome the anisotropy energy barrier. This energy is then dissipated as heat when the particle relaxes to its equilibrium orientation. This mechanism is called *Néel* relaxation. There is also a third mechanism called *Brownian* relaxation that causes both multidomain and single domain particles to heat up. In this process, energy barrier for reorientation of a particle is given by rotational friction due to the rotation of the entire magnetic particle caused by the AMF torque force on the magnetic moment of the particle [9].

The most effective mechanism of heat generation in the current study may be related to *Brownian* relaxation; this is due to that the SPIO NPs were suspended in glycerin which is a highly viscous medium which in turn increases the friction loss where the source for heat generation relies in this case on the friction processes between the NPs and the medium during the physical rotation of the particle induced by the alteration of the external magnetic field.

There are several factors affect on the SAR values. Robert et al. 2005 [10] demonstrated that the heating potential of MNPs for inducing hyperthermia depends on the saturation magnetization, magnetic field strength, field amplitude, duty, duration, type of NPs, size, size distribution, particle structure, shape, and interparticle interactions, all affect the SAR values of the SPIO NPs. However, each contributes in different ways and with different magnitudes and may even be in competition with each other. So, it is very difficult to

give a general theoretical expression of SAR because several equations may be proposed, but these theoretical trends are not always validated by experimental SAR measurements.

Adding to the above factors, the concentration effect was studied in the current research. The results revealed that increasing the concentrations of injected MNPs resulted in increasing the SAR and hence the higher SED and HDR values; all of these lead to increasing the maximum temperature achieved and decreasing the TMT (Figures 6–9). It is worthwhile to mention that the total heat dose values acquired in this study were lower than those of other studies, Dennis et al., 2008 [11], but the time required to reach the therapeutic temperature was short compared to the previous studies, Giri et al., 2005 [12].

It is well known that for hyperthermia treatment enough heat must be generated by the particles to sustain tissue temperature of at least 42°C for 30 minutes. Indeed this condition was achieved in the current study by using different concentrations (400–10³ µg/kg). The optimum concentration of the magnetic suspension was 800 µg/kg, where the amount of total heat dose was sufficient to increase the temperature above 42°C~45°C in short time ~20 min as shown in Figure 8 compared to (400, 600 µg) in the same figure. On the other hand, using high concentration 10³ µg resulted in high SED values in short time; nevertheless the percentage of mortality was 80%, and this may be attributed to high concentration resulting in high over stress on mice under AMF.

In this study, we used two physically different techniques, the magnetic resonance phenomena for acquiring imaging and treatment at the same time. By using noninvasive AMF for MR imaging through its interaction with the protons of the hydrogen atoms of the water molecules (MR images not shown), and at the same time inducing thermal effect on cancer cells through induction of magnetic gradients generated by a clinical MRI system. Although the two techniques occur at the same time, they are completely different in the physical theory and mechanism.

5. Conclusion

The current preliminary study demonstrated that the temperature changes inside tumors related with the variations of SED and HDR values which in turn depend directly on the injected concentrations of magnetic suspension inside tumors.

References

- [1] P. Wust, B. Hildebrandt, G. Sreenivasa et al., “Hyperthermia in combined treatment of cancer,” *Lancet Oncology*, vol. 3, no. 8, pp. 487–497, 2002.
- [2] X. Liang, K. Exu, and X. Jianhe, “Preparation of Immuno-magnetic nanoparticles and their application in the separation of mouse CD34⁺ hematopoietic stem cells,” *Journal of Magnetism and Magnetic Materials*, vol. 321, pp. 1885–1888, 2009.
- [3] B. Thiesen and A. Jordan, “Clinical applications of magnetic nanoparticles for hyperthermia,” *International Journal of Hyperthermia*, vol. 24, no. 6, pp. 467–474, 2008.
- [4] M. H. Khedr, A. A. Omar, and S. A. Abdel-Moaty, “Magnetic nanocomposites: preparation and characterization of Co-ferrite nanoparticles,” *Colloids and Surfaces A: Physicochemical and Engineering Aspects*, vol. 281, no. 1–3, pp. 8–14, 2006.
- [5] J. P. Fortin, C. Wilhelm, J. Servais, C. Ménager, J. C. Bacri, and F. Gazeau, “Size-sorted anionic iron oxide nanomagnets as colloidal mediators for magnetic hyperthermia,” *Journal of the American Chemical Society*, vol. 129, no. 9, pp. 2628–2635, 2007.
- [6] D. L. Zhao, X. W. Zeng, Q. S. Xia, and J. T. Tang, “Preparation and coercivity and saturation magnetization dependence of inductive heating property of Fe₃O₄ nanoparticles in an alternating current magnetic field for localized hyperthermia,” *Journal of Alloys and Compounds*, vol. 469, no. 1–2, pp. 215–218, 2009.
- [7] A. Jordan, P. Wust, H. Faehling, and J. Krause, “Inductive heating of ferrimagnetic particles and magnetic fluids: physical evaluation of their potential for hyperthermia,” *International Journal of Hyperthermia*, vol. 9, pp. 51–57, 1993.
- [8] D. Portet, B. Denizot, E. Rump, J. J. Lejeune, and P. Jallet, “Nonpolymeric coatings of iron oxide colloids for biological use as magnetic resonance imaging contrast agents,” *Journal of Colloid and Interface Science*, vol. 238, no. 1, pp. 37–42, 2001.
- [9] M. Ma, Y. Wu, J. Zhou, Y. Sun, Y. Zhang, and N. Gu, “Size dependence of specific power absorption of Fe₃O₄ particles in AC magnetic field,” *Journal of Magnetism and Magnetic Materials*, vol. 268, no. 1–2, pp. 33–39, 2004.
- [10] I. Robert, J. Sally, D. Wolfgang, and C. Robert, “Application of high amplitude alternating magnetic fields for heat induction of nanoparticles localized in cancer,” *Clinical Cancer Research*, vol. 1, no. 11, pp. 7093s–7103s, 2005.
- [11] C. Dennis, A. Jackson, and J. Borchers, “The influence of magnetic and physiological behavior on the effectiveness of iron oxide nanoparticles for hyperthermia,” *Journal of Physics D: Applied Physics*, vol. 41, Article ID 134020, 2008.
- [12] J. Giri, P. Pradhan, T. Sriharsha, and D. Bahadur, “Preparation and investigation of potentiality of different soft ferrites for hyperthermia applications,” *Journal of Applied Physics*, vol. 97, no. 10, pp. 1–3, 2005.

Research Article

Melatonin Nanoparticles Adsorbed to Polyethylene Glycol Microspheres as Activators of Human Colostrum Macrophages

Cristiane de Castro Pernet Hara, Adenilda Cristina Honorio-França, Danny Laura Gomes Fagundes, Paulo Celso Leventi Guimarães, and Eduardo Luzia França

Institute of Biological and Health Science, Federal University of Mato Grosso, 78600-000 Barra do Garças, MT, Brazil

Correspondence should be addressed to Adenilda Cristina Honorio-França; denifran@terra.com.br

Received 8 November 2012; Revised 16 January 2013; Accepted 16 January 2013

Academic Editor: Suad Rashdan

Copyright © 2013 Cristiane de Castro Pernet Hara et al. This is an open access article distributed under the Creative Commons Attribution License, which permits unrestricted use, distribution, and reproduction in any medium, provided the original work is properly cited.

The effectiveness of hormones associated with polymeric matrices has amplified the possibility of obtaining new drugs to activate the immune system. Melatonin has been reported as an important immunomodulatory agent that can improve many cell activation processes. It is possible that the association of melatonin with polymers could influence its effects on cellular function. Thus, this study verified the adsorption of the hormone melatonin to polyethylene glycol (PEG) microspheres and analyzed its ability to modulate the functional activity of human colostrum phagocytes. Fluorescence microscopy and flow cytometry analyses revealed that melatonin was able to adsorb to the PEG microspheres. This system increased the release of superoxide and intracellular calcium. There was an increase of phagocytic and microbicidal activity by colostrum phagocytes when in the presence of melatonin adsorbed to PEG microspheres. The modified delivery of melatonin adsorbed to PEG microspheres may be an additional mechanism for its microbicidal activity and represents an important potential treatment for gastrointestinal infections of newborns.

1. Introduction

Polyethylene glycol (PEG) microspheres are polymeric particles that have the capacity to adsorb organic compounds and are considered major drug carriers [1]. The adsorption capacity of microspheres for organic compounds can be modified to improve their biological function [2] as well as their ability to modulate the immune response [3, 4]. The microspheres are made of materials that have been developed as controlled release systems for drugs. These synthetic polymers allow for controlled cell recognition and communication, trigger immune responses, cell adhesion, or signal transduction [5], and are important in pathological processes.

Clinical and experimental evidence supports the hypothesis that colostrum is important during infection because it contains soluble and cellular components, such as lipids, carbohydrates, proteins, viable leukocytes (1×10^9 cells mL^{-1} in the first days of lactation), especially neutrophils and macrophages [6], and hormones, which are important for

immune defense [7, 8]. The literature has reported the action of hormones associated with PEG microspheres, which together act as immunomodulators [4].

Melatonin, one of the hormones contained in milk, is produced by the pineal gland and plays an important protective role for infants [7]. Many of the benefits of melatonin and its metabolites are related to their antioxidant, anti-inflammatory [9, 10], and prooxidative effects [11]. Melatonin has been shown to act on human phagocytes [12, 13] as well as rat splenic macrophages [14, 15].

However, the oral bioavailability of melatonin is less than 20% due to extensive first-pass hepatic metabolism and variable rates of absorption [16–18]. Thus, PEG microspheres are a promising agent for the delivery of the hormone melatonin, as they can prevent its degradation and increase its bioavailability within the organism.

It is possible that melatonin affects colostrum by modulating the microbicidal mechanisms of phagocytes, attracting cells to the site of infection, and reducing the possibility of infection. The aim of this study was to verify the adsorption of

the hormone melatonin to PEG microspheres and to analyze the effect of this material on the functional activity of human colostrum phagocytes.

2. Materials and Methods

2.1. Subjects. Upon informed consent, approximately 8 mL of colostrum was collected from clinically healthy women aged 18–35 years at the Health System Program of Barra do Garças, MT, Brazil ($N = 70$). All of the mothers had given birth to healthy full-term babies. The colostrum samples were collected in sterile plastic tubes between 48 and 72 hours postpartum. All of the procedures were submitted for ethical evaluation and received institutional approval.

2.2. Polyethylene Glycol (PEG) Microsphere Preparation. The microspheres were obtained from polyethylene glycol (PEG) 6000 using a modification [3, 4] of a previously described protocol [2]. Briefly, 20 g of PEG 6000 was resuspended in 100 mL of a 2% sodium sulfate solution in phosphate-buffered saline (PBS) and incubated at 37°C for 45 min. After incubation, the PEG microspheres were diluted 3:1 in PBS and washed twice in PBS (500 ×g, 5 min). The PEG microspheres were resuspended in PBS. The formation of the microspheres was thermally induced by subjecting the solution to 95°C for 5 min. For adsorption, the suspensions of PEG microspheres in PBS were incubated with melatonin (Sigma, St. Louis, MO, USA; concentration 100 ng mL⁻¹) at 37°C for 30 minutes. The PEG microspheres with or without adsorbed melatonin were fluorescently labeled overnight at room temperature with a solution of Dylight 488 (Pierce Biotechnology, Rockford, IL, USA; 10 μg mL⁻¹) in dimethylformamide at a 100:1 molar ratio of PEG:Dylight. The samples were then analyzed by fluorescence microscopy.

2.3. Flow Cytometry. Immunofluorescence staining was performed with phycoerythrin (PE, Sigma, St. Louis, MO, USA) to compare the abilities of the PEG and polymethylmethacrylate microspheres (CaliBRITE—BD, San Jose, CA, USA) to bind fluorescent markers. The PEG microspheres were incubated with 5 μL of PE (0.1 mg mL⁻¹) for 30 min at 37°C. After the incubation, the PEG microspheres were washed twice in PBS containing BSA (5 mg mL⁻¹; 500 ×g, 10 min, 4°C). In all of the experiments, the PEG microspheres were analyzed by flow cytometry. The study was performed on a FACSCalibur (BD, San Jose, CA, USA). The PEG microspheres sizes were compared to those of the BD microspheres (6 μm CaliBRITE 3 Beads, BD cat. no. 340486, San Jose, CA, USA) and those bound or unbound to PE. The fluorescence intensity of the PEG microspheres was expressed as the geometric mean fluorescence intensity, and the size was calculated according to the geometric mean of the Forward Scatter (FSC).

2.4. Obtaining Supernatants from Human Colostrum. Colostrum supernatant samples of different mothers were obtained by centrifugation (10 min, 160 ×g, 4°C), the upper fat layer was discarded, and the aqueous supernatant was stored at -70°C to isolate the posterior melatonin hormone.

2.5. Separation of Colostrum Cells. Approximately 15 mL of colostrum was collected in sterile plastic tubes from each woman. The samples were centrifuged (160 ×g, 4°C) for 10 min, which separated the colostrum into three different phases: a cell pellet, an intermediate aqueous phase, and a lipid-containing supernatant, as described by Honorio-França et al. [19]. The cells were separated by a Ficoll-Paque gradient (Pharmacia, Uppsala, Sweden), producing preparations with 98% pure mononuclear cells, and they were analyzed by light microscopy. The purified macrophages were resuspended independently in serum-free medium 199 at a final concentration of 2 × 10⁶ cells mL⁻¹.

2.6. Melatonin Hormone Dosage by Immunoenzymatic Method. Melatonin was extracted by affinity chromatography, concentrated in a speed vacuum, and then quantified by ELISA (Immune-Biological Laboratories, Hamburg). The reaction rates were measured by absorbance at 405 nm in a spectrophotometer. The results were calculated by a standard curve and shown in pg/mL.

2.7. E. coli Strain. The enteropathogenic *Escherichia coli* (EPEC) was isolated from the stools of an infant with acute diarrhea (serotype 0111:H⁻, LA⁺, eae⁺, EAF⁺, bfp⁺). This material was prepared and adjusted to 10⁷ bacteria mL⁻¹, as previously described by Honorio-França et al. [19].

2.8. Release of Superoxide Anion. Superoxide release was determined by cytochrome C (Sigma, St. Louis, MO, USA) reduction [19, 20]. Briefly, mononuclear phagocytes and bacteria were mixed and incubated for 30 min to allow phagocytosis. The cells were then resuspended in PBS containing 2.6 mM CaCl₂, 2 mM MgCl₂, and cytochrome C (Sigma, St. Louis, MO, USA; 2 mg mL⁻¹). The suspensions (100 μL) were incubated for 60 min at 37°C on culture plates. The reaction rates were measured by their absorbance at 630 nm, and the results were expressed as nmol/O₂⁻. All of the experiments were performed in duplicate or triplicate.

2.9. Bactericidal Assay. Phagocytosis and microbicidal activity were evaluated by the acridine orange method [21]. Equal volumes of bacteria and cell suspensions were mixed and incubated at 37°C for 30 min under continuous shaking. Phagocytosis was stopped by incubation on ice. To eliminate extracellular bacteria, the suspensions were centrifuged twice (160 ×g, 10 min, 4°C). The cells were resuspended in serum-free 199 medium and centrifuged. The supernatant was discarded, and the sediment was dyed with 200 μL of acridine orange (Sigma, St. Louis, MO, USA; 14.4 g L⁻¹) for 1 min. The sediment was resuspended in cold 199 medium, washed twice, and observed under an immunofluorescence microscope at 400x and 1000x magnification. The phagocytosis index was calculated by counting the number of cells ingesting at least 3 bacteria in a pool of 100 cells. To determine the bactericidal index, the slides were stained with acridine orange, and 100 cells with phagocytized bacteria were counted. The bactericidal index was calculated as the ratio between orange-stained (dead) and green-stained (alive)

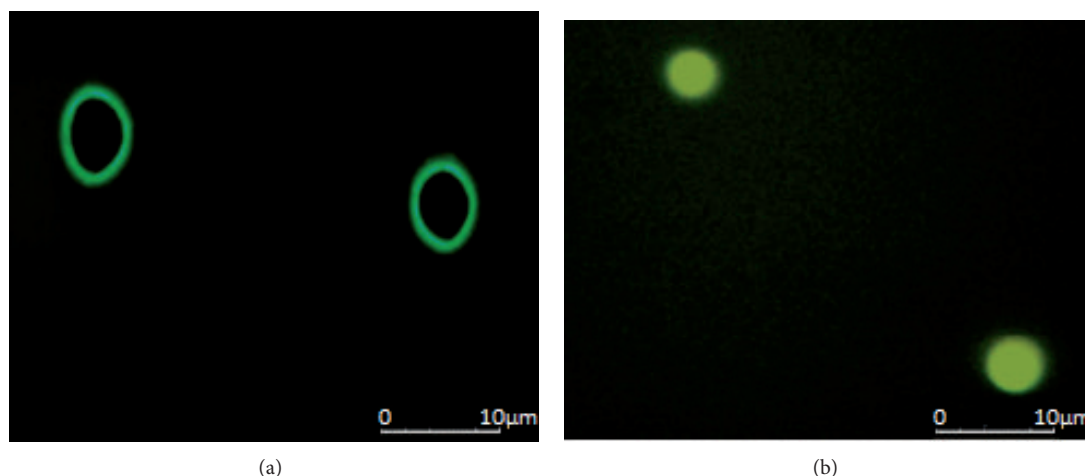


FIGURE 1: Fluorescence microscopy image of the PEG microspheres stained with Dylight 488. (a) represents the PEG microspheres (100x), and (b) represents the PEG microspheres adsorbed to melatonin. The experiments were repeated five times, and the results were comparable.

bacteria $\times 100$ [21]. All of the experiments were performed in duplicate or triplicate.

2.10. Immunofluorescence and Flow Cytometry. Immunofluorescence staining was performed with Fluo-3 (Sigma, St. Louis, MO, USA) to assess intracellular Ca^{2+} release by colostrum phagocytes. The cell suspensions were preincubated with or without $50 \mu\text{L}$ of melatonin (Sigma, final concentration of 10^{-7} M) at 37°C for 30 min under continuous shaking. The phagocytes were centrifuged twice ($160 \times g$, 10 min, 4°C), resuspended in PBS containing BSA (5 mg mL^{-1}), and incubated with $5 \mu\text{L}$ of Fluo-3 ($1 \mu\text{g mL}^{-1}$) for 30 min at 37°C . After the incubation, the cells were washed twice in PBS containing BSA (5 mg mL^{-1} ; $160 \times g$, 10 min, 4°C). In all of the experiments, the cells were analyzed by flow cytometry. The samples were run on a FACSCalibur machine (BD, San Jose, CA, USA). Calibration and sensitivity were routinely checked using CaliBRITE 3 Beads (BD cat. No. 340486, San Jose, CA, USA). Fluo-3 was detected using a 530/30 nm filter for intracellular Ca^{2+} . The ratio of intracellular Ca^{2+} release was expressed as the geometric mean fluorescence intensity of Fluo-3. The experiments were repeated on several occasions, and the data presented in the figures are from single representative experiments.

2.11. Statistical Analysis. An analysis of variance (ANOVA) was used to evaluate superoxide, phagocytosis, the bactericidal index, and intracellular calcium in the presence or absence of PEG microspheres adsorbed to melatonin. Statistical significance was considered when $P < 0.05$.

3. Results

3.1. Characterization of Microspheres with Melatonin. The fluorescence microscopy image (Figure 1(a)) shows the PEG

microspheres that were produced in PBS. This result confirmed that the method produces different sizes of microspheres that are easily separated in suspension. The microspheres retained their ellipsoid structures, had regular sizes, and were homogeneous (Figure 1(a)). The PEG microspheres were able to adsorb the melatonin. Furthermore, the melatonin was distributed throughout the surface (Figure 1(b)), indicating its interfacial deposition under the surface of the microspheres.

Figure 2(a) compares the fluorescence intensity of PEG microspheres, PEG microspheres adsorbed to melatonin, and the BD microspheres (standard). The PEG and BD microspheres had the highest geometric mean fluorescence intensities. The adsorption of melatonin to the PEG microsphere altered the geometric mean fluorescence intensity. The sizes of the PEG microspheres were similar to the standard microspheres (Figures 2(a) and 2(b)). Analysis by flow cytometry showed that the PEG microspheres had a size of approximately $5.8 \mu\text{m}$, the polymethylmethacrylate BD microspheres had a size of $6 \mu\text{m}$, while the microspheres adsorbed to melatonin had a mean size of $5.3 \mu\text{m}$ (Figure 2(c)).

3.2. General Characteristic of Colostrum Components. The number of colostrum phagocytes retrieved was $1.8 \times 10^6 \text{ cell mL}^{-1}$, and the viability (%) was 90.5 ± 2.2 . The colostrum melatonin concentration was $16.0 \pm 4.05 \text{ pg mL}^{-1}$.

3.3. Superoxide Release by Colostrum Phagocytes in the Presence of PEG Microspheres Adsorbed to Melatonin. In the absence of bacteria, melatonin increased the release of superoxide by colostrum phagocytes compared to the spontaneous release (PBS = 1.32 ± 0.3 —melatonin = 3.47 ± 0.69 ; Table 1). (PBS = 1.01 ± 0.24 —melatonin = 2.74 ± 0.37 ; Table 1). The phagocytes incubated with bacteria and melatonin also displayed higher superoxide release than the controls (bacteria plus melatonin = 2.74 ± 0.37 ; PBS = 1.01 ± 0.24). Additionally, the phagocytes exposed to melatonin that had been adsorbed

TABLE 1: Superoxide anion release from phagocytes in human colostrum mononuclear cells.

Phagocytes MN colostrum	Bacteria EPEC	Superoxide anion release (nmol)
Spontaneous	Absent	1.22 ± 0.25
	Present	1.01 ± 0.24
Cell + PEG	Absent	1.50 ± 0.19
	Present	1.41 ± 0.31
Cell + MLT	Absent	3.47 ± 0.69 ^{*#}
	Present	2.74 ± 0.37 ^{*+}
Cell + PEG + MLT	Absent	2.35 ± 0.42 ^{*#}
	Present	1.96 ± 0.55 ^{*+}

The mononuclear cells were incubated with melatonin. In the controls assays, the mononuclear cells were preincubated with PBS. ^{*} $P < 0.05$: comparing the treated and nontreated cells (without bacteria); [#] $P < 0.05$: comparing the different treatments (PBS, melatonin (MLT), and polyethylene glycol (PEG)) without bacteria; ⁺ $P < 0.05$: comparing the different treatments (PBS, MLT, and PEG) with bacteria.

to PEG microspheres displayed increased superoxide release when compared to the phagocytes exposed to the PEG microspheres alone (bacteria plus PEG microsphere = 1.41 ± 0.31, bacteria plus PEG microsphere plus melatonin = 1.96 ± 0.55). The effect of melatonin stimulation alone was higher than that of bacteria and melatonin (melatonin = 3.47 ± 0.69; bacteria plus melatonin = 2.74 ± 0.37). Furthermore, the release of superoxide decreased significantly in the presence of PEG microspheres with adsorbed melatonin compared to the phagocytes exposed to melatonin alone, and this was independent of bacteria (PEG + MLT = 2.35 ± 0.42; bacteria plus PEG + MLT = 1.96 ± 0.55; Table 1).

3.4. Phagocytosis of Colostrum Mononuclear Cells in the Presence of PEG Microspheres Adsorbed to Melatonin. The colostrum phagocytes displayed some phagocytic activity in response to EPEC (34.4 ± 4.6). Phagocytosis increased significantly in the presence of melatonin (48.8 ± 12.8). A comparison of the PEG microspheres adsorbed to melatonin and the PEG microspheres alone showed that phagocytosis was similar (melatonin = 82 ± 5.1; PEG microspheres = 71.5 ± 3; PEG microspheres plus melatonin = 78.5 ± 3; Figure 3).

3.5. Bactericidal Activity of Colostrum Phagocytes in the Presence of PEG Microspheres Adsorbed to Melatonin. The colostrum mononuclear phagocytes that were not stimulated had some bactericidal activity against EPEC (34.9 ± 9.5). The mononuclear phagocytes incubated with melatonin showed increased bactericidal activity (66.9 ± 10). The bacterial killing by colostrum mononuclear phagocytes mediated by PEG microspheres adsorbed to melatonin is shown in Figure 4. The mononuclear phagocytes incubated with PEG microspheres adsorbed to melatonin showed increased microbicidal activity in response to EPEC (61.5 ± 5.8).

TABLE 2: Release of intracellular Ca²⁺ by colostrum phagocytes in the presence of melatonin adsorbed to PEG microspheres.

Colostrum mononuclear phagocytes (MN)	Fluorescence intensity (mean ± SD)
PBS	13.96 ± 2.20
Cell + PEG	21.24 ± 1.26 [*]
Cell + MLT	87.89 ± 8.38 ^{*#}
Cell + PEG + MLT	30.98 ± 5.03 ^{*#}

The intracellular Ca²⁺ release is represented by mean fluorescence intensity and was obtained by flow cytometry. The results represent the mean and SD of five experiments with cells from different individuals. ^{*} $P < 0.05$: comparing the treated cells with non-treated cells (PBS); [#] $P < 0.05$: comparing the different treatments (MLT and PEG microspheres).

3.6. Intracellular Ca²⁺ Release by Colostrum Phagocytes in the Presence of PEG Microspheres Adsorbed to Melatonin. Colostrum phagocytes incubated with melatonin had increased intracellular Ca²⁺ levels (Figure 5). Table 2 shows the rate of intracellular Ca²⁺ release of colostrum phagocytes treated with PEG microspheres adsorbed to melatonin or PEG microspheres alone using Fluo-3 to assess the fluorescence intensity (PBS = 13.97 ± 2.2; PEG + MLT = 30.98 ± 5.03; PEG = 21.24 ± 1.2). The highest intracellular Ca²⁺ release was found in phagocytes treated with melatonin (87.9 ± 8.3), whereas melatonin adsorbed to PEG microspheres decreased the release of intracellular Ca²⁺ by colostrum phagocytes (30.98 ± 5.03; Table 2).

4. Discussion

In this study, microspheres adsorbed to melatonin were produced, and this material was found to stimulate the functional activity of colostrum phagocytes as evidenced by the release of superoxide and intracellular calcium.

Microsphere-based polymeric substances can be used for controlled drug delivery. The release of drugs from a microsphere may be due to the leaching process of the polymer or by the degradation of the polymer matrix, and it is therefore important to understand the physical and chemical properties of the release medium [22]. In this study, the analyses by fluorescence microscopy and flow cytometry showed that the PEG microspheres had ellipsoid shapes and were easily separated from the suspension. The literature has reported the use of flow cytometry as an alternative method for analyzing and visualizing particles [23, 24]. It was observed by flow cytometry that the PEG microspheres had a size of approximately 5.8 μm. The adsorption of melatonin reduced the size to approximately 5.35 μm, suggesting that melatonin may bind at the same site as the marker. These data are in agreement with previous studies, which found that the PEG microspheres changed in size or in the ability to bind fluorescent substances after the adsorption of bioactive molecules [3, 4, 25].

The literature reports that polyethylene glycol in microsphere formulations can allow for the control and development of pores by the molecular weight, and the concentration can modulate the speed at which the drug is released from the

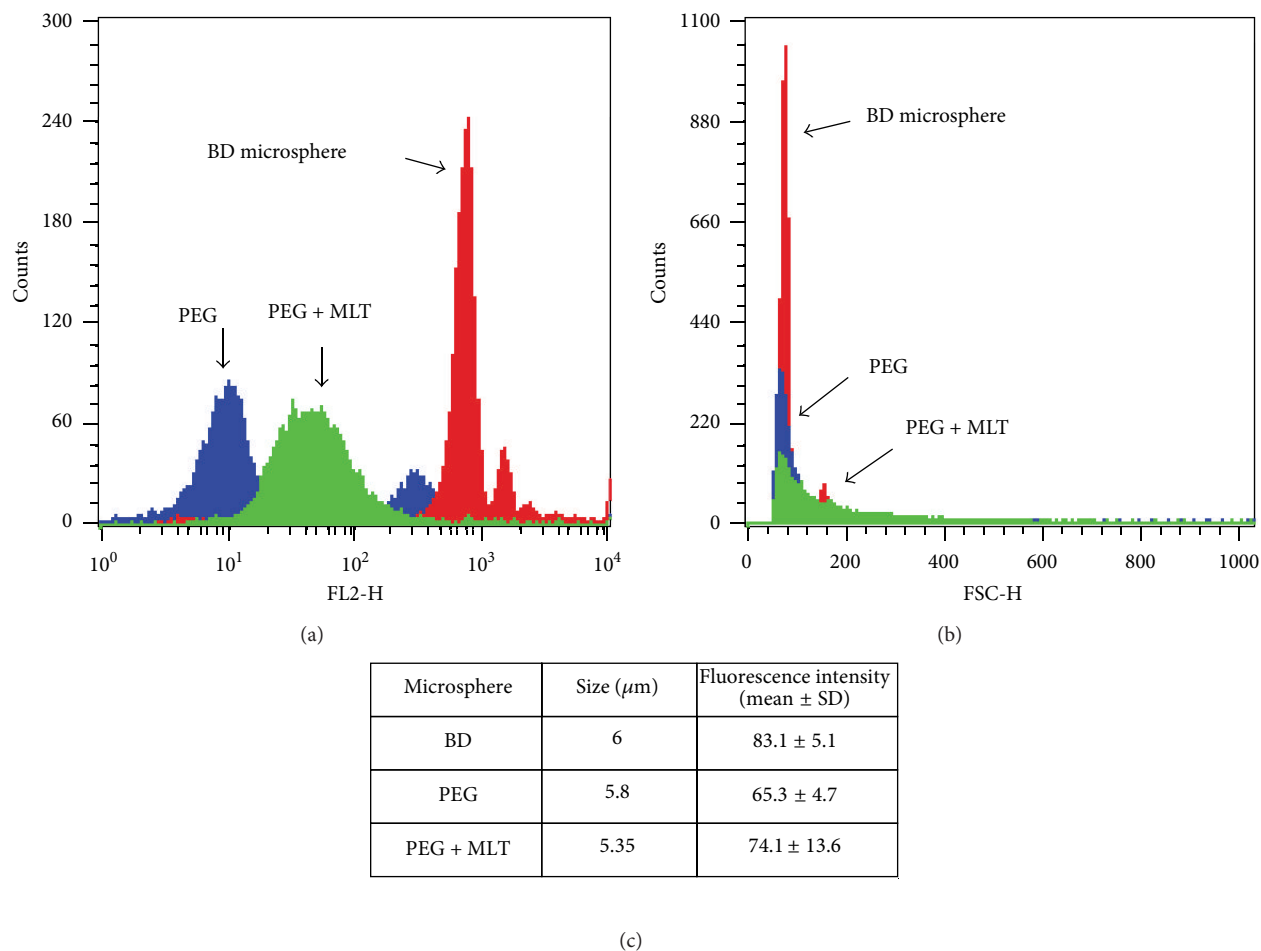


FIGURE 2: The PEG microspheres were stained with phycoerythrin (PE) as described in Section 2. PE-labeled polymethylmethacrylate microspheres were used as a standard. Immunofluorescence and size analyses were carried out by flow cytometry. (a) represents the fluorescence intensity (FL2), (b) represents the size based on Forward Scatter (FSC), and (c) represents the geometric mean fluorescence intensity and the geometric mean of size.

polymer matrix [26]. There are currently several drugs associated with PEG that are widely traded, including interferon alpha (PEGASYS, PEG-Intron) growth hormone (Somavert), asparaginase (Oncaspar), camptothecin, and insulin, and the PEG has been able to prolong the bioavailability of the drugs [27].

The effectiveness of hormones associated with polymer matrices has expanded the possibility of obtaining new drugs to activate the immune system [4]. According to the literature, the generation of free radicals is an important mechanism of protection against infection [28–30].

The results of this work confirm the importance of the superoxide anion in activating colostrum phagocytes in association with modified drug release systems. Melatonin increased the production of these radicals independently of the presence of bacteria. Moreover, when melatonin was adsorbed to PEG microspheres, superoxide anion release decreased, but it remained higher than that found during spontaneous release. These data suggest that the PEG microspheres are able to modify the release of melatonin while maintaining cellular activation. This can minimize the

adverse effects that may occur with high doses of superoxide anion.

The beneficial actions of melatonin are associated with its ability to remove free radicals and increase the enzymatic activity of antioxidants [31–34]. Furthermore, melatonin has immunostimulatory effects [35] and can stimulate cells of the immune system [36, 37]. Phagocytes produce large amounts of superoxide radicals during oxidative stress, an important protective mechanism during infection. Controlling this release is fundamental for appropriate immune responses against infection.

Soluble components present in colostrum interact with cells to increase superoxide release, and this can increase the phagocytic and microbicidal abilities of macrophages [30, 37]. In the present study, phagocytosis was increased independently of the stimulus used. The highest rates of phagocytosis were observed when the cells were directly stimulated by melatonin, which is in agreement with previous studies [13, 38].

Interestingly, the superoxide release by cells exposed to the melatonin-adsorbed PEG microspheres, although in

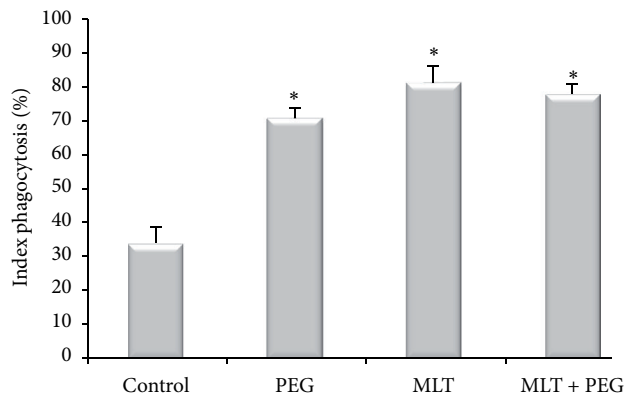


FIGURE 3: Bacterial phagocytosis by colostrum mononuclear cells (mean \pm SD, $N = 10$ for each treatment). Bacterial phagocytosis by colostrum mononuclear cells was determined with the acridine orange method. * indicates differences between treatments (PEG and/or hormone) and 199 medium (ANOVA, $P < 0.05$).

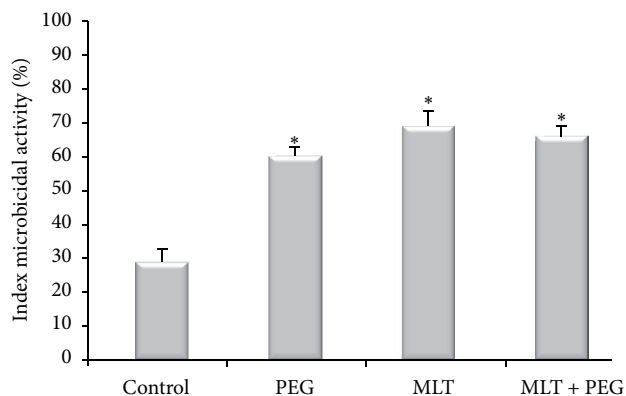


FIGURE 4: Microbicidal activity by colostrum mononuclear cells (mean \pm SD, $N = 10$ in each treatment). Bacterial elimination by mononuclear cells from colostrum was determined with the acridine orange method. * indicates differences between treatments (PEG and/or hormone) and 199 medium (ANOVA, $P < 0.05$).

lower concentration, was sufficient to activate the microbicidal mechanisms of phagocytes. This demonstrated that the microsphere-mediated release of melatonin may be important for the modification of cellular activation because elevated levels of free radicals cause cellular damage that eventually culminates in the activation of cell death pathways [15, 38, 39].

Microbicidal activity promoted by melatonin and the resulting oxidation products may have important clinical applications [40, 41]. Alterations in superoxide anions modify the responses of intracellular calcium and phosphorylation events during oxidative metabolism [42]. Furthermore, melatonin has been reported to increase intracellular calcium in human cells [43].

In the present study, melatonin stimulated the release of intracellular calcium by colostrum phagocytes. The adsorption of melatonin to PEG microspheres decreased this release, suggesting that the PEG microspheres can modify the effect

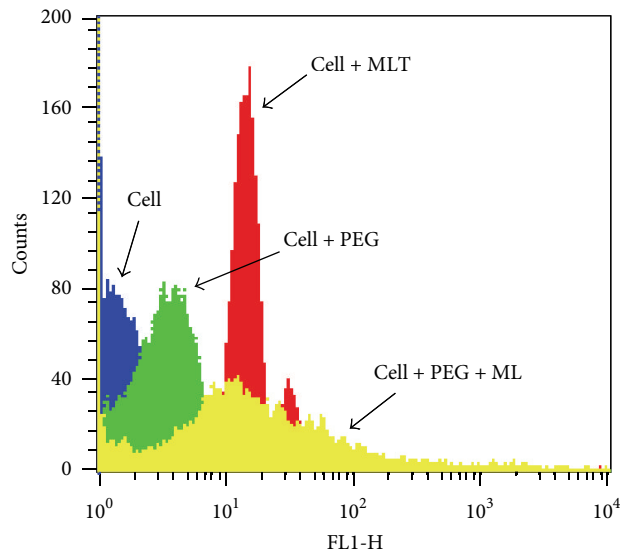


FIGURE 5: Colostrum mononuclear cells stimulated with melatonin adsorbed to PEG microspheres were stained with Fluo-3 to assess intracellular Ca^{2+} release as described in Section 2. Immunofluorescence analyses were carried out by flow cytometry.

of melatonin on intracellular calcium influx. This delivery system provided by melatonin and PEG microspheres may be useful for various diseases because the excessive release of intracellular Ca^{2+} can induce apoptosis [44, 45].

In this study, we found that melatonin is present in colostrum, and the interaction between hormones and cells generates natural protection for the newborn. Due to the immaturity of the newborn digestive system, digestive enzymes and other factors do not destroy the cells received through colostrum. Therefore, the cells likely remain intact throughout the upper portions of the intestine and can interact with each other to protect the mucosa. Some studies have suggested that the cells from the colostrum remain viable within the newborn intestinal mucosa for a period of 4 hours [46, 47] and may exert microbicidal activity and produce antibodies [48]. Importantly, the interaction of hormones associated with modified delivery systems is critical for the newborn, and such systems can utilize colostrum in concentrations that best promote cellular activity.

5. Conclusion

The results indicate that melatonin-adsorbed PEG microspheres modify the release of superoxide and intracellular Ca^{2+} by colostrum phagocytes and increase the microbicidal activity of these cells. The modified delivery system of melatonin via PEG microspheres may be an additional mechanism to improve the immune responses of colostrum phagocytes and represents a fundamentally important mechanism for the protection and treatment of gastrointestinal infections of newborns.

Conflict of Interests

The authors declare that they have no conflict of interests.

Acknowledgments

This research received grants from Fundação de Amparo à Pesquisa de Mato Grosso (FAPEMAT no. 299032/2010) and Conselho Nacional de Pesquisa (CNPq no. 475826/2010-8; no. 475739/2011-6).

References

- [1] J. H. Park, M. Ye, and K. Park, "Biodegradable polymers for microencapsulation of drugs," *Molecules*, vol. 10, no. 1, pp. 146–161, 2005.
- [2] E. A. Scott, M. D. Nichols, R. Kuntz-Willits, and D. L. Elbert, "Modular scaffolds assembled around living cells using poly(ethylene glycol) microspheres with macroporation via a non-cytotoxic porogen," *Acta Biomaterialia*, vol. 6, no. 1, pp. 29–38, 2010.
- [3] E. F. Scherer, A. C. Honorio-França, C. C. P. Hara, A. P. B. Reinaque, M. A. Cortes, and E. L. França, "Immunomodulatory effects of poly(ethylene glycol) microspheres adsorbed with nanofractions of *Momordica charantia* L. on diabetic human blood phagocytes," *Science Advanced Material*, vol. 3, pp. 1–8, 2011.
- [4] D. L. G. Fagundes, E. L. França, C. C. P. Hara, and A. C. Honorio-França, "Immunomodulatory effects of poly(ethylene glycol) microspheres adsorbed with cortisol on activity of colostrum phagocytes," *International Journal of Pharmacology*, vol. 8, pp. 510–518, 2012.
- [5] K. L. Kiick, "Materials science: polymer therapeutics," *Science*, vol. 317, no. 5842, pp. 1182–1183, 2007.
- [6] R. M. Goldblum and A. S. Goldman, "Immunological components of milk: formation and function," in *Journal Handbook Mucosal Immunology*, P. L. Ogra, M. E. Lamm, J. R. McGhee, J. Mestecky, W. Strober, and J. Bienenstock, Eds., Academic Press, New York, NY, USA, 1994.
- [7] H. Illnerová, M. Buresová, and J. Presl, "Melatonin rhythm in human milk," *Journal Clinical Endocrinology and Metabolism*, vol. 77, pp. 838–841, 1993.
- [8] G. N. Pontes, E. C. Cardoso, M. M. S. Carneiro-Sampaio, and R. P. Markus, "Injury switches melatonin production source from endocrine (pineal) to paracrine (phagocytes)—melatonin in human colostrum and colostrum phagocytes," *Journal of Pineal Research*, vol. 41, no. 2, pp. 136–141, 2006.
- [9] R. A. Kireev, A. C. F. Tresguerres, C. Garcia, C. Ariznavarreta, E. Vara, and J. A. F. Tresguerres, "Melatonin is able to prevent the liver of old castrated female rats from oxidative and pro-inflammatory damage," *Journal of Pineal Research*, vol. 45, no. 4, pp. 394–402, 2008.
- [10] R. J. Reiter, D. X. Tan, M. J. Jou, A. Korkmaz, L. C. Manchester, and S. D. Paredes, "Biogenic amines in the reduction of oxidative stress: melatonin and its metabolites," *Neuroendocrinology Letters*, vol. 29, no. 4, pp. 391–398, 2008.
- [11] I. Bejarano, J. Espino, C. Barriga, R. J. Reiter, J. A. Pariente, and A. B. Rodriguez, "Pro-oxidant effect of melatonin in tumour leucocytes: relation with its cytotoxic and pro-apoptotic effects," *Basic and Clinical Pharmacology and Toxicology*, vol. 108, no. 1, pp. 14–20, 2011.
- [12] E. L. França, J. C. Maynié, V. C. Correa et al., "Immunomodulatory effects of herbal plants plus melatonin on human blood phagocytes," *International Journal of Phytomedicine*, vol. 2, pp. 354–362, 2010.
- [13] A. C. França-Botelho, J. L. França, F. M. S. Oliveira et al., "Melatonin reduces the severity of experimental amoebiasis," *Parasites & Vector*, vol. 4, p. 62, 2011.
- [14] E. L. França, N. D. Feliciano, K. A. Silva, C. K. B. Ferrari, and A. C. Honorio-França, "Modulatory role of melatonin on superoxide release by spleen macrophages isolated from alloxan-induced diabetic rats," *Bratislavske Lekarske Listy*, vol. 110, pp. 517–522, 2009.
- [15] A. C. H. França, K. A. Silva, N. D. Feliciano, I. M. P. Calderon, M. V. C. Rudge, and E. L. França, "Melatonin effects on macrophage in diabetic rats and the maternal hyperglycemic implications for newborn rats," *International Journal of Diabetes and Metabolism*, vol. 17, no. 3, pp. 87–92, 2009.
- [16] B. J. Lee, K. A. Parrott, J. W. Ayres, and R. L. Sack, "Design and evaluation of an oral controlled release delivery system for melatonin in human subjects," *International Journal of Pharmaceutics*, vol. 124, no. 1, pp. 119–127, 1995.
- [17] L. Benes, B. Claustrat, F. Horriere et al., "Transmucosal, oral controlled-release, and transdermal drug administration in human subjects: a crossover study with melatonin," *Journal of Pharmaceutical Sciences*, vol. 86, no. 10, pp. 1115–1119, 1997.
- [18] S. Mao, J. Chen, Z. Wei, H. Liu, and D. Bi, "Intranasal administration of melatonin starch microspheres," *International Journal of Pharmaceutics*, vol. 272, no. 1-2, pp. 37–43, 2004.
- [19] A. C. Honorio-França, M. P. S. M. Carvalho, L. Isaac, L. R. Trabulsi, and M. M. S. Carneiro-Sampaio, "Colostrum mononuclear phagocytes are able to kill enteropathogenic *Escherichia coli* opsonized with colostrum IgA," *Scandinavian Journal of Immunology*, vol. 46, no. 1, pp. 59–66, 1997.
- [20] E. Pick and D. Mizel, "Rapid microassays for the measurement of superoxide and hydrogen peroxide production by macrophages in culture using an automatic enzyme immunoassay reader," *Journal of Immunological Methods*, vol. 46, no. 2, pp. 211–226, 1981.
- [21] R. Bellinati-Pires, S. E. Melki, G. M. D. D. Colletto, and M. M. S. Carneiro-Sampaio, "Evaluation of a fluorochrome assay for assessing the bactericidal activity of neutrophils in human phagocyte dysfunctions," *Journal of Immunological Methods*, vol. 119, no. 2, pp. 189–196, 1989.
- [22] G. Ruan and S. S. Feng, "Preparation and characterization of poly(lactic acid)-poly(ethylene glycol)-poly(lactic acid) (PLA-PEG-PLA) microspheres for controlled release of paclitaxel," *Biomaterials*, vol. 24, no. 27, pp. 5037–5044, 2003.
- [23] B. Giehl Zanetti, V. Soldi, and E. Lemos-Senna, "Effect of polyethylene glycols addition in microsphere formulations of cellulose acetate butyrate on efficacy carbamazepine and particles morphology encapsulation," *Brazilian Journal of Pharmaceutical Sciences*, vol. 38, no. 2, pp. 229–236, 2002.
- [24] B. Stadler, A. D. Price, and A. N. Zelikin, "Acritical look at multilayered polymer capsules in biomedicine: drug carriers, artificial organelles and cell mimics," *Advanced Functional Material*, vol. 21, pp. 14–28, 2011.
- [25] A. P. B. Reinaque, E. L. França, E. F. Scherer, M. A. Cortes, F. J. D. Souto, and A. C. Honorio-França, "Natural material adsorbed onto a polymer," *Drug Design, Development and Therapy*, vol. 6, pp. 209–216, 2012.
- [26] J. C. O. Villanova and R. L. Oréfice, "Aplicações Farmacêuticas de Polímeros," *Polímeros*, vol. 20, pp. 51–64, 2010.

- [27] S. Jevš' Evar, J. M. Kunstel, and V. G. Porekar, "PEGylation of therapeutic proteins," *Biotechnology Journal*, vol. 5, pp. 113–128, 2010.
- [28] E. L. França, R. V. Bitencourt, M. Fujimori, T. Cristina de Moraes, I. de Mattos Paranhos Calderon, and A. C. Honorio-França, "Human colostrum phagocytes eliminate enterotoxigenic *Escherichia coli* opsonized by colostrum supernatant," *Journal of Microbiology, Immunology and Infection*, vol. 44, no. 1, pp. 1–7, 2011.
- [29] C. Rodriguez, J. C. Mayo, R. M. Sainz et al., "Regulation of antioxidant enzymes: a significant role for melatonin," *Journal of Pineal Research*, vol. 36, no. 1, pp. 1–9, 2004.
- [30] E. L. França, G. Morceli, D. L. G. Fagundes, M. V. C. Rugde, I. M. P. Calderon, and A. C. Honorio-França, "Secretory IgA- Fc α -Receptor interaction modulating phagocytosis and microbicidal activity by phagocytes in human colostrum of diabetics," *Acta Pathologica, Microbiologica et Immunologica Scandinavica*, vol. 119, pp. 710–719, 2011.
- [31] N. Klepac, Z. Rudeš, and R. Klepac, "Effects of melatonin on plasma oxidative stress in rats with streptozotocin induced diabetes," *Biomedicine and Pharmacotherapy*, vol. 60, no. 1, pp. 32–35, 2006.
- [32] E. J. Sudnikovich, Y. Z. Maksimchik, S. V. Zabrodskaia et al., "Melatonin attenuates metabolic disorders due to streptozotocin-induced diabetes in rats," *European Journal of Pharmacology*, vol. 569, no. 3, pp. 180–187, 2007.
- [33] S. R. Pandi-Perumal, I. Trakht, V. Srinivasan et al., "Physiological effects of melatonin: role of melatonin receptors and signal transduction pathways," *Progress in Neurobiology*, vol. 85, no. 3, pp. 335–353, 2008.
- [34] A. C. Honorio-França, P. Launay, M. M. S. Carneiro-Sampaio, and R. C. Monteiro, "Colostrum neutrophils express Fc α receptors (CD89) lacking γ chain association and mediate non-inflammatory properties of secretory IgA," *Journal of Leukocyte Biology*, vol. 69, no. 2, pp. 289–296, 2001.
- [35] H. O. Besedovsky and A. Del Rey, "Immune-neuro-endocrine interactions: facts and hypotheses," *Endocrine Reviews*, vol. 17, no. 1, pp. 64–102, 1996.
- [36] M. Cutolo, B. Villaggio, F. Candido et al., "Melatonin influences interleukin-12 and nitric oxide production by primary cultures of rheumatoid synovial macrophages and THP-1 cells," *Annals of the New York Academy of Sciences*, vol. 876, pp. 246–254, 1999.
- [37] K. Skwarlo-Sonta, "Bi-directional communication between pineal gland and immune system," *The Journal of Physiology*, vol. 543, pp. 65–75, 2002.
- [38] E. L. França, A. Pereira, S. L. Oliveira, and A. C. Honorio-França, "Chronoimmunomodulation of melatonin on bactericidal activity of human blood phagocytes," *Internet Journal of Microbiology*, vol. 6, pp. 1–13, 2009.
- [39] C. K. B. Ferrari, E. L. França, and A. C. Honorio-França, "Nitric oxide, health and disease," *Journal of Applied Biomedical*, vol. 7, pp. 163–173, 2009.
- [40] S. D. O. Silva, S. R. Q. Carvalho, V. F. Ximenes, S. S. Okada, and A. Campa, "Melatonin and its kynurenin-like oxidation products affect the microbicidal activity of neutrophils," *Microbes and Infection*, vol. 8, no. 2, pp. 420–425, 2006.
- [41] E. Soto-Vega, I. Meza, G. Ramírez-Rodríguez, and G. Benitez-King, "Melatonin stimulates calmodulin phosphorylation by protein kinase C," *Journal of Pineal Research*, vol. 37, no. 2, pp. 98–106, 2004.
- [42] L. Carrichon, A. Picciocchi, F. Debeurme et al., "Characterization of superoxide overproduction by the D-Loop_{Nox4}-Nox2 cytochrome *b*₅₅₈ in phagocytes—differential sensitivity to calcium and phosphorylation events," *Biochimica et Biophysica Acta*, vol. 1808, no. 1, pp. 78–90, 2011.
- [43] S. Kumari and D. Dash, "Melatonin elevates intracellular free calcium in human platelets by inositol 1,4,5-trisphosphate independent mechanism," *FEBS Letters*, vol. 585, no. 14, pp. 2345–2351, 2011.
- [44] J. Espino, I. Bejarano, P. C. Redondo et al., "Melatonin reduces apoptosis induced by calcium signaling in human leukocytes: evidence for the involvement of mitochondria and bax activation," *Journal of Membrane Biology*, vol. 233, no. 1–3, pp. 105–118, 2010.
- [45] J. Espino, I. Bejarano, S. D. Paredes, C. Barriga, A. B. Rodríguez, and J. A. Pariente, "Protective effect of melatonin against human leukocyte apoptosis induced by intracellular calcium overload: relation with its antioxidant actions," *Journal of Pineal Research*, vol. 51, no. 2, pp. 195–206, 2011.
- [46] G. R. Caspari, "The influence of colostrum leukocytes on the course of an experimental *Escherichia coli* infection and serum antibodies in neonatal calves," *Veterinary Immunology and Immunopathology*, vol. 13, pp. 620–624, 1964.
- [47] A. Hughes, J. H. Brock, D. M. V. Parrott, and F. Cockburn, "The interaction of infant formula with macrophages: effect on phagocytic activity, relationship to expression of class II MHC antigen and survival of orally administered macrophages in the neonatal gut," *Immunology*, vol. 64, no. 2, pp. 213–218, 1988.
- [48] M. Xanthou, "Immune protection of human milk," *Biology of the Neonate*, vol. 74, no. 2, pp. 121–133, 1998.